Interaction Notes

Note 336

October 1977

Advanced Aircraft EMP Model Development: Surface Currents and Charges Induced on Cylinders, Crossed Cylinders and Cylinders Crossed with Horizontal Flat Plates by a Normally Incident, Plane Electromagnetic Wave

T. T. Wu, R. W. P. King, D. J. Blejer,
S.-K. Wan, M. Owens, R. W. Burton
L. C. Shen, and M. E. Burton

Gordon McKay Laboratory
Harvard University
Cambridge, MA 02138

ABSTRACT

In this Final Report the complete step-by-step investigation of the currents and charges induced on the surface of a model of an aircraft by an incident plane electromagnetic wave is presented. A combination of numerical, analytical, and experimental methods was used to determine the axial and transverse components of the surface densities of current and charge in both amplitude and phase. The sequence of steps in the investigation included: (1) A complete analytically based study of currents and charges on single, electrically thick, tubular cylinders in both E- and H- polarized fields. (2) An experimental study of the corresponding currents and charges on the single tubular cylinder in an E-polarized field to develop and standardize probes and techniques and to determine the degree to which the experimentally available exciting field approximates a traveling plane wave. (3) An experimental study of crossed tubular cylinders using these probes, techniques, and field. (4) An experimental study of currents and charges on a tubular cylinder with a flat plate as the cross.

SUMMARY

This final report presents the complete step-by-step investigation of the currents and charges induced on the surface of a model of an aircraft by an incident plane electromagnetic wave which represents a single-frequency component of a possible electromagnetic pulse. The coordinated analytical and experimental study to determine the axial and transverse components of the surface densities of current and charge in both amplitude and phase included the following steps: (1) A complete analytically based study of currents and charges on single, electrically thick, tubular cylinders in both E- and H-polarized fields. (2) An experimental study of the corresponding currents and charges on the single tubular cylinder in an E-polarized field to develop and standardize probes and techniques and to determine the degree to which the experimentally available exciting field approximates a traveling plane wave. (3) An experimental study of crossed tubular cylinders using these probes, techniques, and field. (4) An experimental study of currents and charges on a tubular cylinder with a flat plate as the cross.

An introduction to the investigation is given in Section I, along with a more detailed description of the sequence of configurations treated and approaches used. The reader is referred both to later sections of this report and to published papers for further discussion of the results for the individual aspects of the study.

Section II presents a critical review of the approximations and limitations associated with the theory of thin cylinders and crossed thin cylinders that have orthogonal or non-orthogonal intersections. The specific application of thin-cylinder theory to electrically thick cylinders and crossed cylinders is discussed.

The theoretical determination of the distributions of surface densities of current and charge induced on an electrically thick, infinitely thin-walled, perfectly conducting, tubular cylinder by an incident, E-polarized, plane electromagnetic wave is reviewed in Section III. The theory is then applied to a cylinder with $ka = 1$ and $kh = 1.5\pi$ where a is the radius, h the half-length, and k the wave number. Extensive graphs of the axial and transverse distributions of the surface densities of current and of charge are presented. An analytical representation of these in terms of forced and

resonant transverse Fourier components is described and used to interpret the properties displayed in the graphs.

In Section IV the measurement of the surface densities of current and charge in both amplitude and phase over the entire surface of an electrically thick conducting tube (ka = 1) when illuminated by an E-polarized incident field is described. Use is made of a probe system consisting of a short monopole and two small mutually perpendicular shielded loops arranged to move axially as a unit along a groove in a thick-walled aluminum tube which can be rotated through 360°. Graphs of the measured magnitude and phase of the axial and transverse components of the surface density of current and of the surface density of charge on the outside surface of the tube are displayed as functions of the axial and transverse variables. Problems of measurement and of the correlation of measured and theoretical values are discussed. It is concluded that with proper attention to detail accurate measurements can be made and the distributions of current and charge understood.

The theoretical and experimental results presented in Sections III and IV for an electrically thick cylinder (ka = 1) with the resonant half-length kh = 1.5π and illuminated by an E-polarized field are extended in Section V to electrically quite long tubes excited by both E- and H-polarized plane-wave fields. A simple approximate analytical representation of the currents and charges is described in terms of forced and resonant transverse Fourier components for cylinders with lengths not restricted to those that are axially resonant. Extensive theoretical and measured graphs and contour diagrams of the distributions of current and charge density are displayed and compared specifically for tubes with the electrical radius ka = 1 and lengths up to kh = 3.5π.

Section VI describes an experimental study of the surface currents and charges induced on crossed electrically thick (ka = 1) conducting tubes on a ground plane by an incident plane wave. Two locations of the cross along the vertical cylinder and three lengths of the horizontal member are investigated and graphical representations of the distributions of current and charge displayed. The measured currents and charges are compared with the corresponding theoretical and measured quantities on each cylinder when isolated, and significant correlations are established.

In Section VII is described the theoretical and experimental determination of the surface densities of current and charge induced on tubular conducting cylinders and crossed cylinders by a normally incident plane wave when the cylinders are two wavelengths in circumference (ka = 2). Graphs of calculated and measured distributions of charge and current on single cylinders in E- and H-polarized fields and on crossed cylinders are displayed and discussed with special reference to earlier work on cylinders and crossed cylinders with ka = 1 (Sections III - VI). Difficulties arising from propagating waveguide modes and a nonplanar incident field are considered.

With the aid of graphs a detailed description is given in Section VIII of the experimentally determined distributions of the currents and charges induced by a normally incident plane electromagnetic wave on all of the surfaces of a metal cross formed by a vertical tubular cylinder and a horizontal flat plate. The cylinder is a wavelength in circumference and 1.75λ high over a large ground plane. The horizontal plate consists of two equal arms that extend 0.75λ from the surface of the cylinder; it is 0.2125λ wide and 0.0255λ thick. It is centered at a height of 1.25λ from the ground plane. The distributions are compared with the corresponding ones on crossed tubular cylinders and on isolated cylinders.

CONTENTS

ILLUSTRATIONS

TABLES

SECTION I

INTRODUCTION

The purpose of this investigation has been a systematic study of the electric currents and charges induced on the metal skin of a model of an aircraft when illuminated by a plane electromagnetic wave that corresponds to a representative single-frequency component of a possible electromagnetic pulse. The plan of the study includes the coordinated use of both analytical and experimental tools in a step-by-step manner that involves a continuous verification of techniques and results. Like the earlier investigations of thin-wire models which began with the theoretical and experimental determination of currents and charges in single conductors (ref. 1) and were then extended to develop new experimental (ref. 2) and analytical (ref. 3) techniques for crossed wires, the present study has proceeded from single, electrically thick, thin-walled tubular cylinders to crossed thick tubes. The tubular cylinder with circular cross section and open end was chosen as the basic element because it is the only reasonable shape for which a complete theory is available. Specifically, distributions of the surface densities of current and charge can be computed from theoretical formulas for arbitrary lengths and radii with both E- and H-polarizations. The essential quantitative foundation for developing and verifying experimental techniques is thus available. And an aircraft modeled by crossed tubular cylinders, while not accurate in structural detail, is quite comparable in a general three-dimensional sense so that all relevant properties of representative induced transverse and axial currents with the associated charges can be studied. The extension of the model to closed-end tubes for the fuselage and a flat plate for the wings is readily made once accurate experimental techniques have been developed and verified with the crossed cylinders with open ends. Thus the sequence of steps involves (1) a complete analytically based study of currents and charges on single, electrically thick, tubular cylinders in both E- and H-polarized fields; (2) an experimental study of the corresponding currents and charges on the single tubular cylinder in an E-polarized field to develop and standardize probes and techniques and the degree to which the experimentally available exciting field approximates a traveling plane wave; (3) an experimental study of crossed tubular cylinders using these probes, techniques, and field; and

(4) an experimental study of currents and charges on a tubular cylinder with a flat plate as the cross. In all cases the axial and transverse components of the surface density of current and the surface density of charge are determined in both amplitude and phase.

The theoretical calculation of the axial and transverse surface densities of current and charge on electrically thick (ka = 1) tubular cylinders in a plane-wave field is carried out in Section III for an electrical half-length of kh = 1.5π (E-polarization), and in Section V for kh = 3π and 3.5π (E-polarization), and kℓ = 1.5π and 2π (H-polarization). A rotation of the plane of polarization for the normally incident field yields currents and charges that are simple superpositions of the E- and H-polarized values multiplied by cos ϕ and sin ϕ, respectively, where ϕ is the angle about the vertical axis. (No theory is available for vertical angles of incidence other than $\theta = 90°$, the normally incident case, for electrically thick cylinders, and the difficult analytical problem was not undertaken.)

The theoretical formulas are general and can be applied to any desired radius. Specific calculations are reported in Section II with ka = 0.05, in Sections III and V with ka = 1, and in Section VII for ka = 2.

The effect of a linear variation in the radius of a tubular cylinder at constant length and frequency of excitation is manifested primarily in the complex coefficients of the transverse Fourier components. When $ka \ll 1$, the rotationally symmetric, zero component dominates with very small transverse currents. As ka approaches unity, the first transverse resonance develops and the associated first Fourier component becomes dominant with its cos θ distribution of axial current and large transverse currents within a quarter wavelength of the end. As ka is increased further, the first component decreases and the second grows to a relatively large value at ka = 2, the second transverse resonance, with a large cos 2θ component of axial current and corresponding large transverse currents in the quarter wavelength at the open end. The first component is still significant, and the distributions of current and charge involve large parts of both first and second transverse Fourier components. This process continues as ka is increased further. The simple representation in terms of the superposition of forced and resonant transverse Fourier components (ref. 4) applies for all values of the radius.

Measured distributions of current and charge induced on electrically thick cylinders are in Sections IV and V for ka = 1 with kh = 1.5π, 3π, and 3.5π; in Section VII for ka = 2 with kh = 3.5π. The measured distributions on all single cylinders are for E-polarization (TM illumination) since this is the only available polarization when a ground plane is used. Measured distributions for H-polarization (TE illumination) are carried out for the horizontal member of crossed cylinders in Sections VI and VII, and compared to theoretical distributions for an isolated cylinder excited by an H-polarized wave. The transverse distributions are shown to be largely independent of the length of the cylinder in H-polarization.

An experimental study of the distributions of the current and charge densities on a tubular cylinder when the end is open and capped successively with flat and hemispherical metal surfaces is in Section IV for ka = 1 and in Section VII for ka = 2. It is shown that except within very short distances of the end, all of the distributions of outside currents and charges are substantially the same in both amplitude and phase so long as no internal propagating waveguide modes can be excited. It is safe to conclude that this is generally true when ka is at least somewhat below the cut-off value for propagating waveguide modes in the interior.

The general problem of currents and charges on and near junctions of cylindrical conductors is discussed in Section II. A complete determination of the currents and charges per unit length near the junction of electrically thin conductors is in reference 3 and corresponding measurements are in reference 2. As explained in Section II, thin-wire theory determines the rotationally symmetric, total currents and associated charges per unit length to within distances of about 5a from the center of the junction and extrapolates these to the center. The analysis in reference 3 applies to mutually perpendicular crossed cylinders with arbitrary lengths and locations of the junction but with equal radii. The electromagnetic field is assumed to be normally incident with the electric vector parallel to the vertical cylinder. It is further assumed that all transverse currents on the conductors are negligible, that axial currents are approximately rotationally symmetric, and that the surface area of the junction region is so small that charges on it can be neglected. The quantitative significance of these assumptions and the approximate maximum allowable value of ka = $2\pi fa/c$ are discussed in Section II.

Within these limitations, application of the theory has been made in reference 3 to the critical cases involving various combinations of resonant and antiresonant lengths for the vertical and horizontal members. An extension of the theory to symmetrical crossed thin cylinders in an electromagnetic field that is not normally incident has been reported (ref. 5). The generalization of the theory of crossed wires with equal radii to wires with unequal radii is given in Section II. The junction conditions for conductors with unequal radii have been determined in the process of developing a complete theory for the tapered antenna (ref. 6). Finally, the generalization of the analysis in reference 3 to non-orthogonal junctions is discussed in Section II.

Extensive measurements of current and charge distributions on crossed cylinders have been carried out. Measurements made on crossed thin cylinders are in reference 2. Measured surface densities of current and charge on crossed, electrically thick cylinders are described in Sections VI and VII for ka = 1 and ka = 2, respectively. Two different positions of the junction, and three different lengths for the horizontal arm are considered in Section VI. Since no analytical solution is available for determining the surface densities of current and charge in the junction region of crossed electrically thick tubular cylinders, they have been determined by direct measurement. The results for different lengths of the side arms and locations along the vertical cylinder are given and discussed in Sections VI and VII for crossed cylinders with ka = 1 and ka = 2.

Detailed measurements of the surface current and charge densities on all surfaces, including the near vicinity of the junction, of a tubular cylinder and an intersecting flat plate are described in Section VIII together with a discussion of the relative independence of the distributions on the two members except very near their junction. Only a single plate, approximately a half wavelength in width, was investigated because of the structural difficulty of providing an adequate number of slots for probe travel in electrically narrow plates at the high frequency required by the size of the ground plane.

SECTION II

THIN-CYLINDER THEORY: A REVIEW OF ITS APPROXIMATIONS, LIMITATIONS, AND EXTENSIONS

1. THE CONDITIONS THAT UNDERLIE THIN-CYLINDER THEORY

The thin-wire theory of cylindrical antennas involves a number of basic conditions and assumptions without which its relatively simple quasi-one-dimensional form is invalid. For a straight cylinder with radius a and length 2h these conditions are:

$$ka << 1 \quad ; \quad a << h \quad ; \quad kh \geq 1 \tag{1}$$

where $k = 2\pi f/c = 2\pi/\lambda$ is the wave number. The simplifying consequences of these inequalities include approximate rotational symmetry of the surface densities of axial current and charge and the absence of significant transverse currents so that the surface densities of current $\vec{K}(\theta,z)$ and charge $\eta(\theta,z)$ can be simplified as follows:

$$\vec{K}(\theta,z) = \hat{\theta}K_\theta(\theta,z) + \hat{z}K_z(\theta,z) \doteq \hat{z}K_z(\theta,z) \doteq \hat{z}K_z(z) \quad ; \quad K_\theta(\theta,z) \doteq 0 \tag{2}$$

$$\eta(\theta,z) \doteq \eta(z) \tag{3}$$

It follows that the total axial current $I_z(z)$ and the charge per unit length $q(z)$ can be defined as follows:

$$I_z(z) = 2\pi a K_z(z) \quad ; \quad q(z) = 2\pi a \eta(z) \tag{4}$$

The charge density is related to the current density through the equation of continuity as follows:

$$\eta(\theta,z) = -\frac{i}{c}\left[\frac{\partial K_z(\theta,z)}{k\,\partial z} + \frac{1}{ka}\frac{\partial K_\theta(\theta,z)}{\partial\theta}\right] \tag{5}$$

The corresponding simplified equation for the total current and charge per unit length in thin-wire theory is

$$q(z) = -\frac{i}{\omega}\frac{\partial I_z(z)}{\partial z} \tag{6}$$

The actual degree of rotational symmetry in $K_z(\theta,z)$ can be estimated

from the infinitely long conductor in an E-polarized field. Thus, when ka << 1, the general formula for the current density with E-polarization (Eq. 2.3 in ref. 4) reduces to

$$K_z(\theta)/E_z^{inc} = \frac{2}{\pi\zeta_0 ka}\left\{\frac{1}{1 - (2i/\pi)[\ell n(2/ka) + 0.577]} - \pi ka \cos\theta\right\} \quad (7)$$

The relative magnitude of $K_\theta(\theta,z)$ can be obtained from the companion formula (Eq. 2.4 in ref. 4) for H-polarization, for which

$$K_\theta(\theta)/E_x^{inc} = -\frac{1}{\zeta_0}(1 + 2ika\cos\theta) \quad (8)$$

The leading rotationally symmetric terms are

$$[kaK_z(\theta)/E_z^{inc}]_0 = I_z/\lambda E_z^{inc} = \frac{2}{\pi\zeta_0}\left\{\frac{1 + (2i/\pi)[\ell n(2/ka) + 0.577]}{1 + (4/\pi)^2[\ell n(2/ka) + 0.577]^2}\right\} \quad (9)$$

$$[K_\theta(\theta)/E_x^{inc}]_0 = -\frac{1}{\zeta_0} \quad (10)$$

Specifically, when ka = 0.04,

$$\frac{K_z(\theta)}{E_z^{inc}} = 0.0045[1 + i2.89 - 1.15\cos\theta] \quad A/V \quad (11)$$

$$\frac{K_\theta(\theta)}{E_x^{inc}} = -0.00265[1 + i0.08\cos\theta] \quad A/V \quad (12)$$

The normalized magnitudes of $K_z(\theta)$ at $\theta = 0°$, 90° and 180° are:

$$|K_z(\theta)/E_z^{inc}| = 0.013,\ 0.0138,\ 0.0162 \quad A/V \quad (13)$$

It is evident from (11) and (12) that $K_\theta(\theta)$ is negligible compared with $K_z(\theta)$ and that this latter is only roughly rotationally symmetric with a 17% increase over the zero-order term at $\theta = 180°$ on the illuminated side, a 6% decrease at $\theta = 0°$ on the shadow side. These differences decrease as

ka is reduced below ka = 0.04, which is approximately the upper limit for thin-wire theory when interest is in the surface currents and charges and the very near field. For antennas of finite length the transverse distributions vary significantly with the location kz in the axial standing-wave pattern, since they are superpositions of the forced and resonant distributions. This can be seen from Fig. 1 which shows the Fourier components of the axial surface density of current $K_z(\theta,z)$ in terms of the significant complex Fourier components for a resonant length, viz., kh = 1.5π, with ka = 0.05. For a conductor as thin as this only the coefficients A(kz) = $A_R(kz) + iA_I(kz)$ of the rotationally symmetric zero-order term and B(kz) = $B_R(kz)$ of the cos θ term are significant. $B_I(kz)$ and all higher-order terms are negligibly small. On the right are the corresponding coefficients $A = A_R + iA_I$ and $B = B_R + iB_I$ of the infinitely long conductor. As described in detail in Sections III and V,

$$A(kz) = A_f(kz) + A_r(kz) \doteq Ae(kz) + A_r \cos kz \tag{14}$$

$$B(kz) = B_f(kz) + B_r(kz) \doteq Be(kz) + B_r \cos kz \tag{15}$$

for a resonant length. The function e(kz) characterizes the forced current on a conductor of finite length. It has the value one for all values of kz except within the ranges $\pi/2$ of open ends where it decreases smoothly to zero as shown in Fig. 19 (Section III). The superposition of these components yields the distributions of surface current density $K_z(\theta,z)$ and normalized surface charge density $cn(\theta,z)$ shown in amplitude and phase in Fig. 2 for kh = 1.5π and ka = 0.05 with $\theta = 0°$, 90° and 180°. Except close to the open end, the charge density is essentially independent of θ. The current densities at $\theta = 0°$, 90°, and 180° differ in relative amplitudes with generally similar axial distributions. It is noteworthy that the current density is greater on the illuminated side than in the shadow between kz = slightly less than 0.5π and 1.5π, but greater on the shadow side between kz = 0 and slightly less than 0.5π. This is a consequence of the fact that the forced current is added to the resonant current between kz = 0.5π and 1.5π, subtracted from it between kz = 0 and 0.5π. The actual transverse distributions of $K_z(\theta,z)$ are shown in Fig. 3 for a range of values of kz. Also shown is the transverse distribution for the infinitely long cylinder

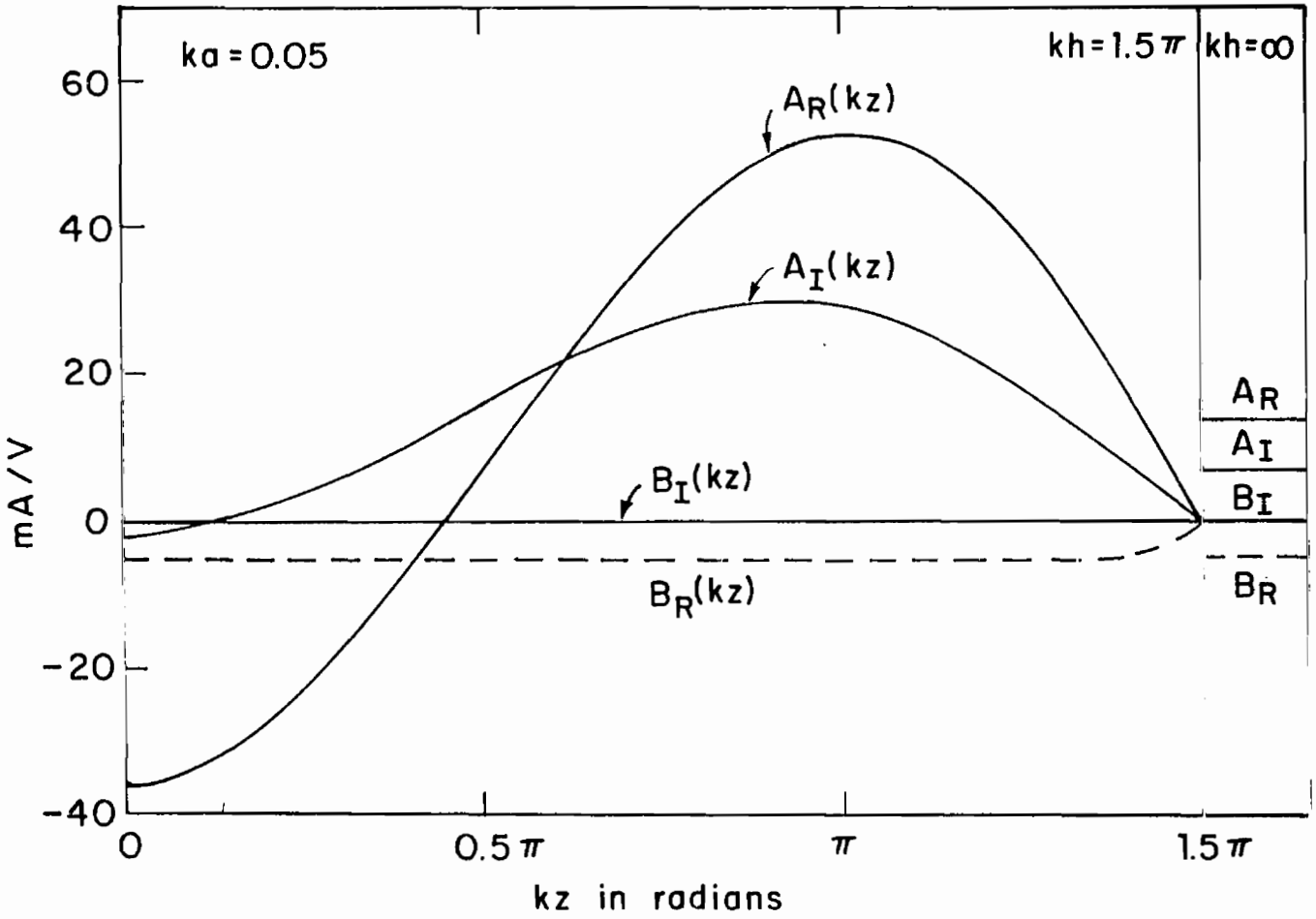

Fig. 1. The complex Fourier coefficients of the axial surface density of current, $K_z(\theta,z) = A(kz) + B(kz)\cos\theta$.

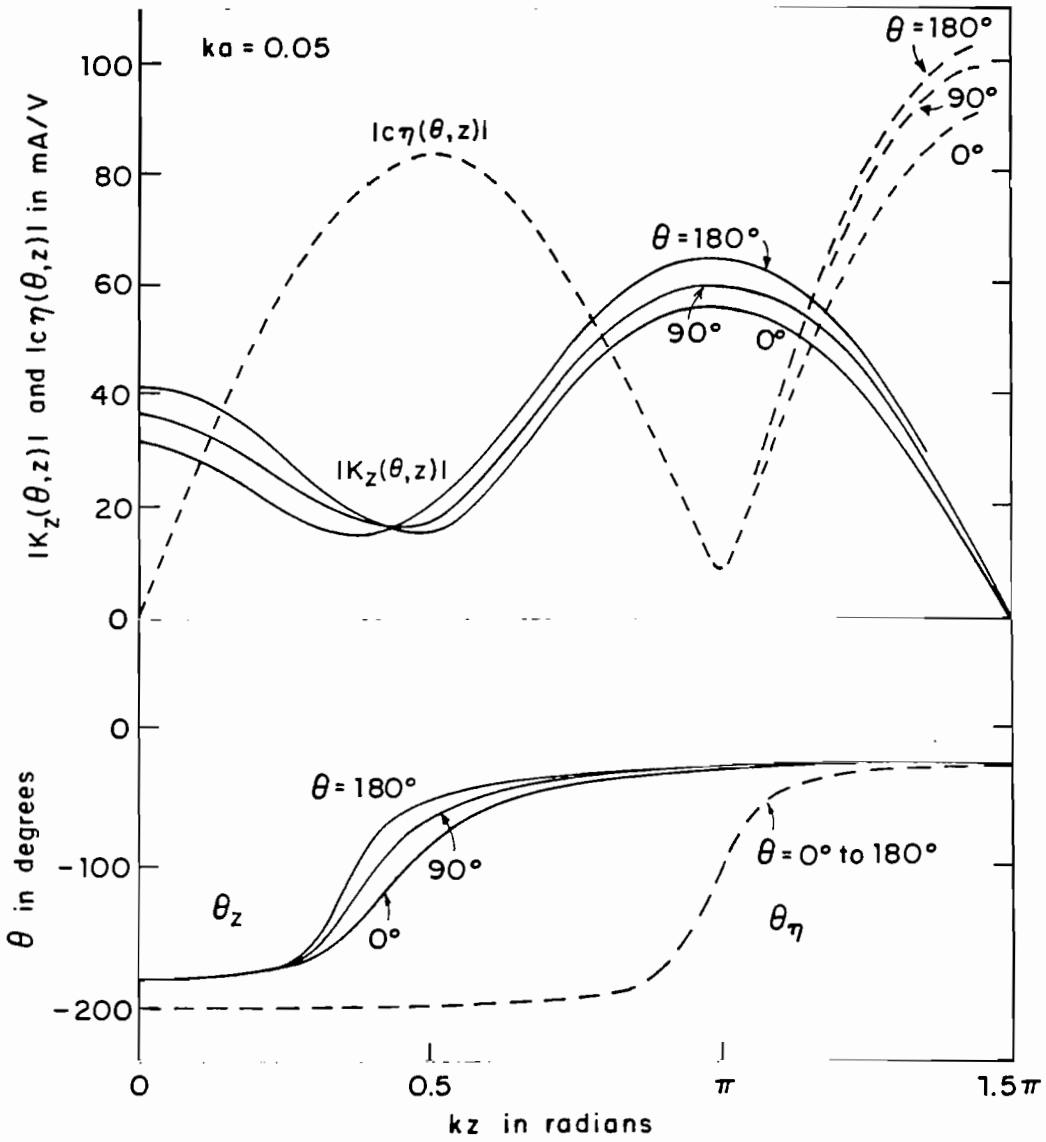

Fig. 2. Axial distributions of the surface densities of axial current $K_z(\theta,z)$ and charge $c\eta(\theta,z)$ for tubular cylinder in normally incident E-polarized field; kh = 1.5π ($c = 3 \times 10^8$ m/sec).

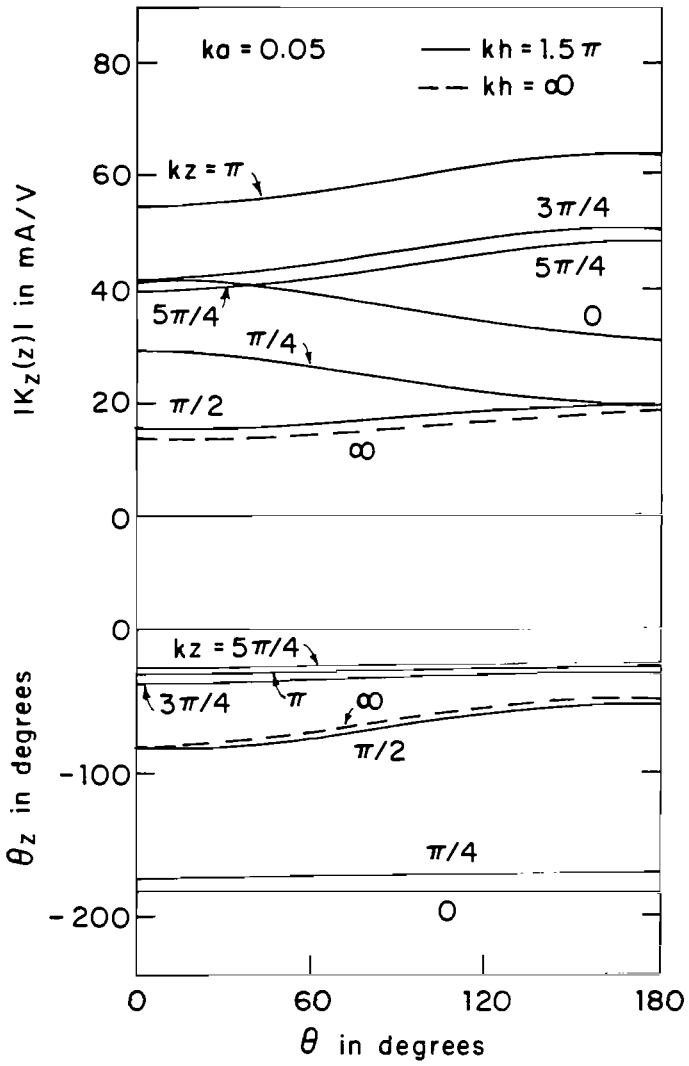

Fig. 3. Transverse distributions of axial surface density of current on tubular cylinder in normally incident E-polarized field, kh = 1.5π and ∞.

with ka = 0.05. This is seen to follow closely the distribution with kz = 0.5π, where the resonant current vanishes and only the forced current remains.

The end conditions for thin-wire theory require the total axial current $I_z(z)$ to vanish at the open ends, $|z| = h$, of thin-walled tubular cylinders. That is,

$$I_z(\pm h) = 0 \tag{16}$$

If this condition is rigorously enforced, the total currents and charges are correctly determined when $ka \ll 1$. However, the axial distribution of the current and especially of the charge per unit length vary rapidly near the open end so that low-order solutions usually do not provide the correct slope for the current. It follows that within a fraction of a wavelength of the open end the charge per unit length calculated from a low-order solution can be in error by as much as a factor 2. The outside current and charge per unit length on thin tubular cylinders with open ends, with flat end caps, and hemispherical end caps are quite similar if the total axial length is the same.

2. THE CONDITIONS THAT UNDERLIE THE THEORY OF ORTHOGONALLY INTERSECTING THIN CYLINDERS

Consider two electrically thin cylinders that lie, respectively, along the x and z axes with their junction centered at the origin of coordinates. The vertical wire extends from $z = -h_1$ to $z = h_2$ with radius a_1, the horizontal wire from $x = -\ell_1$ to $x = \ell_2$ with radius a_3. For the four parts of the cross the conditions for thin-wire theory apply. That is,

$$ka_1 \ll 1, \quad a_1 \ll h_1, \quad a_1 \ll h_2, \quad kh_1 \geq 1, \quad kh_2 \geq 1 \tag{17}$$

$$ka_3 \ll 1, \quad a_3 \ll \ell_1, \quad a_3 \ll \ell_2, \quad k\ell_1 \geq 1, \quad k\ell_2 \geq 1 \tag{18}$$

At each open end the total current vanishes so that

$$I_{1z}(-h_1) = I_{2z}(h_2) = I_{3x}(-\ell_1) = I_{4x}(\ell_2) = 0 \tag{19}$$

The comments regarding the currents and charges near the open ends made

relative to (14) and (15) apply to each of the four ends.

The junction conditions at $z = 0$ for thin-wire theory are:

$$I_{1z}(0) - I_{2z}(0) + I_{3x}(0) - I_{4x}(0) = 0 \tag{20}$$

$$q_1(0)\Psi_1 = q_2(0)\Psi_2 = q_3(0)\Psi_3 = q_4(0)\Psi_4 \tag{21}$$

where, for conductors at least a quarter wavelength long,

$$\Psi_1 = \Psi_2 = 2[\ell n(2/ka_1) - 0.5772] \quad , \quad \Psi_3 = \Psi_4 = 2[\ell n(2/ka_3) - 0.5772] \tag{22}$$

For shorter conductors,

$$\Psi_1 = \Psi_2 \doteq 2\ \ell n(\sqrt{h_1 h_2}/a_1) \quad , \quad \Psi_3 = \Psi_4 \doteq 2\ \ell n(\sqrt{\ell_1 \ell_2}/a_3) \tag{23}$$

In (20) and (21), $I_j(0)$ and $q_j(0)$, $j = 1, 2, 3, 4$, are fictitious rotationally symmetric currents and charges per unit length extrapolated to $z = 0$ or $x = 0$ from $z \sim 5a_1$ or $x \sim 5a_3$ where the currents and charges per unit length are approximately rotationally symmetric. The junction conditions are designed to assure that the currents and charges at distances greater than $5a_j$ from $x = 0$, $z = 0$ are correct. Closer to the junction than $|x| = 5a_3$ or $|z| = 5a_1$, the currents and charges per unit length have complicated transverse distributions that are not rotationally symmetric but are determined by the geometry and proximity of the junction region. Thin-cylinder theory is incapable of determining these distributions, and they are irrelevant to the evaluation of I and q at all points given by $|z| > 5a_1$, or $|x| > 5a_3$ so long as $ka \ll 1$.

The conditions (17) and (18) include the following:

$$kh_1 \geq 1 \quad , \quad kh_2 \geq 1 \quad , \quad k\ell_1 \geq 1 \quad , \quad k\ell_2 \geq 1 \tag{24}$$

These have serious consequences in the low-frequency modeling of aircraft by crossed electrically thin cylinders since they require each of the four arms with lengths h_1, h_2, ℓ_1 and ℓ_2 to be at least $\lambda/6$ in length. Thus, thin-cylinder theory cannot be expected to give accurate results in the determination of the currents and charges per unit length if the frequency is lower than allowed by the following conditions:

$$f \geq c/2\pi h_1 \quad , \quad f \geq c/2\pi h_2 \quad , \quad f \geq c/2\pi \ell_1 \quad , \quad f \geq c/2\pi \ell_2 \tag{25}$$

where $c = 3 \times 10^8$ m/sec even though the conditions $ka_1 << 1$, $ka_3 << 1$ are satisfied. In effect this means that a thin-wire model of an aircraft must be at least a half wavelength long at the lowest frequency.

Even when all of the conditions of the thin-cylinder theory of crossed cylinders are well satisfied, the solutions obtained do not provide the actual distributions of current and charge density on the surfaces within distances of $5a_1$ or $5a_3$ of the center of the junction. It gives only a fictitious, rotationally symmetric average that does not take account of the actual geometry of the junction region.

The solutions for the currents in a thin-wire cross in reference 3 have been carried out for conductors of equal radius. The generalization to conductors with different radii involves only the addition of subscripts 1 and 3 respectively on the Ψ functions derived from integrals along the z-directed and x-directed coordinates.

3. THIN-CYLINDER THEORY AND CYLINDERS THAT ARE NOT ELECTRICALLY THIN

Tubular cylinders that are not electrically thin have very much more complicated distributions of the surface densities of current and charge than cylinders that are electrically thin when illuminated by a normally incident plane wave. With E-polarization (electric field parallel to the axis of the cylinder) the surface density of current has axial and transverse components which are both functions of the axial and transverse variables. Thus, $\vec{K}(\theta,z) = \hat{\theta}K_\theta(\theta,z) + \hat{z}K_z(\theta,z)$. The two-dimensional vector $\vec{K}(\theta,z)$ is in general elliptically polarized since $K_\theta(\theta,z)$ and $K_z(\theta,z)$ are not simply related in amplitude or phase. The transverse component $K_\theta(\theta,z)$ is generally small except within a half wavelength of an open end where it rises to very large values. The transverse distributions of both $K_z(\theta,z)$ and $K_\theta(\theta,z)$ are not rotationally symmetric. They are determined from sums of transverse Fourier components of which the first or zero-order term in the series for $K_z(\theta,z)$ is alone rotationally symmetrical. Only when all higher-order terms have negligibly small amplitudes is the zero-order term an adequate representation of $K_z(\theta,z)$, and it is this term only that is determined by thin-cylinder theory in the form $I_z(z) = 2\pi a[K_z(z)]_0$. This is

meaningful only when ka << 1. There is no way of determining the higher-order terms from the first term and as ka increases from small values they become dominant. The transverse component $K_\theta(\theta,z)$ is assumed to be completely absent in thin-wire theory so it cannot be determined or even roughly estimated. Zero cannot be extrapolated to a meaningful finite value!

With H-polarization (magnetic field parallel to the axis of the cylinder), $\vec{K}(\theta,x)$ has both transverse and axial components with $K_\theta(\theta,x)$ large for all values of the axial variable when ka is not small. Both components of current combine with the charge density to form complicated standing-wave patterns over the entire cylindrical surface. Thin-cylinder theory takes no account of any currents excited by an H-polarized field since they are all assumed to be negligible — which is an acceptable approximation only when ka << 1. Thus, there is no way of determining either the transverse variation of the axial current or any part of the entire transverse current from thin-cylinder theory or computer codes based on it. When the thin-cylinder conditions are reduced or eliminated, the theory loses its validity.

The axial distribution of the axial component of current $K_z(\theta,z)$ resembles $I_z(z)$ along a thin cylinder with the same length for some values of the transverse variable θ for either polarization. Both are superpositions of forced and resonant components, but the proportions vary with θ when ka is not small with the forced components dominant on the illuminated side, the resonant ones on the shadow side. Thus, it is possible to exhibit somewhat comparable axial distributions of the amplitude of $K_z(\theta,z)$ along a thick cylinder and of $K_z(z) = I_z(z)/2\pi a$ along a thin one at selected values of θ. However, there is no way of determining the appropriate value of θ from thin-cylinder theory. Hence, $K_z(\theta,z)$ for all other values of θ on the thick cylinder remains unavailable.

The practical upper bound on $ka = 2\pi fa/c$ limiting the use of thin-cylinder theory for single cylinders of finite length is more severe when interest is in surface currents and charges and the associated near fields than when only far fields are required. The upper bound is determined by the degree of error in the amplitudes that is acceptable. Specifically, the allowable maximum difference between $K_z(\theta,z)$ at $\theta = 180°$ on the illuminated side and the thin-cylinder approximation $K_z(z) = I_z(z)/2\pi a$ must be specified

together with the maximum allowable transverse current $K_\theta(\theta,z)$. It has already been shown that when ka = 0.04, $|K_z(180°,z)|$ differs from $|K_z(z)| = |I_z(z)/2\pi a|$ for the infinitely long cylinder by approximately 17%. This is also an approximate value near current minima along a resonant cylinder of finite length with the same value of ka. The minima of current occur near $kz = n\pi/2$, $n = 0, 1, 2, \ldots$.

The end conditions for the current density on tubular cylinders with open ends and unrestricted values of ka are contained in the boundary conditions on the tangential component of the electric and magnetic fields on the surfaces of the cylinder. These are $E_z(\theta,z) = 0$, $E_\theta(\theta,z) = 0$ for all values of θ and $-h \leq z \leq h$ on both inside and outside surfaces of the thin-walled tube. The inside and outside surface densities of current are given by $\vec{K}(\theta,z) = -\hat{n} \times \vec{B}/\mu_0$ where $\hat{n}$ is the external normal to the surfaces. Note that $\hat{n}$ is in the inward radial direction for the inside current, the outward radial direction for the outside current. These conditions are equivalent to requiring the total $K_z(\theta,z)$, i.e., the sum of outside and inside currents, to vanish at $z = \pm h$ and $K_\theta(\theta,z)$ to satisfy an edge condition. When ka << 1, the boundary condition $E_\theta(\theta,z) = 0$ is ignored, $K_\theta(\theta,z)$ is assumed to be negligible, and only the condition $K_z(\theta,z) \doteq K_z(z) = 0$ at $z = \pm h$ is applied directly. Since the inside current is negligibly small when ka << 1, $K_z(z) = I_z(z)/2\pi a$ applies to the outside current. It is evident that the thin-wire end conditions are incapable of correctly bounding the transverse currents which are highly significant near open ends.

4. THIN-CYLINDER THEORY AND INTERSECTING CYLINDERS THAT ARE NOT ELECTRICALLY THIN

The junction conditions (20) and (21) for intersecting thin cylinders are expressed in terms of fictitious rotationally symmetrical total currents and charges per unit length at an idealized junction with so small a surface area that charges on it are ignorable. The thin-wire junction conditions are designed to give the correct currents and charges per unit length at distances greater than about five times the radius of the conductor, but provide no detailed information about the current and charge densities near and on the surfaces of the junction. Clearly, they have no useful application when ka is not small. The nonrotational nature of the

axial currents, the presence of significant transverse currents, the fact that the surface area of the junction itself is not electrically small and carries large currents and charges, and the dependence of the surface density of charge on the spatial rates of change of both axial and transverse components of current make the thin-cylinder conditions meaningless for cylinders that are not electrically thin. The conditions at the junction of electrically thick cylinders are contained in the requirement that the component of the electric field tangent to all parts of the conducting surface of the junction vanish. In the sharp grooves at the junctions of the intersecting circular cylinders, the component of the electric field perpendicular to the surface must vanish since the normal to one of the intersecting surfaces has a component tangent to the other surface. It follows that the charge density at the bottom of the grooves must vanish and with it the component of surface current along the bottom of the groove. Thus, the vector surface density of current must be directed perpendicular to each groove. These conditions apply equally to intersecting electrically thick and electrically thin cylinders and must be used for all values of ka if the distributions of current and charge on and very near the junction are to be determined. With electrically thin intersecting cylinders ($ka << 1$) a knowledge of the distributions of charge and current on and near the junction is not required to determine the total currents and charges per unit length away from the junction. These are independent of the shape of the junction region so long as its surface area is electrically of the order of magnitude of $k^2a^2 <<< 1$.

The theory of crossed electrically thin cylinders developed in reference 3 provides quantitatively useful approximations of the total currents and charges per unit length at all points along cylinders that permit the simplifications of thin-wire theory because $ka << 1$ except on and very near the junction. Here rotationally symmetric currents and charges do not actually exist, and the fictitious ones determined by thin-wire theory are equivalent to the actual complicated distributions only in permitting the determination in a quasi-one-dimensional form of all properties not too close to the junction. The actual current and charge densities within 5a of the junction cannot be determined with thin-wire theory no matter how small ka may be. When ka is not very small, the limitations of thin-wire theory are most pronounced (a) near the open ends where the effects of

nonrotational symmetry, transverse currents and the associated charges are most significant, and (b) on conductors excited by a component in the H-polarization with significant transverse currents and associated charges along its entire length.

5. THEORY OF NON-ORTHOGONALLY INTERSECTING ELECTRICALLY THIN CYLINDERS; THIN-WIRE MODEL OF SWEPT-WING AIRCRAFT

In order to apply thin-cylinder theory to the determination of the total currents and charges per unit length on crossed conductors that intersect at angles other than 90° either as continuing crosses or to simulate a swept-wing configuration, all of the thin-wire conditions previously imposed with orthogonal crosses are required. An additional restriction on the angle of intersection must also be used in order to keep the junction region electrically small enough to preserve the assumption that the total charge on its surfaces is negligible. The new condition is

$$\left|ka/\sin\theta\right| \ll 1 \tag{26}$$

where θ is the angle between the crossed conductors. For orthogonal intersection, $\theta = \pi/2$; and (26) reduces to the previously imposed, less restrictive, $ka \ll 1$.

The integral equations for the currents in non-orthogonally intersecting electrically thin cylinders are derived in the same manner as for the orthogonal cross (ref. 3), but numerous additional integrals occur since the crossed conductors are now coupled inductively as well as capacitively. This substantially increases the complication of both the zero-order and especially the first-order solutions. Unlike the simpler orthogonal geometry for which all first-order integrals can be reduced to nothing more complicated than tabulated integral sine and cosine functions, the non-orthogonal geometry involves integrals that must be evaluated numerically.

The actual formulation of the swept-wing configuration of non-orthogonally intersecting, electrically thin cylinders is not included here since it is not closely related to any of the other work reported on orthogonally intersecting thick and thin cylinders. The more severe restriction on the radius of the cylinders makes the theory even less useful at low frequencies since the conditions $\left|ka/\sin\theta\right| \ll 1$ and $kh \ll 1$ for all intersecting

members are difficult to satisfy simultaneously for dimensions comparable with those of actual aircraft. It would appear that the current and charge densities on the swept-wing configuration should be determined by an experimental study at both low and high frequencies using a tubular cylinder to represent the fuselage and successively tubular cylinders and flat plates to model the wings of an aircraft in the manner carried out in Sections VI, VII and VIII for the orthogonal cases. Measurements at both high and low frequencies should be made and the latter should be correlated with the fully developed and, where necessary, numerically evaluated thin-cylinder theory. In this manner it should be possible to determine whether a range of reasonable quantitative approximation exists for this theory. Since the junction region is expanded and the theory can give no detailed information about current and charge densities on and near the junction within distances of $5a/\sin\theta$, this is doubtful.

SECTION III

ELECTRICALLY THICK CYLINDER IN E-POLARIZED, NORMALLY INCIDENT, PLANE-WAVE FIELD, THEORY, kh = 1.5π, ka = 1

1. INTRODUCTION

When a rocket or aircraft is exposed to an electromagnetic field, currents are induced on the metal surfaces with complicated standing-wave distributions that depend on the frequencies, the shape and size of the structure, and its orientation in the wave fronts. In general, the metal surfaces have apertures and joints through which the field may penetrate. Its magnitude can be estimated from the surface densities of current and charge on the same structure with an unbroken metal skin (ref. 7). Since the determination of these densities is difficult, a systematic, step-by-step approach has been followed in order to gain insight into the physical and mathematical aspects of the problem. The first step was a theoretical review and experimental study of the currents and charges induced on a perfectly conducting cylinder that is electrically thin but unrestricted in length when in an arbitrarily incident plane wave (ref. 1). In this the significant differences between the distributions of current along a thin driven cylinder and a parasitic cylinder of the same length and radius were noted. The next step was a complete theoretical (ref. 3) and experimental (ref. 2) investigation of currents and charges on crossed electrically thin cylinders in an incident field. This involved a specification of the conditions at the junction of the four confluent wires and the formulation and solution of a new integral equation. Graphs from both theoretical and experimental investigations were displayed showing the currents and charges on all members of the cross when the junction was located at various points in the standing-wave patterns on the axial and transverse members including especially maxima and minima of charge per unit length near the junction.

Distributions of current and charge along electrically thin conductors are much simpler than on the surfaces of electrically thick structures because transverse currents on the thin conductors and the charge on the junction are negligible. Furthermore, the surface currents can be combined into a total axial current, $I_z = 2\pi a K_z$, where K_z is the surface density of axial current, and the surface charges into a charge per unit length, $q = 2\pi a \eta$,

where η is the surface density of charge. On an electrically thick structure these simplifications are not possible because rotational symmetry does not obtain and transverse currents are not negligible. Also, the surface area of a junction is not electrically small and its surface charge cannot be neglected.

Since a complete theory of the thick* tubular cylinder is available for both E and H polarizations (refs. 8-11), the same sequence in the investigation of thick cylinders can be pursued as was followed in the study of thin wires. The first step is a review of the theoretical treatment of the thick tubular cylinder followed by a display and discussion of the induced distributions of surface current and charge on typical cylinders. This is the subject of this section, specifically for E-polarization. The next step is the measurement of currents and charges on such a cylinder and a comparison with theory as a means of standardizing the experimental procedures and calibrating the probes. This is the subject of Section IV. Later steps will involve the currents and charges on crossed electrically thick cylinders.

2. THEORETICAL CURRENTS ON THE INFINITELY LONG CYLINDER

The theory of the scattering of electromagnetic waves by an infinitely long, perfectly conducting cylinder of any thickness is well known (ref. 12). A cross section of the cylinder in an incident field is shown in Fig. 4. Complete descriptions of the physical properties of the electric and magnetic fields at and near the surface of such a cylinder are available in reference 13. The distribution of the axial surface density of current $K_z(\theta)$ for E-polarization and that of the transverse surface density of current $K_\theta(\theta)$ for H-polarization have also been described (ref. 13). Graphs of the magnitude and phase** of $K_z(\theta) = |K_z(\theta)| \exp(i\theta_z)$ are shown in Fig. 5 for an infinite, perfectly conducting cylinder with $ka = 1$ in an E-polarized, normally incident electromagnetic field. The choice $ka = 1$ is made since this size involves most of the characteristics of electrically thick cylinders without

---

*This means with electrically large cross section; it does not refer to the thickness of the metal walls which are assumed to be infinitely thin.

**Graphs of the real and imaginary parts of $K_z(\theta) = K_{zR}(\theta) + iK_{zI}(\theta)$ are included in Fig. 8.

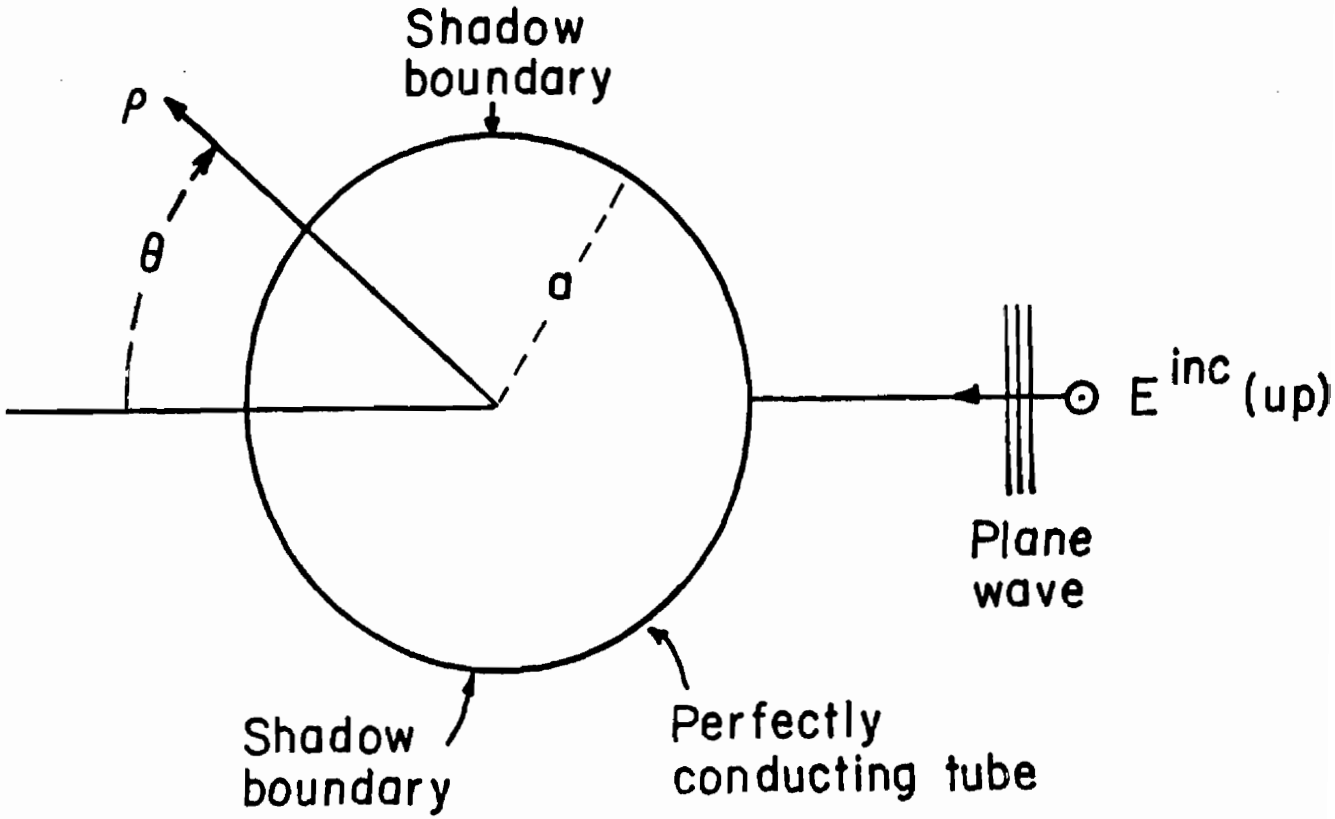

Fig. 4. Conducting cylinder in incident E-polarized plane-wave field.

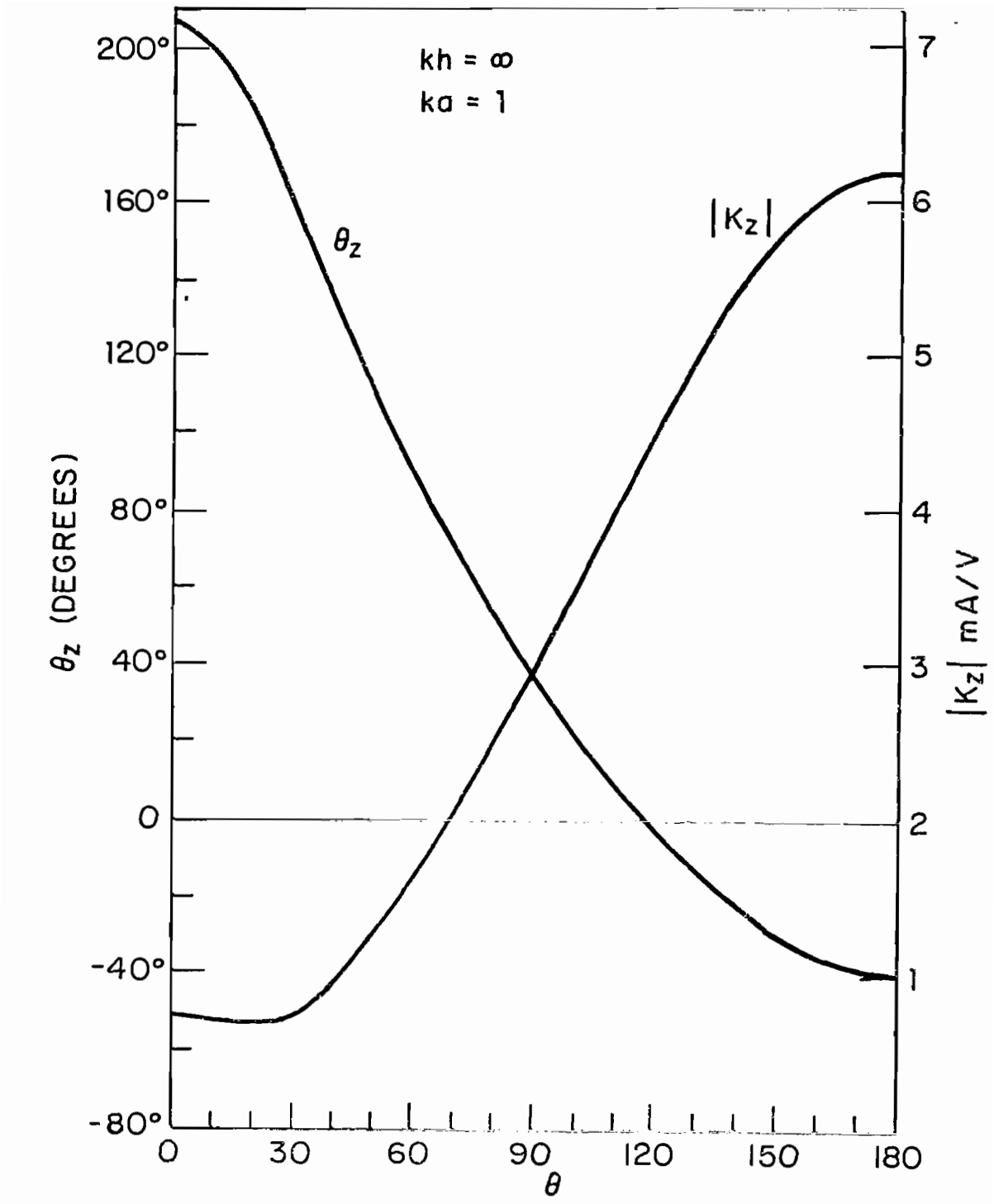

Fig. 5. Theoretical axial surface density of current $K_z = |K_z|e^{i\theta_z}$ on infinite cylinder; E-polarization.

the added complication of higher-order transverse resonances. Note that for E-polarization $K_\theta(\theta) = 0$ at all points on the cylinder and the surface density of charge η is everywhere zero since $\partial K_z(\theta)/\partial z = 0$.

The surface density of current when the electric vector is parallel to the axis of the cylinder is given by the series

$$K_z(\theta) = \frac{2E_z^{inc}}{\pi\zeta_0 ka} \sum_{n=0}^{\infty} \frac{\alpha_n i^n}{H_n^{(1)}(ka)} \cos n\theta \tag{27}$$

where $\alpha_n = 1$ for $n = 0$, $\alpha_n = 2$ for $n > 0$ and k is the wave number. For ka= 1,

$$K_z(\theta) \doteq A + B\cos\theta + C\cos 2\theta + D\cos 3\theta + E\cos 4\theta + F\cos 5\theta \tag{28}$$

where A through F are the Fourier coefficients with $E_z^{inc} = 1$ volt/m. The coefficients to two decimal places are given in Table 1. The principal components are seen to be A_R, B_R, B_I and C_I.

3. THEORETICAL CURRENTS AND CHARGES ON A CYLINDER OF FINITE LENGTH

When the cylinder extends from z = -h to z = h instead of from $z = -\infty$ to $z = \infty$, the determination of the current on its surface is a difficult three-dimensional problem that involves coupled axial and transverse components. These latter are generated near the open ends of the tube because the exciting field is not rotationally symmetric about the cylinder. Thus, the current at any point (a,θ,z) on the tube (which in the theoretical analysis is assumed to have infinitely thin, perfectly conducting walls with radius a) is a vector $\vec{K}(\theta,z) = \hat{\theta}K_\theta(\theta,z) + \hat{z}K_z(\theta,z)$. In references 8 and 9, Kao has shown that the determination of the two components can be reduced to the solution of two integral equations of which the one involves only $K_\theta(\theta,z)$, the other both $K_\theta(\theta,z)$ and $K_z(\theta,z)$. This involved an elaborate computer program (refs. 8 and 10) that has been extended by B. Sandler to include the surface density of charge $\eta(\theta,z)$ given by

$$\eta(\theta,z) = -\frac{i}{c}\left[\frac{\partial K_z(\theta,z)}{k\,\partial z} + \frac{1}{ka}\frac{\partial K_\theta(\theta,z)}{\partial\theta}\right] \tag{29}$$

where $c = 3 \times 10^8$ m/sec. $K_z(\theta,z)$ is calculated from the truncated series:

$$K_z(\theta,z) = A(kz) + B(kz)\cos\theta + C(kz)\cos 2\theta + D(kz)\cos 3\theta + E(kz)\cos 4\theta + F(kz)\cos 5\theta \tag{30}$$

Table 1

FOURIER COEFFICIENTS IN mA/V FOR $K_z(\theta)$ ON INFINITELY LONG CYLINDER;

E-POLARIZATION, kh = ∞, ka = 1

A	B	C	D	E	F
2.18 - i0.25	-3.28 + i1.85	-0.14 - i2.04	0.58 + i0.00	0.00 + i0.10	0.01 + i0.00

The coefficients are given in Table 2 for kh = 1.5π and ka = 1. Note that C(kz), D(kz), E(kz), and F(kz) are constant at the values C, D, E, and F for the infinite cylinder as given in Table 1 except within a quarter wavelength of the end where they decrease smoothly to zero. $K_\theta(\theta,z)$ is calculated from the series:

$$K_\theta(\theta,z) \doteq i[B'(kz)\sin\theta + C'(kz)\sin 2\theta + D'(kz)\sin 3\theta] \qquad (31)$$

The coefficients are given in Table. 3.

4. GRAPHS OF THEORETICALLY DETERMINED CURRENTS

a. Axial Currents

The axial distribution of $K_z(\theta,z)$ in terms of its magnitude $|K_z(\theta,z)|$, its phase angle θ_z referred to the incident field along the axis, and its real and imaginary parts $K_{zR}(\theta,z)$ and $K_{zI}(\theta,z)$ is shown in Figs. 6 - 8 as a function of kz (measured from the center of the cylinder) and the angle θ (measured from the center of the shadow region). It is seen in Figs. 6 and 7 that at θ = 0° in the shadow region, $|K_z(0°,z)|$ and θ_z have strongly resonant forms while at θ = 180° in the illuminated region, $|K_z(180°,z)|$ has a very low standing-wave ratio and θ_z is virtually constant over the entire length — both characteristics of a predominantly forced current. The graphs of $K_{zR}(\theta,z)$ and $K_{zI}(\theta,z)$ in Fig. 8 show that the transverse distributions of these quantities differ significantly from one another at different values of kz. They are like those along an infinitely long cylinder with the same radius only where kz is near 0.5π, where resonant currents have a minimum. Since the infinitely long cylinder supports no resonant currents, this resemblance is readily understood. It is evident from Figs. 5 - 8 and from Fig. 1 in reference 1 that the distribution of the axial component of current on an electrically thick cylinder cannot be constructed simply by combining the axial distribution of current along an electrically thin cylinder of the same length with the transverse distribution around an infinitely long cylinder of the same radius.

b. Transverse Currents

On a thick cylinder of finite length a very significant transverse component of current $K_\theta(\theta,z)$ is excited by periodically varying charge distributions at the ends. The real and imaginary parts of $K_\theta(\theta,z)$ when kh = 1.5π

Table 2

FOURIER COEFFICIENTS IN mA/V FOR $K_z(\theta,z)$ ON TUBULAR CYLINDER; E-POLARIZATION, kh = 1.5π, ka = 1

kz	A(kz)	B(kz)	C(kz)	D(kz)	E(kz)	F(kz)
0	0.50 + i0.20	-4.83 + i1.76	-0.17 - i2.04	0.58 - i2.13	0.00 + i0.10	0.01 + i0.00
0.25π	1.02 + i0.11	-4.44 + i1.90	-0.17 - i2.04	0.58 - i2.09	0.00 + i0.10	0.01 + i0.00
0.50π	2.28 - i0.13	-3.45 + i2.22	-0.16 - i2.02	0.58 - i1.97	0.00 + i0.10	0.01 + i0.00
0.75π	3.52 - i0.48	-2.23 + i2.43	-0.14 - i1.99	0.58 - i1.76	0.00 + i0.10	0.01 + i0.00
1.00π	3.94 - i0.84	-1.24 + i2.26	-0.12 - i1.94	0.58 - i1.49	0.00 + i0.10	0.01 + i0.00
1.25π	3.02 - i0.96	-0.66 + i1.54	-0.08 - i1.75	0.53 - i1.12	0.00 + i0.09	0.01 + i0.00
1.50π	0	0	0	0	0	0

Table 3

FOURIER COEFFICIENTS IN mA/V FOR $K_\theta(\theta,z)$ ON TUBULAR CYLINDER;

E-POLARIZATION, kh = 1.5π, ka = 1

kz	B'(kz)	C'(kz)	D'(kz)
0	0.00 + i0.00	0.00 + i0.00	0.00 + i0.00
0.25π	0.18 - i0.15	0.00 + i0.00	0.00 + i0.00
0.50π	0.24 - i0.30	0.01 + i0.00	0.00 + i0.00
0.75π	0.06 - i0.45	0.02 - i0.02	0.00 + i0.00
1.00π	-0.56 - i0.61	0.02 - i0.08	0.00 + i0.00
1.25π	-2.32 - i0.81	0.02 - i0.33	0.03 + i0.00
1.30π	-3.04 - i0.88	0.01 - i0.47	0.05 + i0.01
1.40π	-5.57 - i1.09	0.01 - i1.18	0.16 + i0.05
1.50π	∞	∞	∞

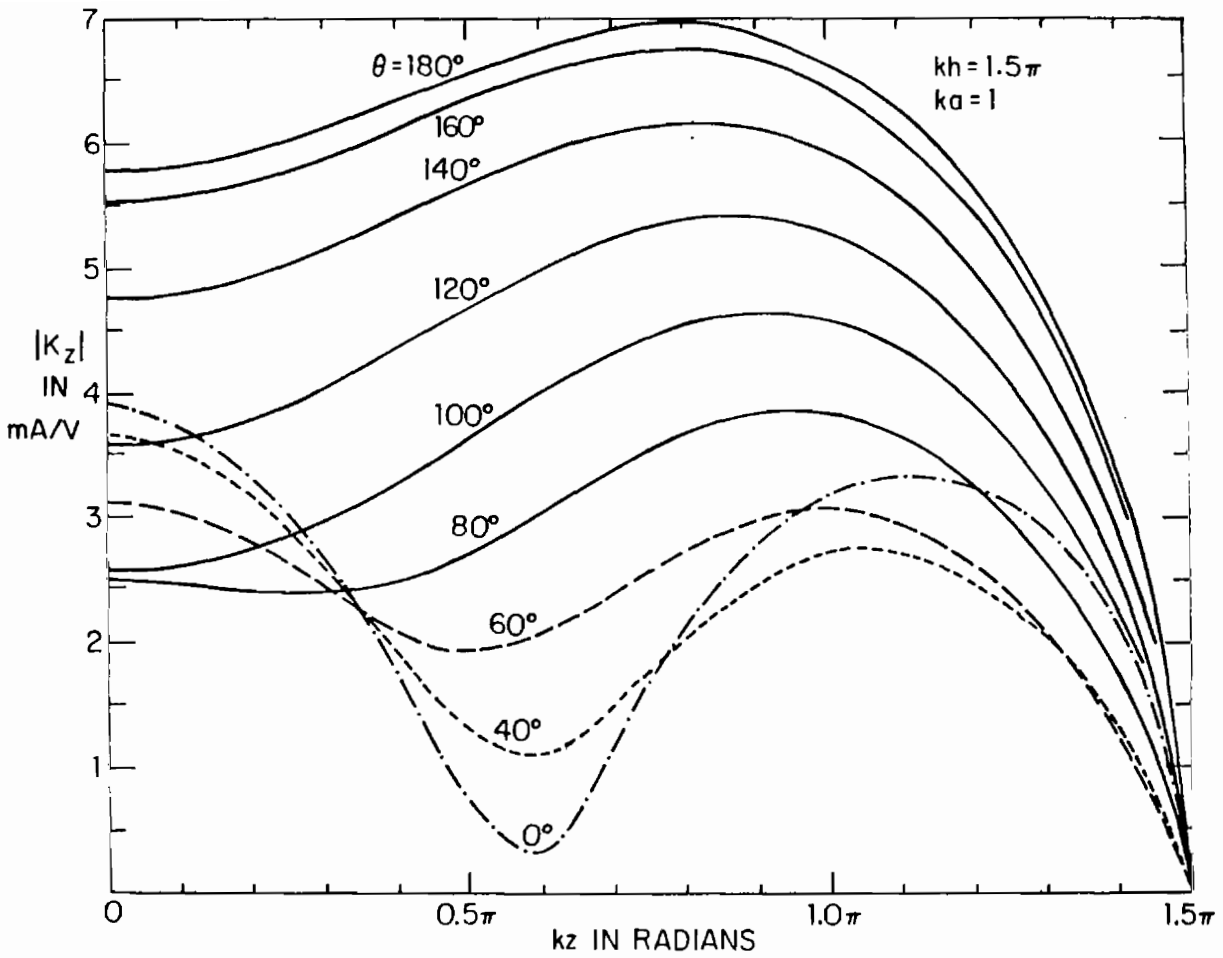

Fig. 6. Theoretical amplitude of axial surface density of total current on tubular cylinder; E-polarization, normal incidence.

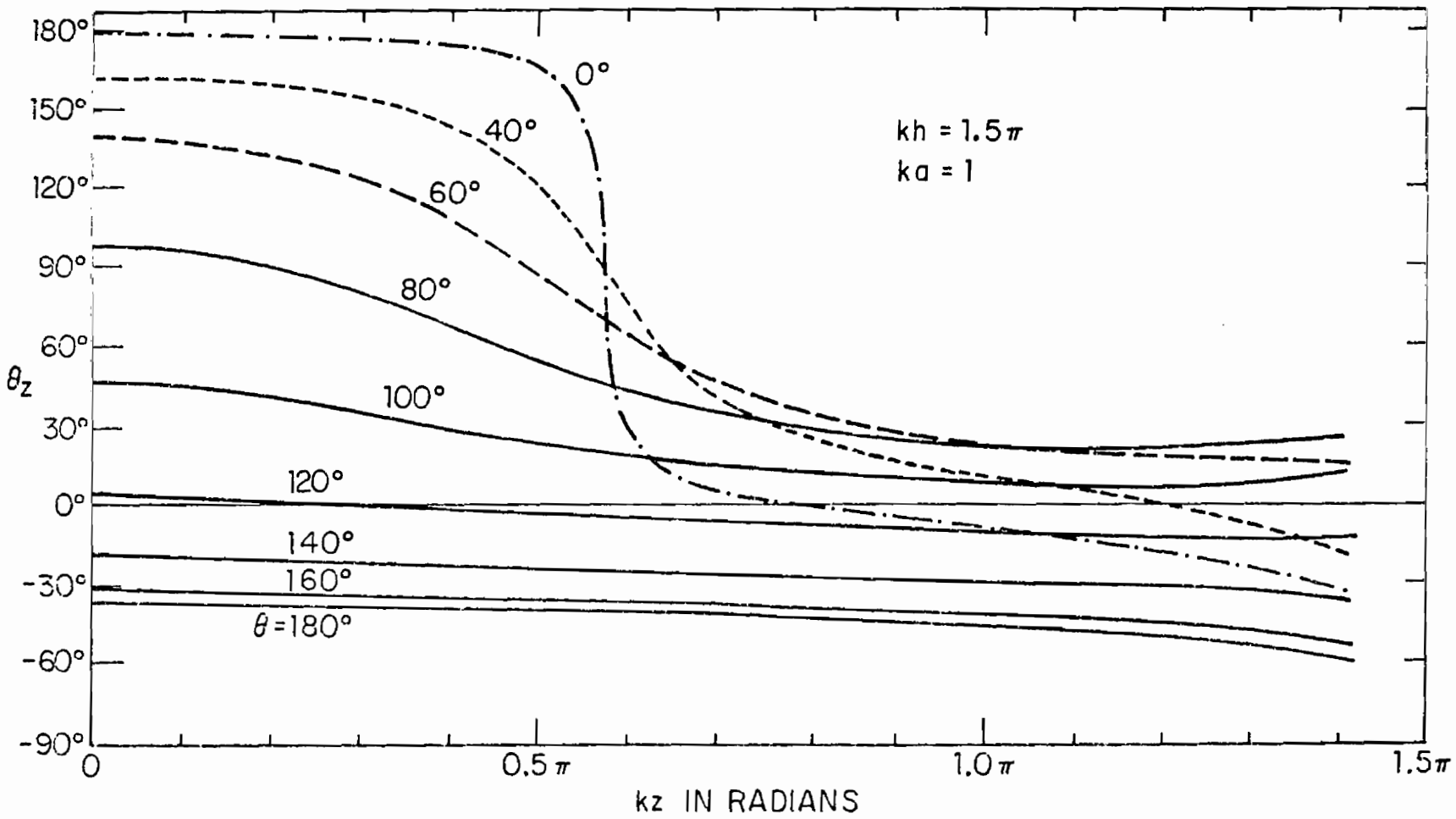

Fig. 7. Theoretical phase of axial surface density of total current on tubular cylinder; E-polarization, normal incidence.

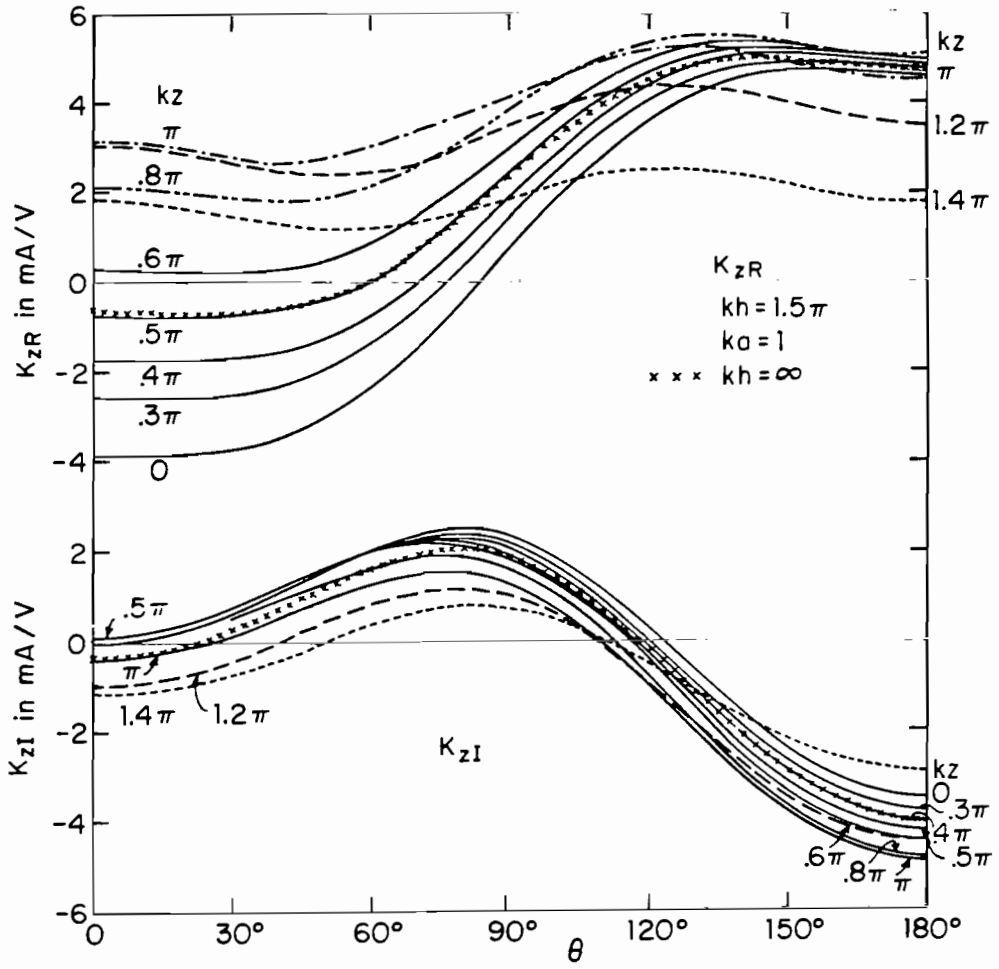

Fig. 8. Real and imaginary parts of $K_z(\theta,z)$ on tubular cylinder with kh = 1.5π; $K_z(\theta)$ with kh = ∞.

and ka = 1 are shown in Fig. 9. Note that $|K_\theta(\theta,z)| = [K_{\theta R}^2 + K_{\theta I}^2]^{1/2}$ vanishes at $\theta = 0°$ and 180° and has a maximum near $\theta = 90°$ for all values of kz. It follows from Table 3 that

$$K_\theta(\theta,z) \doteq iB'(kz)\sin\theta \tag{32}$$

$K_\theta(\theta,z)$ is very small compared with $K_z(\theta,z)$ except near the open ends of the cylinder where it rises steeply to very large values. In the idealization of a perfectly conducting, infinitely thin tube, $K_\theta(\theta,h) = \infty$. Significant transverse currents are confined to the relatively small area defined by $40° \leq \theta \leq 140°$, $1.1\pi \leq kz \leq 1.5\pi$, and a similar area on the other side of the cylinder. Note that $K_\theta(-\theta,z) = -K_\theta(\theta,z)$.

c. Current Vectors

Both $K_\theta(\theta,z)$ and $K_z(\theta,z)$ are complex so that at each point (a,θ,z) on the cylinder, $\vec{K}(\theta,z)$ is represented by

$$\vec{K}(\theta,z) = \vec{K}_R(\theta,z) + i\vec{K}_I(\theta,z) \tag{33}$$

where $\vec{K}_R(\theta,z) = \hat{\theta}K_{\theta R}(\theta,z) + \hat{z}K_{zR}(\theta,z)$ and $\vec{K}_I(\theta,z) = \hat{\theta}K_{\theta I}(\theta,z) + \hat{z}K_{zI}(\theta,z)$. The real vectors $\vec{K}_R(\theta,z)$ and $\vec{K}_I(\theta,z)$ at uniformly spaced points on the surface of the cylinder are shown drawn to scale in Fig. 10. At each point the length of the vector is proportional to $|\vec{K}_R(\theta,z)|$ on the left, $|\vec{K}_I(\theta,z)|$ on the right; the direction of the vector gives the direction of the part of the current represented. The general directions of flow and the standing-wave pattern in the shadow are evident.

The real instantaneous current at each point is obtained from (33) through multiplication by $e^{-i\omega t}$ and the selection of the real parts. The components of the time-varying vector $\vec{K}(\theta,z;t)$ are given by

$$\vec{K}(\theta,z;t) = \hat{\theta}K_\theta(\theta,z;t) + \hat{z}K_z(\theta,z;t) \tag{34}$$

where

$$K_\theta(\theta,z;t) = K_{\theta R}(\theta,z)\cos\omega t + K_{\theta I}(\theta,z)\sin\omega t \tag{35}$$

$$K_z(\theta,z;t) = K_{zR}(\theta,z)\cos\omega t + K_{zI}(\theta,z)\sin\omega t \tag{36}$$

It is readily shown that $\vec{K}(\theta,z;t)$ is elliptically polarized as illustrated in Fig. 11.

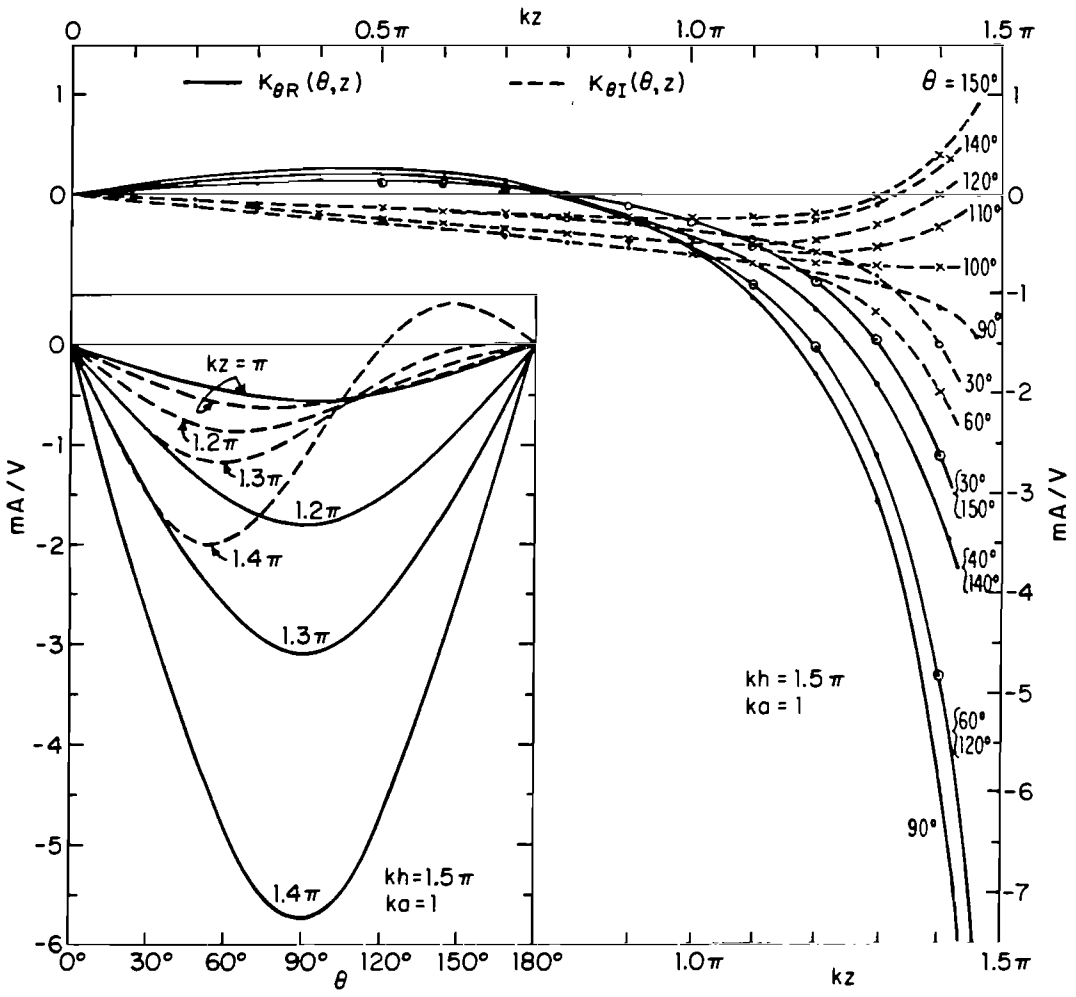

Fig. 9. Real and imaginary parts of $K_\theta(\theta,z)$ on tubular cylinder.

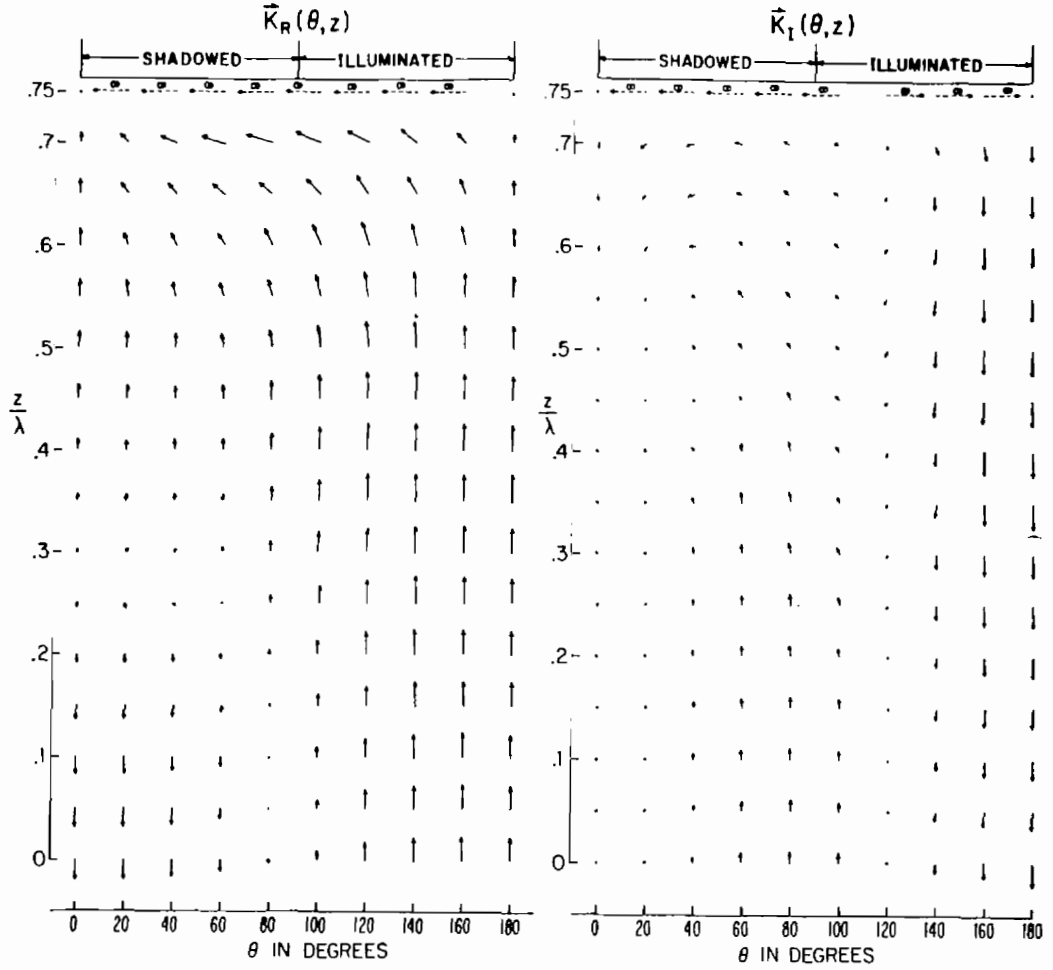

Fig. 10. $\vec{K}_R(\theta,z)$ and $\vec{K}_I(\theta,z)$ on tubular cylinder for E-polarization; kh = 1.5π, ka = 1.

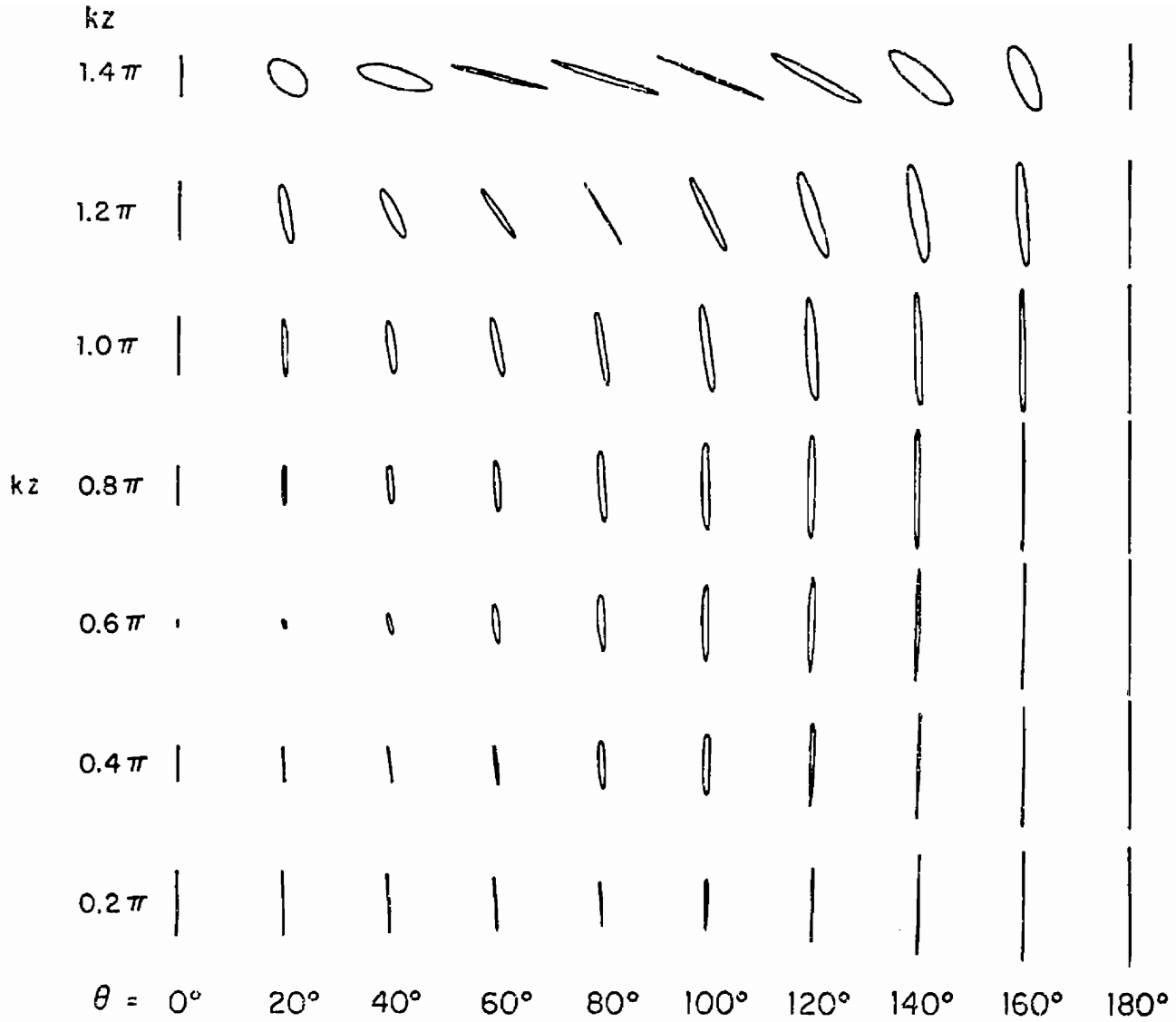

Fig. 11. Theoretical polarization ellipses of $\vec{K}(\theta,z)$; kh = 1.5π, ka = 1.

5. GRAPHS OF THEORETICALLY DETERMINED CHARGES

Whenever there are standing waves of current on a conducting surface, there must also be standing-wave concentrations of charge. The surface density of charge $\eta(\theta,z)$ is defined by the equation of continuity (29). It depends on the rates of change of both $K_z(\theta,z)$ and $K_\theta(\theta,z)$. Graphs of the magnitude $|\eta(\theta,z)|$ and phase θ_η are shown in Figs. 12 and 13. The origins for the several curves are displaced continuously in Fig. 12 for clarity. The charge density is seen to have a simple standing-wave pattern with zero amplitude at the center, $kz = 0$, a maximum near $kz = 0.5\pi$, a minimum near $kz = \pi$ and another, much higher maximum at the end of the tube, $kz = kh = 1.5\pi$. The standing-wave ratio is low in the illuminated region ($\theta = 180°$) and increases steadily around the cylinder to a maximum in the center of the shadow ($\theta = 0°$). The corresponding phase change is shown in Fig. 13. The axial variation of the charge density on the electrically thick cylinder is similar to that of the charge per unit length $q = 2\pi a\eta$ along an electrically thin cylinder ($ka = 0.04$) of the same length, $kh = 1.5\pi$ (see Fig. 1 in reference 1), but it is not rotationally symmetrical.

A clear picture of the overall distribution of charge is obtained from Figs. 14 and 15 which show contours of constant magnitude and constant phase. The essential characteristics in Fig. 14 are the increasingly high maximum all around the cylinder as the open end is approached, a secondary peak of charge at $kz \doteq 0.5\pi$, $\theta = 0°$ in the shadow, and a deep valley of charge all around the cylinder between the contours marked 1.5. Figure 15 shows the corresponding contours of constant phase. These lie along the valley and seem to converge to or diverge from the centers of maximum charge.

6. FOURIER COMPONENTS OF THE SURFACE CURRENT

The graphical representations in Figs. 5 through 11 show the total axial and transverse surface densities of current. In the actual evaluation of these currents the individual transverse Fourier components are calculated and then summed. In the interpretation of the total currents the properties of the individual Fourier components are useful.

Graphs of the axial distributions of the complex Fourier coefficients $A(kz) = A_R(kz) + iA_I(kz)$, $B(kz) = B_R(kz) + iB_I(kz)$, $C(kz) = C_R(kz) + iC_I(kz)$, and $D(kz) = D_R(kz) + iD_I(kz)$ of $K_z(\theta,z)$ are shown in Fig. 16 for $kh = 1.5\pi$

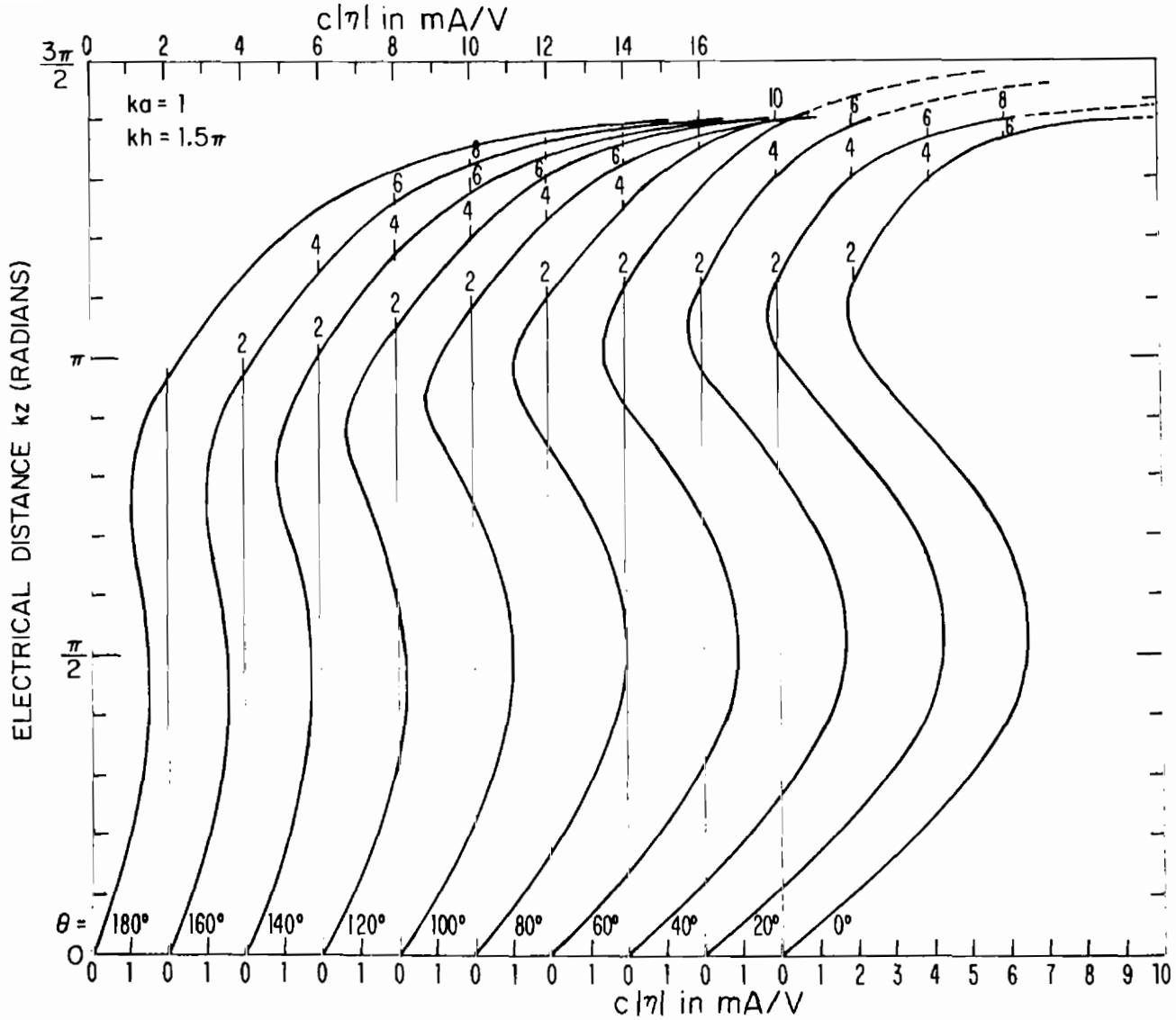

Fig. 12. Theoretical magnitude of surface density of charge $c|\eta|$ on tubular cylinder; E-polarization. ($c = 3 \times 10^8$ m/sec.)

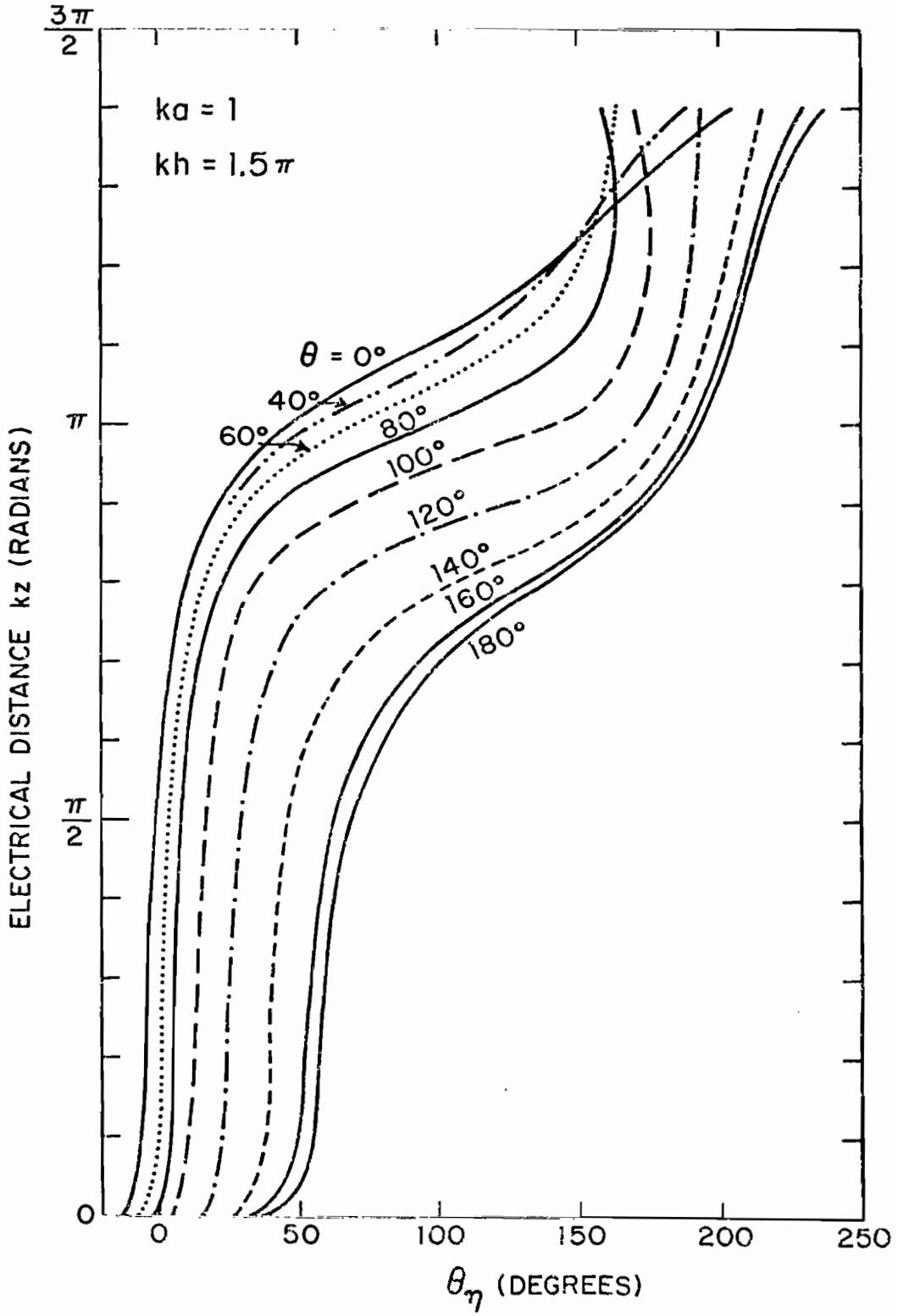

Fig. 13. Theoretical phase of surface density of charge θ_η on tubular cylinder; E-polarization.

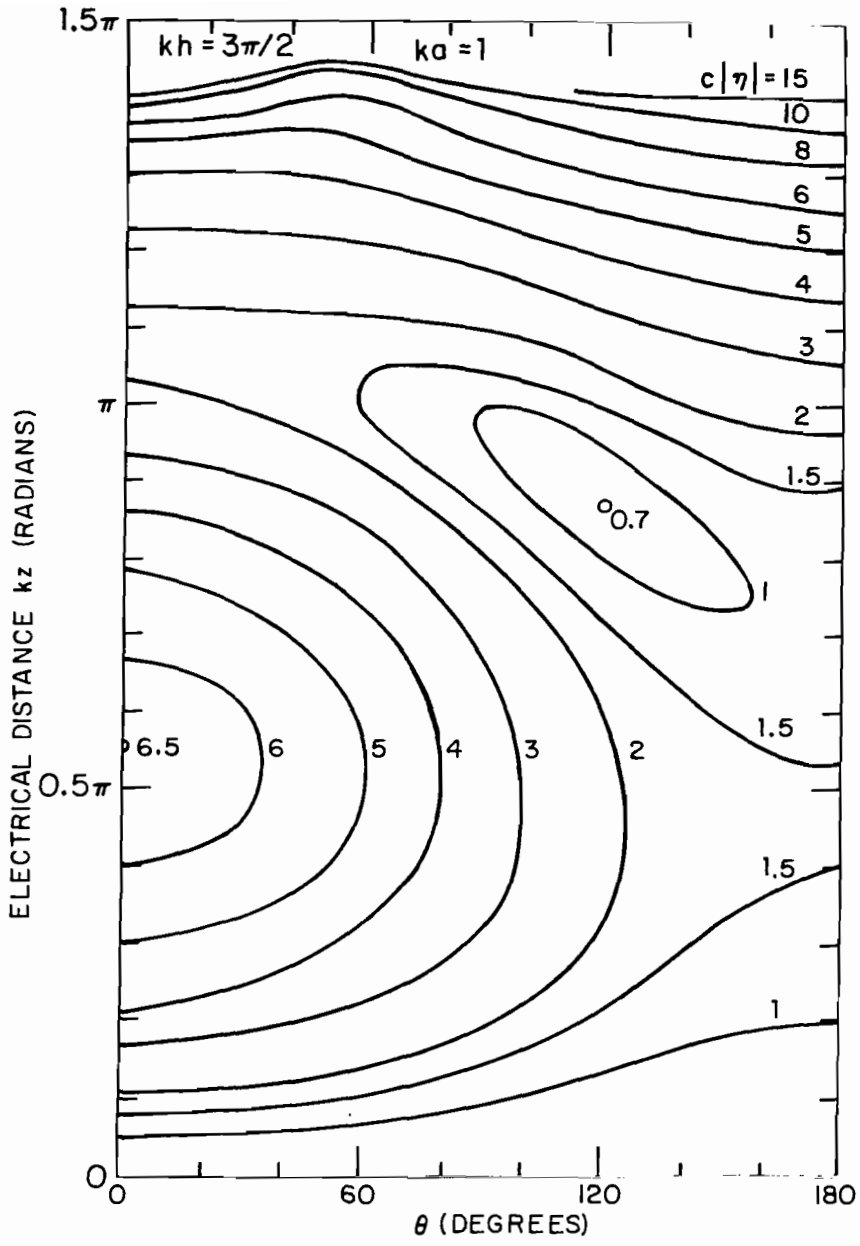

Fig. 14. Theoretical contours of constant magnitude of surface density of charge, $c|\eta|$ in mA/V, on tubular cylinder; E-polarization. ($c = 3 \times 10^8$ m/sec.)

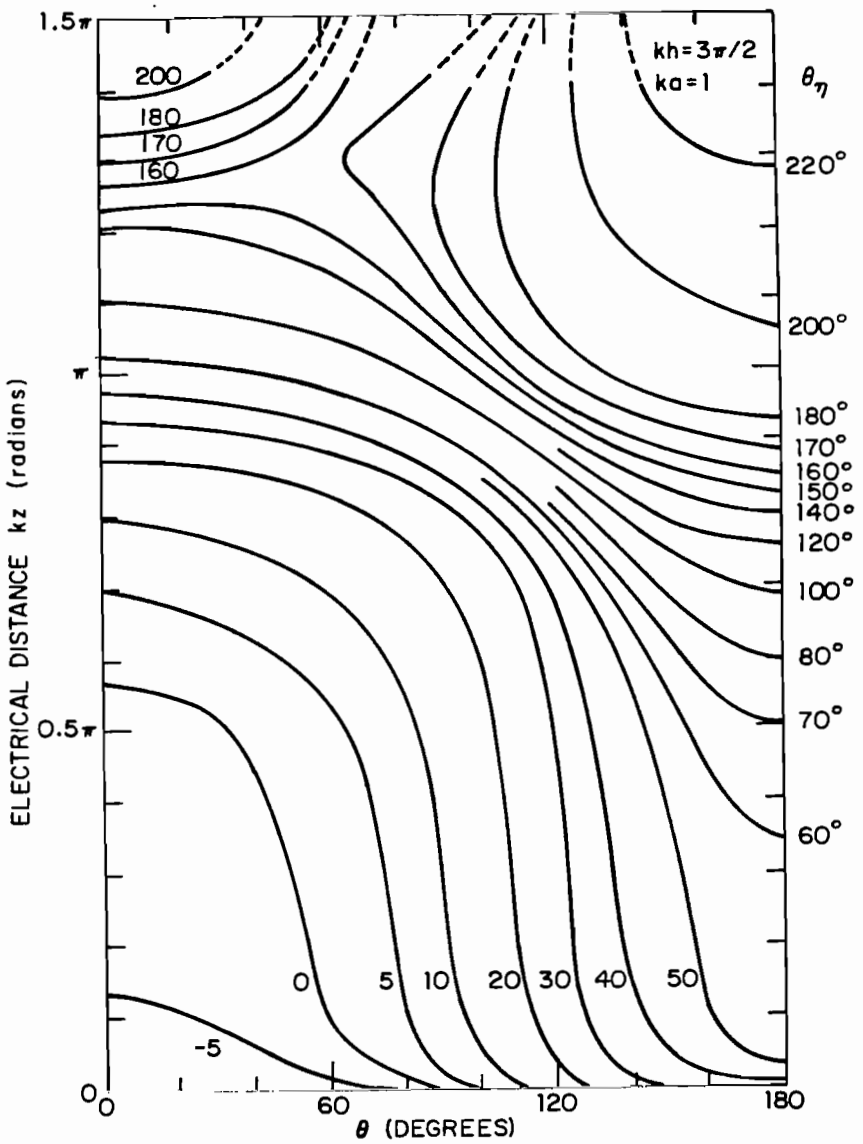

Fig. 15. Theoretical contours of constant phase of surface density of charge θ_η on tubular cylinder; E-polarization.

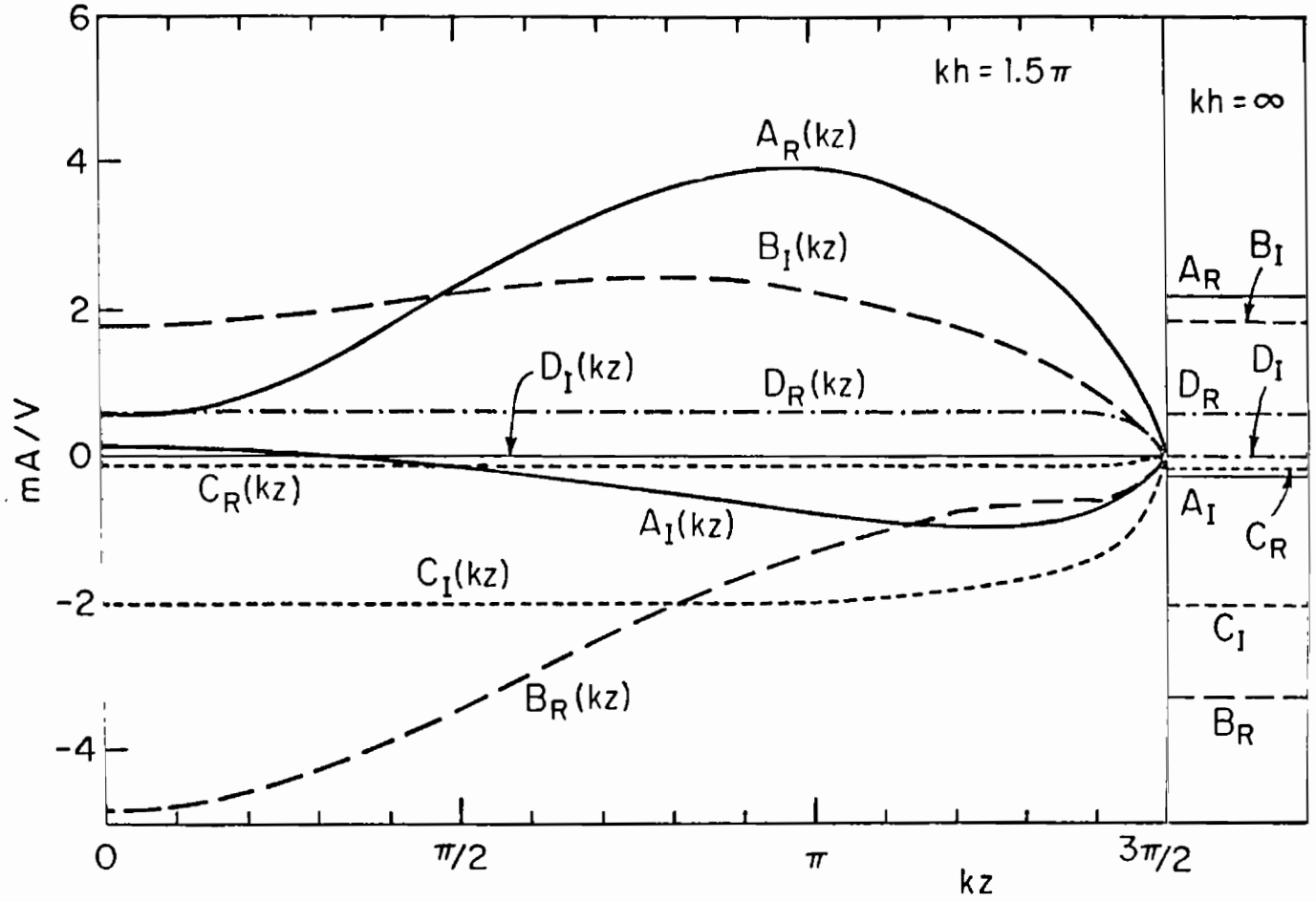

Fig. 16. Fourier components of axial surface density of current on tubular cylinder; E-polarization, ka = 1. $K_z(\theta,z) \doteq A(kz) + B(kz)\cos\theta + C(kz)\cos 2\theta + D(kz)\cos 3\theta$.

and ka = 1. E(kz) and F(kz) contribute negligibly to the total current. The constant coefficients $A = A_R + iA_I$, $B = B_R + iB_I$, $C = C_R + iC_I$, and $D = D_R + iD_I$ for the infinitely long tube with the same cross section are on the right in the figure. It is seen that C(kz) and D(kz) differ negligibly from the constants C and D, respectively, except within short distances of the end where they decrease smoothly to zero. This type of distribution is conveniently called a forced current on a finite cylinder and is distinguished by a subscript f. Thus, in Fig. 16

$$C(kz) = C_f(kz) \doteq C \qquad \text{for } |kz| < kh - 0.5\pi \tag{37}$$

$$D(kz) = D_f(kz) \doteq D \qquad \text{for } |kz| < kh - 0.5\pi \tag{38}$$

Similar forced components are a part of A(kz) and B(kz) but these also include superimposed resonant components. An approximate procedure for obtaining $A_f(kz)$ and $B_f(kz)$ is to assume ideal resonant components

$$A_r(kz) = A_r \cos kz \quad , \quad B_r(kz) = B_r \cos kz \tag{39}$$

such that

$$A(kz) = A_f(kz) + A_r \cos kz \quad ; \quad B(kz) = B_f(kz) + B_r \cos kz \tag{40}$$

The amplitudes A_r and B_r can be determined for the real and imaginary parts in each case by noting that $A_{rR}(kz)$, $A_{rI}(kz)$, $B_{rR}(kz)$, and $B_{rI}(kz)$ must each vanish at $kz = 0.5\pi$. Graphs of these ideal resonant distributions and of the associated forced components $A_{fR}(kz)$, $A_{fI}(kz)$, $B_{fR}(kz)$, and $B_{fI}(kz)$ are shown in Fig. 17 together with the constants A_R, A_I, B_R, and B_I. It is seen that the forced components have the general form of $C_f(kz)$ and $D_f(kz)$ but with small oscillations that are not simple sinusoids superimposed on the constants A_R, A_I, B_R, and B_I.

The transverse current $K_\theta(\theta,z)$ has no forced components and is given to a good approximation by

$$K_\theta(\theta,z) \doteq i[B'(kz)\sin\theta + C'(kz)\sin 2\theta] \tag{41}$$

where $B'(kz) = B'_R(kz) + iB'_I(kz)$ and $C'(kz) \doteq iC'_I(kz)$ are shown in Fig. 18.

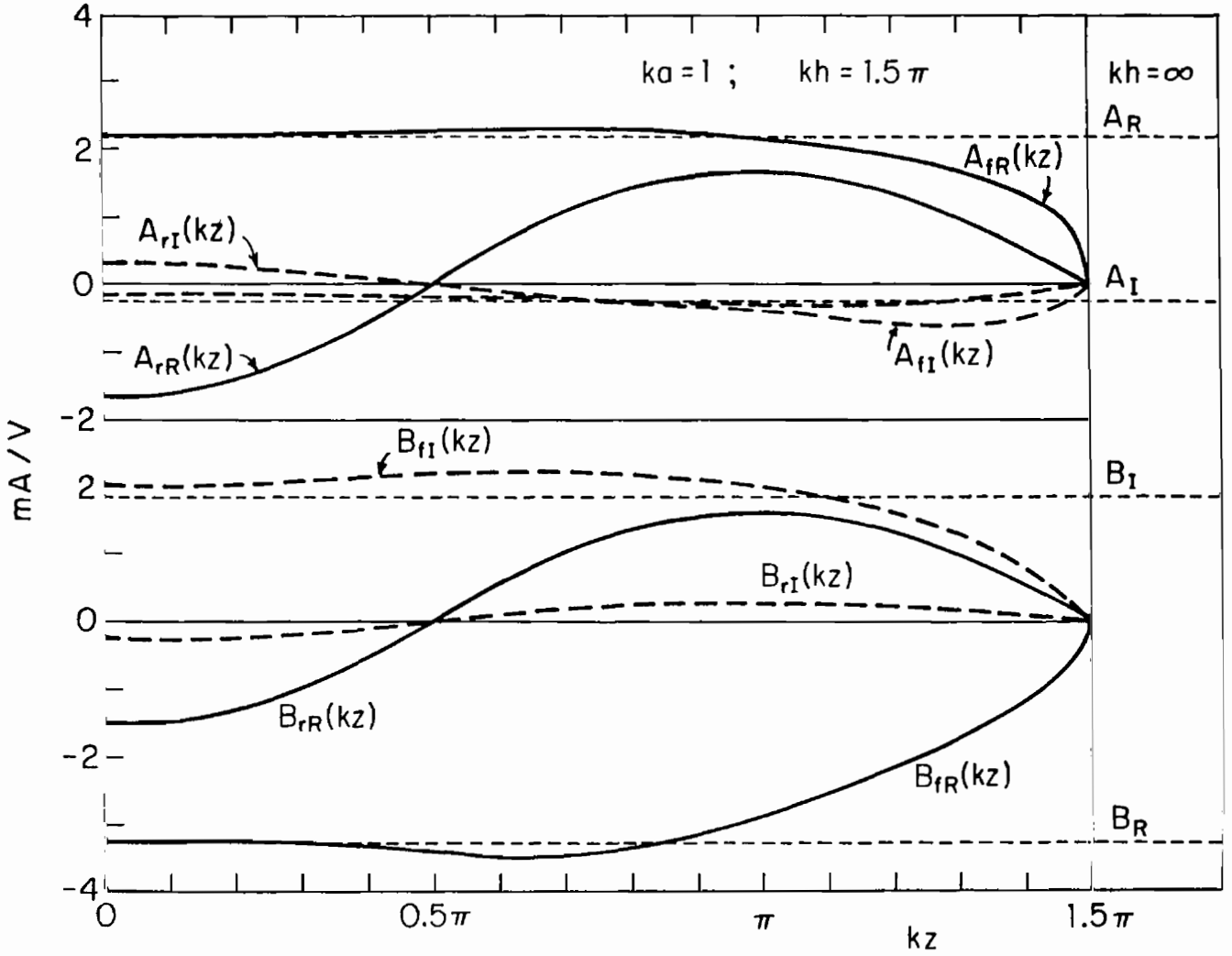

Fig. 17. Fourier coefficients A(kz) and B(kz) of $K_z(\theta,z)$ resolved into resonant and forced components.

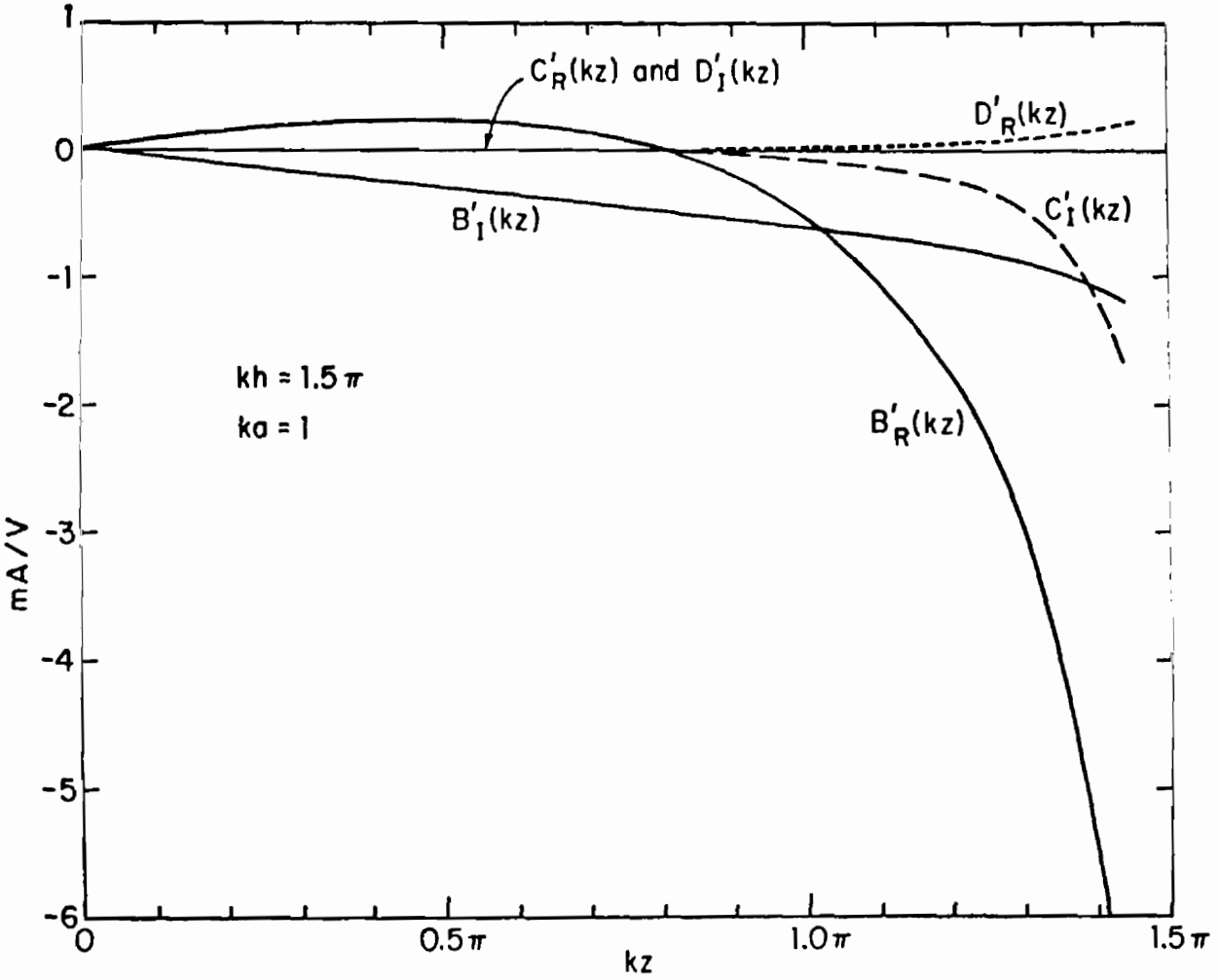

Fig. 18. Fourier coefficients B'(kz), C'(kz), and D'(kz) of $K_\theta(\theta,z)$.

7. APPROXIMATE ANALYTICAL REPRESENTATION OF THE SURFACE DENSITIES OF CURRENT AND CHARGE ON A CYLINDER WITH ka = 1, kh = 1.5π

The distributions of the axial and transverse components of the surface density of current $\vec{K}(\theta,z) = \hat{\theta}K_\theta(\theta,z) + \hat{z}K_z(\theta,z)$ on the tubular cylinder with ka = 1 and kh = 1.5π are readily represented analytically in terms of the transverse Fourier components. A convenient approximate representation is achieved if a distribution function e(kz) is defined to represent the purely forced parts of the current on cylinders of finite length. The required function has a constant value of unity over the entire length of the cylinder except within about a quarter wavelength of the ends where it decreases smoothly to zero. The actual shape and range of this decreasing part of the curve varies somewhat with the different Fourier components and with the real and imaginary parts of each. However, for a simple approximate representation for qualitative purposes a cosinusoidal form in the quarter wavelength at each end is adequate. This is illustrated in Fig. 19. An analytical representation is

$$e(kz) = U(kz + kh - 0.5\pi)[1 - U(kz - kh + 0.5\pi)] + U(kz - kh + 0.5\pi) \times \sin k(h - z) + [1 - U(kz + kh - 0.5\pi)]\sin k(h + z) \qquad (42)$$

where U(t) is the Heaviside or step function defined by U(t) = 1 when $t \geq 0$, 0 when $t < 0$. In terms of this function and (37)- (40), the Fourier components of the axial current are approximated by $A(kz) \doteq Ae(kz) + A_r \cos kz$, $B(kz) \doteq Be(kz) + B_r \cos kz$, $C(kz) \doteq Ce(kz)$, and $D(kz) \doteq De(kz)$. It follows that

$$K_z(\theta,z) = (A + B\cos\theta + C\cos 2\theta + D\cos 3\theta)e(kz) + (A_r + B_r\cos\theta)\cos kz \qquad (43)$$

where A, B, C, and D are given in Table 1 for the cylinder with ka = 1. This representation is in error by the differences between $A_f(kz)$ and Ae(kz), $B_f(kz)$ and Be(kz), $C_f(kz)$ and Ce(kz), and $D_f(kz)$ and De(kz) in the ranges $-kh \leq kz \leq -(kh - 0.5\pi)$; $(kh - 0.5\pi) \leq kz \leq kh$.

The transverse distribution $K_\theta(\theta,z)$ associated with the axial distribution $K_z(\theta,z)$ is given in (41) with $B'(kz) = B'_R(kz) + iB'_I(kz)$ and $C'(kz) =$

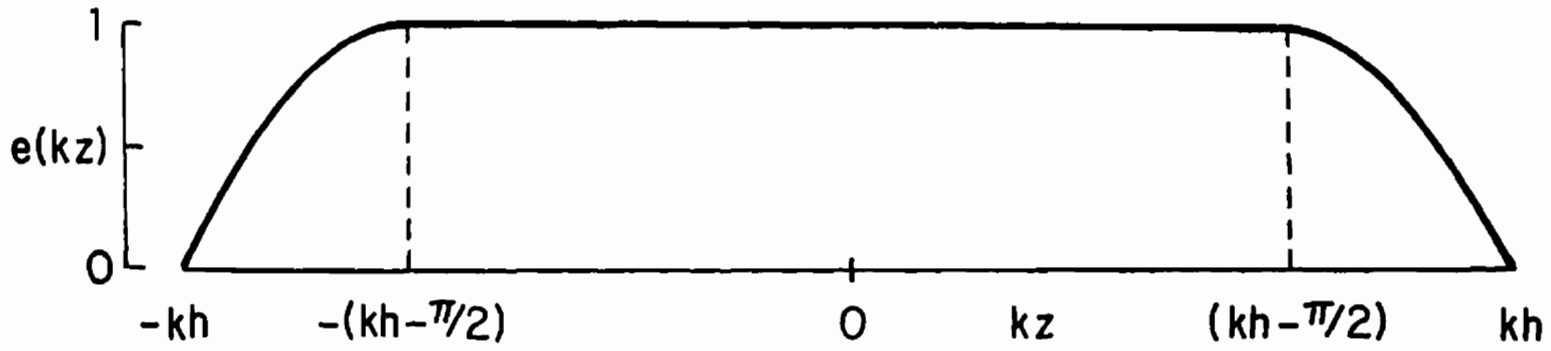

Fig. 19. The function e(kz).

$C'_R(kz) + iC'_I(kz)$. The real and imaginary parts of $B'(kz)$ and $C'(kz)$ are shown graphically in Fig. 18.

The approximate distribution of the surface density of charge can be obtained from the components of the current with the help of the equation of continuity (29). Since this involves differentiation and the function $e(kz)$ is only approximate especially with regard to its slope, it is to be anticipated that the derivatives of $e(kz)$ will not be quantitatively accurate within a quarter wavelength of each end. With (41) and (43) it follows from (29) that

$$\eta(\theta,z) \doteq -(i/c)\Big[(A + B\cos\theta + C\cos 2\theta + D\cos 3\theta)\{-U(kz - kh + 0.5\pi) \times \cos k(h - z) + [1 - U(kz + kh - 0.5\pi)]\cos k(h + z)\} - (A_r + B_r \times \sin\theta)\sin kz + (i/ka)[B'(kz)\cos\theta + C'(kz)\cos 2\theta]\Big] \qquad (44)$$

The surface density of current consists of the largely constant forced part with $e(kz)$ as coefficient and a resonant part with its axial and transverse components. The associated surface density of charge includes a part localized near the ends associated with the forced current and a part associated with the resonant currents in a standing-wave pattern on the cylinder.

8. INTERPRETATION OF THE GRAPHS OF SURFACE DENSITIES OF CURRENT AND CHARGE ON A TUBULAR CYLINDER WITH E-POLARIZATION

With distributions of the total surface density of current $\vec{K}(\theta,z) = \hat{\theta}K_\theta(\theta,z) + \hat{z}K_z(\theta,z)$ displayed in various forms in Figs. 6 through 11 and of the surface density of charge $\eta(\theta,z)$ in Figs. 12 through 15, and with representations of these available in terms of the transverse Fourier components shown in Figs. 16 through 18, all of the information needed for a systematic interpretation of the underlying physical phenomena is at hand. Consider first the simple and fundamental distribution along an infinitely long cylinder with the same cross section. With E-polarization it consists of only $K_z(\theta)$ which is independent of z. There is no transverse current and no surface density of charge anywhere on the cylinder. The axial current is entirely forced; there is no resonant component. The real and imaginary parts of the surface density of current (in milliamperes per volt) for the cylinder with $ka = 1$ are well approximated by:

$$K_{zR}(\theta) \triangleq A_R + B_R \cos\theta + D_R \cos 3\theta = 2.18 - 3.28 \cos\theta + 0.58 \cos 3\theta \quad (45)$$

$$K_{zI}(\theta) \triangleq A_I + B_I \cos\theta + C_I \cos 2\theta = -0.25 + 1.85 \cos\theta - 2.04 \cos 2\theta \quad (46)$$

These purely transverse distributions are shown in Fig. 8 in crossed lines. Note that the real part reverses its direction once at $\theta = 60°$, the imaginary part twice near $\theta = 23°$ and 118°.

When the infinite cylinder is cut off beyond $kz = \pm kh = \pm 1.5\pi$ to obtain a cylinder with the finite length $2kh = 3\pi$, an important new condition has to be satisfied: the total axial current $K_z(\theta,z)$ must vanish at $z = \pm h$. This must also be true of each of the mutually independent transverse Fourier components so that $A(kz) = B(kz) = C(kz) = D(kz) = \ldots = 0$ at $z = \pm h$.

The reduction to zero of the forced part of the total axial current on a finite tubular cylinder is accomplished very simply by properly distributed, high concentrations of charges with equal magnitudes and opposite sign within a quarter wavelength or less of the ends. This charge is so distributed that each Fourier component of forced current with its characteristic transverse distribution is combined with a corresponding component of reflected current that has a magnitude at $z = \pm h$ equal to the corresponding component A, $B \cos\theta$, $C \cos 2\theta$, etc. for the infinite cylinder but is oppositely directed. These reflected components decrease rapidly to negligible values within a quarter wavelength of each end. Although the manner in which these reflected currents decrease actually varies with each Fourier component, a rough approximation for each of them is $[1 - e(kz)]$ where $e(kz)$ is defined in (42). Thus, the forced current on the finite cylinder is like that on the infinite one in its transverse distribution and also in the constant axial distribution except within a quarter wavelength of the ends where it decreases to zero. The large concentrations of charge associated with the forced current exist only near the ends.

A cylinder of finite length has natural resonant modes that are excited by suitably distributed concentrations of charge at the ends. Specifically, the rotationally symmetric distribution of charge associated with the rotationally symmetric current $A(kz)$ excites the axially resonant current $A_r(kz) = A_r \cos kz$ in a characteristic standing-wave pattern with maxima at $kz = 0, \pi$. Associated with it is the part of the charge distribution in (44) given

by the term $(i/c)A_r \sin kz$ which has maxima at $kz = 0.5\pi, 1.5\pi$. Similarly, the charges at the ends associated with the component of current $B(kz)\cos\theta$ excite resonant axial components of current with the transverse distribution $\cos\theta$. This means that the resonant currents $B_r(kz)\cos\theta$ on the illuminated half of the cylinder, where $90° < \theta < 270°$ and $\cos\theta$ is negative, are equal and opposite to the currents at the corresponding points on the shadowed half of the cylinder, where $-90° < \theta < 90°$ and $\cos\theta$ is positive. In effect, the halves of the cylinder on each side of the plane $\theta = 90°, -90°$ are equivalent to a two-conductor transmission line. The associated equal and opposite charges near the ends of the cylinder also have the transverse distribution $\cos\theta$. Since with $ka = 1$ the distance around the cylinder from $\theta = 0°$ to $\theta = 180°$ is a half-wavelength, near resonant transverse currents $iB'(kz)\sin\theta$ are also excited near the ends where the amplitude of the charges with the distribution $\cos\theta$ is large. Thus, the two-conductor transmission line formed by the halves of the cylinder with the axial currents $B(kz)\cos\theta$ is, in effect, short-circuited at the ends which carry the transverse currents $iB'(kz)\sin\theta$ around the cylinder. Evidently, the resonant part $B_r(kz)$ of the Fourier component $B(kz)$ of the axial current combines with the component $iB'(kz)$ of the transverse current to form a two-dimensional standing-wave pattern on the surface of the tubular cylinder. The tube with $ka = 1$ and $kh = 1.5\pi$ provides resonant transmission-line-like paths for both the axial and the transverse currents. The illuminated half of the cylinder is one conductor, the shadowed half is the other conductor. They carry equal and opposite currents. They are, in effect, terminated at the ends by short-circuiting rings that carry the transverse currents from the one conductor to the other in parallel paths, each a half wavelength long. Associated with these currents are the parts of the charges in (44) (with $ka = 1$) given by $(i/c)[B_r \sin\theta \sin kz - iB'(kz) \times \cos\theta]$ where $iB'(kz)$ is large only very near $kz = \pm kh$. Although the axial distribution $\sin kz$ is the same as that of the charge associated with the symmetric component of current $A_r(kz)$, this latter consists of rotationally symmetric rings of charge with maximum amplitudes near $kz = 0.5\pi, 1.5\pi$, whereas the charges associated with the resonant currents $B_r(kz)$ and $iB'(kz)$ are not rotationally symmetric. They have the transverse dependence $B_r(kz) \times \cos\theta$ so that they have opposite signs in the illuminated and shadowed regions. Thus, a rotationally symmetric positive charge maximum at $kz = 0.5\pi$

associated with $A_r(kz)$ combines with a likewise positive charge maximum of $B_r(kz)$ at $kz = 0.5\pi$, $\theta = 0°$ to form a strong charge maximum and with the equal negative charge maximum of $B_r(kz)$ at $kz = 0.5\pi$, $\theta = 180°$ to form a region with greatly reduced charge concentration. A similar combination of charges associated with $A_r(kz)$ and $B_r(kz)$ occurs at $kz = 1.5\pi$, but here these resonant charges are superimposed on the much larger charge distributions associated with the forced components of current. These observations clarify the charge distributions shown in Figs. 12 and 14.

The components of current associated with the higher-order Fourier components C, D, etc. do not generate significant axially resonant currents when $ka = 1$. The transverse component $iC'(kz)\sin 2\theta$ is significant but only extremely close to the ends at $z = \pm h$.

The current on the surface of a cylinder but not within a quarter wavelength of the ends consists predominantly of the axial forced current, $A + B\cos\theta + C\cos 2\theta + D\cos 3\theta + \ldots$, like that on an infinitely long cylinder and the superimposed axial resonant current, $(A_r + B_r\cos\theta)\cos kz$. In the quarter wavelength at each end the axial forced current decreases to zero in a complicated manner approximated by the function $e(kz)$ and transverse currents with large amplitudes are generated. These combine with the axially directed currents into the elliptically polarized vectors shown in Figs. 10 and 11.

9. INSIDE AND OUTSIDE CURRENTS

The idealized tube used in the analysis consists of a single layer of moving electric charges. However, by definition

$$\vec{K} = -\mu_0^{-1}\hat{\rho} \times (\vec{B}_+ - \vec{B}_-) \equiv \vec{K}_+ + \vec{K}_- \tag{47}$$

$$\eta = -\varepsilon_0\hat{\rho} \cdot (\vec{E}_+ - \vec{E}_-) \equiv \eta_+ + \eta_- \tag{48}$$

where the subscripts + and - refer to the regions outside and inside of the open-ended tube. The identities on the right in (47) and (48) define, respectively, outside currents and charges associated with the field at $\rho = a_+$ and inside currents and charges associated with the field at $\rho = a_-$. This separation is artificial but unique. It is useful in comparing

theoretical results with currents measured on the outside surface of a tubular metal cylinder with wall thickness large compared to the skin depth.

Theoretical graphs of the inside and outside values of $K_z(\theta,z)$ and $K_\theta(\theta,z)$ are in Figs. 20 and 21, of $\eta(\theta,z)$ in Fig. 22. Since the inside of the tube is a waveguide beyond cut-off with ka = 1, the inside currents and charges decay rapidly in from the end. The outside currents and charges can be compared with the total ones in Figs. 6, 9 and 12. It is seen that they differ negligibly beyond a short distance from the end.

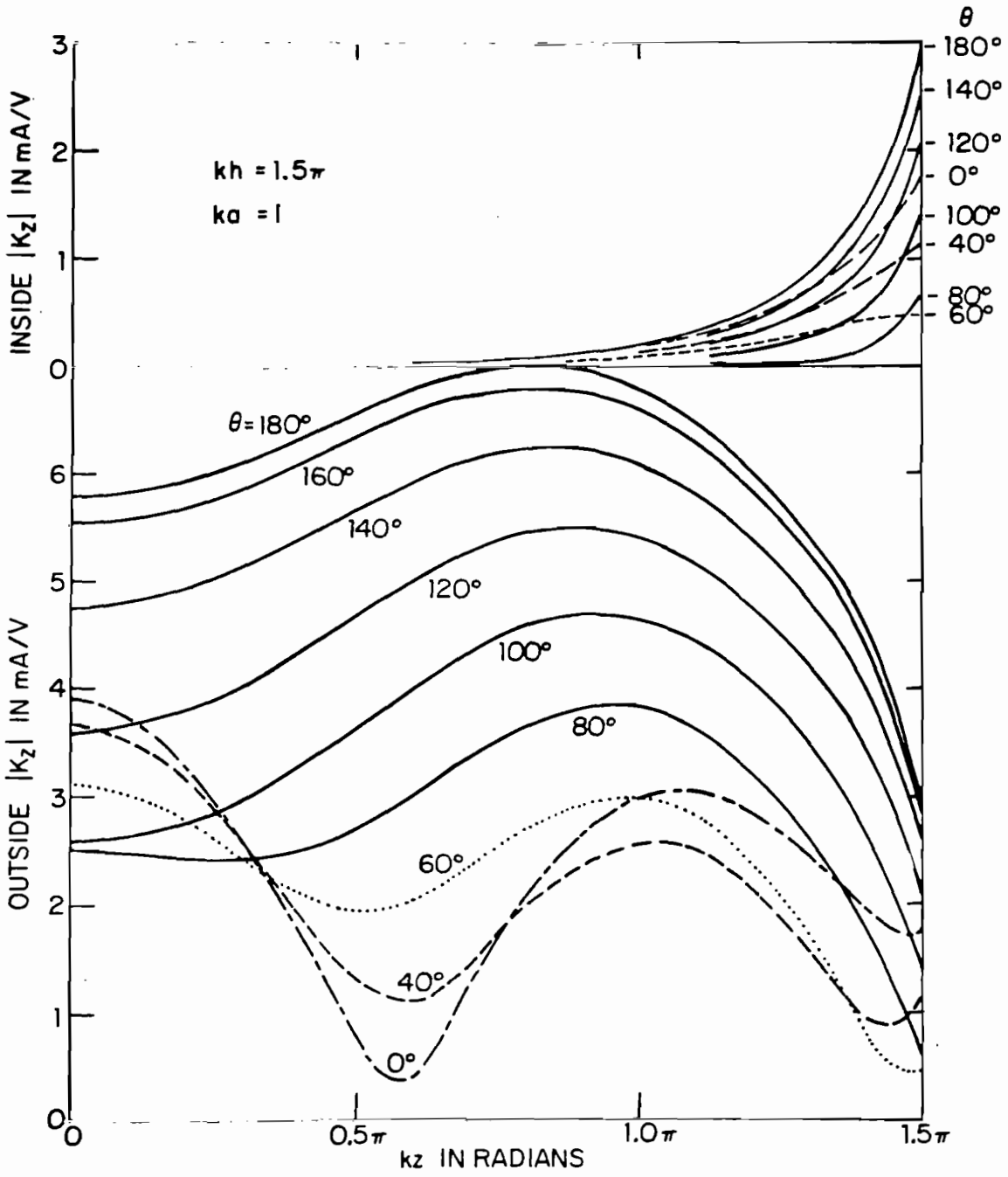

Fig. 20. Theoretical amplitude of surface density of outside and inside axial currents on tubular cylinder; E-polarization.

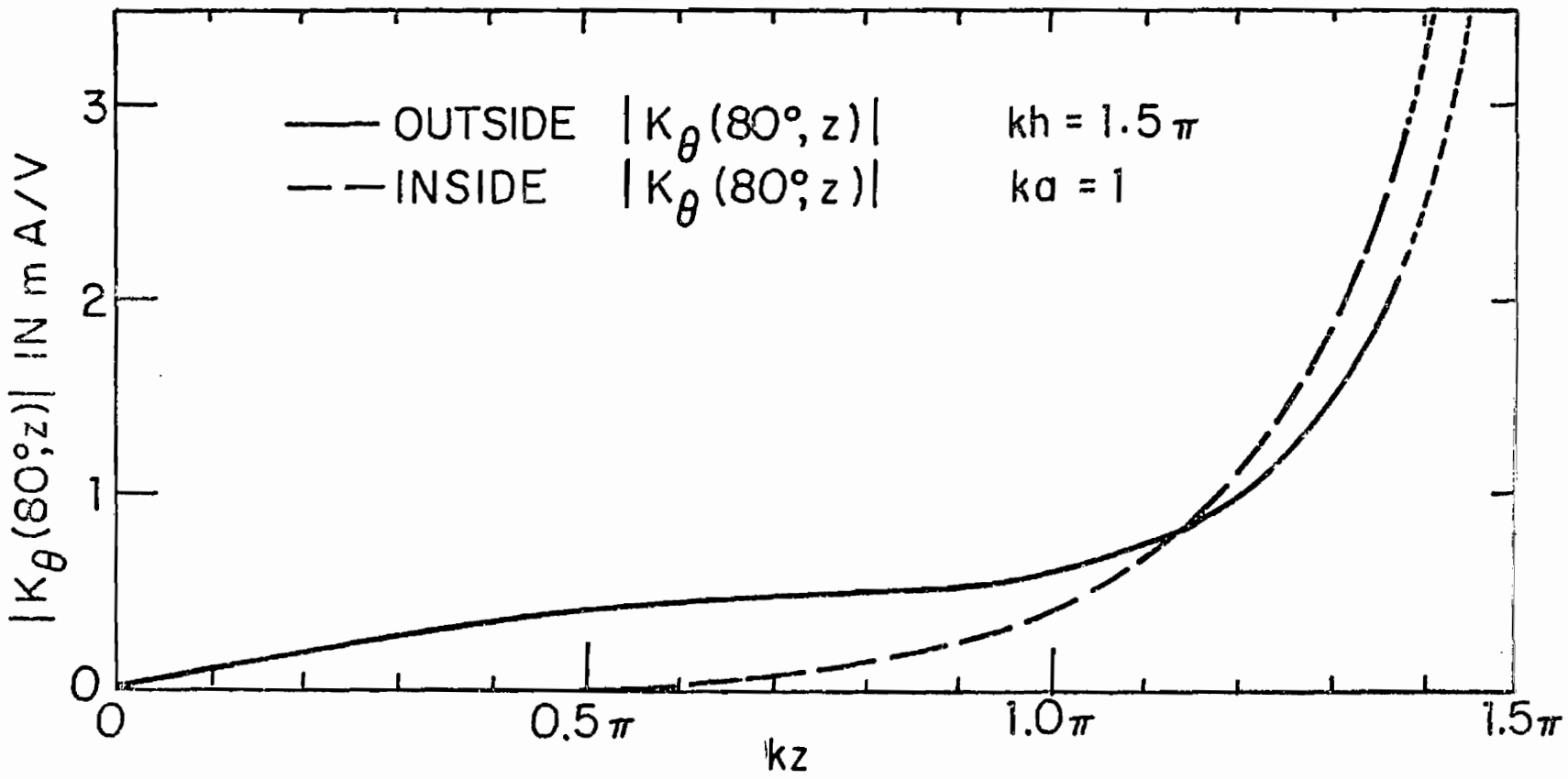

Fig. 21. Theoretical amplitude of surface density of outside and inside transverse currents on tubular cylinder; E-polarization.

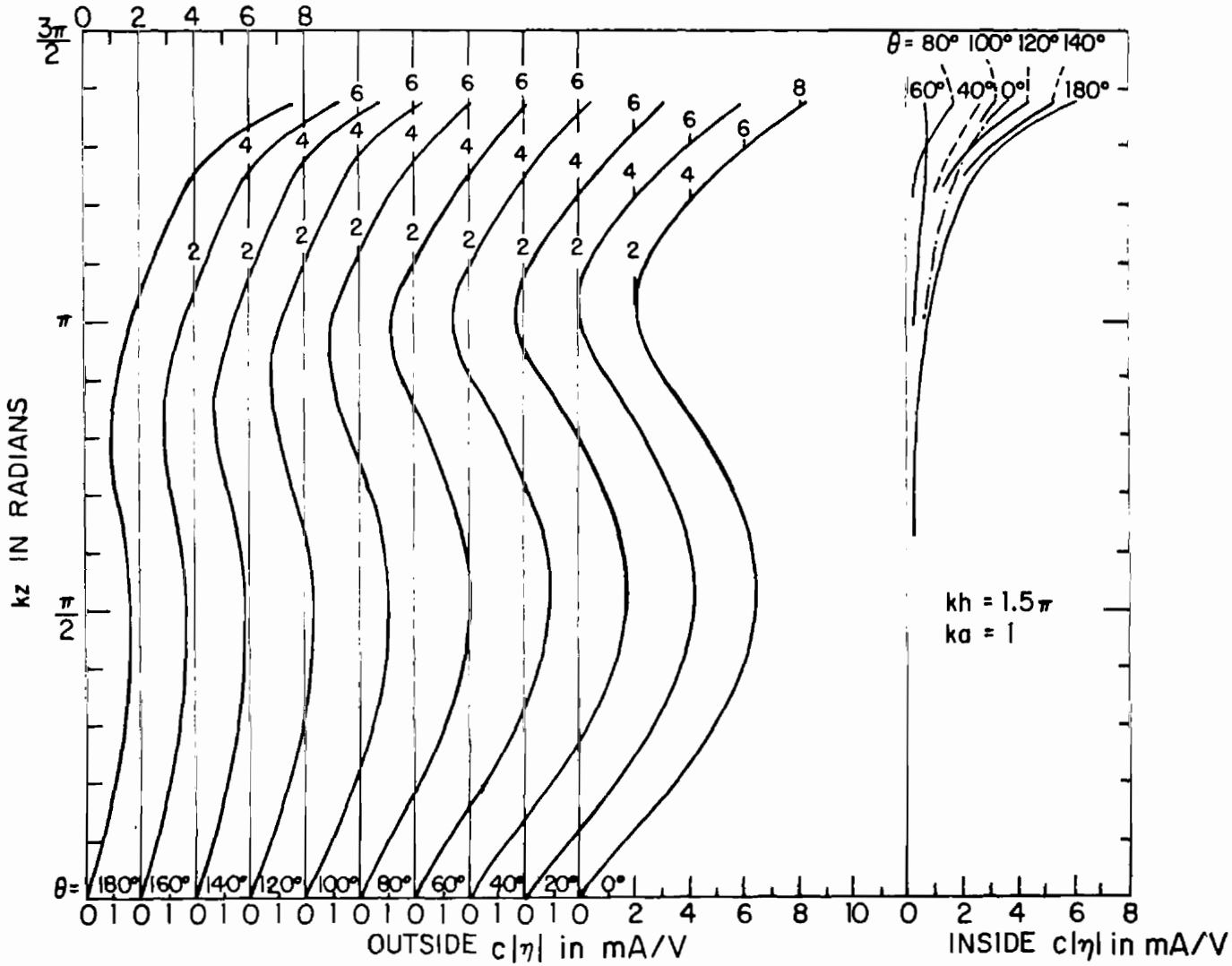

Fig. 22. Theoretical amplitude of surface density of outside and inside transverse currents on tubular cylinder; E-polarization.

SECTION IV

ELECTRICALLY THICK CYLINDER IN E-POLARIZED, NORMALLY INCIDENT, PLANE-WAVE FIELD, MEASUREMENTS, kh = 1.5π, ka = 1

1. THE APPARATUS AND TECHNIQUES OF MEASUREMENT

An important application of the detailed theoretical study in Section III of the distribution of current and charge on the surface of a conducting tube is to provide a dependable standard of reference for apparatus and techniques designed for measuring these quantities on electrically large conducting surfaces when exposed to an externally generated electromagnetic field. The equipment and procedures developed for this purpose are an adaptation of those found accurate and useful in earlier, closely related measurements of currents and charges per unit length on electrically thin cylinders (refs. 1 and 2) and of current densities on electrically thick tubular cylinders (ref. 14). As shown schematically in Fig. 23(a), it consists of an electrically thick conducting cylinder (of aluminum with 6 in. O.D. and 0.25 in. wall thickness) mounted on a ground plane (length ℓ, width w) and arranged so that it can be rotated through 360°. A suitably shaped groove [Fig. 23(a and b)] is cut in the wall the full length of the cylinder to guide the probe-carrying slider shown in Fig. 23(c). Three probes are mounted on the slider, viz., a short monopole to measure the radial electric field E_ρ (proportional to the surface density of charge η) and two mutually perpendicular, shielded semi-circular loops to measure the axial and transverse components of the magnetic vector, viz., B_z and B_θ (proportional, respectively, to the transverse and axial components K_θ and K_z of the surface density of current). The outputs from the probes are supplied to a vector voltmeter and used to obtain both amplitudes and relative phases of the currents and charges.

The currents and charges on the conducting cylinder are induced by the electromagnetic field maintained by a transmitting antenna consisting of a suitable monopole located at a distance d from the axis of the cylinder in a corner reflector as shown on the right in Fig. 23(a). The antenna is base-driven by a generator at the operating frequency of 626.5 MHz selected to make the electrical radius of the scattering cylinder ka = 1. Measurements were made of $\eta(\theta,z)$, $K_\theta(\theta,z)$ and $K_z(\theta,z)$ at suitable intervals in the

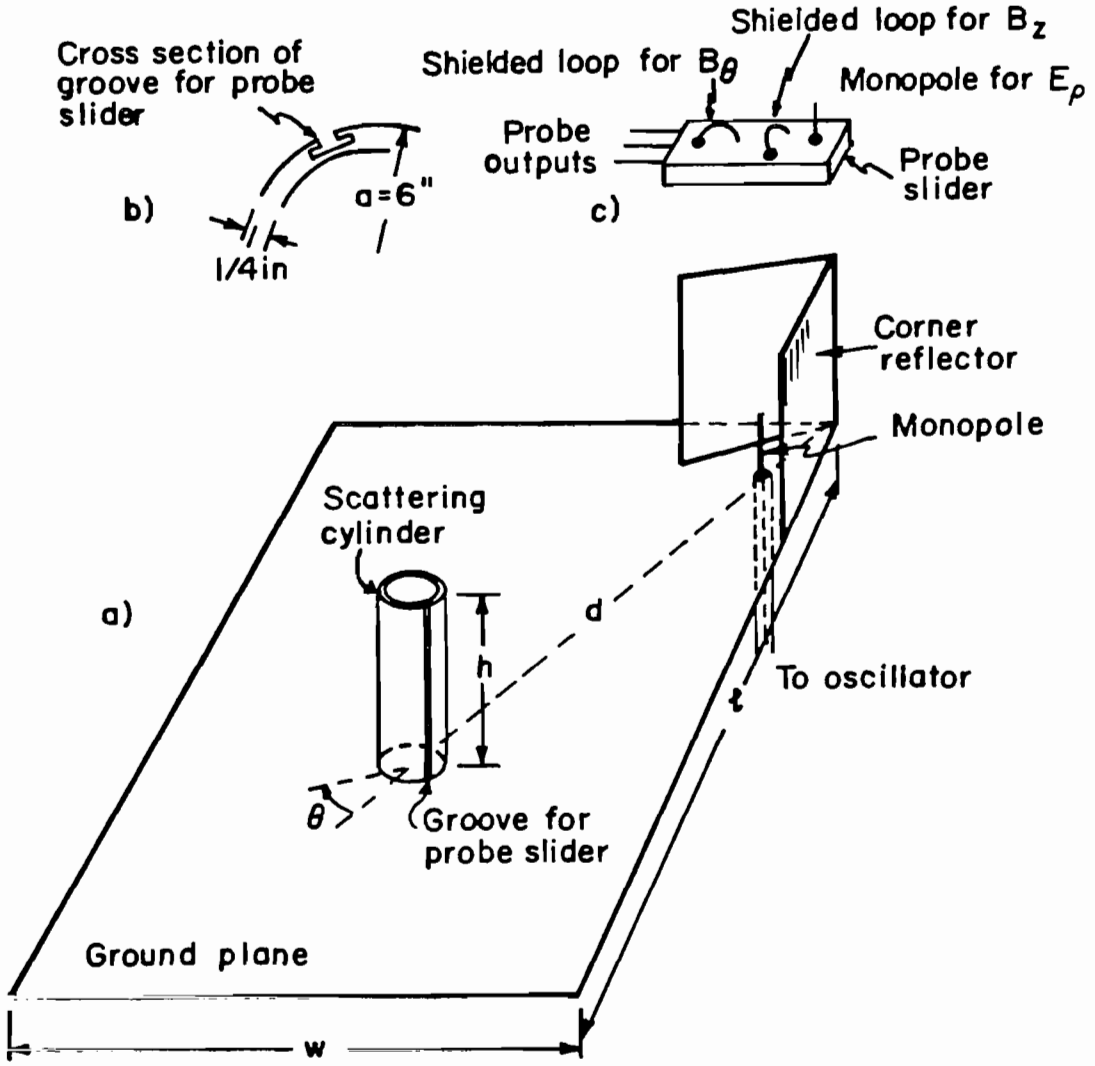

Fig. 23. Schematic diagrams of a) scattering cylinder on ground plane, b) cross section of groove in cylinder, and c) probes on slider.

range between $z = 0$ and $z = h$, $\theta = 0°$ and $\theta = 180°$ for a cylinder with $kh = 1.5\pi$.

2. PHYSICAL LIMITATIONS AND THEORETICAL ASSUMPTIONS

The practical conditions of the experiment necessarily differ from the ideal ones implicit and explicit in the theory in a number of potentially important ways.

a. The ground plane is neither infinite in extent nor perfectly conducting but is a rectangle of aluminum with the dimensions $\ell \times w$ which are 30.5×15.25 wavelengths for a large outdoor ground plane and 6.3×4.2 wavelengths for a small indoor ground plane. The presence of the boundaries at finite distances involves reflections that modify the ideal outward traveling field.

b. The distance d from the axis of the cylinder to the source of the incident electromagnetic waves is not infinite (as is implicit for the incident plane waves assumed in the theory) but 10 wavelengths for the large outdoor ground plane, 4 wavelengths for the small indoor plane. As a consequence, the field incident on the surface of the cylinder with $kh = 1.5\pi$ and $ka = 1$ is approximately plane when $d = 10\lambda$, much less so when $d = 4\lambda$.

c. The scattering cylinder does not have the infinitely thin, perfectly conducting walls assumed in the theory. Actually the walls have the thickness $t = 0.25$ in. and their conductivity is that of aluminum. An important consequence is the replacement of the infinitely thin sheaths of current $\vec{K}(\theta,z)$ and charge $\eta(\theta,z)$ at $\rho = a$ in the theory by two thin layers of current and charge on the outside ($\rho = a$) and inside ($\rho = a - t$) of the tube. Since the thickness t of the walls is large compared with the skin depth in aluminum, the two sets of currents and charges are separate. The former is determined by the tangential magnetic and normal electric fields just outside the tube, the latter by these fields just inside the tube. So long as ka is sufficiently small to preclude waveguide modes in the interior of the tube, the inside currents and charges are confined to short distances near the open end. The thin sheath of current used in the theory is defined in terms of the total discontinuity in the tangential magnetic field from just inside ($\rho = a_-$) to just outside ($\rho = a_+$) the sheath of current. It is possible to associate a part of the current $\vec{K}_+(\theta,z)$ with the

magnetic field at a_+, a part $\vec{K}_-(\theta,z)$ with the field at a_-. Then $\vec{K}(\theta,z) = \vec{K}_+(\theta,z) + \vec{K}_-(\theta,z)$. Note that $K_z(\theta,h) = 0$ so that $K_{z-}(\theta,h) = -K_{z+}(\theta,h)$. It is necessary to associate the measured outside current with $\vec{K}_+(\theta,z)$, not with $\vec{K}(\theta,z)$. However, where $\vec{K}_-(\theta,z)$ is sufficiently small, $\vec{K}(\theta,z) \doteq \vec{K}_+(\theta,z)$.

d. The slider that supports the three probes moves in a groove that does not penetrate to the interior of the tube but does constitute an irregularity in the otherwise smooth outside surface. Cover plates in small sections were provided to eliminate this difficulty. However, since no observable differences in the measurements were noticed with the slot open or completely closed, the time-consuming routine of keeping the slot covered was omitted, and all measurements were made without covers on the groove.

The quantitative significance of most of the differences between the actual structure used in the measurements and the ideal conditions assumed in the theory cannot be resolved analytically. However, their combined effects can be observed from a detailed comparison of the graphs of corresponding quantities determined experimentally and theoretically. Suitable interpretation can then be made. For this purpose complete sets of measurements that parallel the theoretical results presented graphically in Section III are required.

Preliminary measurements were first made with a cylinder of electrical length $kh = 1.5\pi$ erected on a small ground plane (2 m × 3 m) in a large room in the laboratory. The axis of the scattering cylinder was 4 wavelengths from the driven monopole in the corner reflector. Originally this small indoor ground plane was to be used only to test the apparatus and perfect the technique and procedures of measurement more quickly and conveniently than could be done on the large outdoor ground plane. However, since the measured quantities with the small plane were in remarkably good agreement with their theoretical counterparts, it seemed desirable to obtain a complete set of measurements both for purposes of testing and for comparison with a second set obtained later on the large outdoor ground plane with the same apparatus. The description, comparison, and critical evaluation of the two sets of experimentally determined graphs of $K_z(\theta,z)$, $K_\theta(\theta,z)$ and $\eta(\theta,z)$, and the corresponding theoretical set in Section III provide the essential validation of the experimental method and its procedures.

3. MEASURED SURFACE DENSITY OF AXIAL CURRENT $K_z(\theta,z)$

The measured amplitude and phase of the axial surface density of current $K_z(\theta,z)$ on the outside of the tube are shown as functions of z with θ as the parameter in Figs. 24 and 25 with the large ground plane and in Figs. 26 and 27 with the small ground plane. The corresponding theoretical graphs for the total surface density of axial current are in Figs. 6, 7 and 20. For simplicity the same symbols are used for the measured outside quantities and the theoretical total quantities since, as seen from Fig. 20, they are comparable except within short distances of the open end where there are significant inside currents. The agreement between the theoretical graphs and the measured ones for the large outdoor ground plane are excellent for both amplitude and phase. The graphs of the currents with the cylinder on the small indoor ground plane are generally in good agreement with the others. The principal differences are in the curves in the range $\theta = 0°$ to $60°$ in the shadow region where the second maximum of current near $z = 24$ cm is somewhat higher with the smaller ground plane than with the larger one or the theoretical values. For many applications the results obtained with the small ground plane should be satisfactory.

The same complete agreement between theory and measurements over the large outdoor ground plane exists among the measured graphs in Figs. 28 and 29 and the comparable theoretical graphs displayed in Figs. 22a and 22b of reference 4. Of course, account must again be taken of the fact that the theoretical curves are for the total current, the measured ones for the outside current only. The amplitudes of the curves for the current in the upper quarter wavelength, i.e., $z \geq 24$ cm or $kz \geq \pi$, clearly show that the theoretical total current approaches zero at $kz = kh = 1.5\pi$ whereas the measured outside current approaches a significant value at $z = h = 36$ cm. The corresponding graphs for the small indoor ground plane are in Figs. 30 and 31. They are in good general agreement with small differences due to the slightly higher maxima in the ranges $\theta = 0°$ to $60°$, $z > 24$ cm of the shadow region.

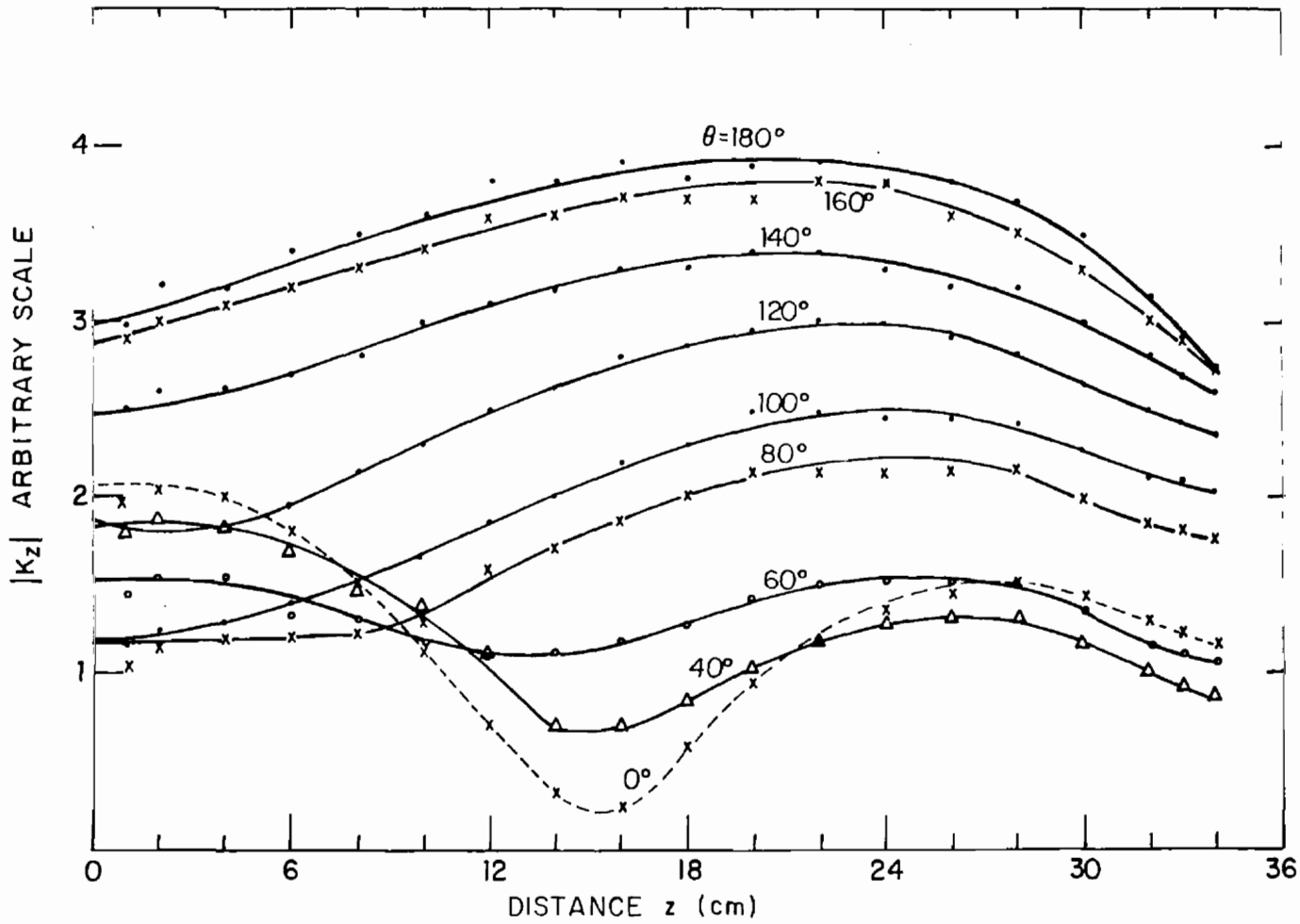

Fig. 24. Measured amplitude of axial surface density of outside current on tubular cylinder; E-polarization, large outdoor ground screen.

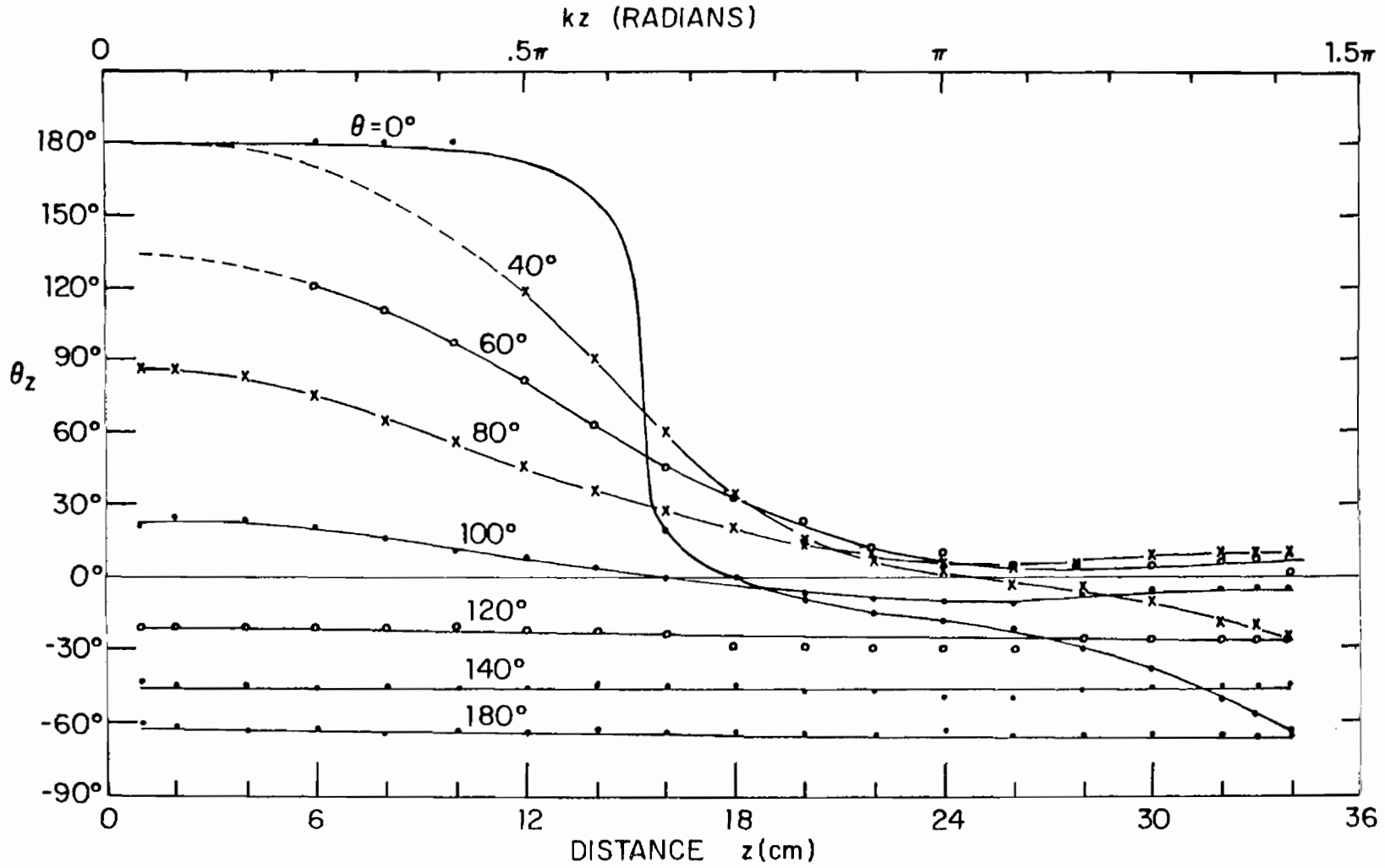

Fig. 25. Measured phase of axial surface density of outside current on tubular cylinder; normalization: $-\theta_{obs}$, large outdoor ground screen.

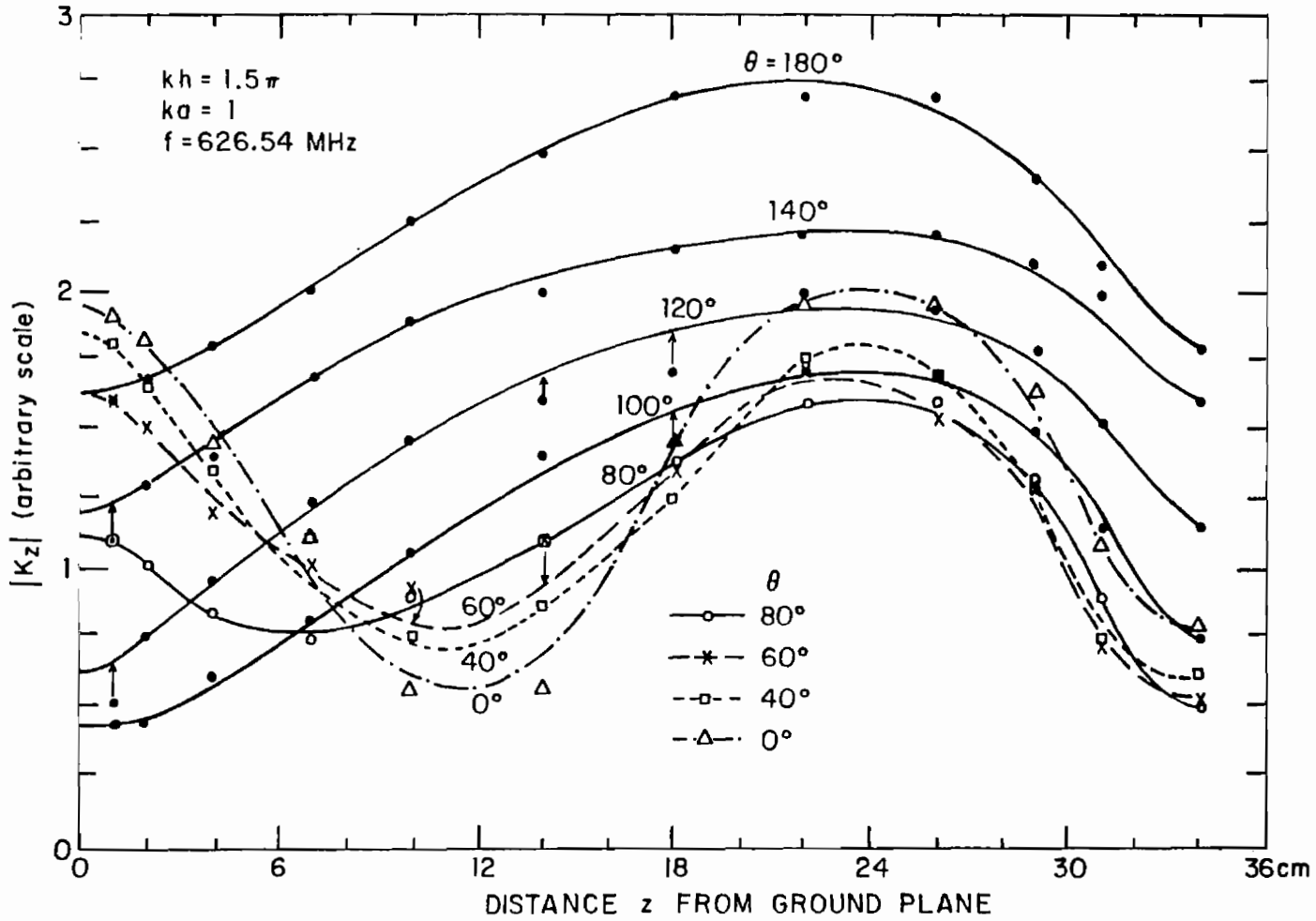

Fig. 26. Measured amplitude of axial surface density of outside current on tubular cylinder; E-polarization, small indoor ground screen.

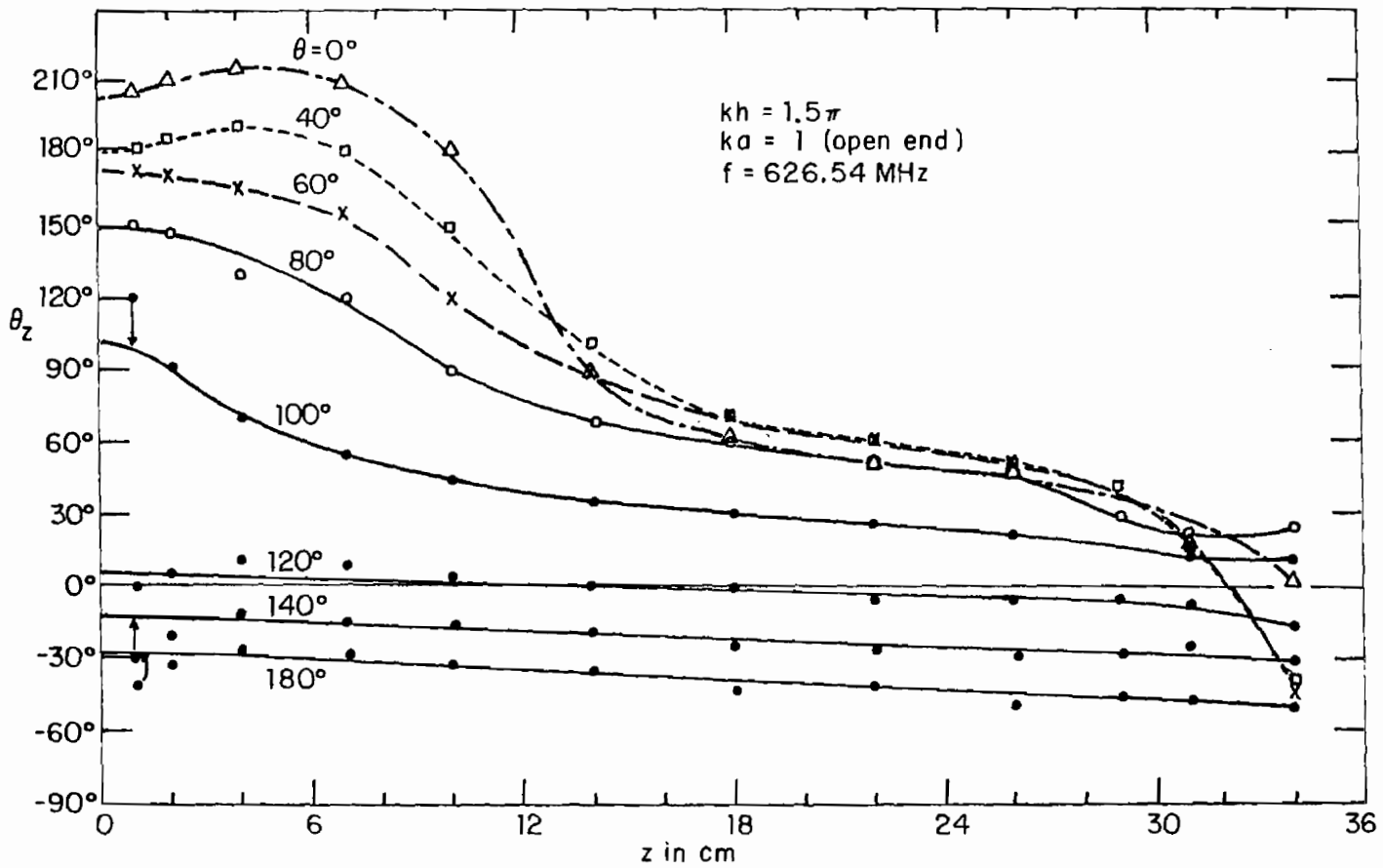

Fig. 27. Measured phase of axial surface density of outside current on tubular cylinder; E-polarization, small indoor ground screen.

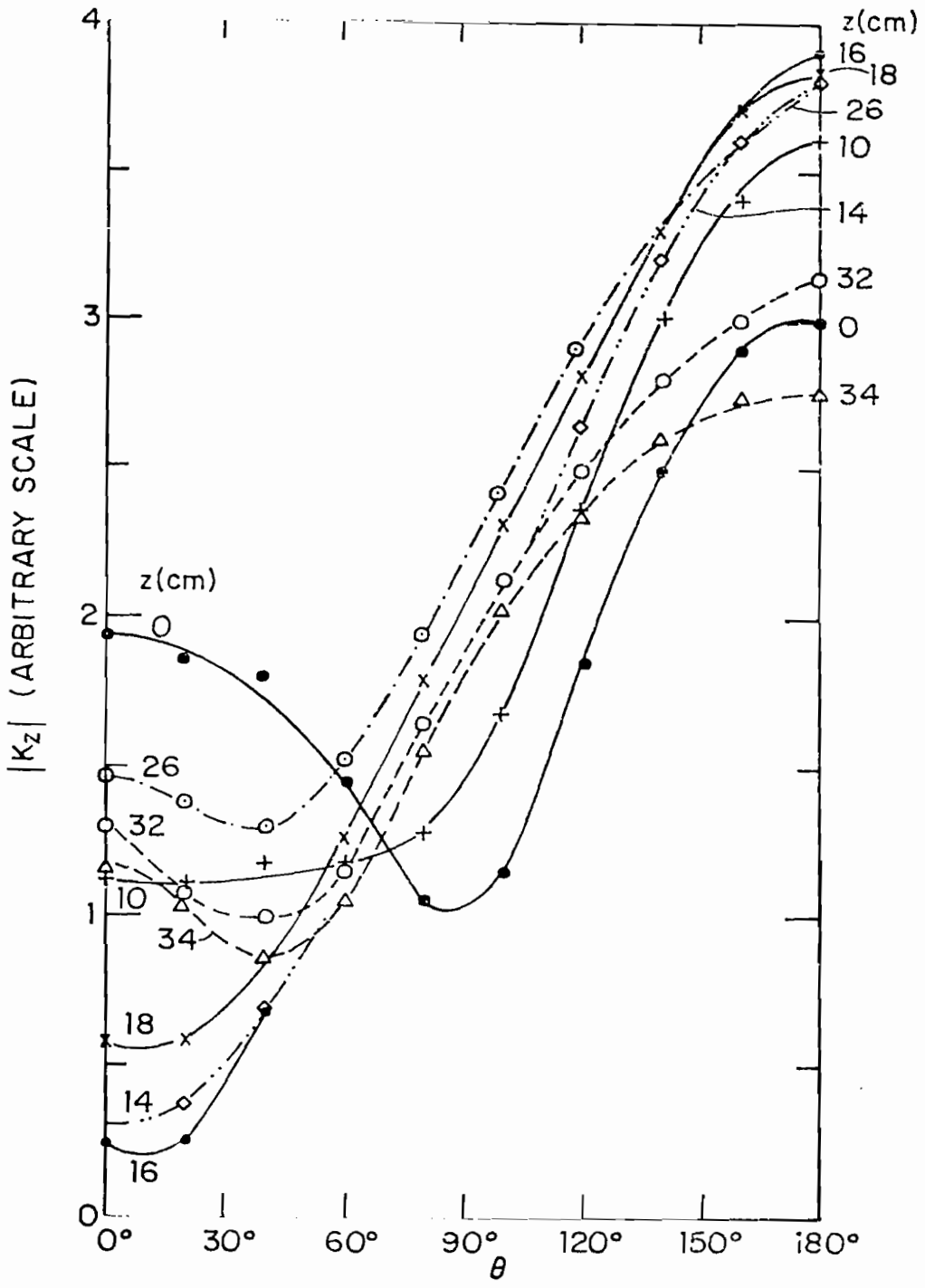

Fig. 28. Measured amplitude of axial surface density of outside current on tubular cylinder; E-polarization, large outdoor ground screen.

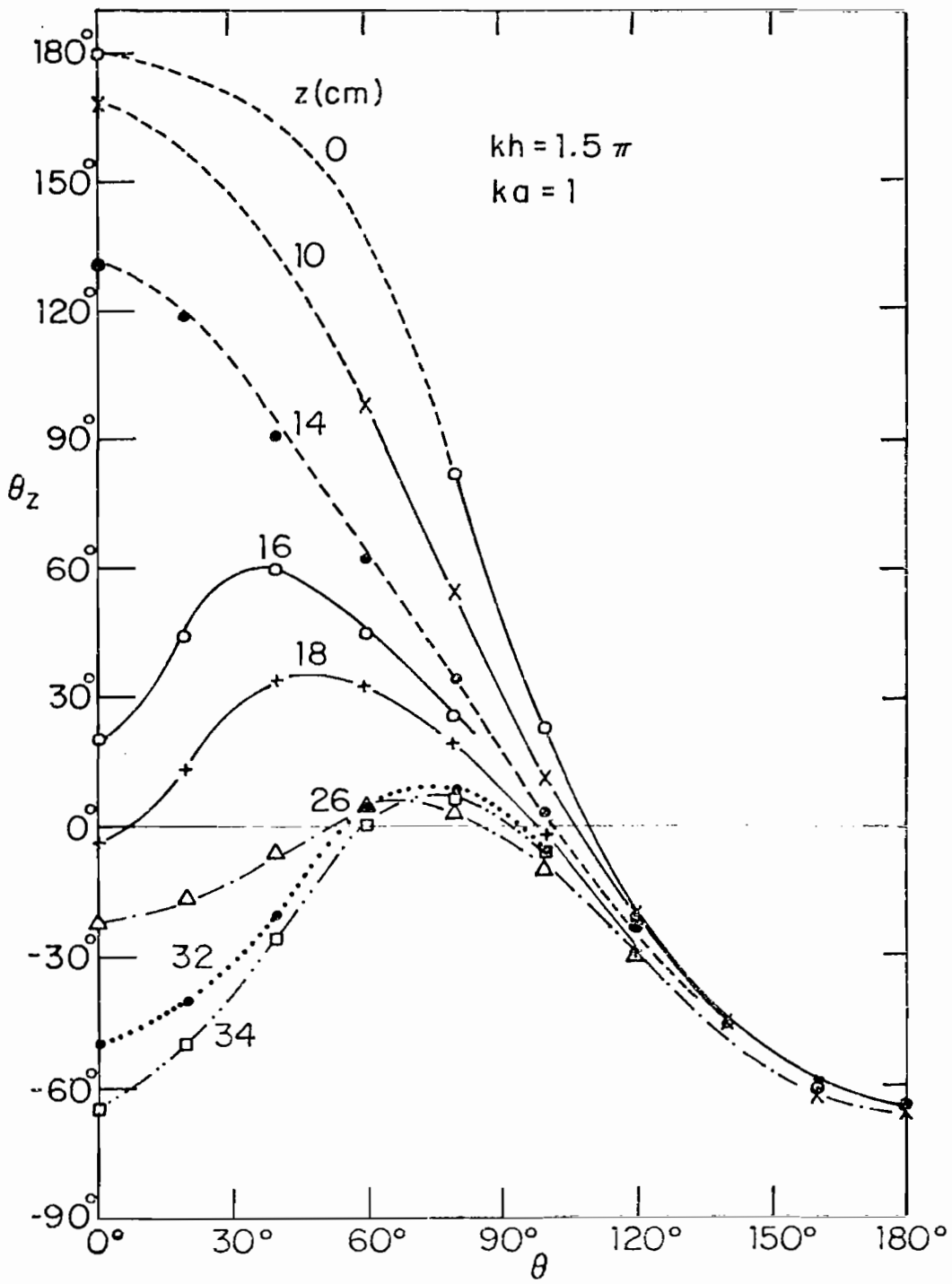

Fig. 29. Measured phase of axial surface density of outside current on tubular cylinder; E-polarization, large outdoor ground screen.

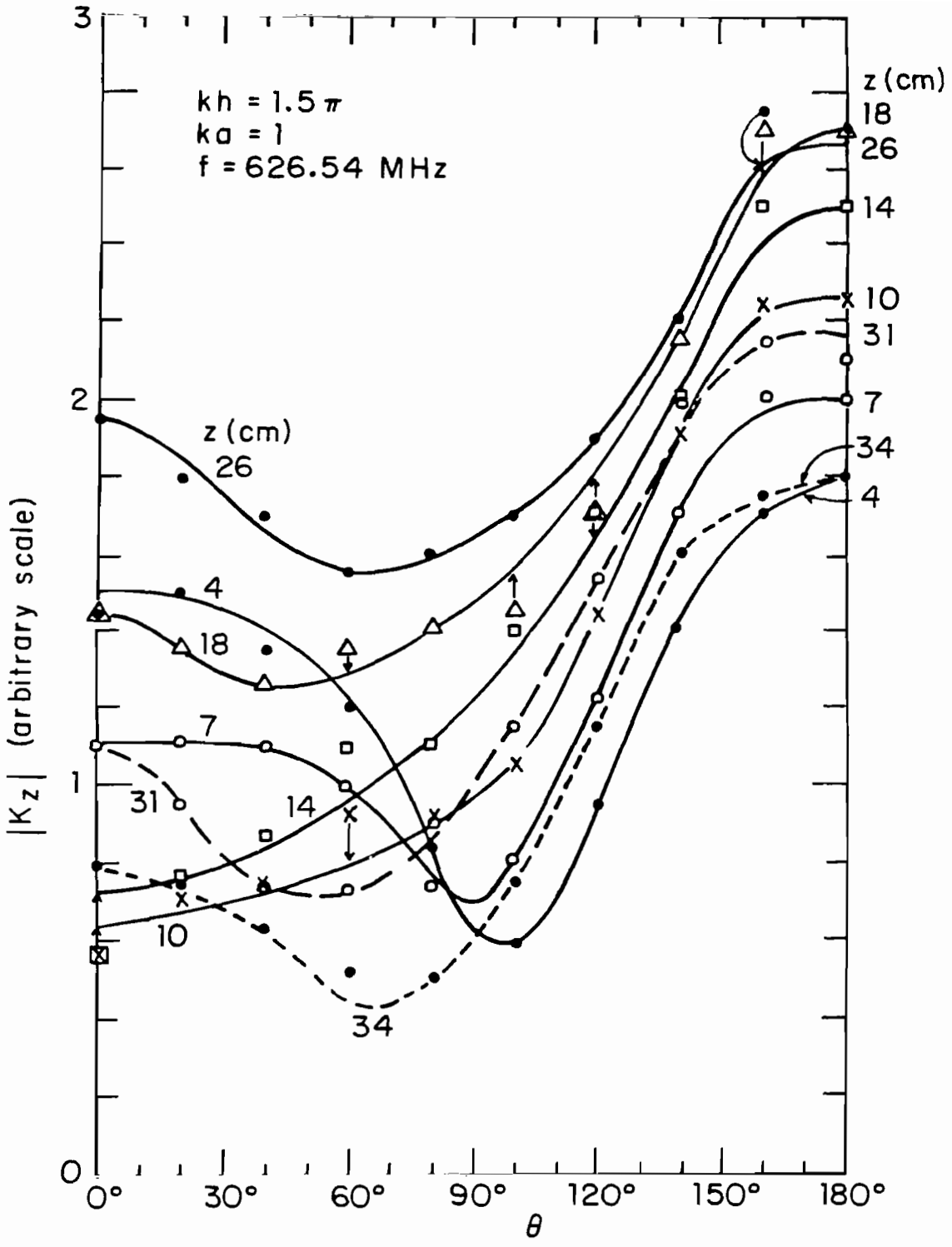

Fig. 30. Measured amplitude of axial surface density of outside current on tubular cylinder; E-polarization, small indoor ground screen.

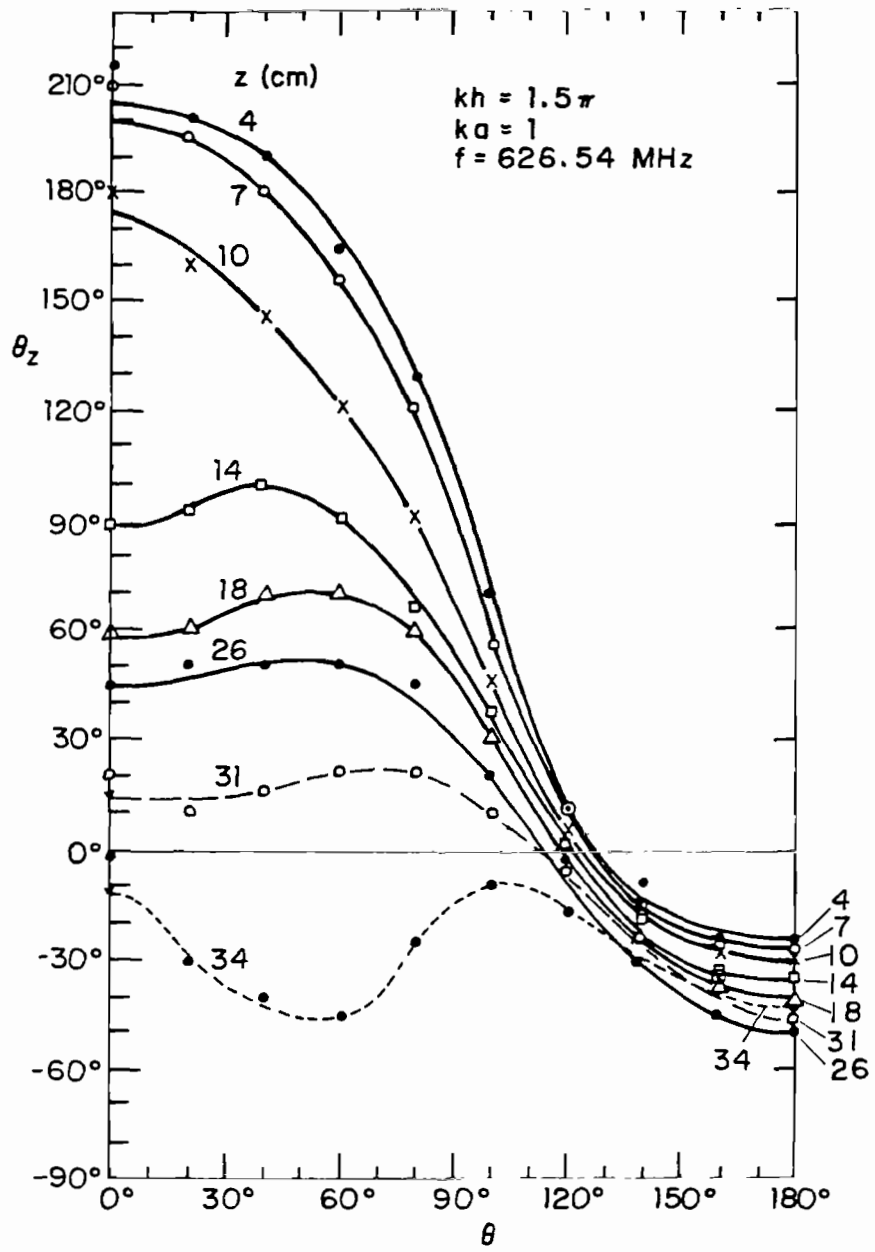

Fig. 31. Measured phase of axial surface density of outside current on tubular cylinder; E-polarization, small indoor ground screen.

4. MEASURED SURFACE DENSITIES OF TRANSVERSE CURRENT $K_\theta(\theta,z)$; POLARIZATION ELLIPSES

The measured amplitudes and phases of the transverse component of current $K_\theta(\theta,z)$ are shown graphically in Figs. 32 and 33 for the large outdoor ground plane and in Figs. 34 and 35 for the small indoor ground plane. The corresponding graphs of the theoretical amplitudes and phases of the transverse current are in Figs. 23a and 23b of reference 4. The amplitudes are in excellent agreement, the phases somewhat less so with measurements over the large ground plane. The measurements over the small ground plane are only slightly different. The differences between the theoretical and measured phases occur principally where $|K_\theta(\theta,z)|$ is very small and accurate phase measurements are difficult to make. In any event, the phases of these very small currents are not important in determining the principal properties of the current on the cylinder.

The polarization ellipses of the measured components of current on the cylinder over the small ground plane are shown in Fig. 36. They are in good general agreement with the corresponding theoretical ellipses in Fig. 11 except along the lines $\theta = 0°$ and $\theta = 180°$ where the measured values are clearly inaccurate. Along these lines the current is linearly polarized; there can be no transverse component of current. It was later discovered that the alignment of the small loop to measure the transverse current was not exact so that a very small component of the relatively large axially directed current contributed to what should have been a response due exclusively to the transverse current. The measured currents with an accurately aligned pair of loops have been verified to give linearly polarized currents along the vertical lines for $\theta = 0°$ and $180°$. The original data are retained in Fig. 36 in order to point out the high precision required in the construction of the small probes.

5. MEASURED SURFACE DENSITIES OF CHARGE

The measured surface densities of charge on the cylinder are shown* in Fig. 37 for the large ground plane, in Figs. 38 and 39 for the small ground

*Owing to a malfunctioning of the phase meter, no phase data are given over the large ground plane.

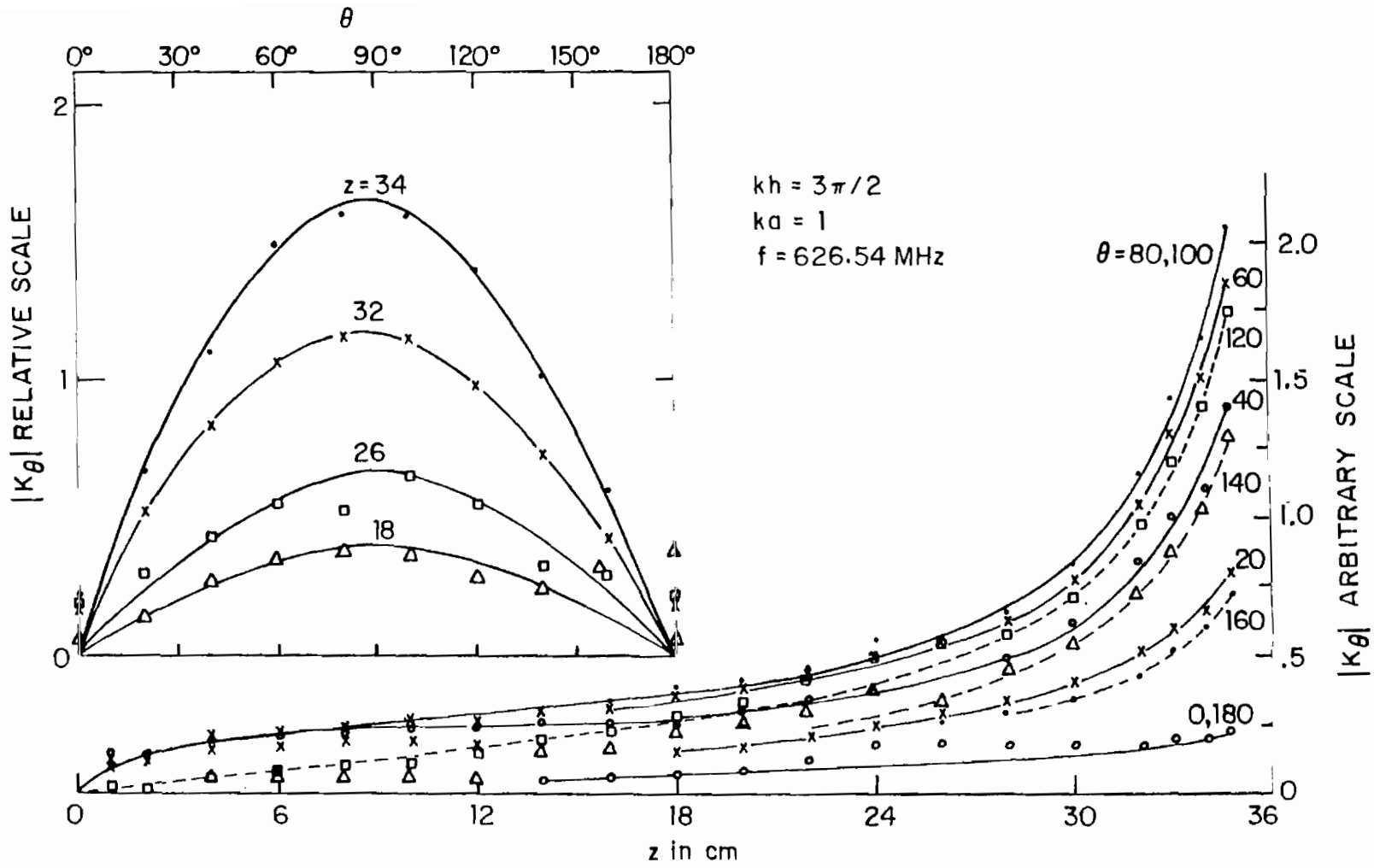

Fig. 32. Measured amplitude of surface density of transverse current on tubular cylinder; E-polarization, large outdoor ground screen.

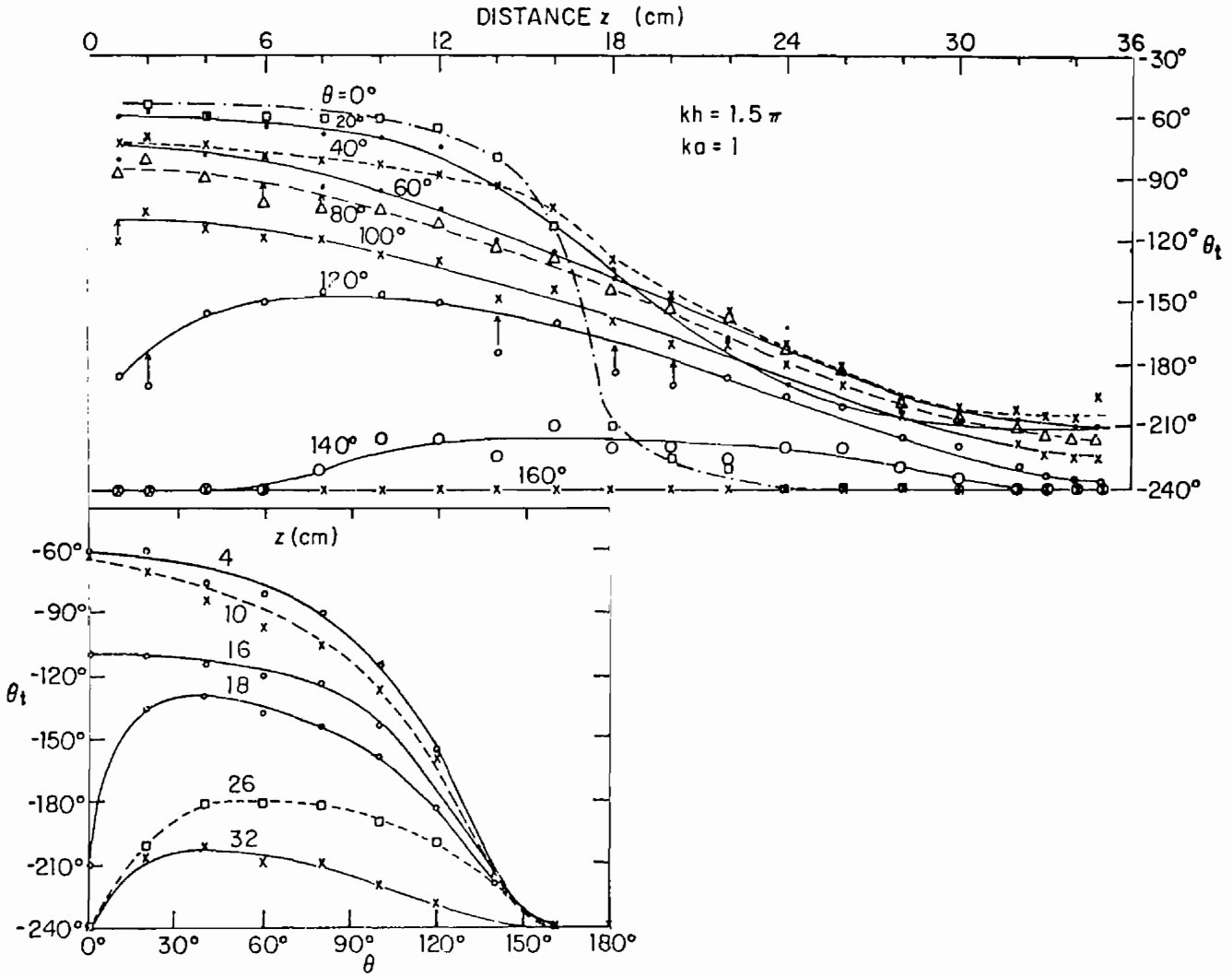

Fig. 33. Measured phase of surface density of transverse current on tubular cylinder; E-polarization, large outdoor ground screen.

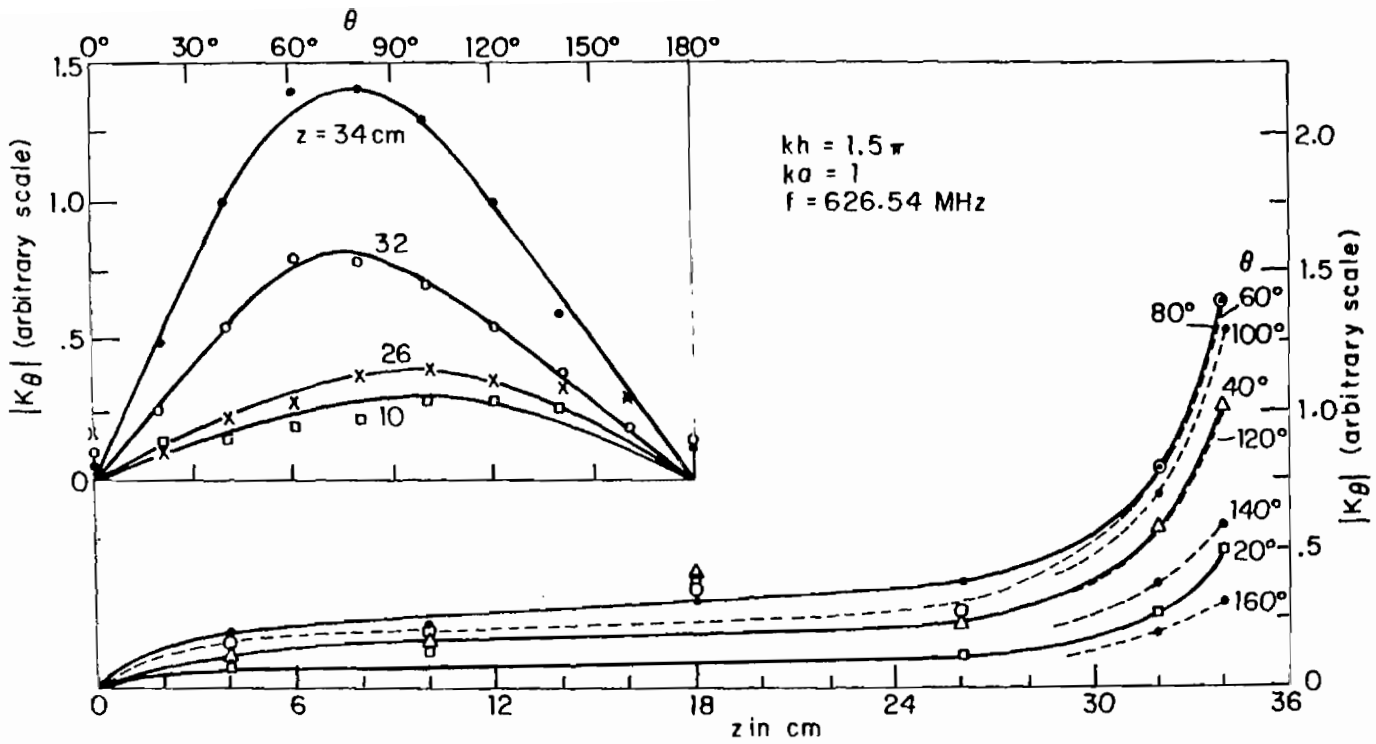

Fig. 34. Measured amplitude of surface density of transverse current on tubular cylinder; E-polarization, small indoor ground screen.

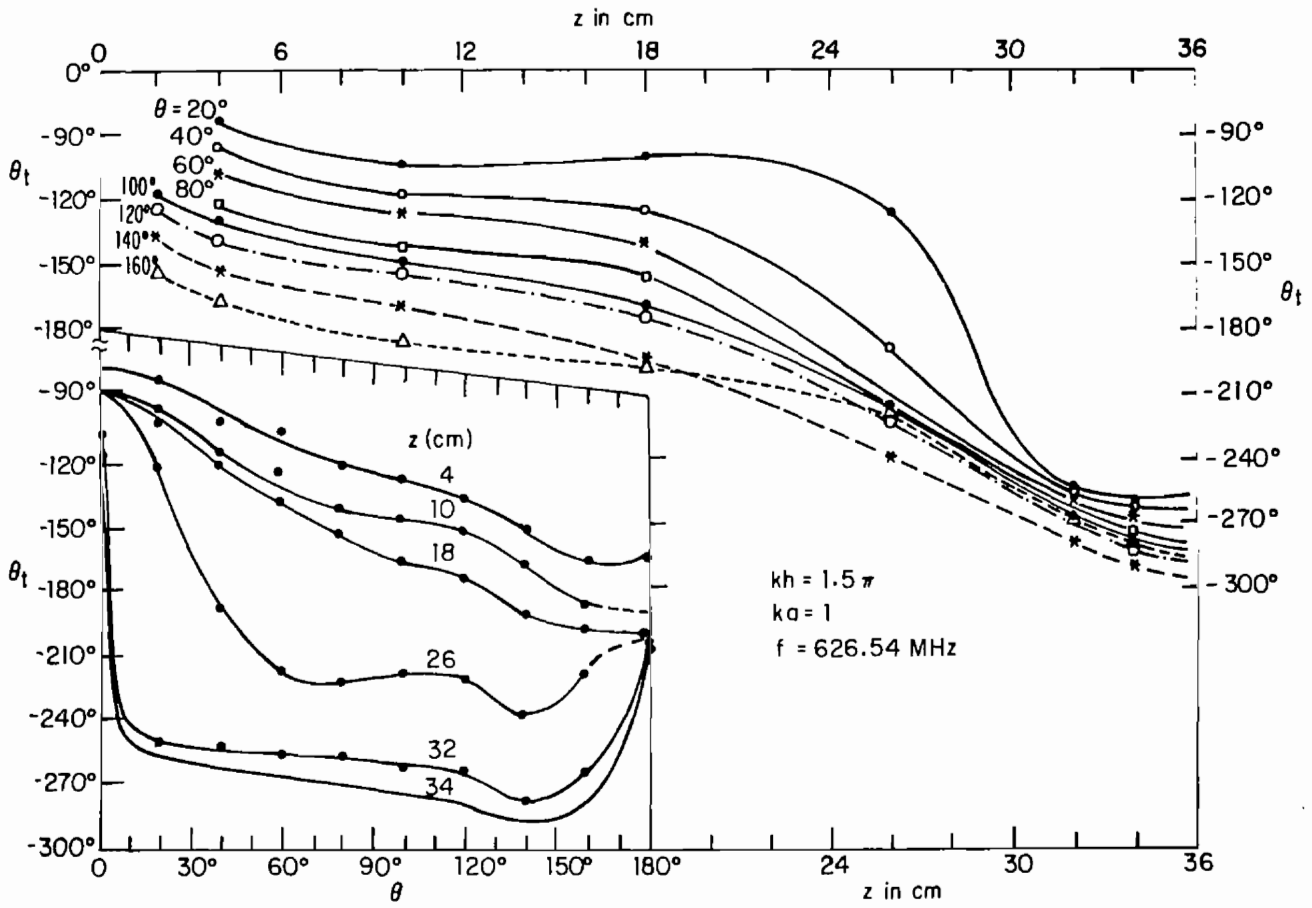

Fig. 35. Measured phase of surface density of transverse current on tubular cylinder; E-polarization, small indoor ground screen. Phase normalization: $300° - \theta_{obs} - 360° = -(\theta_{obs} + 60°)$.

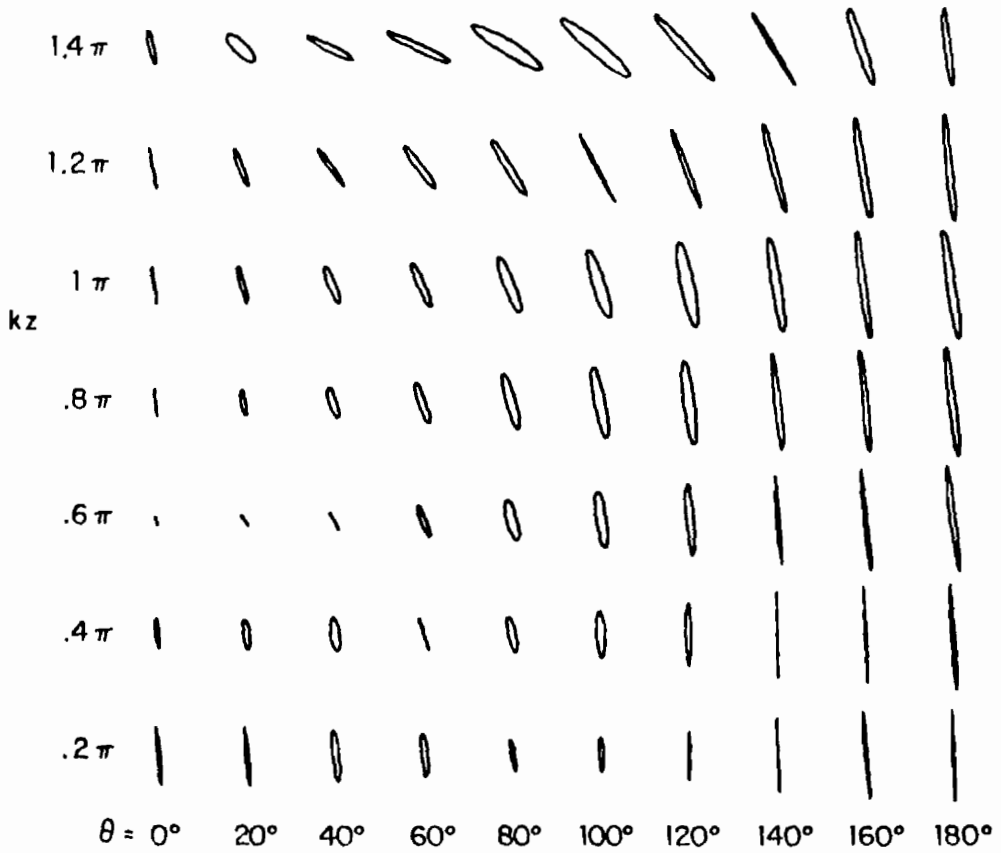

Fig. 36. Measured polarization ellipses of $\vec{K}(\theta,z)$; kh = 1.5π, ka = 1, small indoor ground screen.

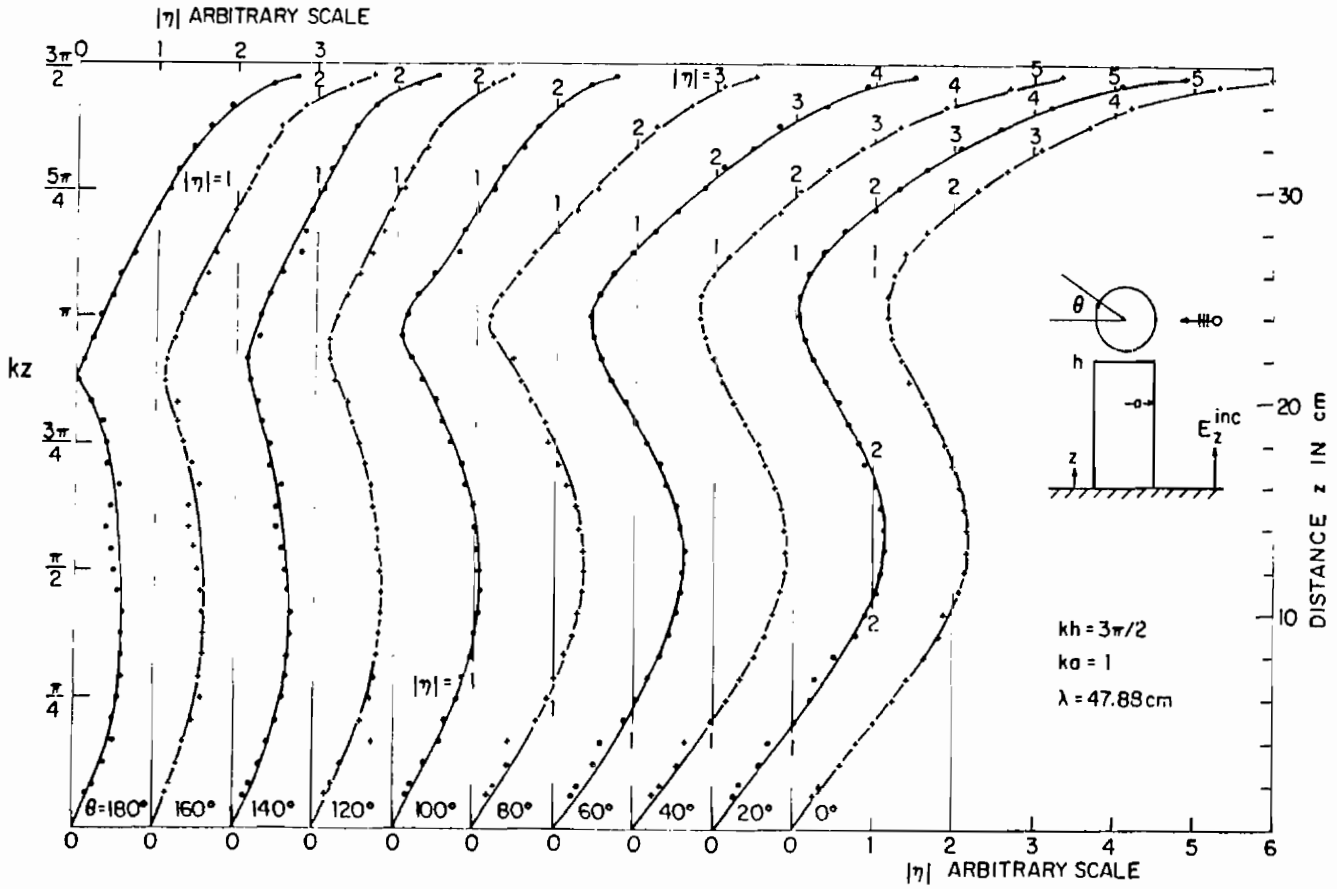

Fig. 37. Measured magnitude of surface density of charge $\eta = |\eta| e^{i\theta_\eta}$ on tubular cylinder; E-polarization, large outdoor ground screen.

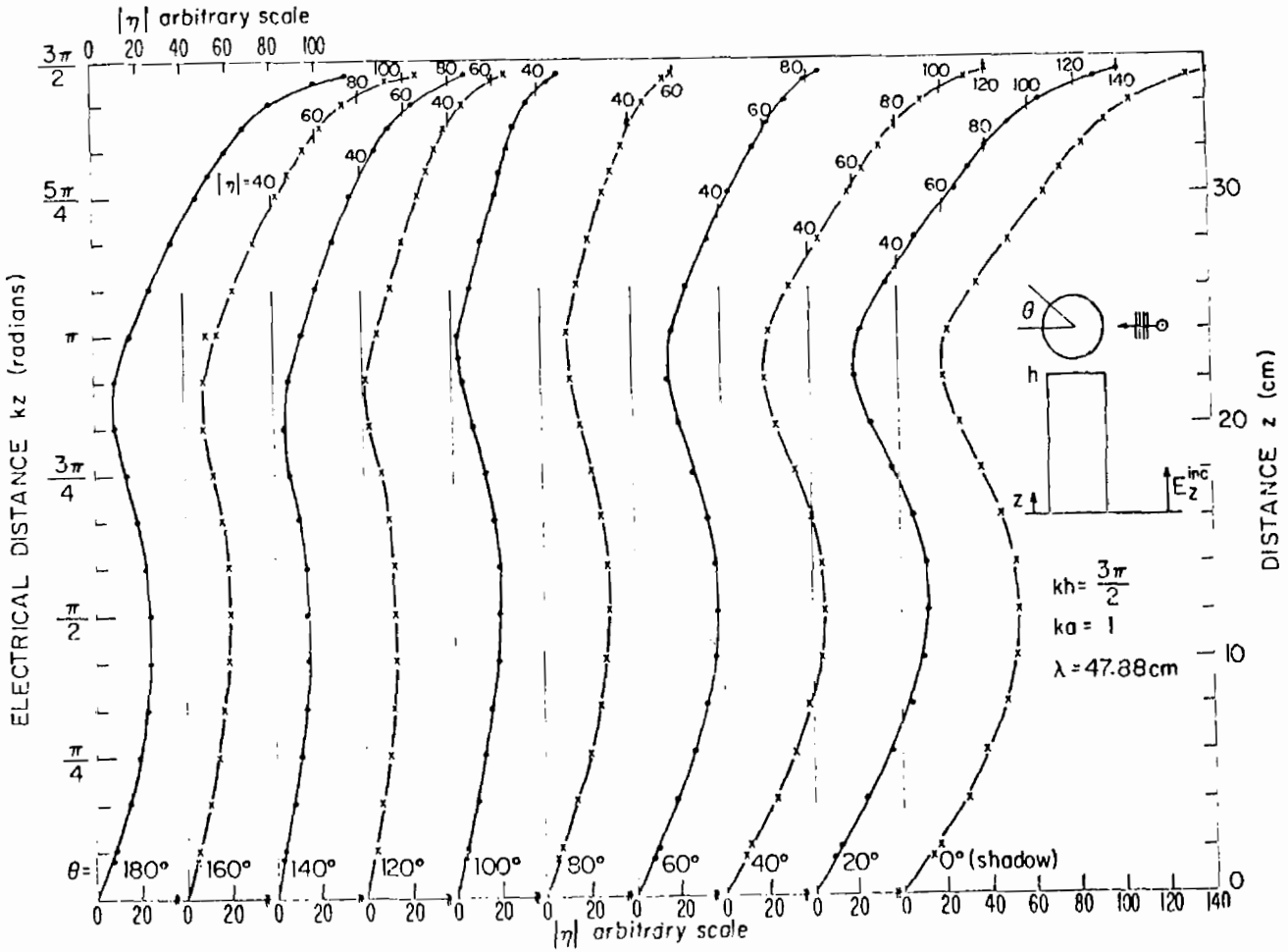

Fig. 38. Measured magnitude of surface density of charge $\eta = |\eta| e^{i\theta_\eta}$ on tubular cylinder; E-polarization, small indoor ground screen.

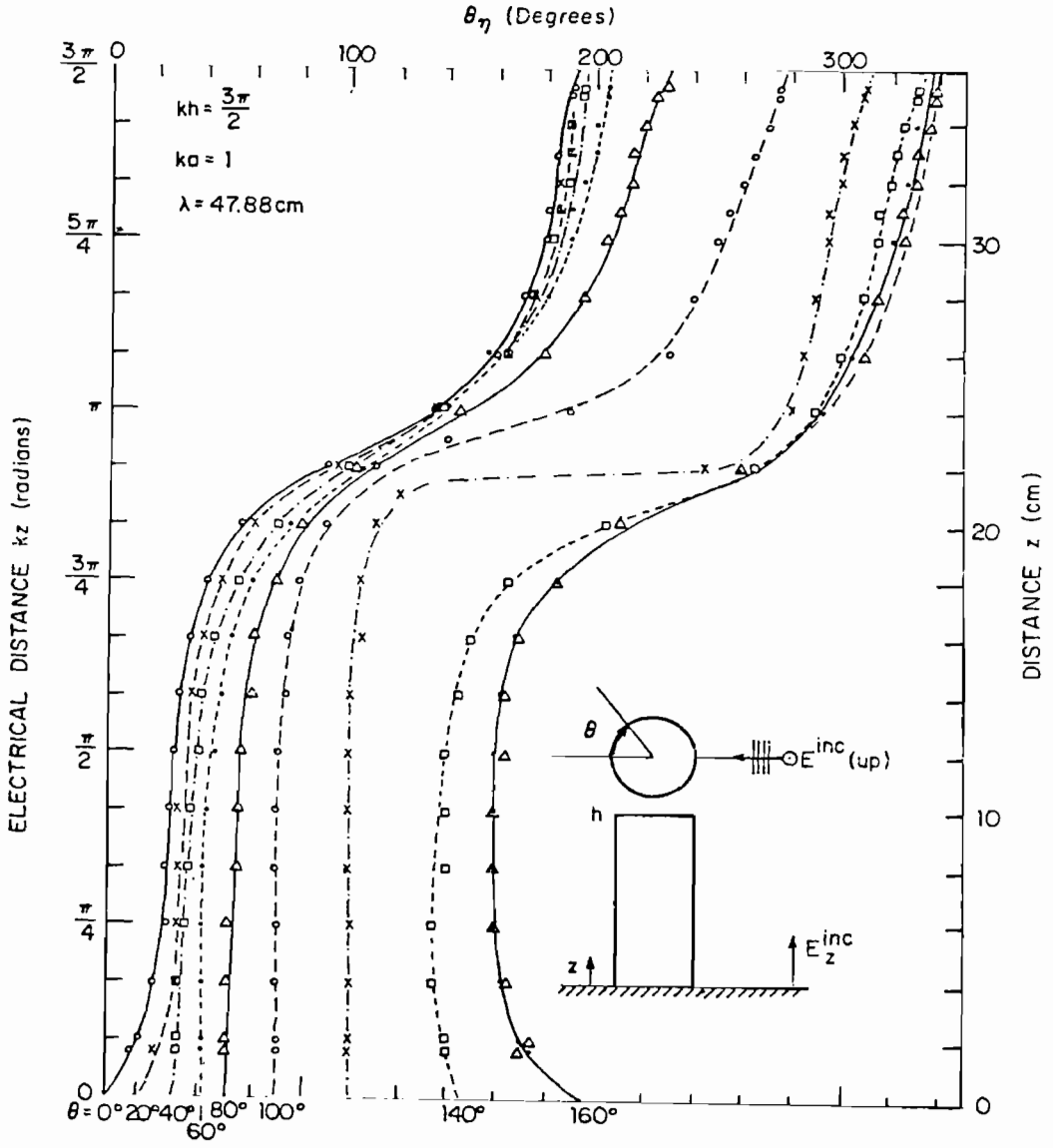

Fig. 39. Measured phase of surface density of charge $\eta = |\eta| e^{i\theta_\eta}$ on tubular cylinder; E-polarization, small indoor ground screen.

plane. The corresponding theoretical graphs are in Figs. 12, 13 and 22. The general agreement among the measured and theoretical sets of graphs is very good. There are small differences in the depths of the minima between $kz = 0.75\pi$ and $kz = \pi$ but their relative magnitudes and locations are in agreement. There are more substantial differences in the relative magnitudes of the charge density as the end of the cylinder at $z = h$ is approached. These differences are related to the quite different slopes of the curves for the theoretical total current and the theoretical and measured outside current. Similar differences occur between the measured curves in Figs. 40 through 42, which show the charge density in magnitude and phase as a function of θ with kz as the parameter, and the corresponding theoretical graphs (not shown). These curves are in generally good agreement except when $kz > \pi$ or $z > 24$. In this range the slopes of the components of total theoretical current and outside measured current and the associated charge densities are necessarily different.

Perhaps the most revealing comparison of distributions of charge density as measured over the large outdoor ground plane and as calculated theoretically is displayed in Figs. 43 and 14, respectively. These show contours of constant charge density (magnitude) on half of the cylinder with the shadowed side on the left, the illuminated side on the right. The agreement is seen to be excellent except very close to the open end at the top where differences necessarily exist since different quantities are represented. Note in both diagrams the peak of charge near $\theta = 0°$, $kz \doteq 0.5\pi$, and the continuing decrease in amplitude along the coordinate $kz = 0.5\pi$ from $\theta = 0°$ to $\theta = 180°$. Note also the deep minimum in the neighborhood of $kz = \pi$ extending from $\theta = 0°$ to $\theta = 180°$. From $kz = \pi$ to $kz = 1.5\pi$ there is a rapid increase for all values of θ but with certain differences in the θ distributions and in the rate of increase due to the actually different quantities represented. A further comparison with the corresponding measurements on the small ground plane can be carried out with the aid of Fig. 44. This shows the same general topography with a peak at $\theta = 0°$, $kz = 0.5\pi$, a deep valley near $kz = \pi$ extending from $\theta = 0°$ to $\theta = 180°$, and steep increases for all values of θ as kh is approached from $kz \doteq \pi$. The measured transverse distributions for $kz > \pi$ are quite similar for the two ground planes.

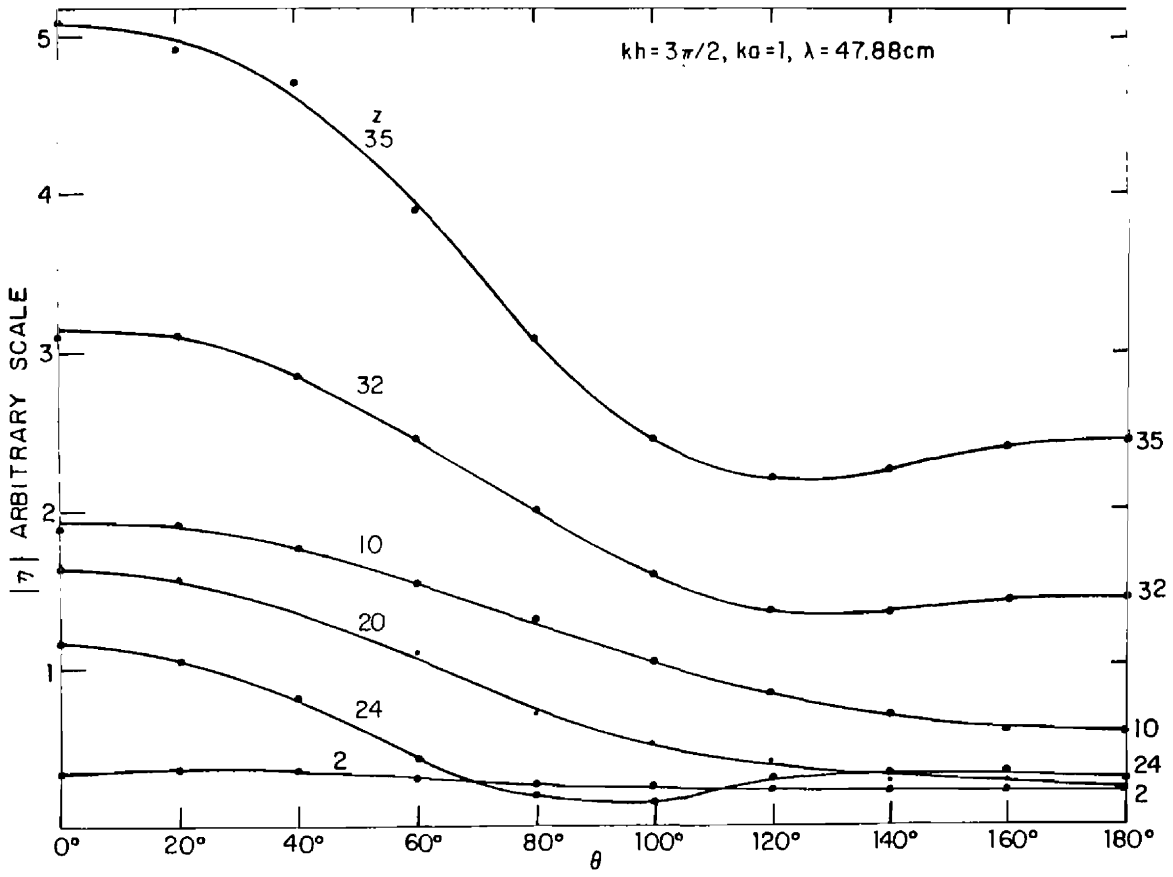

Fig. 40. Measured magnitude of surface density of charge $\eta = |\eta| e^{i\theta_\eta}$ on tubular cylinder; E-polarization, large outdoor ground screen.

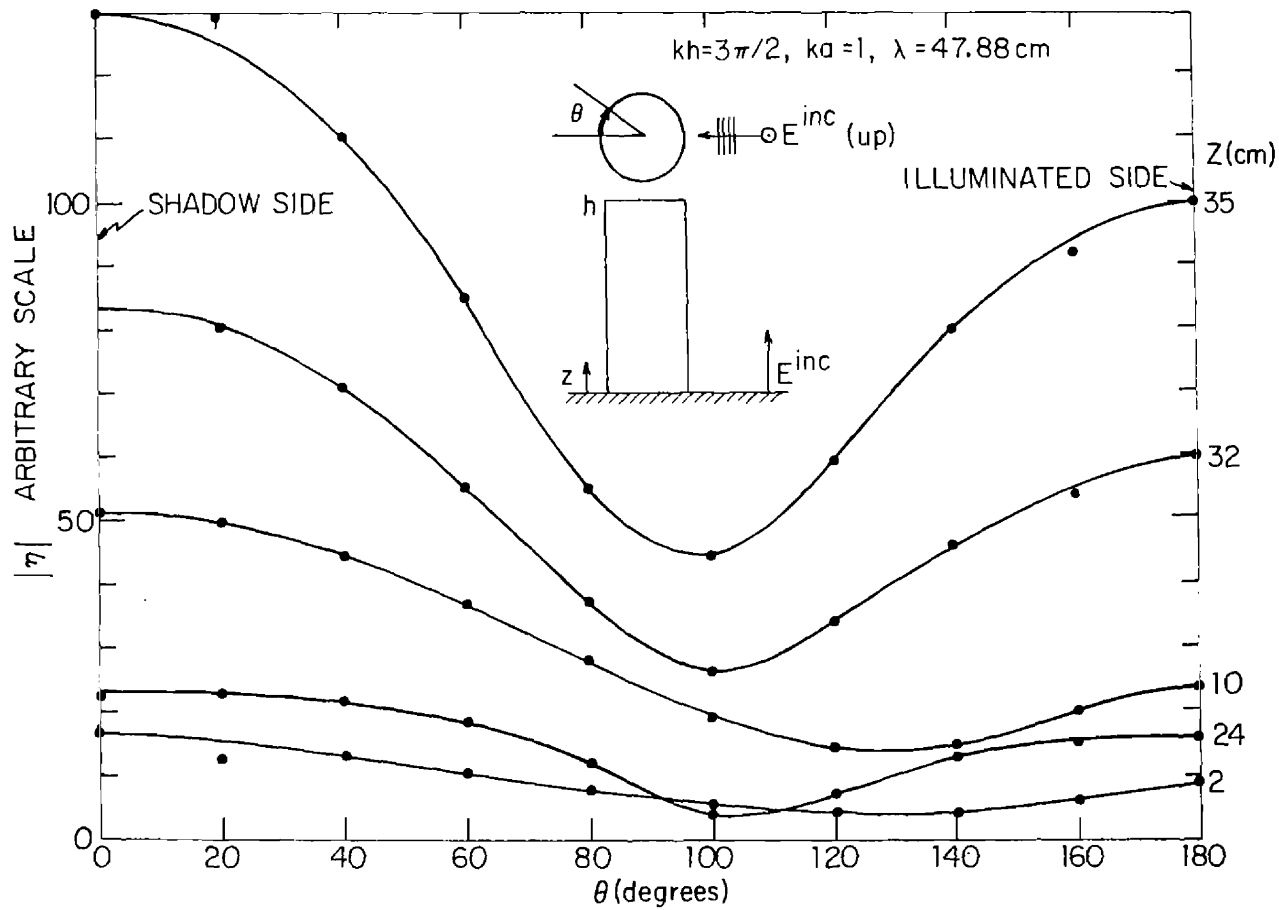

Fig. 41. Measured magnitude of surface density of charge $\eta = |\eta| e^{i\theta_\eta}$ on tubular cylinder; E-polarization, small indoor ground screen.

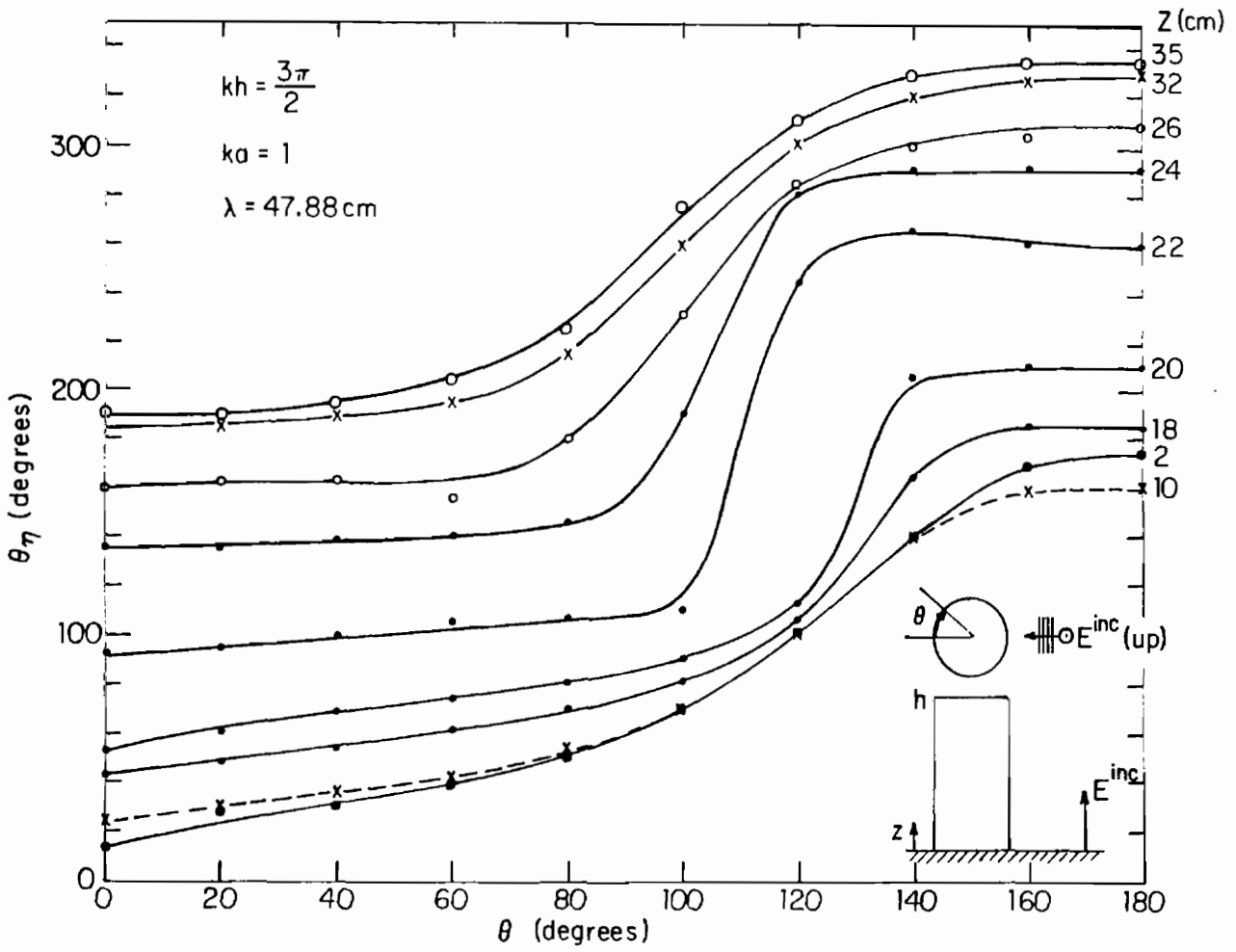

Fig. 42. Measured phase of surface density of charge $\eta = |\eta| e^{i\theta_\eta}$ on tubular cylinder; E-polarization, small indoor ground screen.

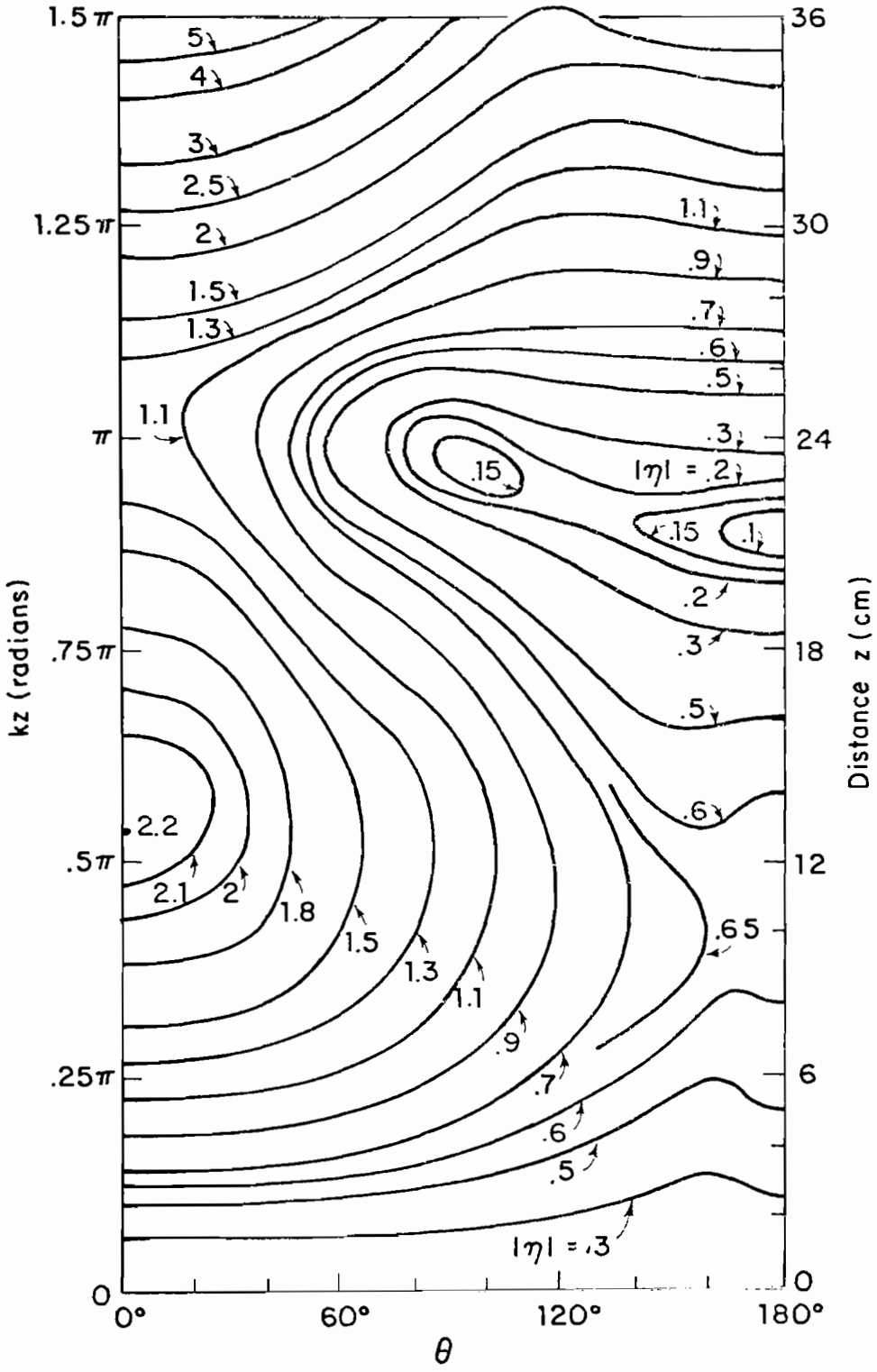

Fig. 43. Measured contours of constant magnitude of surface density of charge; kh = 1.5π, ka = 1, large outdoor ground screen.

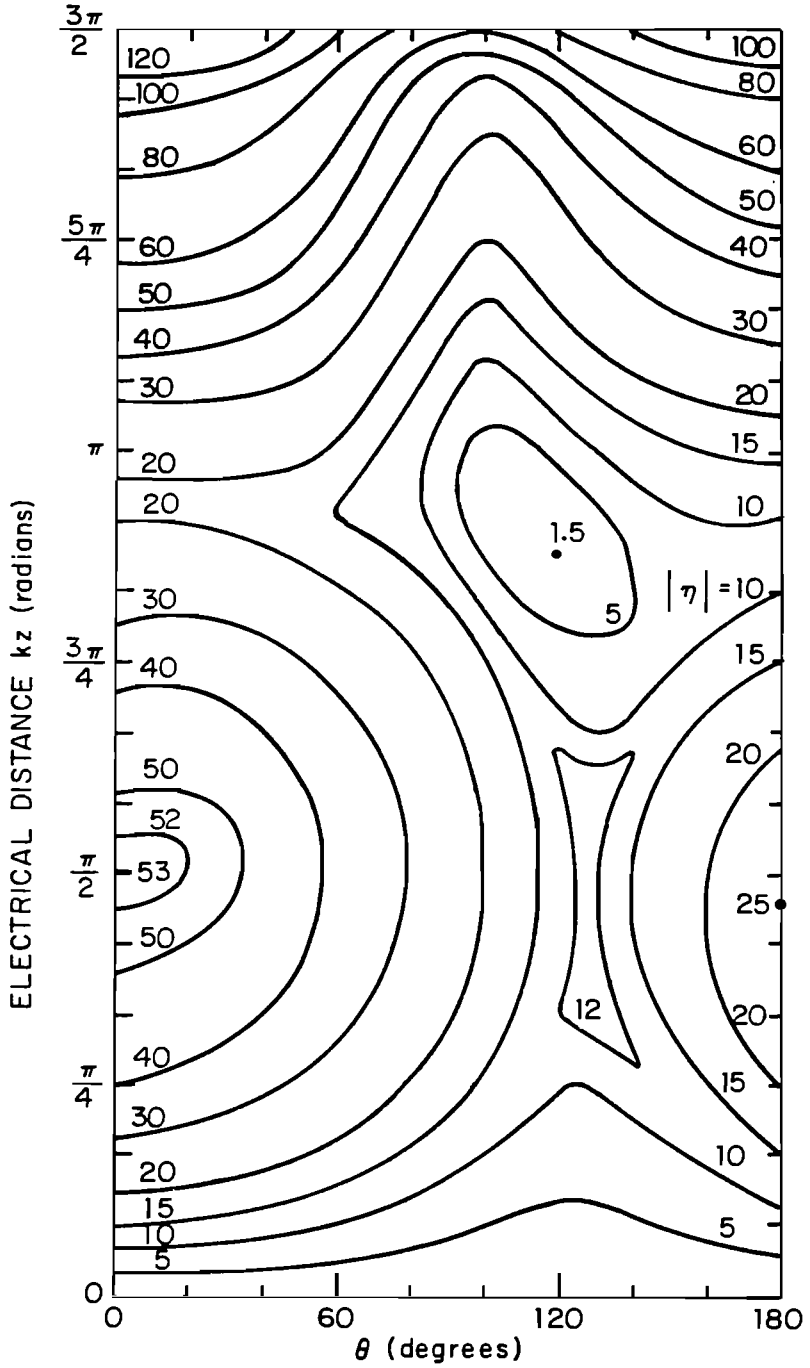

Fig. 44. Measured contours of constant magnitude of surface density of charge; kh = 1.5π, ka = 1, small indoor ground screen.

The most interesting and significant differences between the measured contours in Figs. 43 and 44 are on the illuminated half of the cylinder between $\theta = 120°$ and $180°$ and with $0 \leq kz < \pi$. It is also instructive to examine the corresponding ranges in the theoretically determined diagram in Fig. 14. This shows that across the cylinder at $kz = 0.5\pi$ from $\theta = 0°$ to $\theta = 180°$ the charge density decreases continuously from the high peak at $\theta = 0°$ to a very low valley at $\theta = 180°$. Note that the two contours marked 1.5 continue to approach each other until very nearly $\theta = 180°$ where they show signs of beginning to diverge. This means that the continuing decrease has reached a valley. This effect is substantially greater on the measured curves for the large ground screen in Fig. 43. Here the analogous contours for $|\eta| \sim 0.6$ begin to diverge at about $\theta = 172°$. This diverging trend is also evident in the contours for $|\eta| \sim 0.3$ and 0.5. The same behavior is seen as well in Fig. 44 for the small ground plane but very much accentuated. The divergence of the contours $|\eta| \sim 10$ begins at $\theta = 120°$, and on the circumferential line $kz = 0.5\pi$ the steady decrease from $\theta = 0°$ continues only to $\theta = 120°$ where there is a leveling off and then a steady increase, rather than a decrease, to $\theta = 180°$. It is significant that this shifting of the bottom of the valley along $kz = 0.5\pi$ proceeds from $\theta \doteq 180°$ for an infinite ground plane to $\theta \doteq 172°$ for the large ground plane and to $\theta = 120°$ for the small ground plane. Since the entire effect is limited to the illuminated side, it is reasonable to assume that it is related to the nature of the incident field and that the effect of the sequence from infinite, to large, to small ground plane is not so much determined by the distance to the edges of the ground plane as by the distance from the cylinder to the transmitting dipole which decreases from infinity to 10 wavelengths to 4 wavelengths. The significant difference is the shape of the wave front and specifically the relative phase distribution over the illuminated side. For the theoretical curves the wave front is plane, with the source at a distance of 10 wavelengths it is almost plane, with it at only 4 wavelengths it has appreciable curvature. It is plausible to assume that this departure from the ideal plane-wave front is primarily responsible for the shift in the valley along $kz = 0.5\pi$. The phase fronts associated with Figs. 44 and 14 are shown, respectively, in Figs. 45 and 15. They show surfaces of constant phase across the deep valley with curvatures that suggest waves originating at and diverging from $\theta = 180°$, $z = h$ and converging to $\theta = 0°$, $z = 0$.

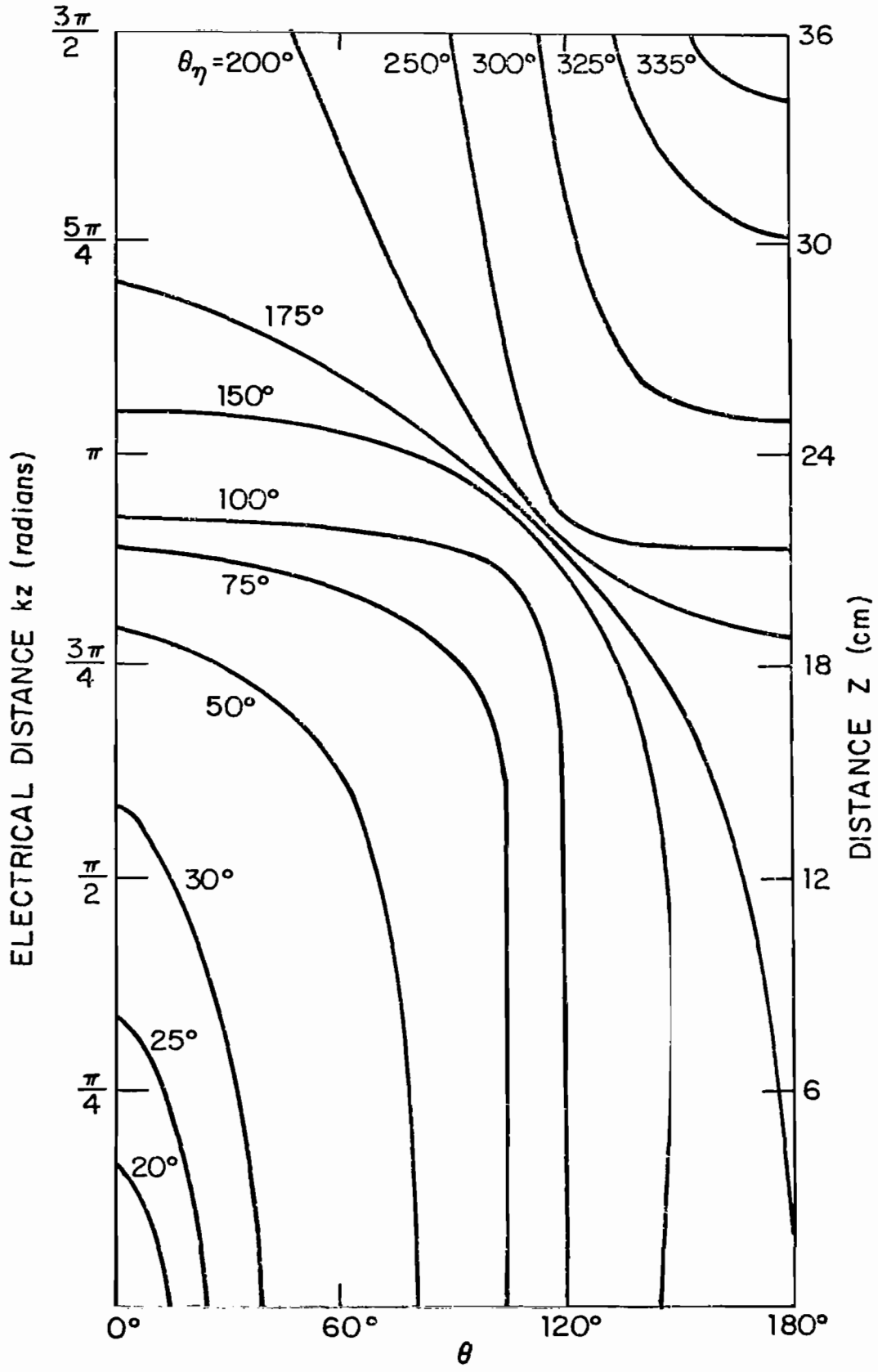

Fig. 45. Measured contours of constant phase of surface density of charge; kh = 1.5π, ka = 1, small indoor ground screen.

6. CURRENTS AND CHARGES ON CYLINDERS WITH END CAPS

No theoretical formulas are available for the distributions of the surface densities of current and charge on a tubular cylinder of length 2h and radius a in an incident plane-wave field when the caps are not open (as assumed in the theory of C. C. Kao) but closed with metal caps. However, the effect of adding caps is readily determined experimentally for E-polarization with a cylinder of length h erected on a large metal ground plane.

In Fig. 46 are shown graphs of the measured magnitude and phase of the axial component of surface current $K_z(\theta,z)$ on the outside of the cylinder as a function of z for four values of θ extending from $\theta = 180°$ in the center of the illuminated region to $\theta = 0°$ in the center of the shadow. Measured values are represented for the tube with the end open and closed with a flat metal disk and a hemispherical cap. The length of the tube with open and closed flat ends was h = 84 cm = 1.75λ; with the hemispherical cap the axial length was 85.6 cm = 1.78λ. The differences in the distributions are seen to be minor in both magnitude and phase except within a quarter wavelength of the end. The upward axial current on the outside surface of the open tube becomes a downward current on the inside surface when it reaches the end at z = h. Similarly, the upward axial current on the outside surface of the tube with the flat end becomes an inward radial current on the surface of the end cap; the axial current continues upward and inward on the hemispherical cap. The three current densities are quite comparable in the illuminated region ($\theta = 180°$, 120°). The radial currents onto the flat end and upward on the hemispherical cap are somewhat smaller than the downward current on the inner surface of the open tube in the shadow region ($\theta = 0°$). The differences are greatest near the shadow boundary ($\theta = 80°$). The phases are seen to be essentially the same for all angles θ.

In Fig. 47 are shown graphs of the measured magnitude and phase of the surface density of charge on the outside of the cylinder with an open end and with flat and hemispherical metal end caps. It is seen that the charge density near the end is slightly greater with the open end than with the two metal end caps for all angles θ. However, the differences are not great.

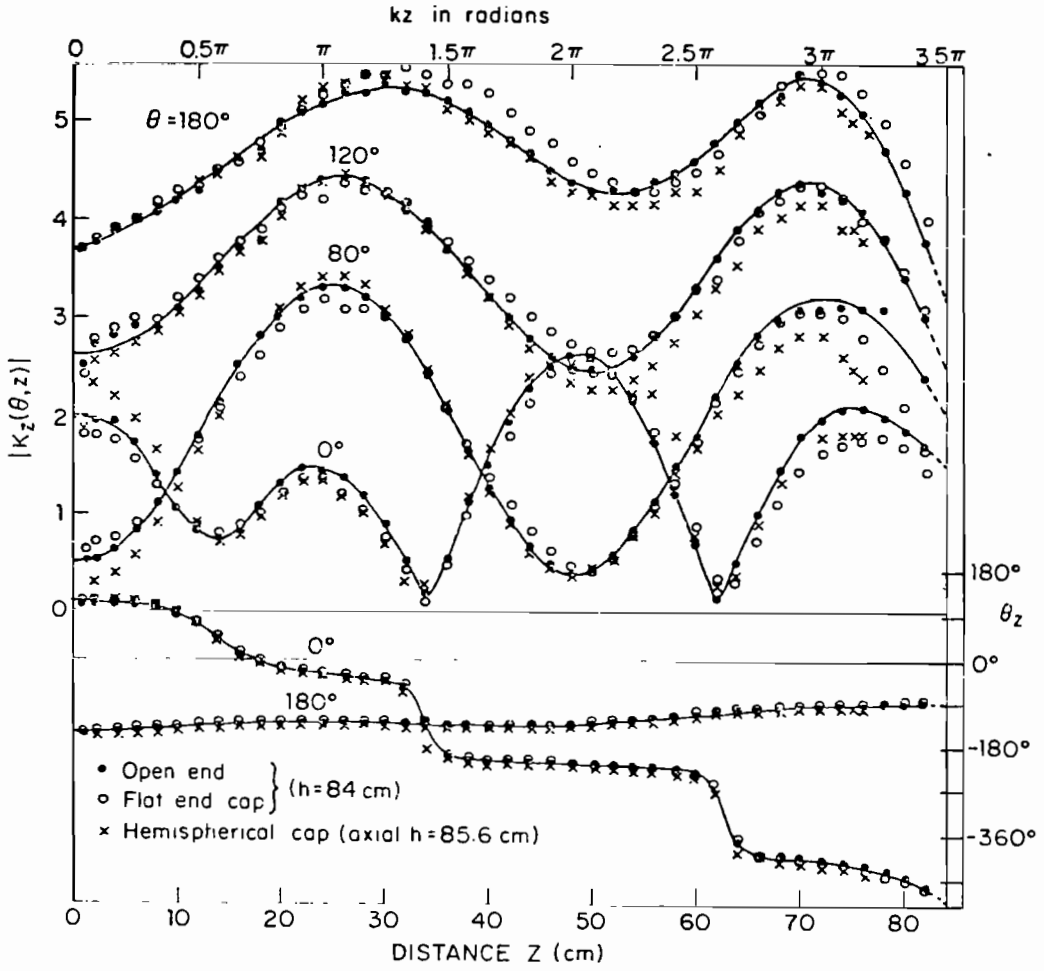

Fig. 46. Measured magnitude and phase of surface density of outside axial current on tubular cylinder with open end, flat and hemispherical end caps; E-polarization. ($|K|$ in arbitrary units.)

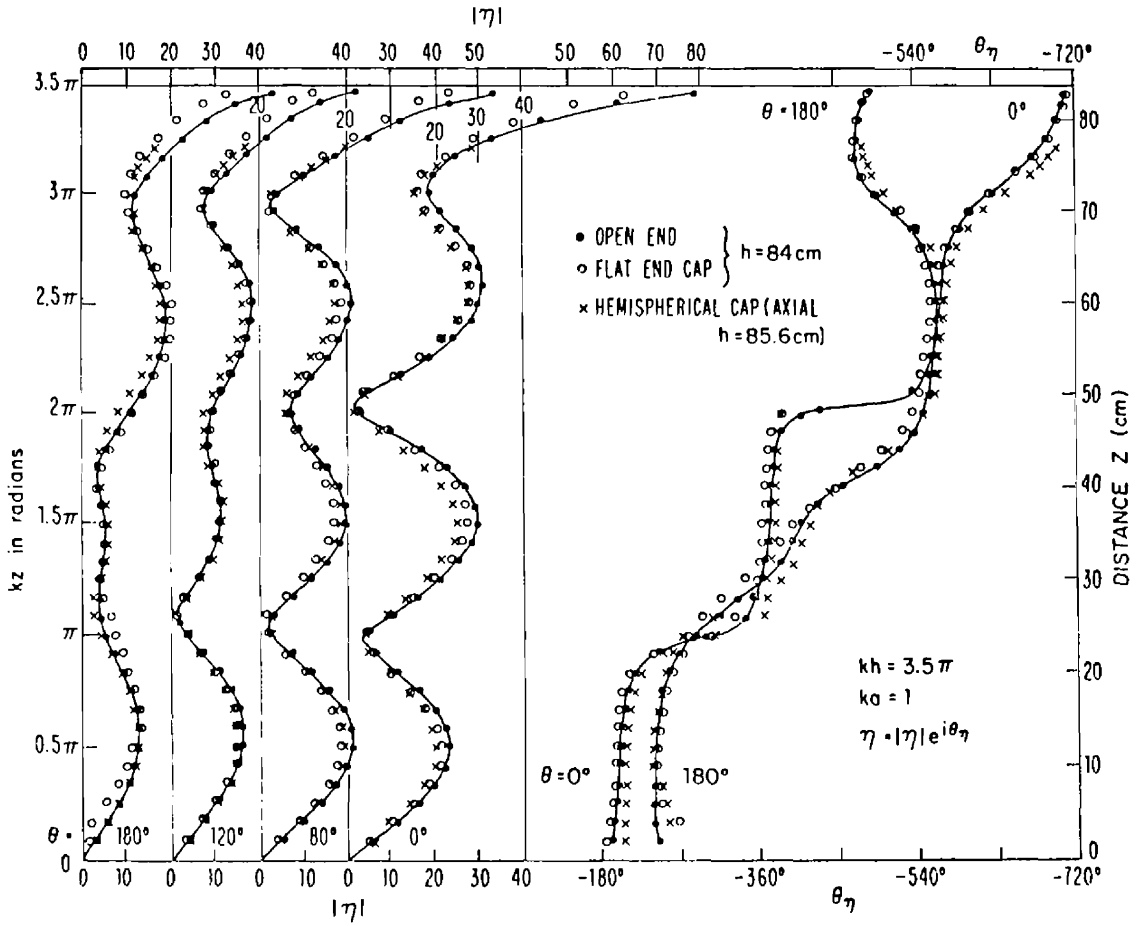

Fig. 47. Measured magnitude and phase of surface density of charge on tubular cylinder with open end, flat and hemispherical end caps; E-polarization. ($|K|$ in arbitrary units.)

It may be concluded that the distributions of surface current and charge on tubular cylinders with ka = 1 and equal axial lengths are not significantly different when the ends are open or closed with flat metal disks or hemispherical caps except within a quarter wavelength of the ends where small differences are observed especially in the shadow region near the shadow boundary.

7. CONCLUSION

A critical study of the extensive sets of theoretical and measured graphs of the surface densities of current $\vec{K}(\theta,z) = \hat{\theta}K_\theta(\theta,z) + \hat{z}K_z(\theta,z)$ and charge $\eta(\theta,z)$ on a highly conducting cylinder with ka = 1 and kh = 1.5π in an approximately plane E-polarized incident field leads to the following observations:

a. The apparatus and techniques developed for measuring $K_z(\theta,z)$, $K_\theta(\theta,z)$ and $\eta(\theta,z)$ in both amplitude and relative phase yield results in excellent agreement with theoretical predictions for an electrically thick tubular cylinder. If proper differences between theoretical total currents and charges and measured outside currents and charges are recognized, the three probes traveling on a slider in an uncovered groove can be depended on to give correct distributions.

b. In view of the overall good agreement with theory, it can be assumed that the aluminum tube with walls 1/4 in. thick is approximately equivalent to an infinitely thin, perfectly conducting tube of the same size. If quantitative agreement near the open end is required, the theoretical outside currents and charges must be used. At small distances from the ends the theoretical total and outside currents differ negligibly when ka = 1.

c. The finite distance between the scattering cylinder and the source of the incident electromagnetic waves and the consequent nonplanar wave fronts appear to be responsible for shifts in the standing-wave pattern revealed by the contours of constant charge. These shifts increase with decreasing distance to the source and appear to be limited to a section of the cylinder near the center of the illuminated region. A definitive verification that these shifts are due to the nonplanar wave front rather than reflections from the edges of the ground plane could be obtained simply

by repeating the measurements with $d = 4\lambda$ on the large outdoor ground plane.

d. The complete set of measurements of currents and charges on the cylinder when this was mounted on a small ground plane (with dimensions $4.2\lambda \times 6.3\lambda$) only 4λ from the transmitting monopole is in quite adequate agreement with measurements on the large outdoor ground plane and with theory for many practical applications. Since the major differences appear to be due to the nearness of the source, it would appear that doubling this distance (and the length of the ground plane) should permit the use of an indoor ground plane for virtually all measurements of currents and charges on electrically thick structures not much longer than $kh = 1.5\pi$. The actual limitations on the length remain to be determined. It is perhaps well to note that these conclusions cannot be extended to the currents and charges induced in electrically thin conductors. These are much more sensitive to the nature of the incident wave front owing to the sharpness of resonance and the one-dimensional nature of the oscillations.

SECTION V

ELECTRICALLY THICK CYLINDERS IN E- AND H-POLARIZED, NORMALLY INCIDENT, PLANE-WAVE FIELDS, THEORY AND MEASUREMENTS, ka = 1, kh = 3π, 3.5π, kℓ = 1.5π, 2π

1. INTRODUCTION

The currents and charges induced on the surface of a rocket or aircraft by an externally generated, intense electromagnetic field are of practical concern in the determination of adequate shielding for sensitive apparatus within the enclosing, imperfect metal shell. A systematic theoretical and experimental study to gain insight into the nature of the standing-wave patterns induced on crossed electrically thick and long metal structures has advanced from electrically thin wires (refs. 1 and 2) and crossed thin wires (refs. 3 and 6) to resonant electrically thick tubes. In particular, the surface densities of current $\vec{K}(\theta,z)$ and of charge $\eta(\theta,z)$ on a resonant tubular cylinder with electrical radius ka = 1 and electrical half-length kh = 1.5π in an E-polarized plane-wave field have been reviewed and computed graphs displayed in Section III. Measured graphs corresponding to the theoretical ones follow in Section IV for the currents and charges on an aluminum tube 6 in. in diameter with walls 1/4 in. thick mounted on a ground plane and illuminated by a monopole with a corner reflector from distances of 4 to 10 wavelengths. The frequency used was 626.5 MHz. The agreement between theory and experiment is excellent except for certain aspects in the distribution of the charge density on the illuminated side of the cylinder which have been explained in terms of the differences between the incident ideal plane and the actual spherical wave fronts. It is the purpose of this section to study cylinders that are longer and not restricted to resonant lengths when illuminated by both E- and H-polarized incident fields in order to determine the nature of the axial and transverse periodicities in the distributions of current and charge in anticipation of similar studies with crossed electrically thick tubes.

The previously studied cylinder with kh = 1.5π is resonant in the sense that the axial current $K_z(\theta,z)$ includes, superimposed on a largely constant forced component proportional to the function e(kz) (which equals one except within λ/4 of each open end where it decreases smoothly to zero),

a simple resonant part that is proportional to cos kz. This part has a relatively large resonant amplitude since it satisfies both boundary conditions, viz., $K_z(\theta,h) = 0$ and $[\partial K_z(\theta,z)/\partial z]_{z=0} \sim \eta(\theta,0) = 0$. One purpose of the present study is to provide an analytical representation of the currents and charges when $kh \neq (2n + 1)\pi/2$, $n = 1, 2, \ldots$, and in particular, when $kh = n\pi$, $n = 1, 2, \ldots$. In these cases a simple resonant current of the form $K_z(\theta,z) \sim \cos kz$ satisfies the condition $[\partial K_z(\theta,z)/\partial z]_{z=0} \sim \eta(\theta,0) = 0$ but not $K_z(\theta,h) = 0$. It follows that the axial distribution of the transverse Fourier components described in Section III is not applicable and must be generalized.

A detailed study is made of the distributions of current and charge on cylinders specifically with $kh = 3\pi$ and 3.5π, $ka = 1$, in an E-polarized field since these are representative of long cylinders and the latter is useful as the vertical member of crossed electrically thick cylinders with a horizontal member centered at $kz = 2\pi$ or 2.5π. A similar study is made of the currents and charges induced on cylinders with electrical half-length $k\ell = 1.5\pi$ and 2π, $ka = 1$, in an H-polarized field since these too are typical and can be related to currents and charges on the horizontal member of crossed cylinders illuminated by a plane wave with its electric vector parallel to the vertical cylinder, the magnetic vector parallel to the horizontal one. A knowledge of the complete distributions of current and charge on each member when isolated is a valuable introduction to the empirical study of these quantities on the cylinders when joined to form a cross.

2. CURRENTS AND CHARGES ON CYLINDERS IN AN E-POLARIZED FIELD

A comprehensive picture of the variations with kh of the axial component of current density $K_z(\theta,z) = K_{zR} + iK_{zI}$ is shown in Fig. 48 for $\theta = 0°$, 90°, and 180° with $1.4\pi \leq kh \leq 3\pi$. As in the previous sections, $\theta = 0°$ is at the center of the shadow, $\theta = 90°$ at the shadow boundary, and $\theta = 180°$ at the center of the illuminated region. The sequence of graphs in this figure reveals the important information that the distributions with $kh = kh_1$ and $kh = kh_2 = kh_1 + n\pi$, $n = 1, 2, \ldots$, are virtually identical from $k(h - z) = 0$ to $k(h - z) = kh_1$. Specifically, all of the curves for $kh = 2\pi$ essentially coincide with the curves for $kh = 3\pi$ in the range from $kz = 3\pi$ to $kz = \pi$. The same is true of the curves for $kh = 1.8\pi$ and 2.8π, 1.6π and 2.6π, 1.4π and 2.4π, etc.

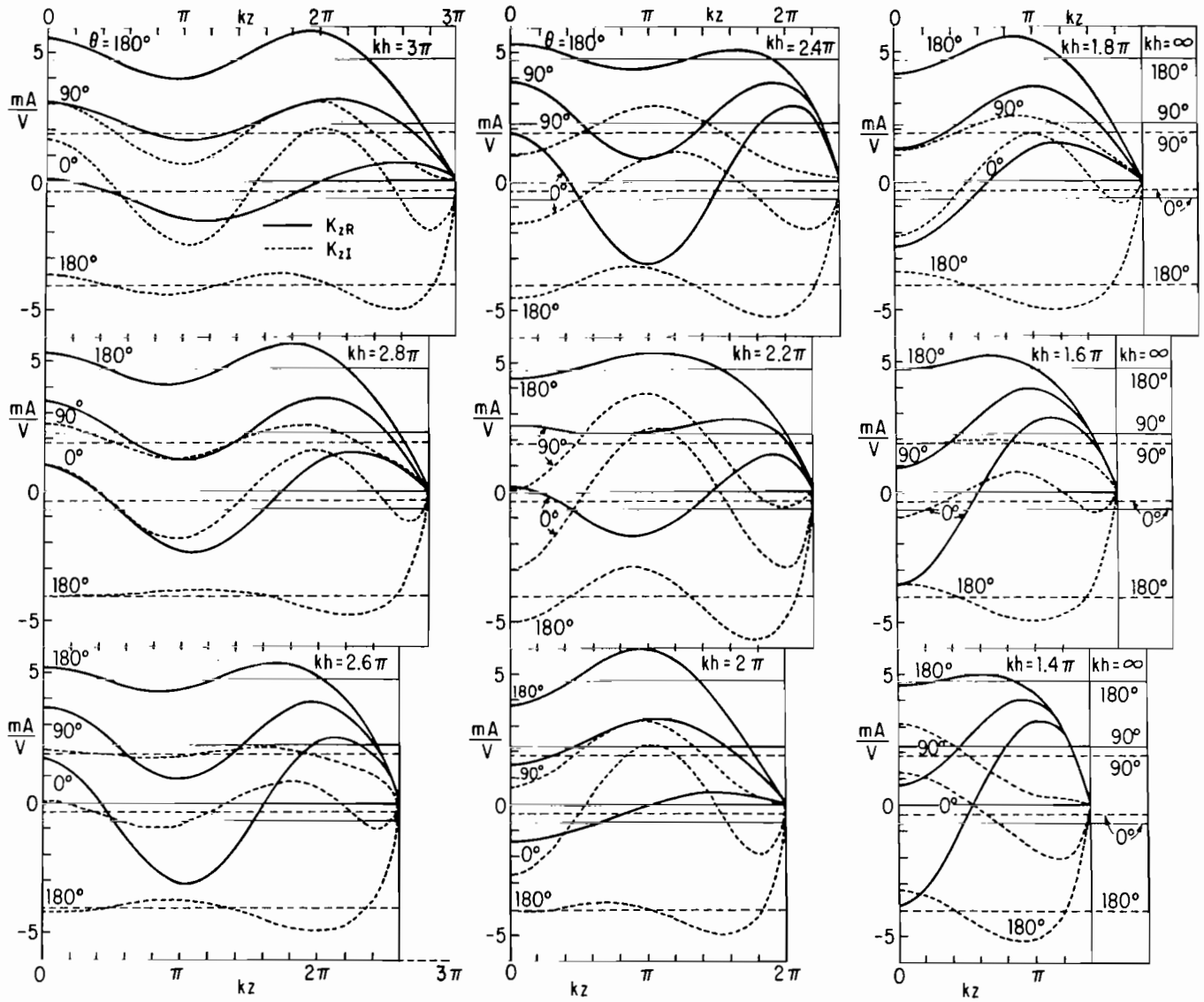

Fig. 48. Theoretical surface density of axial current, $K_z(\theta,z) = K_{zR} + iK_{zI}$, on tubular cylinder; E-polarization, ka = 1.

Figures 49 and 50 show the distributions of the vectors $\vec{K}_R(\theta,z)$ and $\vec{K}_I(\theta,z)$ for kh = 3π and 3.5π; the corresponding polarization ellipses are in Figs. 51 and 52. The axial variation of $K_z(\theta,z)$ is shown in Fig. 53; the axial and transverse variations of $K_\theta(\theta,z)$ in Fig. 54. These graphs are all consistent with the corresponding ones for kh = 1.5π in Section III. Of interest is the observation that for all lengths the transverse component of current is significant only within a distance less than λ/4 of the open end so that $\vec{K}(\theta,z) \doteq \hat{z}K_z(\theta,z)$ except near the open end. The associated distributions of the magnitude of the charge $|\eta(\theta,z)|$ are shown in Figs. 55 and 56 as a function of kz with θ as the parameter. The phase of $\eta(\theta,z)$ for kh = 3.5π is shown in Fig. 57. Contour diagrams of $|\eta(\theta,z)|$ are in Figs. 58 and 59. It is important to note in all of these graphs that the axial distributions in the range $0 \leq kz \leq 2\pi$ are essentially the same for kh = 3π and kh = 3.5π and, presumably, for all lengths between these values. The distribution in the range $2\pi \leq kz \leq 3.5\pi$ when kh = 3.5π is simply compressed into the range $2\pi \leq kz \leq 3\pi$ when kh = 3π. Evidently the boundary condition $\eta(\theta,0) = 0$ dominates and the axial distribution of charge is substantially $\eta(\theta,z) \sim \sin kz$ for all lengths — resonant, antiresonant and in between — with suitable compression only within a half wavelength of the open end. This is clearly seen in Figs. 55 and 56 and especially in the contour diagrams in Figs. 58 and 59. Both of these show essentially the same three ridges of axially maximum charge around the cylinders near kz = 0.5π, 1.5π and 2.5π for both kh = 3π and 3.5π with transverse maxima at θ = 0° in the center of the shadow. When kh = 3π, the charge maximum at kz = 2.5π is superimposed on the large and rapid increase at λ/4 from the open end instead of on the smaller and more gradual increase at λ/2 from the open end when kh = 3.5π. The graphs in Figs. 50 - 59 indicate that the distributions of current density and charge density are similar and in major outline quite simple in their axial variations for a wide range of values of kh except close to an open end, where the transverse component of current and the decrease in the forced part proportional to e(kz) in the axial current become important together with the associated charge densities. Away from the end the charge density is approximately proportional to sin kz for all kh. The corresponding current distribution includes a forced part proportional to e(kz) and a resonant part proportional to cos kz only when $kh = (2n + 1)\pi/2$; the more general form for other lengths must now be determined together with the associated transverse distributions.

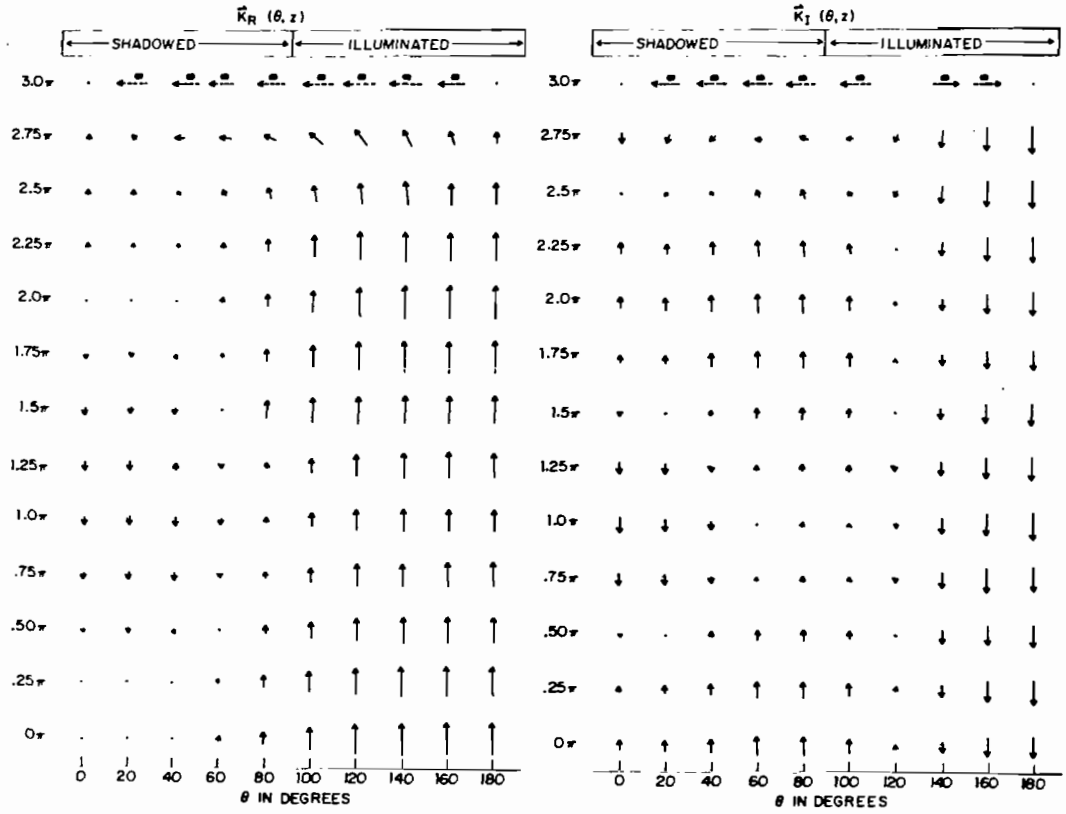

Fig. 49. Theoretical distributions of $\vec{K}_R(\theta,z)$ and $\vec{K}_I(\theta,z)$ on tubular cylinder; E-polarization, kh = 3π, ka = 1.

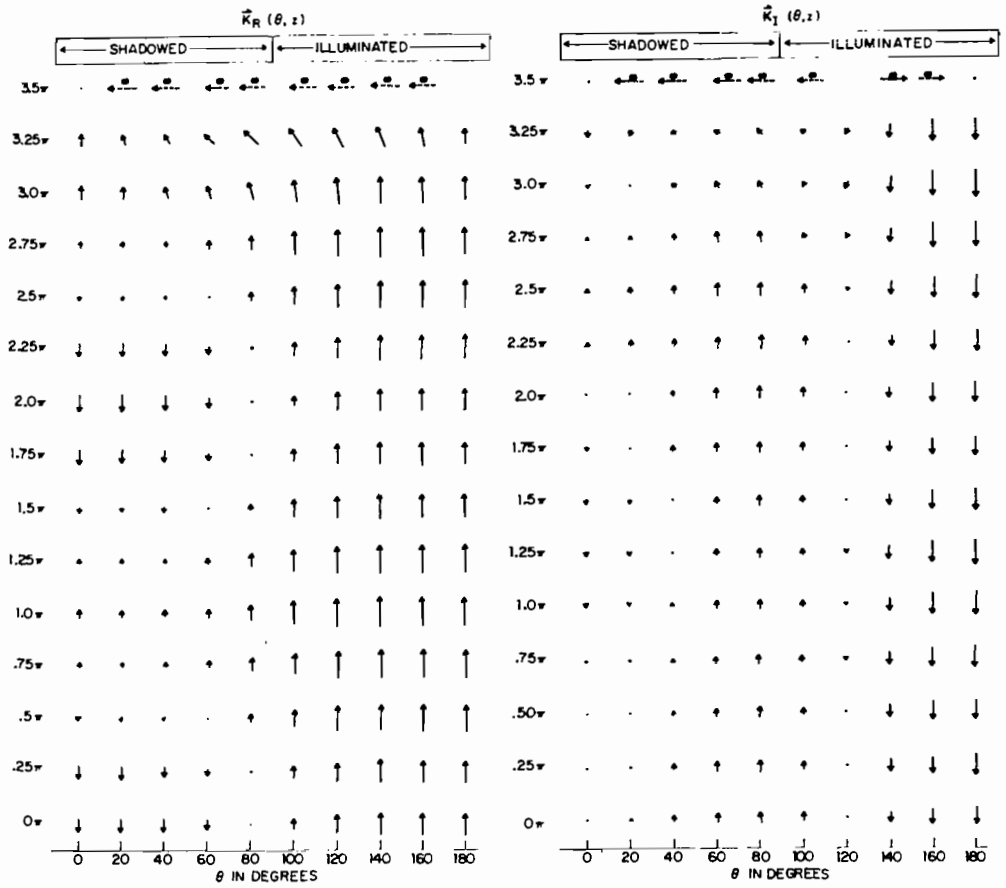

Fig. 50. Theoretical distributions of $\vec{K}_R(\theta,z)$ and $\vec{K}_I(\theta,z)$ on tubular cylinder; E-polarization, kh = 3.5π, ka = 1.

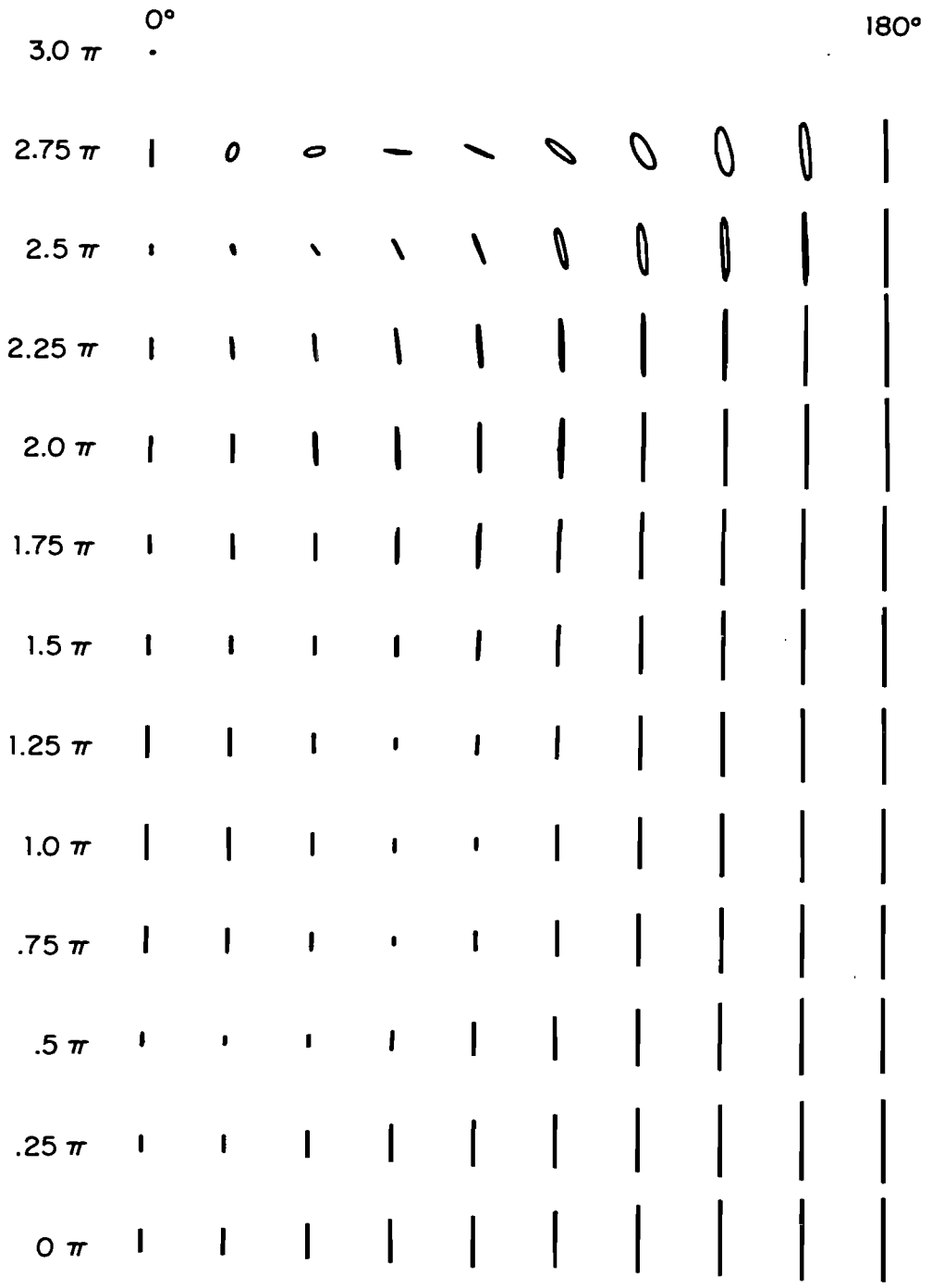

Fig. 51. Theoretical polarization ellipses of $\vec{K}(\theta,z)$ on tubular cylinder; E-polarization, kh = 3π, ka = 1.

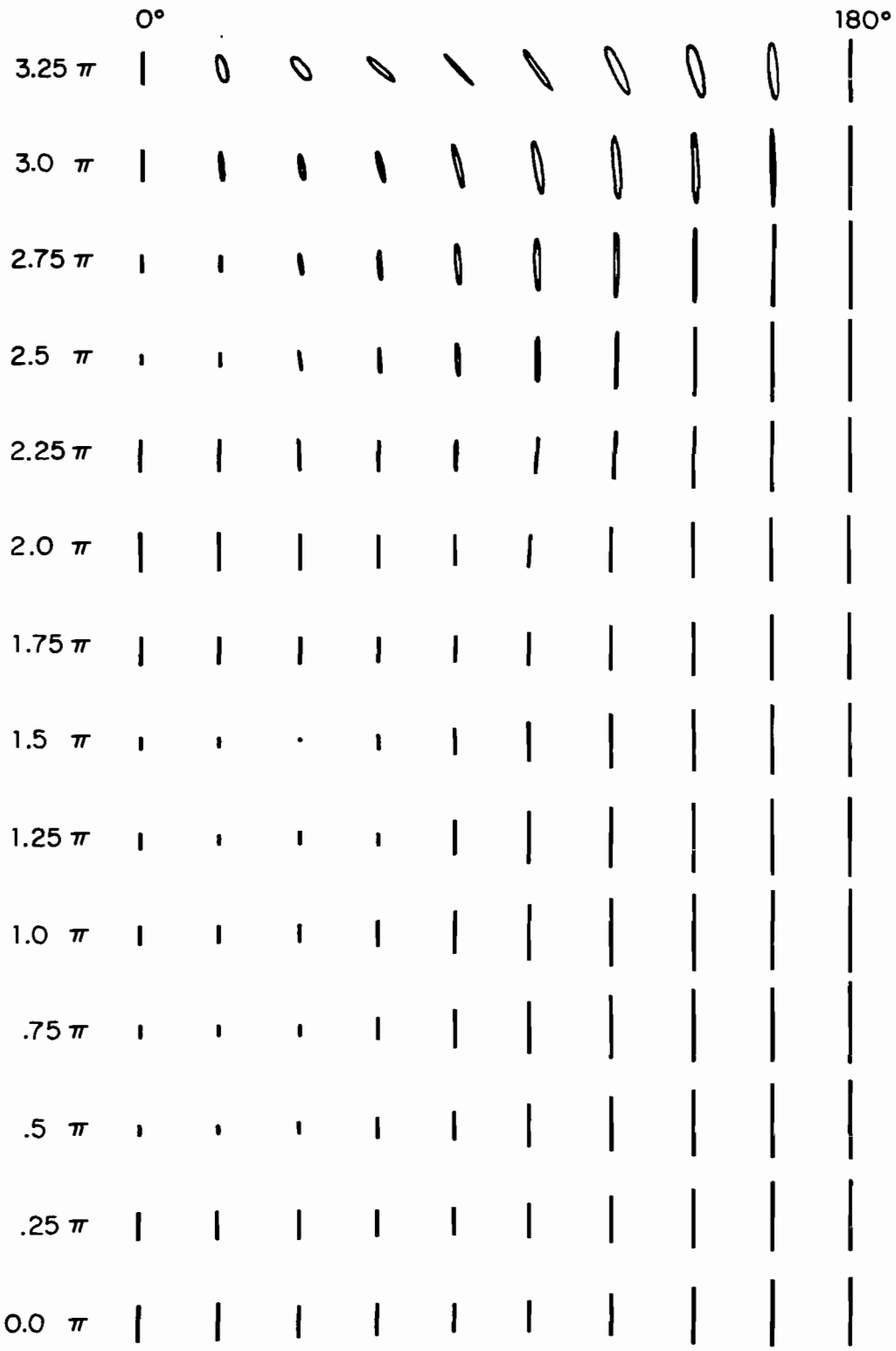

Fig. 52. Theoretical polarization ellipses of $\vec{K}(\theta,z)$ on tubular cylinder; E-polarization, kh = 3.5π, ka = 1.

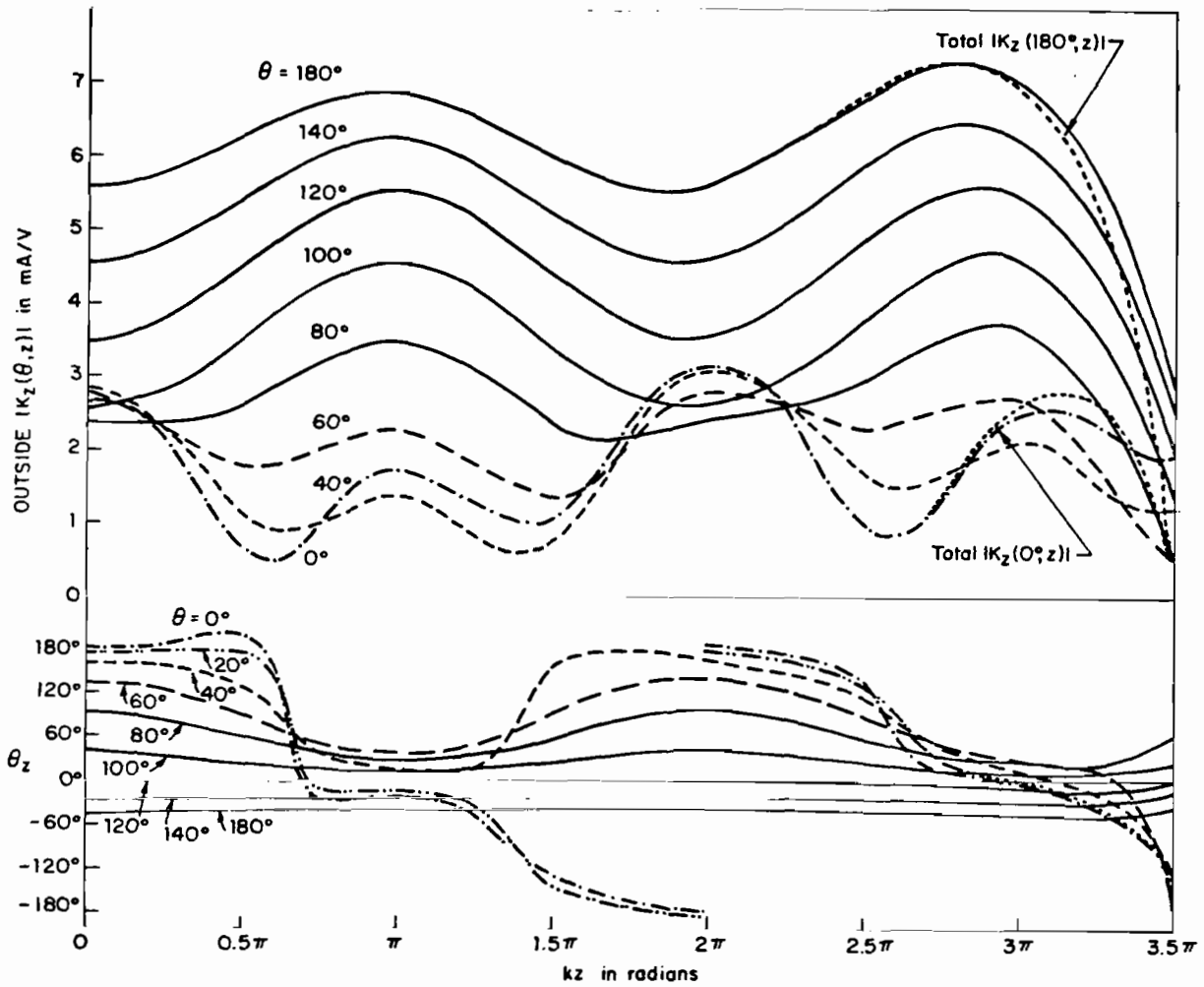

Fig. 53. Theoretical magnitude and phase of surface density of outside axial current on tubular cylinder; E-polarization, kh = 3.5π, ka = 1.

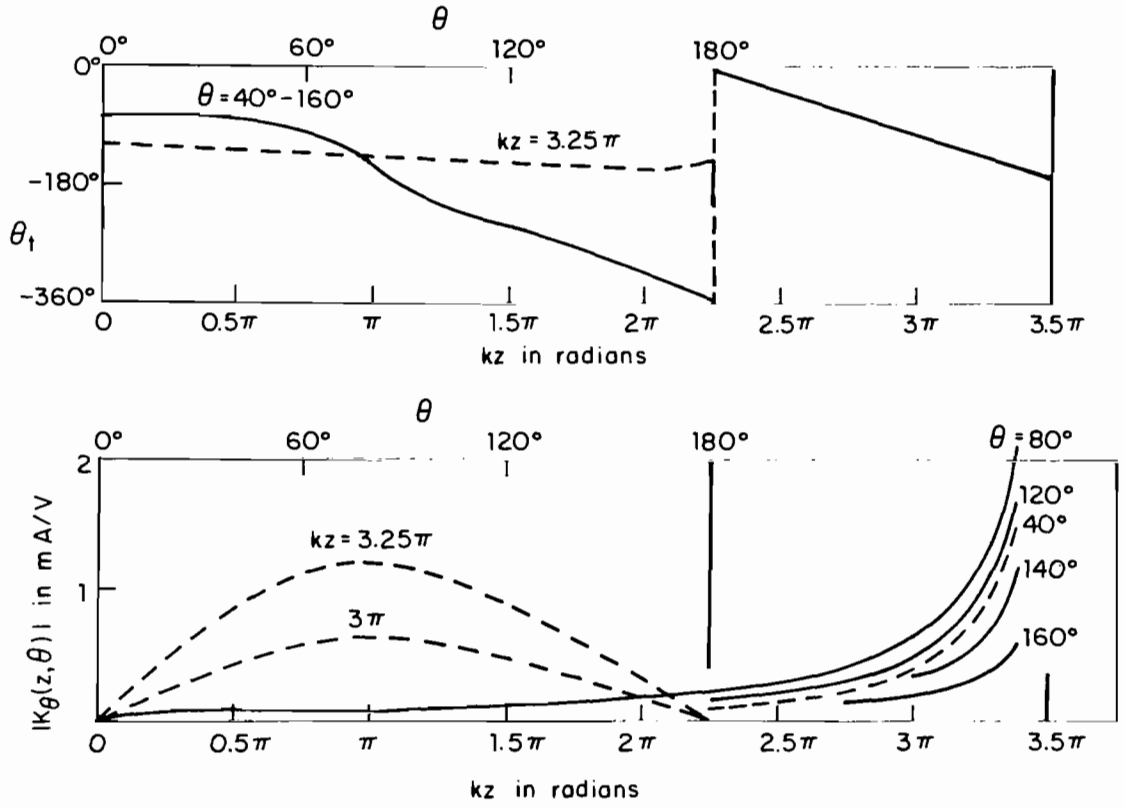

Fig. 54. Theoretical magnitude and phase of surface density of outside transverse current on tubular cylinder; E-polarization, kh = 3.5π, ka = 1.

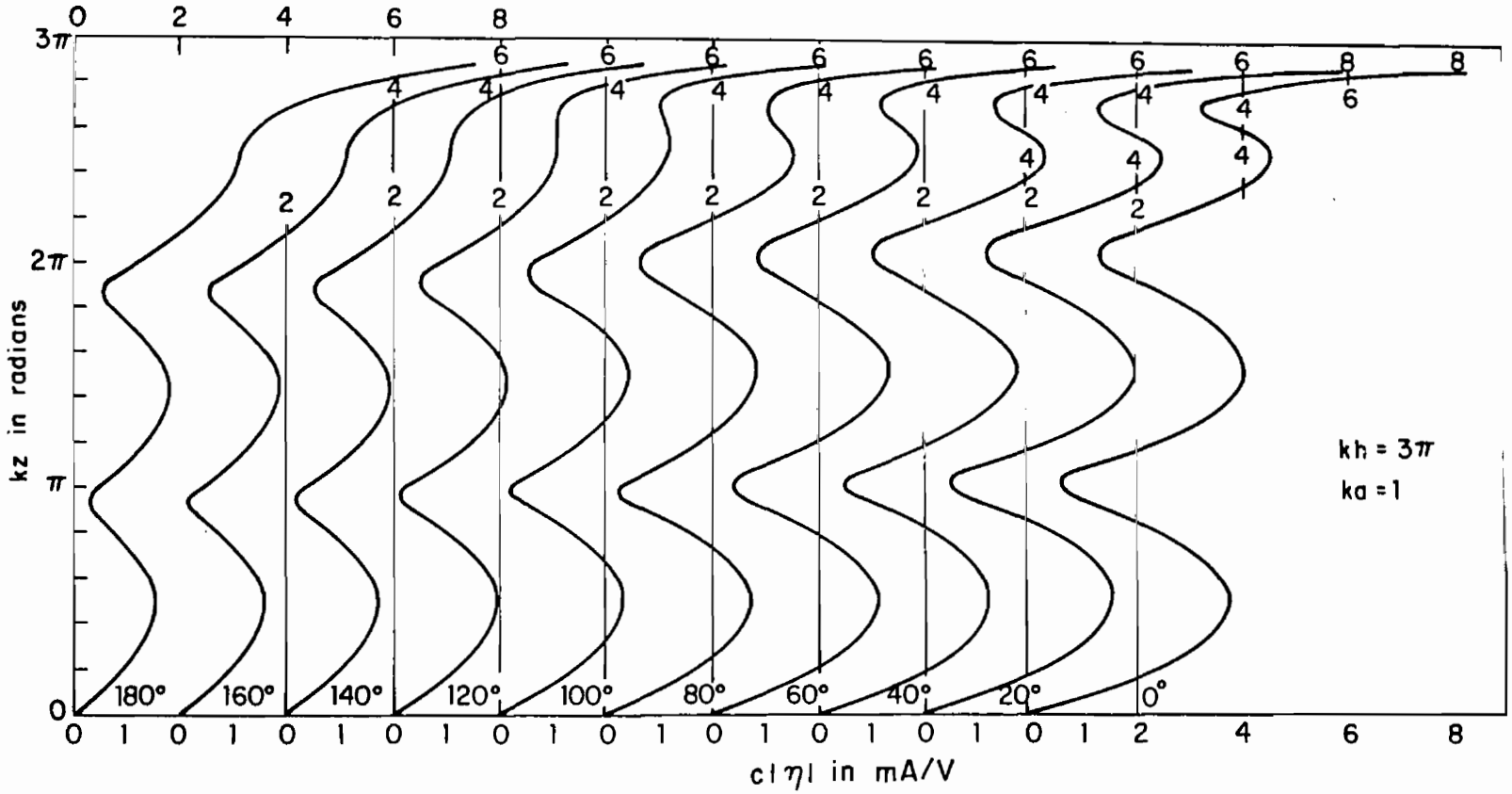

Fig. 55. Theoretical magnitude of surface density of outside charge $c|\eta|$ on tubular cylinder; E-polarization. ($c = 3 \times 10^8$ m/sec.)

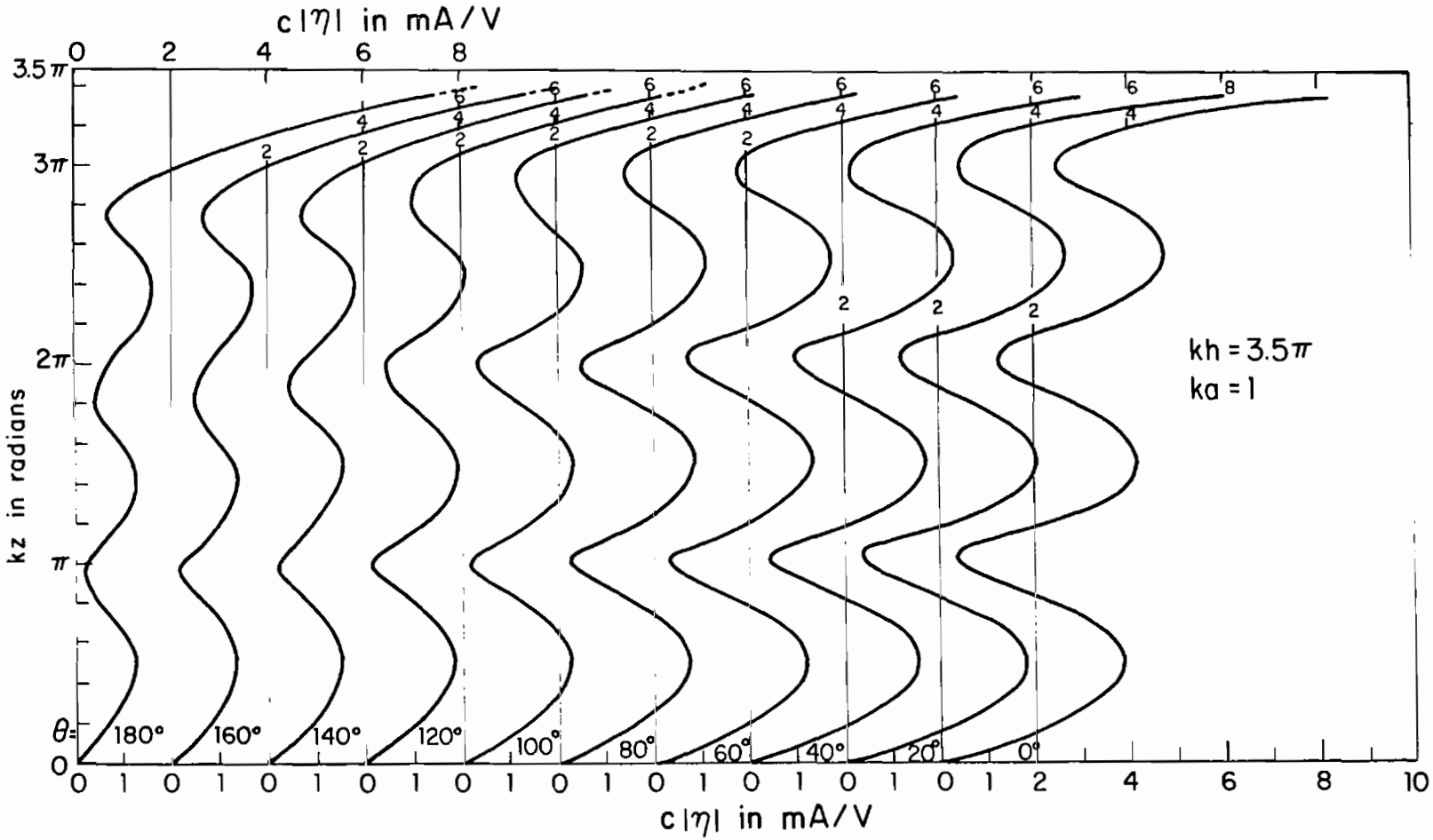

Fig. 56. Theoretical magnitude of surface density of outside charge $c|\eta|$ on tubular cylinder; E-polarization. ($c = 3 \times 10^8$ m/sec.)

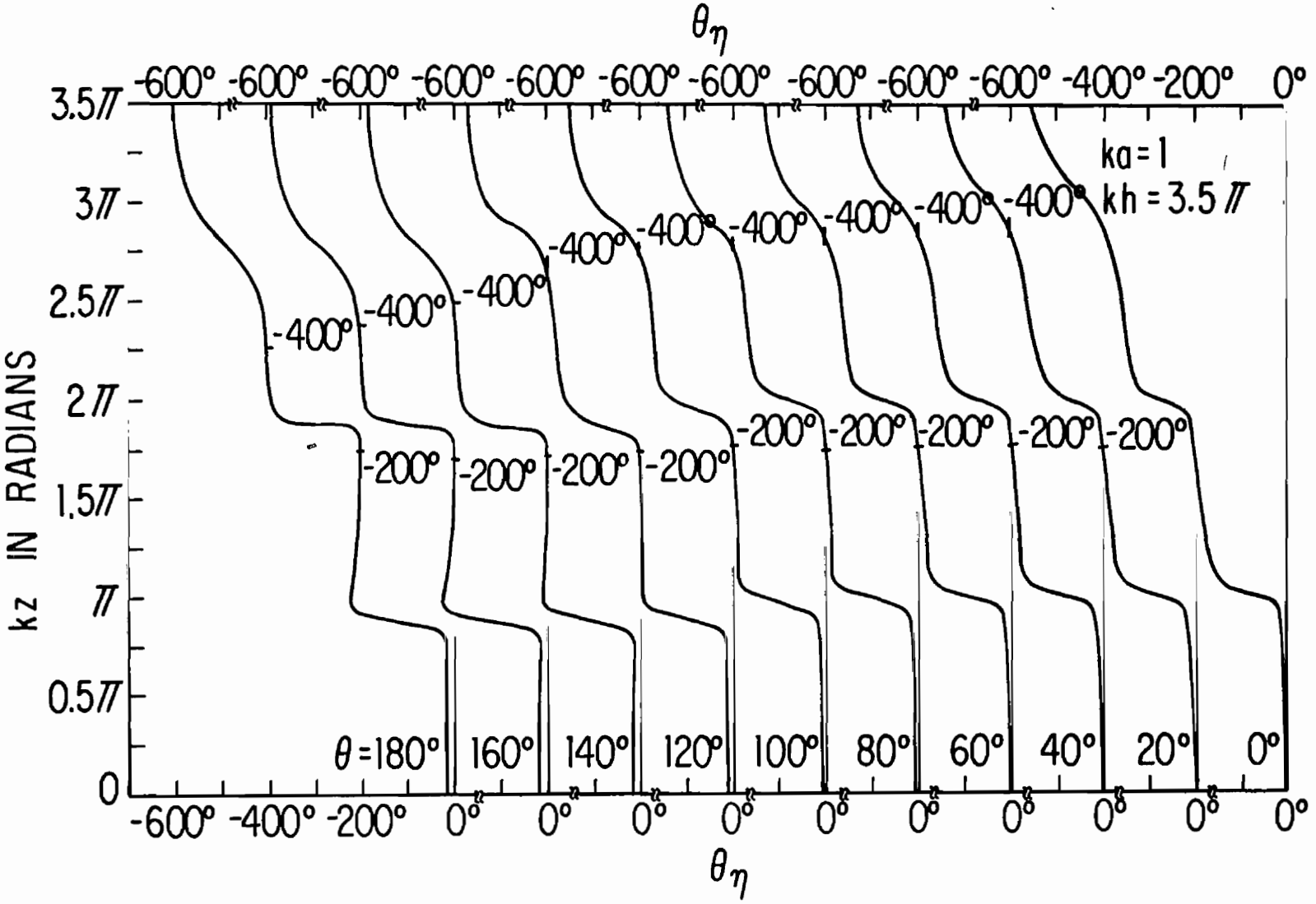

Fig. 57. Theoretical phase of surface density of outside charge θ_η on tubular cylinder; E-polarization.

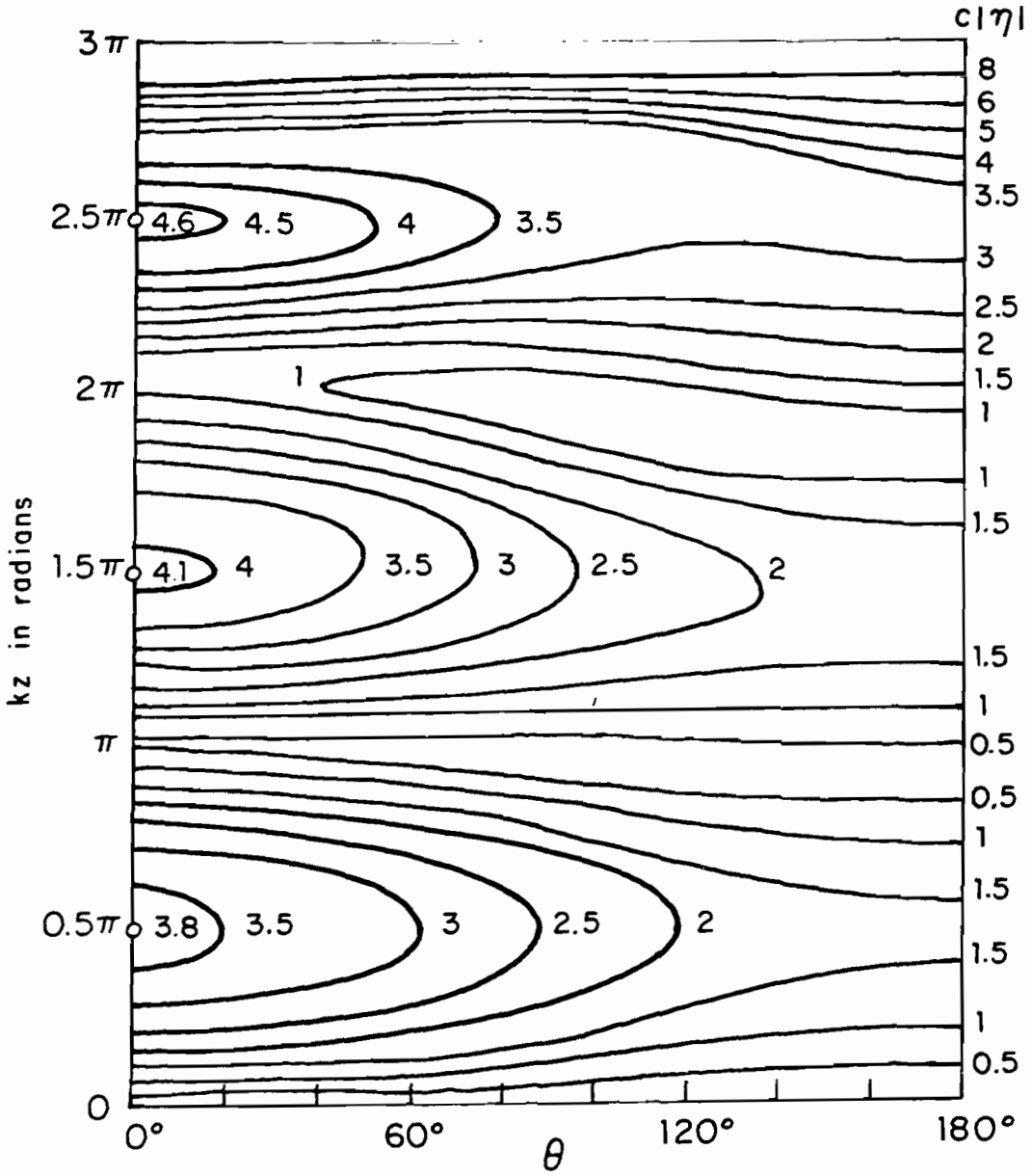

Fig. 58. Contour diagram of theoretical surface density of outside charge, $c|\eta(\theta,z)|$ in mA/V, on tubular cylinder; E-polarization, kh = 3π, ka = 1. ($c = 3 \times 10^8$ m/sec.)

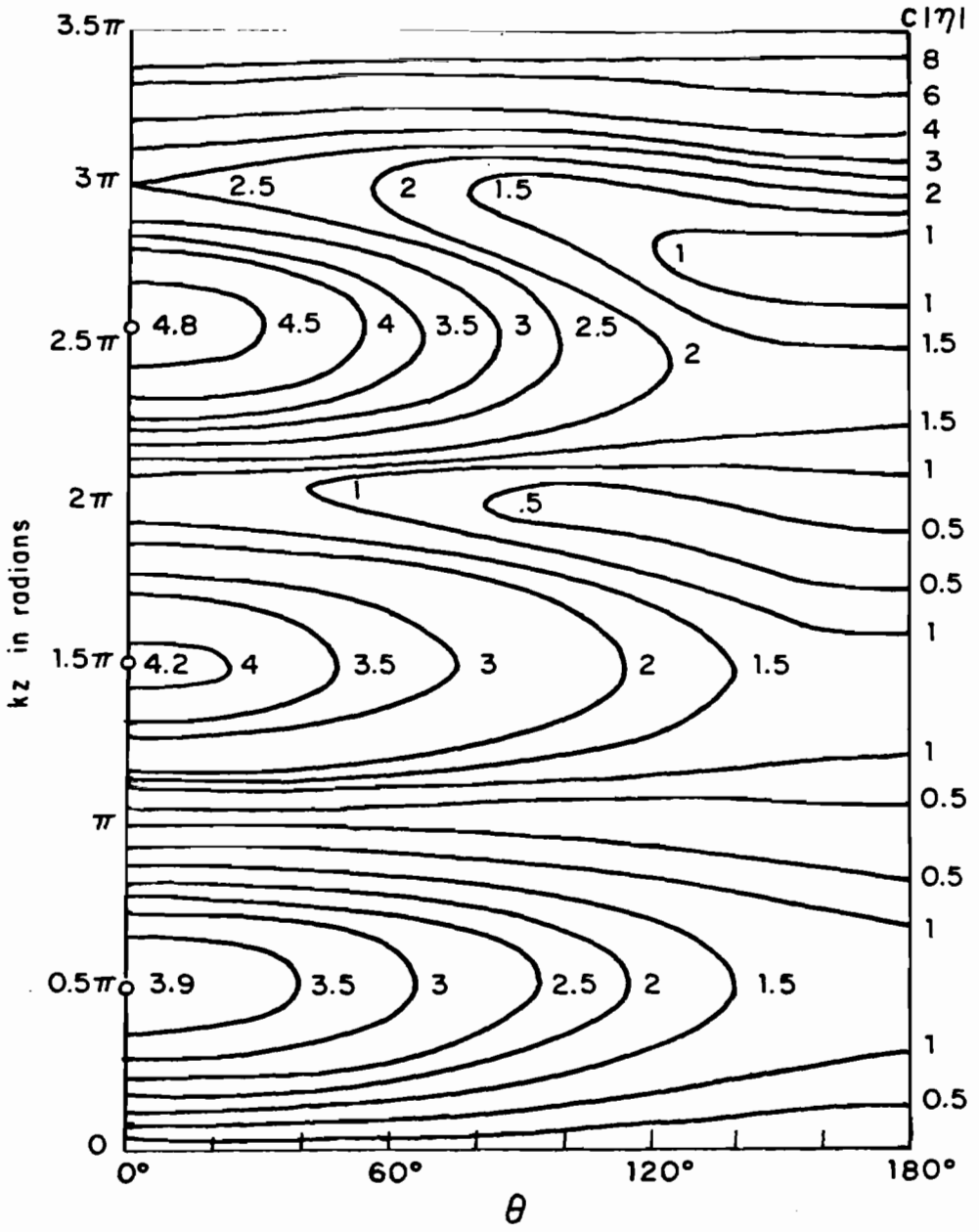

Fig. 59. Contour diagram of theoretical surface density of outside charge, $c|\eta(\theta,z)|$ in mA/V, on tubular cylinder; E-polarization, kh = 3.5π, ka = 1. ($c = 3 \times 10^8$ m/sec.)

3. REPRESENTATION BY TRANSVERSE FOURIER COMPONENTS

In Section III.6. the representation of the current on the conducting cylinder in the form of a series of Fourier components is discussed and applied specifically to an axially resonant cylinder with ka = 1, kh = 1.5π. The representations for the axial and transverse components of the vector surface density of current, $\vec{K}(\theta,z) = \hat{\theta}K_\theta(\theta,z) + \hat{z}K_z(\theta,z)$, are:

$$K_z(\theta,z) = A(kz) + B(kz)\cos\theta + C(kz)\cos 2\theta + D(kz)\cos 3\theta + E(kz)\cos 4\theta + \ldots \quad (49)$$

$$K_\theta(\theta,z) = i[B'(kz)\sin\theta + C'(kz)\sin 2\theta + \ldots] \quad (50)$$

where A(kz), B(kz), etc. are complex functions of kz. Graphs of the real and imaginary parts of the four functions that contribute significantly to $K_z(\theta,z)$ are shown in Fig. 60 for the axially resonant lengths kh = 1.5π, 2.5π and 3.5π, and in Fig. 61 for the general lengths kh = 2π to 3π in steps of 0.2π. The numerical values for ka = 1, kh = 3π are in Table 4 for the coefficients of $K_z(\theta,z)$ and in Table 5 for the coefficients of $K_\theta(\theta,z)$. These distributions are all quite similar in the sense that C(kz) and D(kz) are sensibly constant except near the open end where they reduce to zero and both A(kz) and B(kz) consist of more or less cosinusoidal variations in kz superimposed on constant values.

It is shown in Sections III.6. and III.7. that for axially resonant cylinders with kh = (2n + 1)π/2, n = 1, 2, ..., the axial current can be approximated by:

$$K_z(\theta,z) \doteq (A + B\cos\theta + C\cos 2\theta + D\cos 3\theta)e(kz) + (A_r + B_r\cos\theta)\cos kz \quad (51)$$

where A, B, C and D are the Fourier coefficients of an infinitely long cylinder with ka = 1 (see Table 1) and e(kz) is a function that is constant at the value one along the entire length of the cylinder except within a quarter wavelength of an open end where it decreases rapidly and smoothly to zero. It is defined in (42) and illustrated in Fig. 19. A_r and B_r in (51) are the complex amplitudes of the resonant parts of the zero-order and

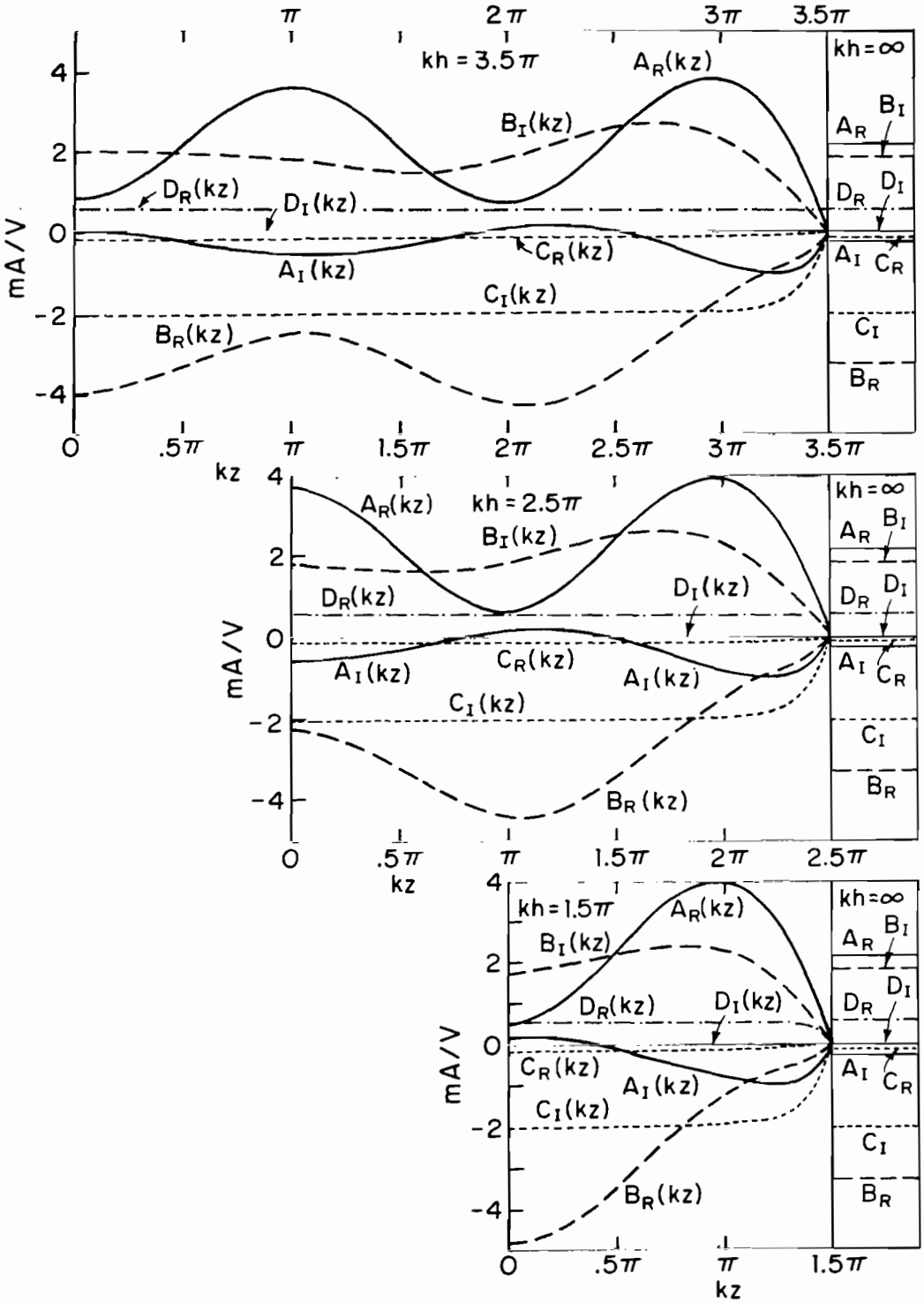

Fig. 60. Fourier coefficients of surface density of axial current on tubular cylinder, $K_z(\theta,z) \triangleq A(kz) + B(kz)\cos\theta + C(kz)\cos 2\theta + D(kz)\cos 3\theta$; E-polarization, ka = 1.

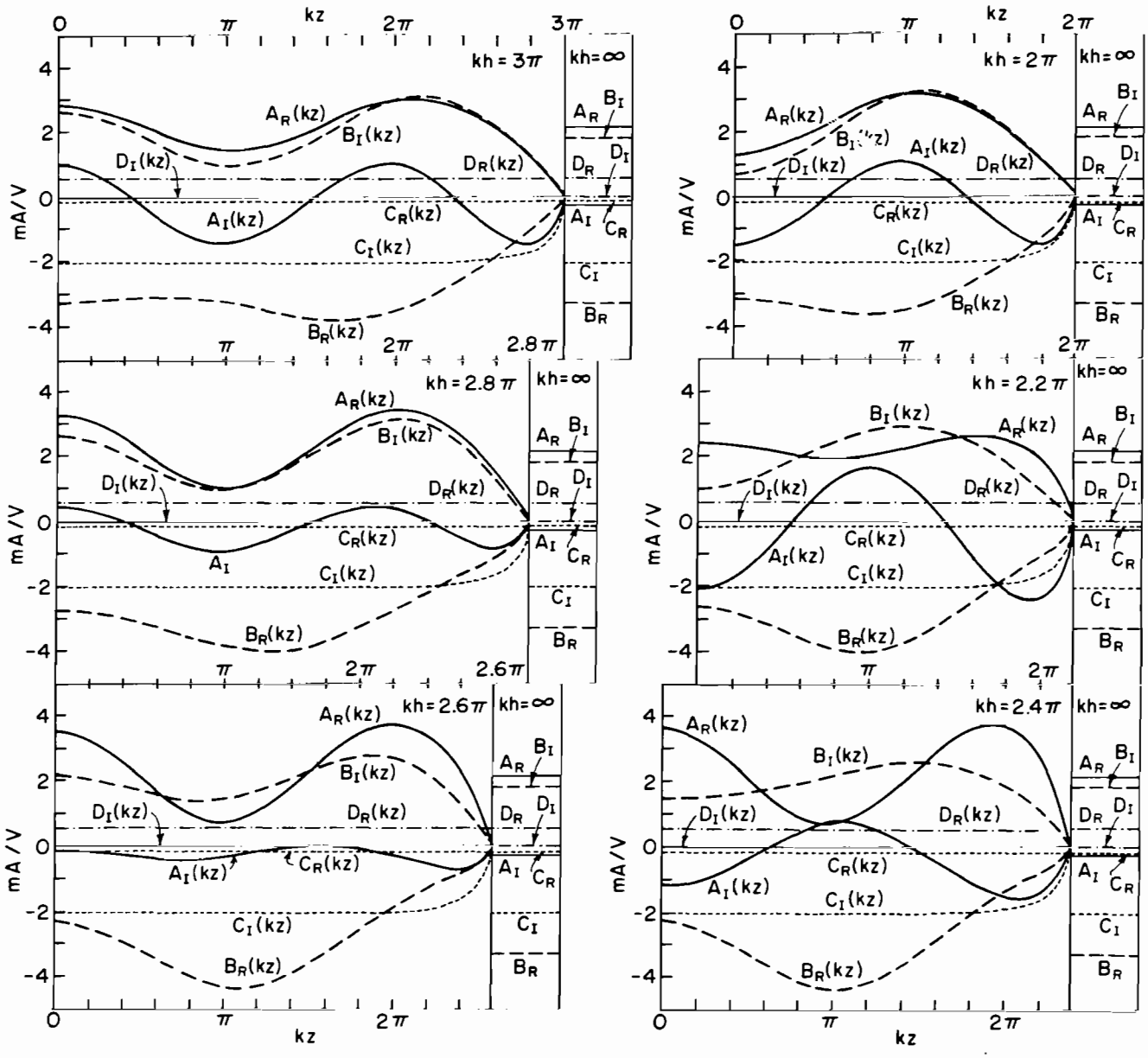

Fig. 61. Fourier coefficients of surface density of axial current on tubular cylinder, $K_z(\theta,z) \doteq A(kz) + B(kz)\cos\theta + C(kz)\cos 2\theta + D(kz)\cos 3\theta$; E-polarization, ka = 1.

Table 4

FOURIER COEFFICIENTS IN mA/V FOR $K_z(\theta,z)$ ON TUBULAR CYLINDER;

E-POLARIZATION, kh = 3π, ka = 1

kz	A(kz)	B(kz)	C(kz)	D(kz)	E(kz)
0	2.89 + i0.93	-3.26 + i2.66	-0.14 - i2.03	0.58 + i0.00	0.00 + i0.10
0.25π	2.70 + i0.57	-3.22 + i2.44	-0.14 - i2.03	0.58 + i0.00	0.00 + i0.10
0.50π	2.21 - i0.30	-3.15 + i1.88	-0.14 - i2.03	0.58 + i0.00	0.00 + i0.10
0.75π	1.70 - i1.14	-3.14 + i1.28	-0.14 - i2.04	0.58 + i0.00	0.00 + i0.10
1.00π	1.44 - i1.45	-3.26 + i0.96	-0.14 - i2.05	0.58 + i0.00	0.00 + i0.10
1.25π	1.58 - i1.01	-3.49 + i1.12	-0.15 - i2.05	0.58 + i0.00	0.00 + i0.10
1.50π	2.06 - i0.09	-3.71 + i1.70	-0.15 - i2.04	0.58 + i0.00	0.00 + i0.10
1.75π	2.65 + i0.76	-3.75 + i2.45	-0.16 - i2.03	0.58 + i0.00	0.00 + i0.10
2.00π	3.03 + i0.99	-3.48 + i3.00	-0.16 - i2.01	0.58 + i0.00	0.00 + i0.10
2.25π	2.96 + i0.40	-2.90 + i3.03	-0.15 - i1.99	0.58 + i0.00	0.00 + i0.10
2.50π	2.38 - i0.68	-2.15 + i2.44	-0.12 - i1.94	0.57 + i0.00	0.00 + i0.10
2.75π	1.42 - i1.45	-1.32 + i1.39	-0.08 - i1.75	0.53 + i0.00	0.00 + i0.09
3.00π	0	0	0	0	0

Table 5

FOURIER COEFFICIENTS IN mA/V FOR $K_\theta(\theta,z)$ ON TUBULAR CYLINDER;

E-POLARIZATION, kh = 3π, ka = 1

kz	B'(kz)	C'(kz)
0	0	0
0.25π	-0.03 + i0.07	0.00 + i0.00
0.50π	-0.04 + i0.11	0.00 + i0.00
0.75π	-0.00 + i0.11	0.00 + i0.00
1.00π	0.06 + i0.05	0.00 + i0.00
1.25π	0.11 - i0.04	0.00 + i0.00
1.50π	0.11 - i0.14	0.00 + i0.00
1.75π	0.03 - i0.21	0.00 + i0.00
2.00π	-0.14 - i0.20	0.00 - i0.01
2.25π	-0.37 - i0.01	-0.02 - i0.02
2.50π	-0.65 + i0.54	-0.08 - i0.02
2.75π	-1.04 + i2.10	-0.33 - i0.03
3.00π	∞	∞

first-order modes. This representation was applied in Section III to the cylinder with ka = 1, kh = 1.5π. It also applies directly to cylinders with kh = 2.5π and 3.5π for which the axial distributions of the first four transverse Fourier modes are shown in Fig. 60.

When the cylinder is not axially resonant, the representation must be generalized by the substitution of the shifted cosine (cos kz - cos kh) for cos kz in order to satisfy the boundary conditions $K_z(\theta,h) = 0$ and $\eta(\theta,0) = 0$. However, this change also involves the addition of the nonzero constant cos kh multiplied by the appropriate complex amplitude A_r or B_r. This must be subtracted within a quarter wavelength of the end. The proposed generalized representation is:

$$K_z(\theta,z) \doteq [(A + A_r \cos kh) + (B + B_r \cos kh)\cos\theta + C \cos 2\theta + D \cos 3\theta]e(kz) + (A_r + B_r \cos\theta)(\cos kz - \cos kh) \quad (52)$$

This evidently reduces to (51) when $kh = (2n + 1)\pi/2$ and to zero when $z = h$ for all kh. The derivative of (52) vanishes at $z = 0$.

In order to illustrate the application of (52), it is appropriate to select ka = 1 and $kh = 3\pi$, an antiresonant length. Thus,

$$K_z(\theta,z) \doteq [(A - A_r) + (B - B_r)\cos\theta + C \cos 2\theta + D \cos 3\theta]e(kz) + (A_r + B_r \cos\theta)(\cos kz + 1) \quad (53)$$

From Table 1 the Fourier coefficients for the infinitely long cylinder with ka = 1 are: $A_R = 2.18$, $A_I = -0.25$, $B_R = -3.28$, $B_I = 1.85$. The evaluation of $A_r = A_{rR} + iA_{rI}$ and $B_r = B_{rR} + iB_{rI}$ can be carried out as follows. Consider first $A_R(kz) = (A_R - A_{rR})e(kz) + A_{rR}(\cos kz + 1)$. Evidently, $A_{rR} \doteq (1/2)[A_R(0) - A_R(\pi)] \doteq (1/2)[A_R(2\pi) - A_R(\pi)]$. With Table 4 the two values on the right are 0.72 and 0.80. The average of these two approximate quantities gives $A_{rR} \doteq 0.76$. Similarly for A_{rI}, the two values are 1.19 and 1.22 with the average $A_{rI} \doteq 1.20$. It follows that:

$$A(kz) \doteq (1.42 - i1.45)e(kz) + (0.76 + i1.20)(\cos kz + 1) \quad (54)$$

Similarly,

$$B(kz) \triangleq (-3.22 + i10.92)e(kz) + (-0.06 + i0.93)(\cos kz + 1) \qquad (55)$$

For all lengths,

$$C(kz) \triangleq Ce(kz) = -(0.14 + i2.04)e(kz) \qquad (56)$$

$$D(kz) \triangleq De(kz) = 0.58e(kz) \qquad (57)$$

$$E(kz) \triangleq Ee(kz) = i0.10e(kz) \qquad (58)$$

In general, E(kz) can be neglected when ka = 1.

Graphs of $A_R(kz)$, $A_I(kz)$, etc. are shown on the left in Fig. 62 as given in Table 4 and on the right as computed from the approximate formulas (54) - (58). It is seen that the correspondence is generally good with differences resulting primarily from the simplifying assumption that the behavior of all functions in the quarter wavelength nearest the end is adequately represented by the same approximate function e(kz) with the form $\sin k(h - |z|)$ in the range $(kh - 0.5\pi) \leq kz \leq kh$. While a more accurate representation can easily be made, the present simple form should serve well except in the quarter wavelength nearest the open end where moderate errors in the current and larger errors in its slope (charge) occur. Graphs of the individual components of the first two modes are in Fig. 63.

4. COMPARISON WITH MEASUREMENTS; THE INCIDENT FIELD

With the same apparatus described in Section IV measurements were made of the distributions of current and charge density along a cylinder with ka = 1, kh = 3.5π. The axial distributions of current and charge density are shown in Figs. 64 - 67. The charge density is also displayed on the relief map shown in Fig. 68. When compared respectively with Figs. 53 and 56, the agreement for the current is very good, that for the charge is good on the shadow half of the cylinder. On the illuminated half the measured graphs are different from the theoretical ones in that the first and third maxima at kz near 0.5π and 2.5π are relatively larger, the second maximum near kz = 1.5π increasingly smaller as the center of the shadow at θ = 0° is approached. Indeed, when θ = 0° the second maximum is nonexistent.

The explanation for the significant difference between the theoretical and measured distributions of charge density η(θ,z) on the illuminated side

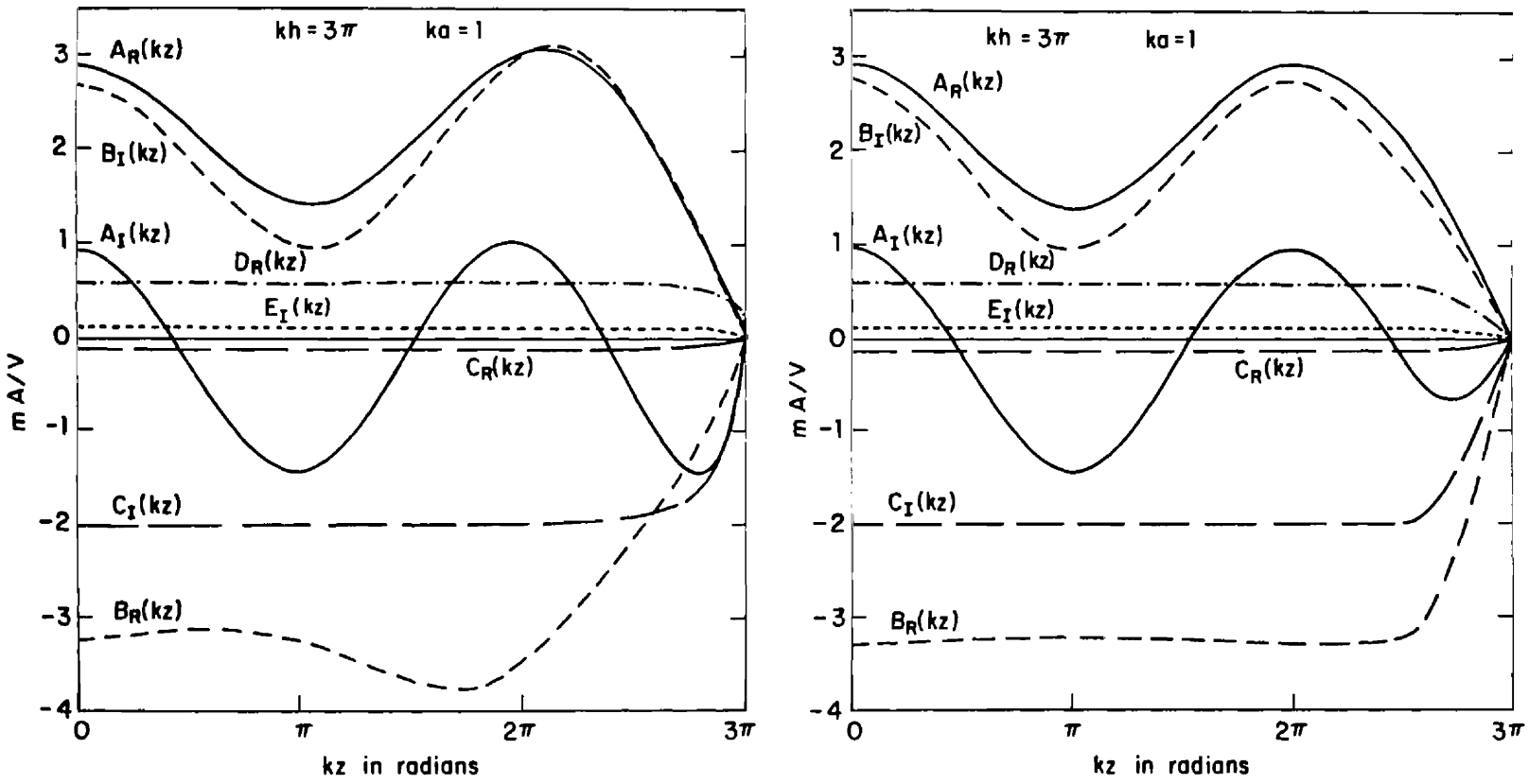

Fig. 62. Theoretical (left) and approximate (right) representation of Fourier coefficients of surface density of axial current $K_z(\theta,z)$ on tubular cylinder; E-polarization.

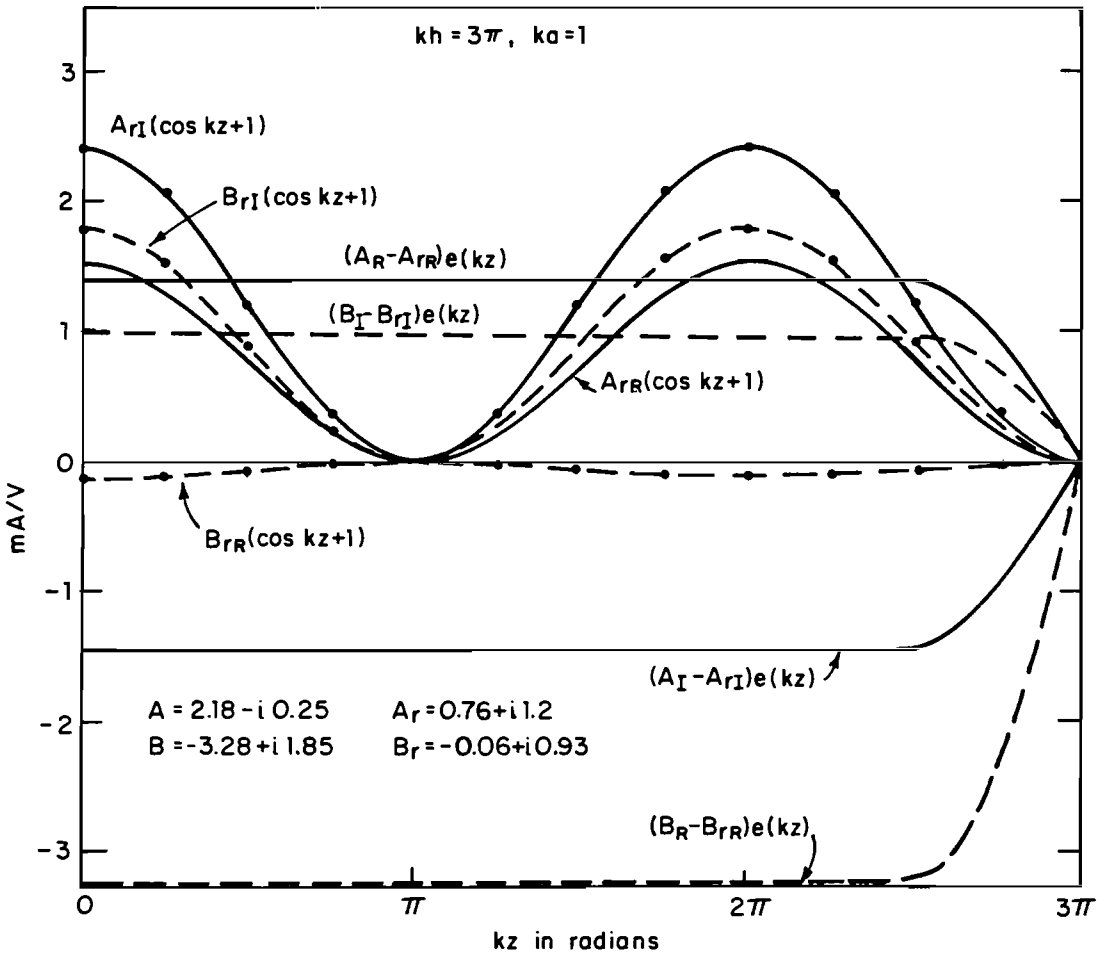

Fig. 63. Components $A(kz) = (A - A_r)e(kz) + A_r(\cos kz + 1)$ and $B(kz) = (B - B_r)e(kz) + B_r(\cos kz + 1)$ in the approximate representation of Fourier coefficients shown on the right in Fig. 62.

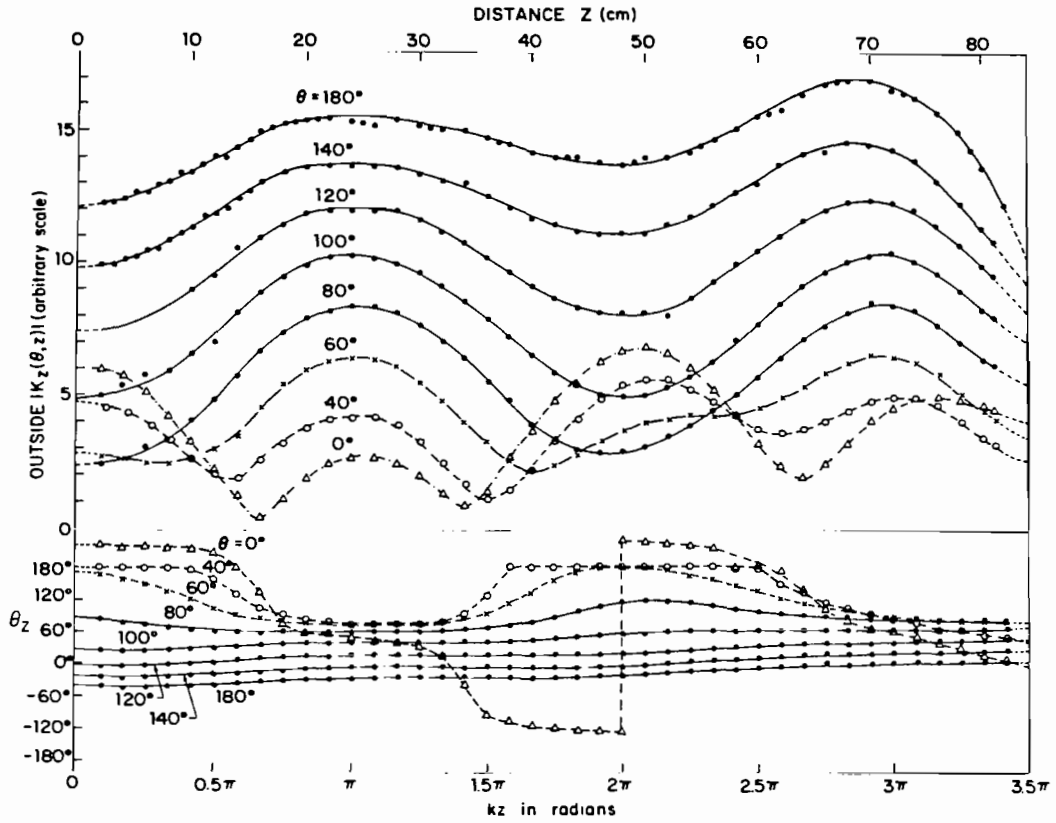

Fig. 64. Measured magnitude and phase of surface density of outside axial current on tubular cylinder; E-polarization, kh = 3.5π, ka = 1, λ = 48.0 cm.

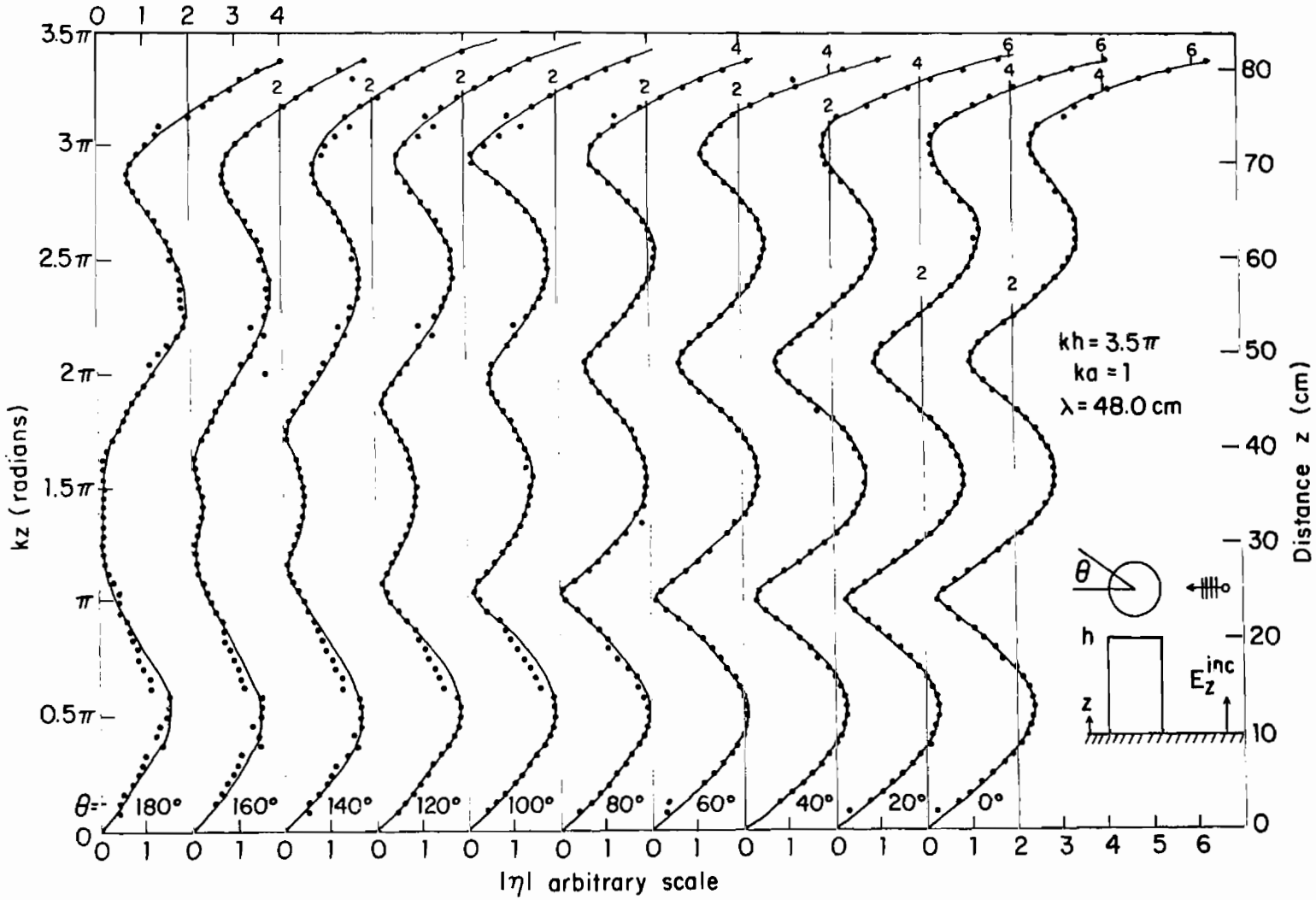

Fig. 65. Measured magnitude of surface density of outside charge on tubular cylinder; E-polarization.

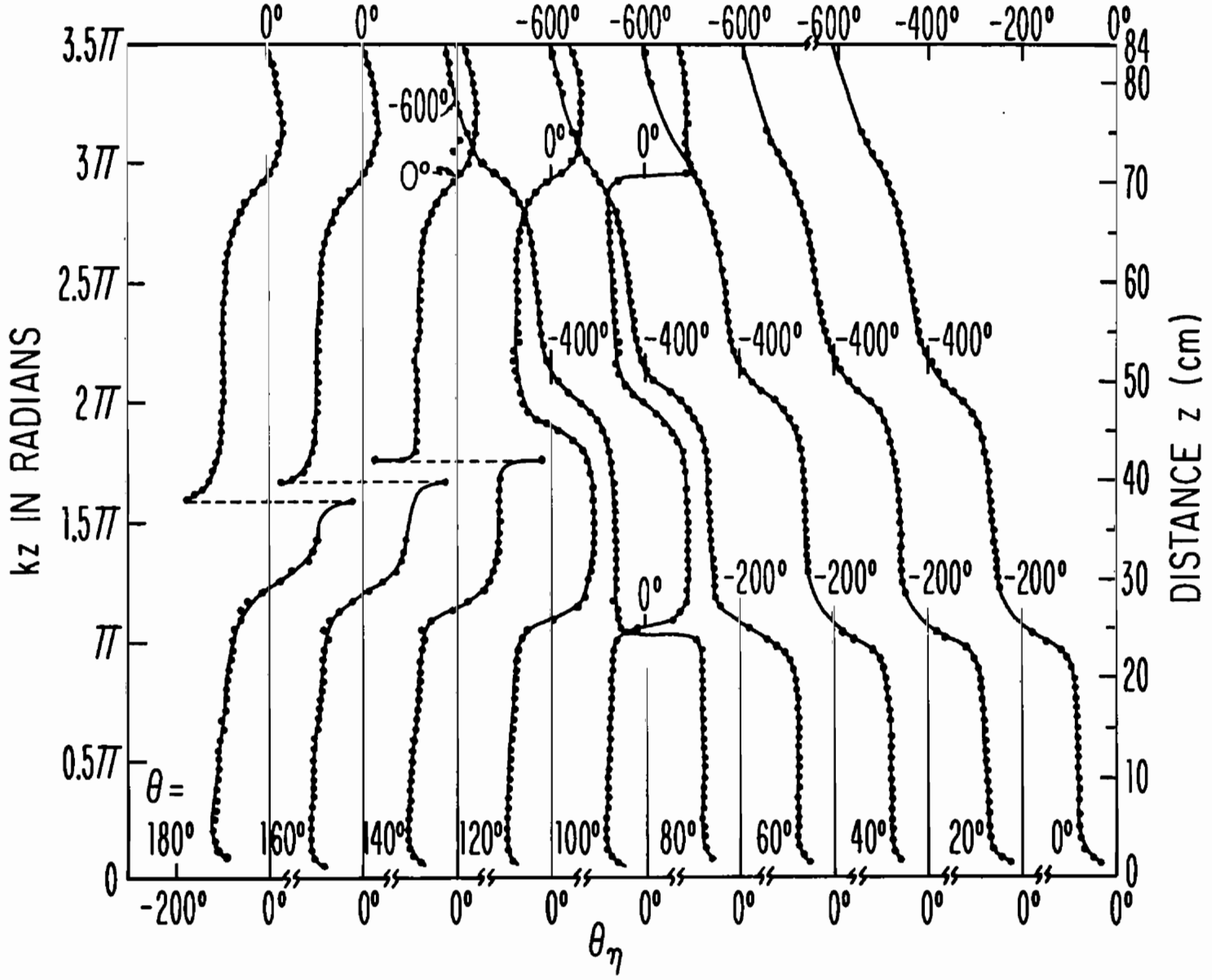

Fig. 66. Measured phase of surface density of outside charge on tubular cylinder; E-polarization, ka = 1.

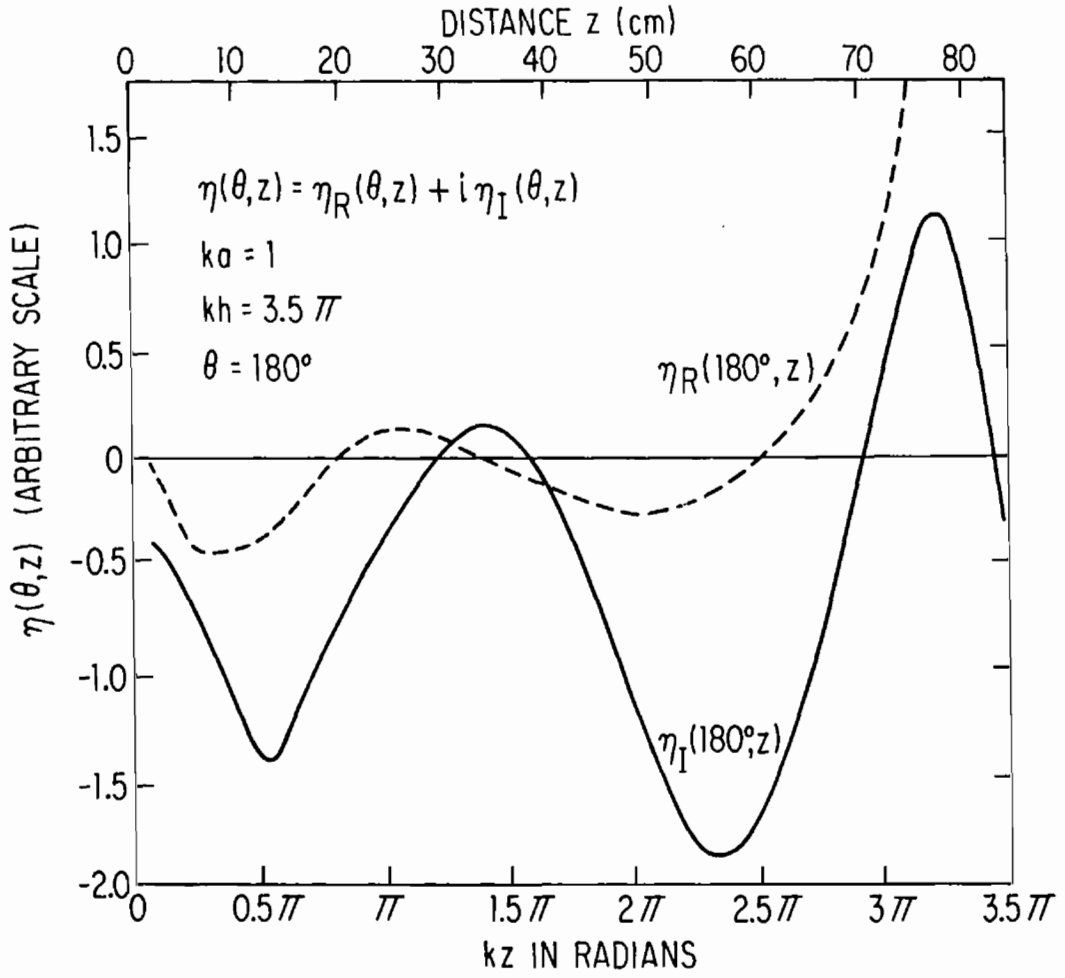

Fig. 67. Measured real and imaginary parts of surface density of outside charge on illuminated side of tubular cylinder; E-polarization.

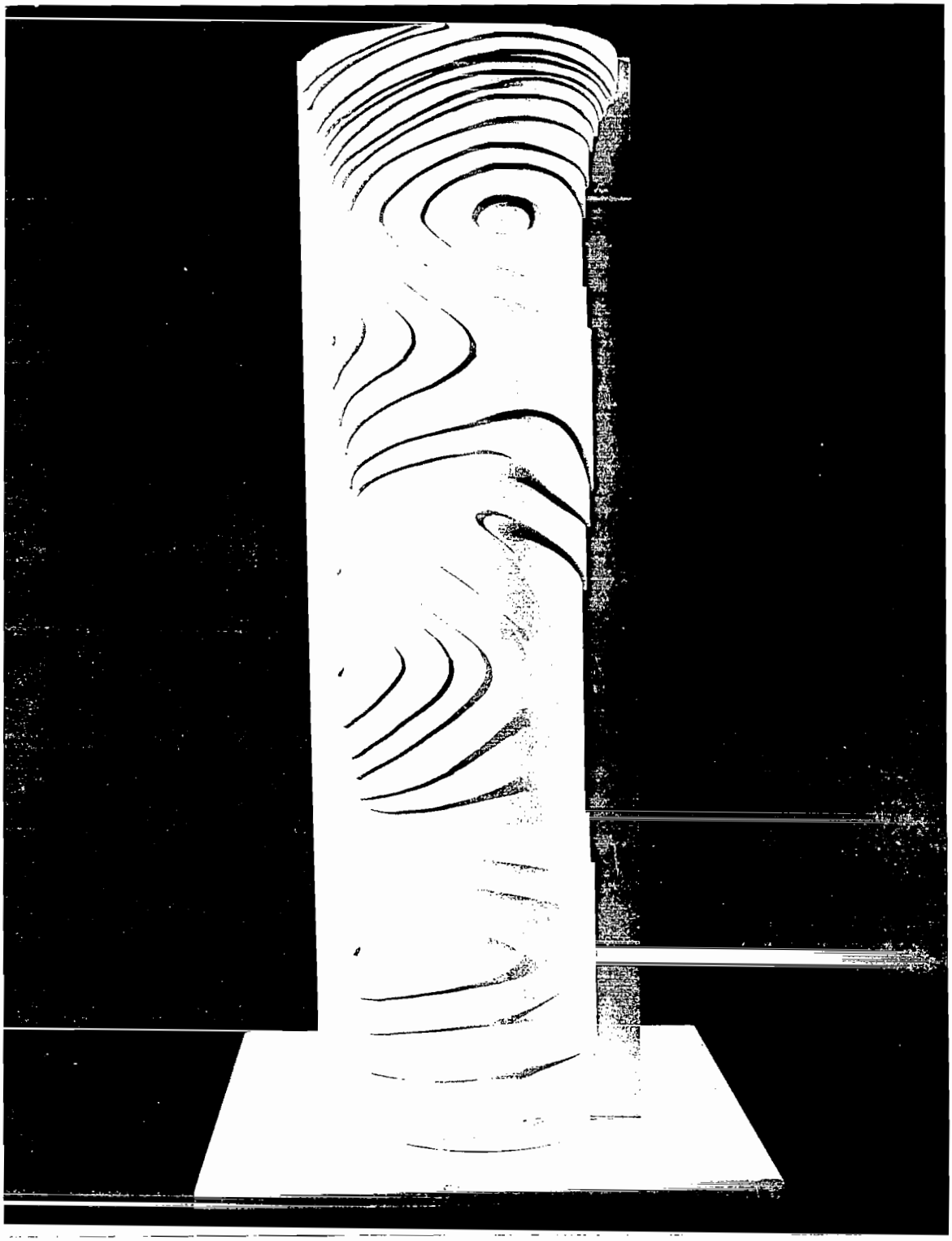

Fig. 68. Relief map of the magnitude of the charge density $\eta(\theta,z)$ on a cylinder of electrical length $kh = 3.5\pi$ and radius $ka = 1$ on a ground plane in an E-polarized field. (Measured data.)

of the cylinder is found in the properties of the incident fields. For the theoretical graphs in Figs. 56 and 57 the incident electric field is parallel to the axis and to the surface of the cylinder since it is part of a normally incident, E-polarized, plane electromagnetic wave. It induces a distribution of charge and an associated scattered radial electric field E_η as a consequence of reflections at the ends. For the measured graphs in Figs. 65 - 67 the incident electric field is the component E_θ^{inc} of a spherical wave originating 7.5 wavelengths away. As shown in Fig. 69, it has a component E_θ^{inc} cos θ cos Θ perpendicular to the surface of the cylinder that is largest at the centers of the illuminated and shadow sides (θ = 180°, 0°) and decreases to zero at the shadow boundary (θ = 90°). The total radial electric field at the surface of the cylinder is the sum of the scattered field E_η due to the charges induced on the cylinder by reflections at its ends and the component of the incident field perpendicular to the surface. That is, $E_\rho = E_\eta + E_\theta^{inc}$ cos θ cos Θ. Since the charge density $\eta(\theta,z)$ due to the standing waves generated by reflections from the ends is much greater in the shadow than on the illuminated side, the contribution by E_θ^{inc} cos θ cos Θ to the total radial field is relatively much larger on the illuminated side than in the shadow.

The dashed lines in Fig. 70 represent the real and imaginary parts of the theoretical charge density $\eta(\theta,z) = \eta_R + i\eta_I$ on a tubular cylinder (ka = 1, kh = 3.5π) when illuminated by a normally incident, E-polarized wave. The phase is referred to E_z^{inc} on the surface of the cylinder at θ = 180°. Except quite near the open end (where the transverse component $K_\theta(\theta,z)$ is significant), the charge density on the cylinder is given by $\eta = \eta_R + i\eta_I = -(i/kc)[(\partial K_{zR}/\partial z) + i(\partial K_{zI}/\partial z)]$ where $K_z = K_{zR} + iK_{zI}$ is the axial component of the surface density of current; K_{zR} is in phase, K_{zI} in phase quadrature with the incident electric field. It follows that η_I is also in phase with E_θ^{inc} at θ = 180° on the surface. Let the charge density induced on the cylinder at θ = 180° by the component E_θ^{inc} cos θ cos Θ be η_E = C cos θ cos Θ = -C cos Θ at θ = 180°. C is the appropriate amplitude. The total charge density at θ = 180° is $\eta_t = \eta_{tR} + i\eta_{tI}$ where $\eta_{tR} = \eta_R$ and $\eta_{tI} = \eta_I$ - C cos Θ. The curve -C cos Θ is shown in Fig. 70 in dot-dashed lines with C arbitrarily set equal to 15.4 so that C cos Θ = 1.15 at kz = 1.5π. The total charge density is shown in dotted lines. The original theoretical magnitude $|\eta| = \left[\eta_R^2 + \eta_I^2\right]^{1/2}$ and the magnitude of the new total

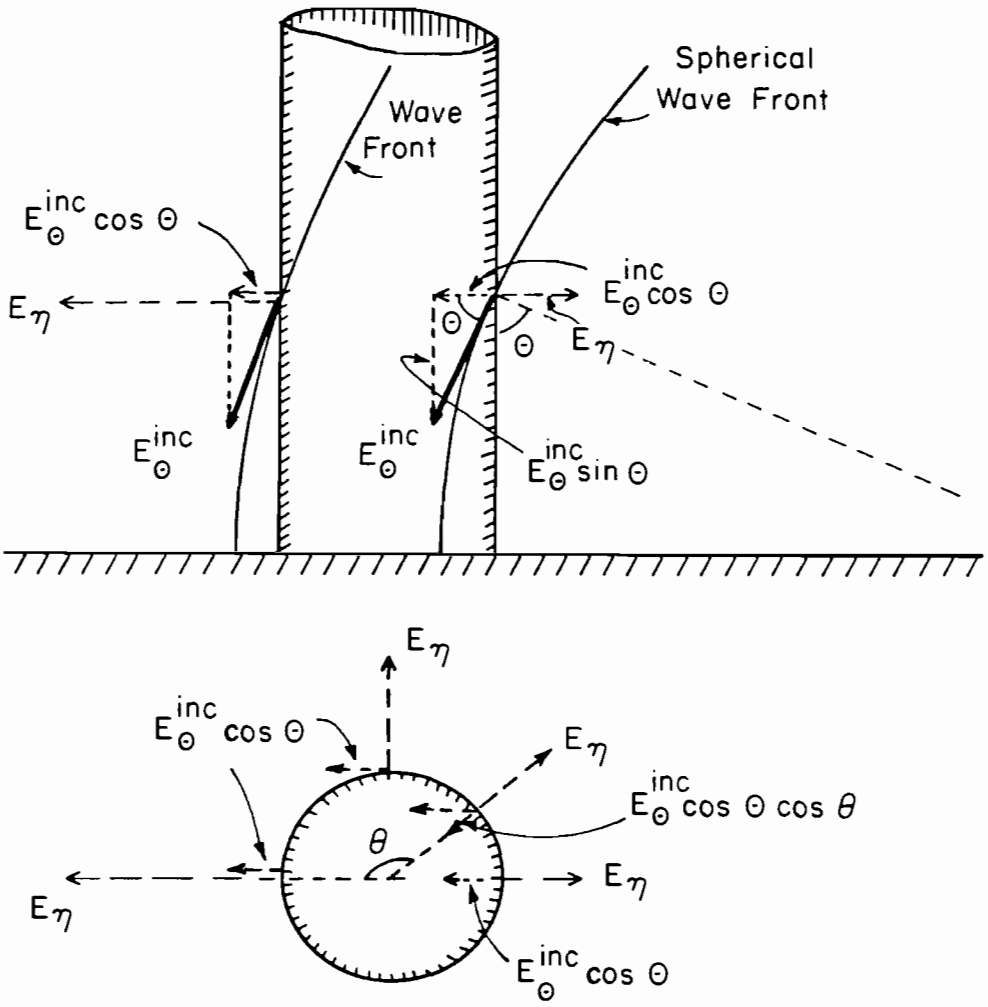

Fig. 69. Spherical wave front incident on electrically thick tubular cylinder.

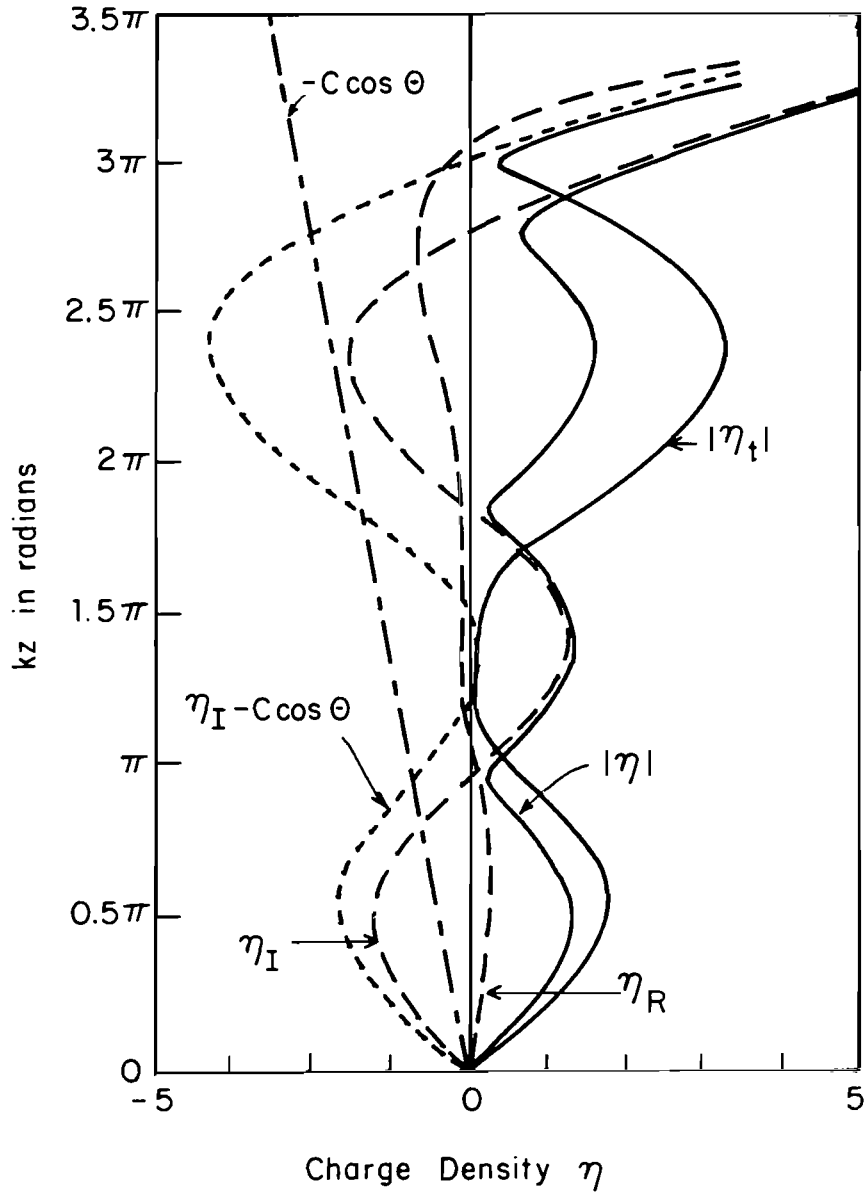

Fig. 70. Surface densities of charge $|\eta| = [\eta_R^2 + \eta_I^2]^{1/2}$ and $|\eta_t| = [\eta_R^2 + (\eta_I - C \cos \Theta)^2]^{1/2}$ for incident plane and spherical waves, respectively.

charge $|\eta_t| = [\eta_R^2 + (\eta_I - C \cos \Theta)^2]^{1/2}$ are both shown. The new total magnitude $|\eta_t|$ — which includes a correction for the charge density induced by the component of the incident field perpendicular to the surface of the cylinder — is seen to resemble the measured magnitude in Fig. 65 at $\theta = 180°$. The maxima at $kz = 0.5\pi$ and 2.5π are enhanced; the maximum at $kz = 1.5\pi$ is suppressed. If the phase of the theoretical charge density is referred to the electric field on the surface of the cylinder at each angle θ and the imaginary part is combined with $\eta_E = C \cos \theta \cos \Theta$, graphs can be obtained of $|\eta_t|$ resembling those at angles θ in Fig. 65 other than $\theta = 180°$.

Note that this demonstration has ignored the fact that the incident spherical wave (unlike an incident plane wave) not only has a component perpendicular to the cylinder, but also a tangential component that decreases in amplitude and phase with increasing distance z along the cylinder from the ground plane. When the distance from the axis of the cylinder to the source is 7.5λ, the amplitude changes by 2.6%, the phase by 72°.5 over the length from $kz = 0$ to $kz = 3.5\pi$. For a plane wave, both amplitude and phase are constant over the entire length of the cylinder.

Like the graphs for the amplitudes in Figs. 56 and 65, those for the phases in Figs. 57 and 66 show good agreement in the shadow ($0° \leq \theta \leq 90°$) and substantial differences on the illuminated side. Here the phases change very rapidly over short distances in the vicinity of $kz = 1.5\pi$ when $140° \leq \theta \leq 180°$. This is more readily understood in terms of the graphs of the real and imaginary parts of the charge density shown in Fig. 67 specifically for $\theta = 180°$ where the effect is largest. These show that except near the open end, the charge density is determined primarily by its imaginary part $\eta_I(\theta,z)$, which oscillates about a vertically shifted axis such that there are two large negative lobes on each side of $kz = 1.5\pi$ and only a very small positive lobe near $kz = 1.5\pi$. Because the amplitude of this small positive lobe is comparable to the amplitude of the generally small real part $\eta_R(\theta,z)$, the phase angle $\theta_\eta = \tan^{-1}(\eta_I/\eta_R)$ goes through a full 360° in a short range containing $kz = 1.5\pi$. This displacement is believed to be due to the nonplanar incident field with its component of the electric field perpendicular to the metal cylinder.

Extensive measurements and comparisons with the theory for incident plane waves have shown that except for the charge-density distributions

near the center of the illuminated side, the measured currents and charges are in good agreement with the theory, thus verifying the adequacy of the apparatus and techniques of measurement and justifying their use in measurements of currents and charges on structures not susceptible to accurate analyses.

5. CURRENTS AND CHARGES ON CYLINDERS IN AN H-POLARIZED FIELD

A tubular cylinder with radius a and length 2ℓ illuminated by a normally incident, H-polarized, plane wave is shown in Fig. 71. The tube is parallel to the x-axis; the incident wave travels in the positive y direction.

As with E-polarization, it is advantageous to review briefly the induced currents and charges when the cylinder is infinitely long. In this case, the entire current is transverse and given by

$$\frac{K_\theta(\theta)}{E_z^{inc}} = \frac{2}{\pi\zeta_0 ka} \sum_{n=0}^{\infty} \frac{\alpha_n i^{n-1}}{H_n^{(1)\prime}(ka)} \cos n\theta \tag{59}$$

where $\zeta_0 \doteq 120\pi$ ohms and $\alpha_n = 1$ for $n = 0$, $\alpha_n = 2$ for $n \neq 0$. Note that $E_z^{inc}/\zeta_0 = B_x^{inc}/\mu_0 = H_x^{inc}$. This distribution is shown in Fig. 72 as a function of θ for $ka = 1$. The Fourier coefficients introduced when (59) is written in the form

$$K_\theta(\theta) = A_H + B_H \cos\theta + C_H \cos 2\theta + D_H \cos 3\theta + E_H \cos 4\theta + \ldots \tag{60}$$

(with $E_z^{inc} = 1$ V/m) are given in Table 6 for $ka = 1$. It is seen that only A_H through D_H are significant. The associated distribution of the surface density of charge is given by

$$\frac{\eta(\theta)}{E_z^{inc}} = \frac{2i\varepsilon_0}{\pi k^2 a^2} \sum_{n=0}^{\infty} \frac{n\alpha_n i^{n-1}}{H_n^{(1)\prime}(ka)} \sin n\theta \tag{61}$$

In normalized form with $c = 3 \times 10^8$ m/sec,

$$c\eta(\theta) = (i/ka)[B_H \sin\theta + 2C_H \sin 2\theta + 3D_H \sin 3\theta + 4E_H \sin 4\theta + \ldots] \tag{62}$$

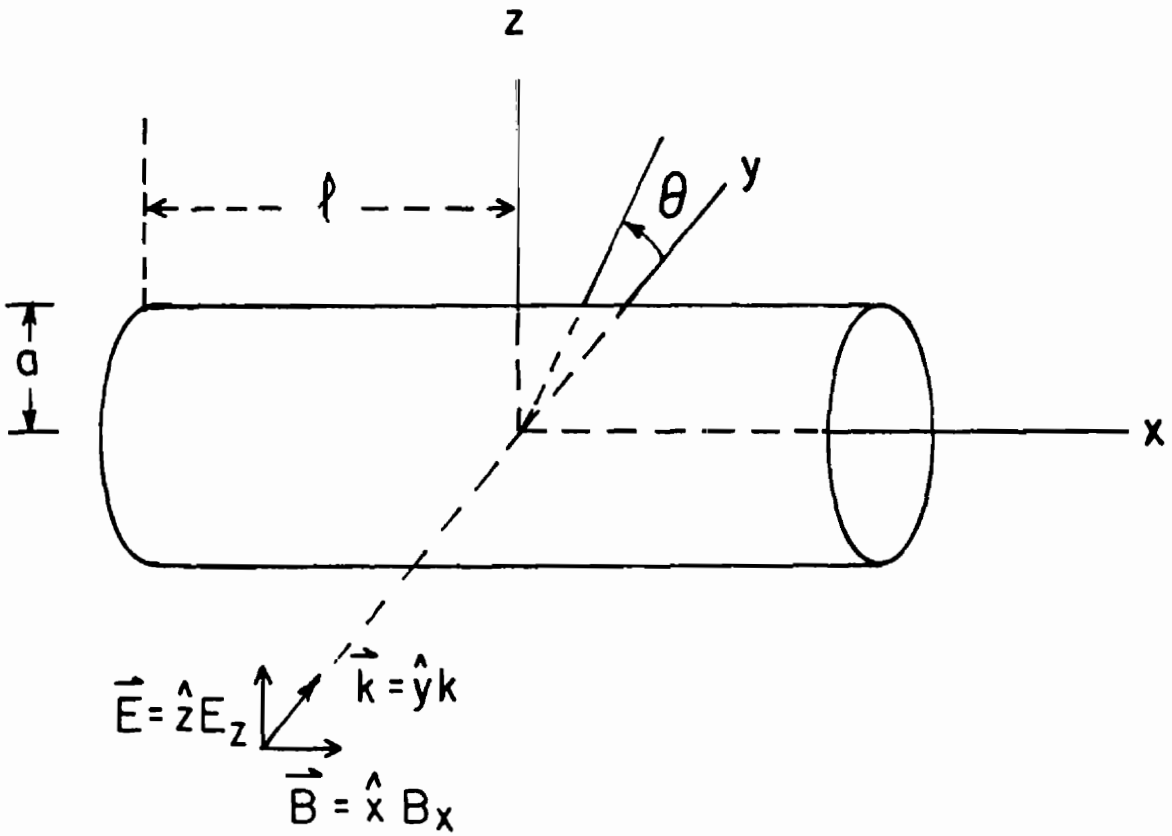

Fig. 71. Tubular cylinder in H-polarized, normally incident, plane-wave field.

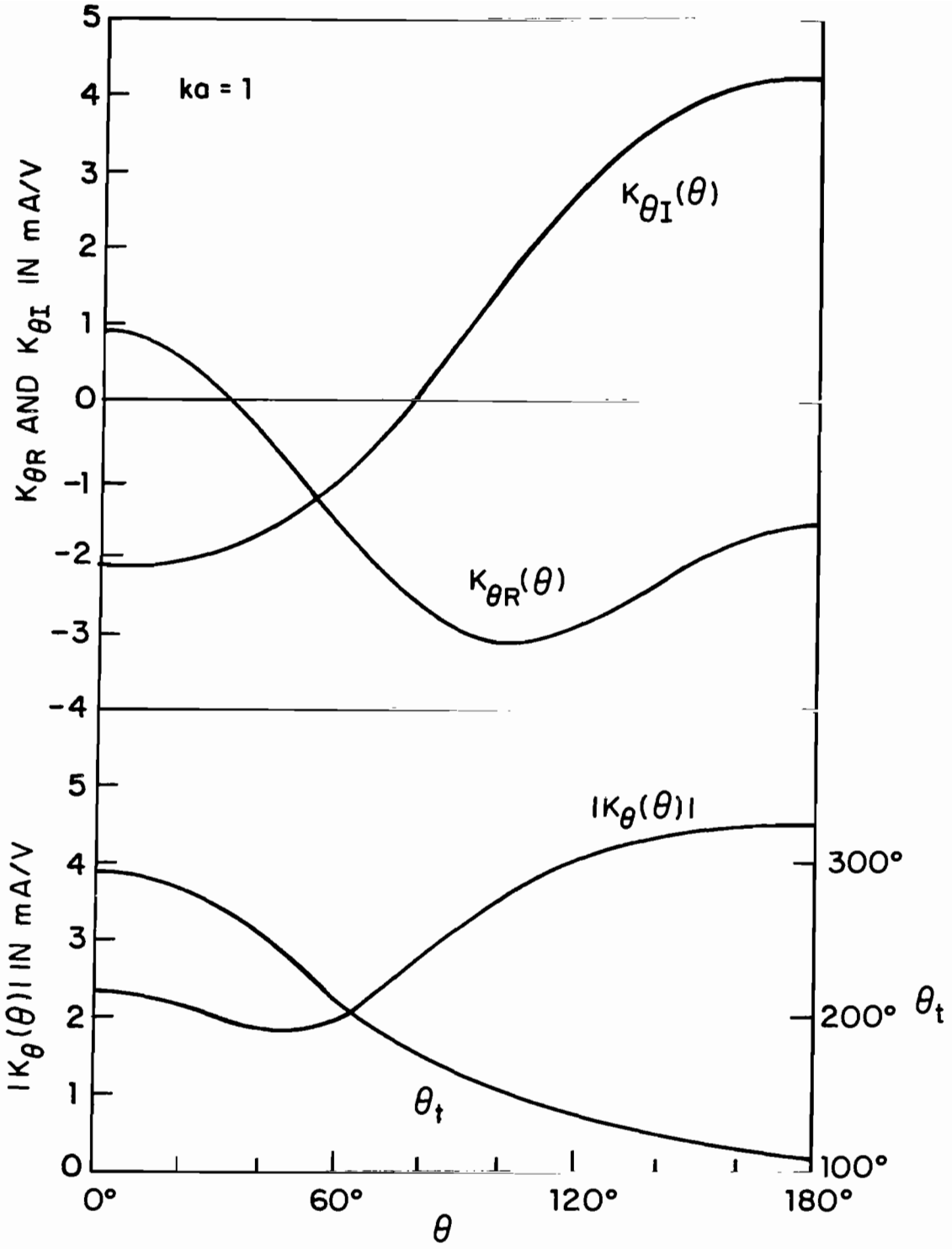

Fig. 72. Theoretical surface density of transverse current on infinitely long tubular cylinder; H-polarization.

Table 6

FOURIER COEFFICIENTS IN mA/V FOR $K_\theta(\theta)$ ON INFINITELY LONG CYLINDER;

H-POLARIZATION, $k\ell = \infty$, $ka = 1$

A_H	B_H	C_H	D_H	E_H
-1.64 + i0.93	1.27 - i3.41	1.33 + i0.11	0.00 + i0.21	0.03 + i0.00

This quantity is shown in Fig. 73 for ka = 1. Note that the charge density on the infinitely long cylinder in an E-polarized field is much simpler since it is everywhere zero.

The surface density of current on an isolated tubular cylinder with the finite length 2ℓ in a normally incident, H-polarized field can be calculated from the theory of C. C. Kao (refs. 8-11). The relevant formulas with all significant terms for ka = 1 are:

$$K_\theta(\theta,x) \doteq A_H(kx) + B_H(kx)\cos\theta + C_H(kx)\cos 2\theta + D_H(kx)\cos 3\theta \qquad (63)$$

$$K_x(\theta,x) \doteq i[B'_H(kx)\sin\theta + C'_H(kx)\sin 2\theta] \qquad (64)$$

The Fourier coefficients for $k\ell = 2\pi$ are in Table 7, those for $k\ell = 1.5\pi$ in Table 8. Their real and imaginary parts are shown as functions of kx in Fig. 74 for $k\ell = 2\pi$ and Fig. 75 for $k\ell = 1.5\pi$, along with the constant values for the infinitely long cylinder obtained from Table 6. It is seen that except very near the open end at $x = \ell$, $C_H(kx)$ and $D_H(kx)$ differ negligibly from C_H and D_H. Furthermore, $A_H(kx)$ and $B_H(kx)$ vary relatively little from A_H and B_H except in the range $(k\ell - 0.5\pi) \leq kx \leq k\ell$. At the infinitely thin knife edge at $x = \ell$, all of the coefficients for $K_\theta(\theta,x)$ become infinite. The total transverse currents $K_\theta(\theta,x)$ at $\theta = 0°$, 90° and 180° are shown in Figs. 76 and 77 as functions of kx for $k\ell = 2\pi$ and $k\ell = 1.5\pi$. Except near the open end, they are quite well approximated by $K_\theta(\theta)$ for the infinitely long tube. The transverse variations of $K_\theta(\theta,x) = K_{\theta R}(\theta,x) + iK_{\theta I}(\theta,x) = |K_\theta(\theta,x)|\exp(i\theta_t)$ at different values of kx are shown in Figs. 78 and 79 when $k\ell = 2\pi$ and 1.5π. The graphs are all quite similar except when kx is close to $k\ell$. They are also similar to the values shown in Fig. 72 of $K_\theta(\theta)$ for the infinitely long cylinder. It may be concluded that for all lengths the very simple relation, $K_\theta(\theta,x) \doteq K_\theta(\theta)$, is a good approximation except when kx is within 0.5π of an open end.

There is no axial component of current $K_x(\theta,x)$ on the infinitely long cylinder in an H-polarized field. When the cylinder is finite in length, an axial current is generated by the large accumulations of charge associated with $K_\theta(\theta,x)$ near and at the ends of the cylinder. Graphs of the theoretical value of $K_x(\theta,x)$ are shown in Figs. 80 and 81, respectively, for $k\ell = 2\pi$ and 1.5π. At the top in each figure is the transverse

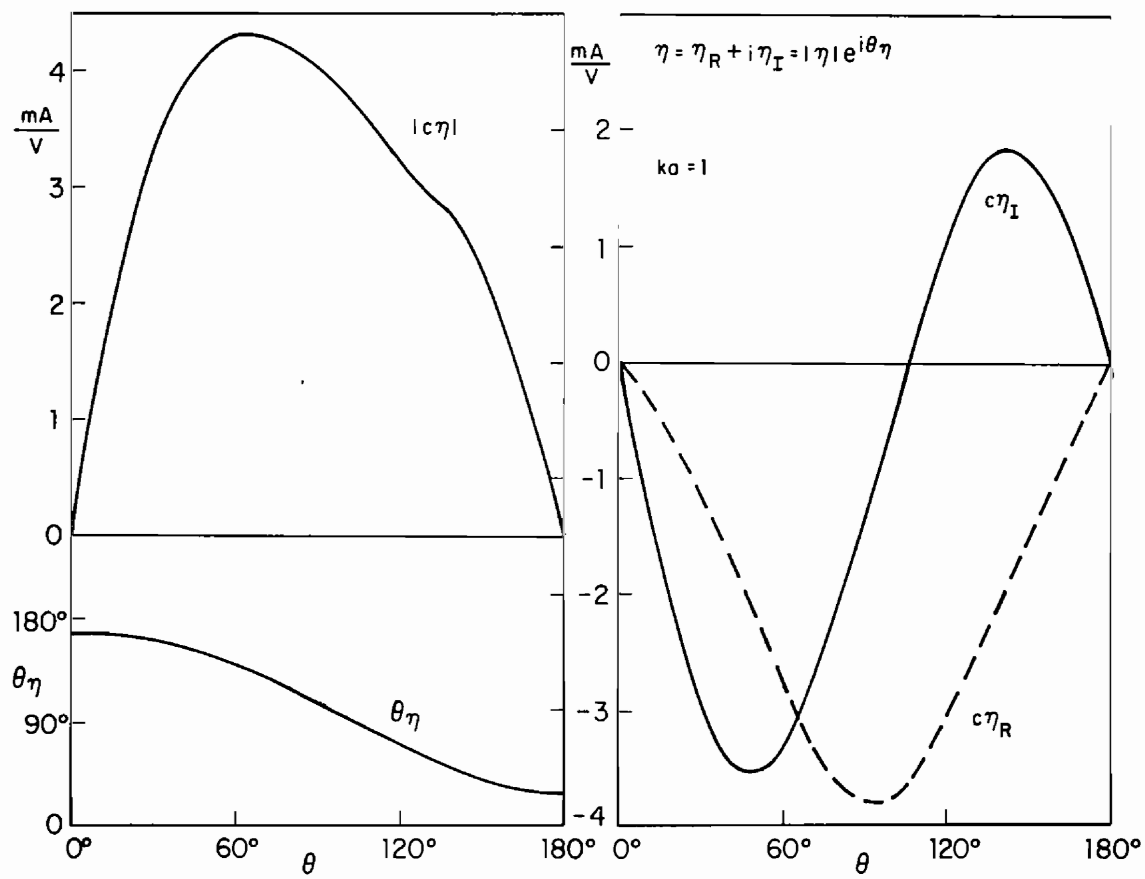

Fig. 73. Theoretical surface density of charge on infinitely long tubular cylinder; H-polarization. $E_z^{inc} = cB_x^{inc} = 1$ volt/m; $c = 3 \times 10^8$ m/sec. (The quantity shown in $-c\eta$.)

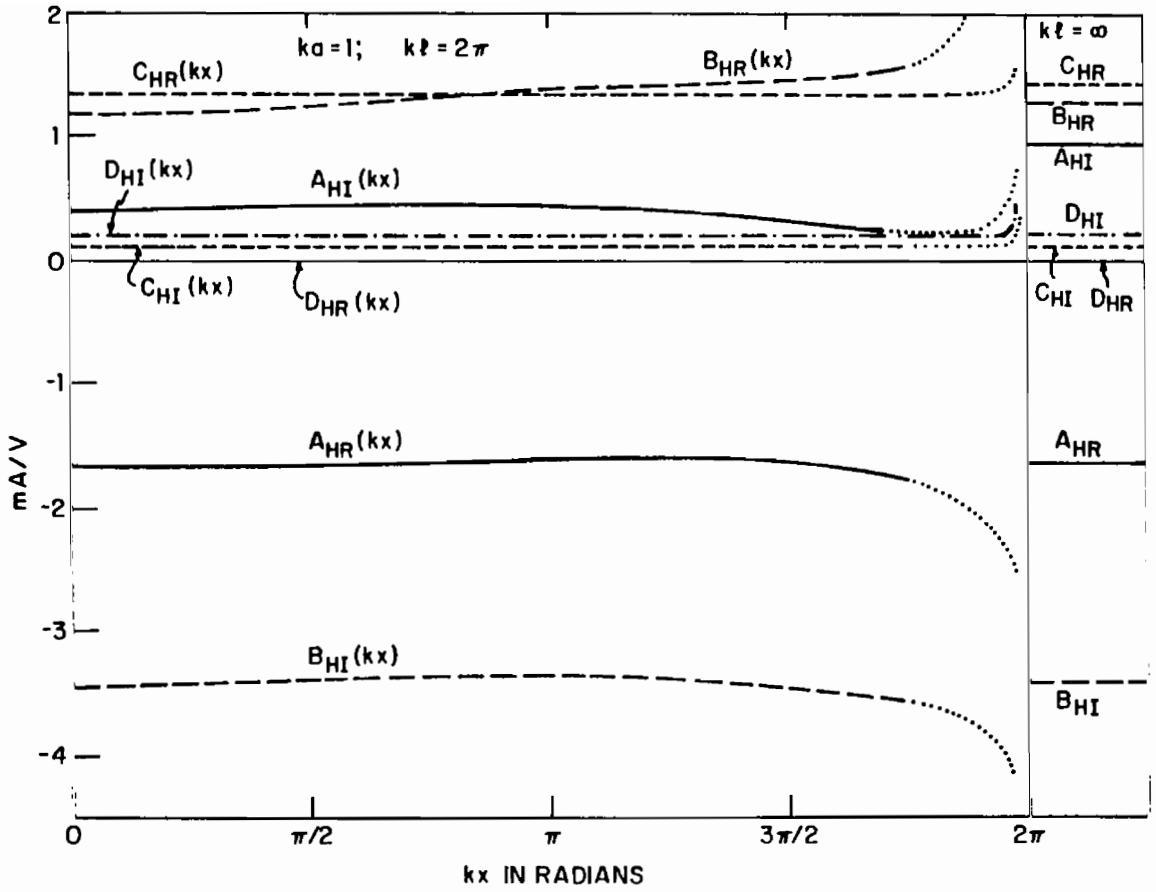

Fig. 74. Fourier coefficients of surface density of outside transverse current on tubular cylinder, $K_\theta(\theta,x) \triangleq A_H(kx) + B_H(kx)\cos\theta + C_H(kx)\cos 2\theta + D_H(kx)\cos 3\theta$; H-polarization.

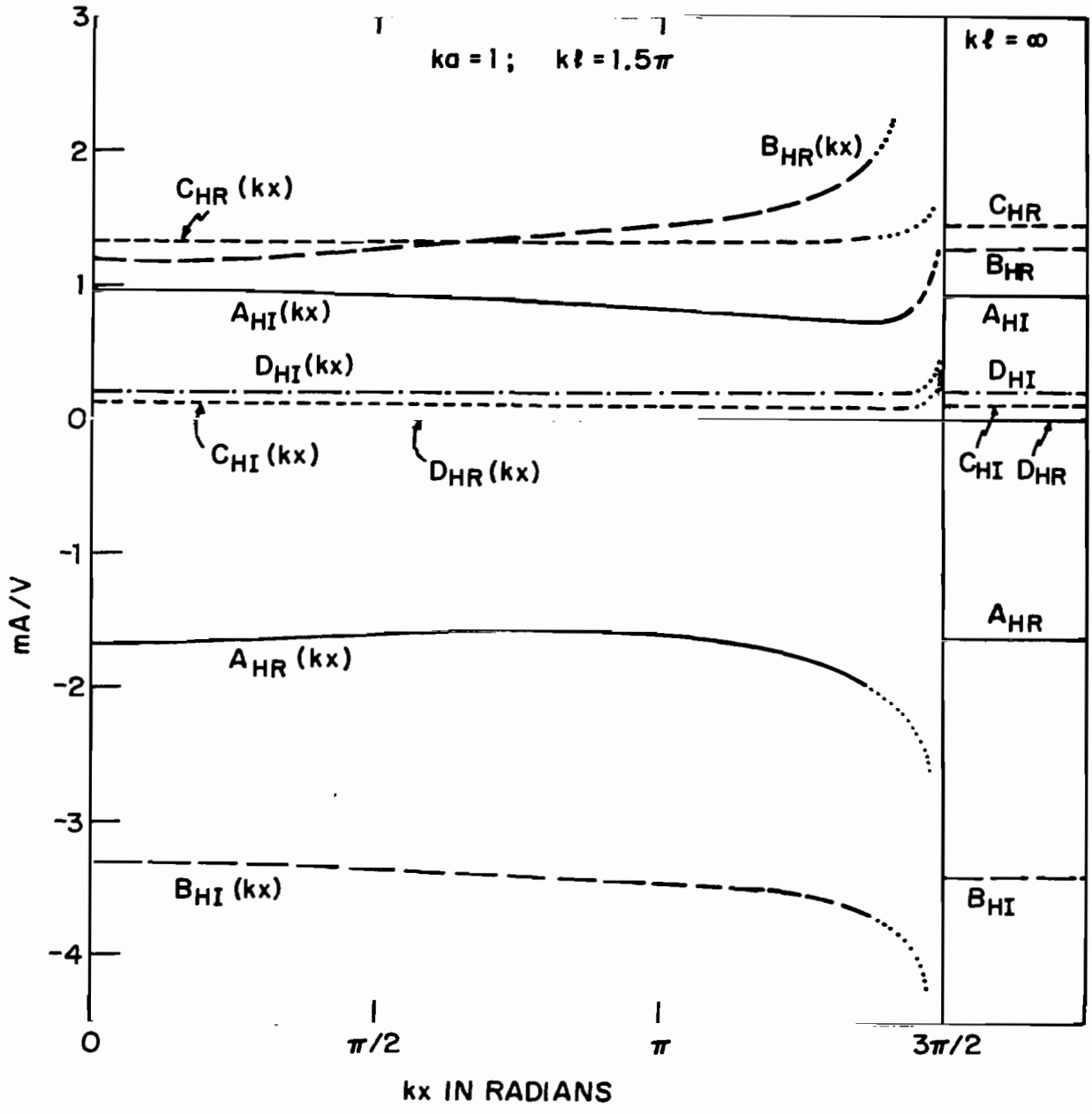

Fig. 75. Fourier coefficients of surface density of outside transverse current on tubular cylinder, $K_\theta(\theta,x) \doteq A(kx) + B_H(kx)\cos\theta + C_H(kx)\cos 2\theta + D_H(kx)\cos 3\theta$; H-polarization.

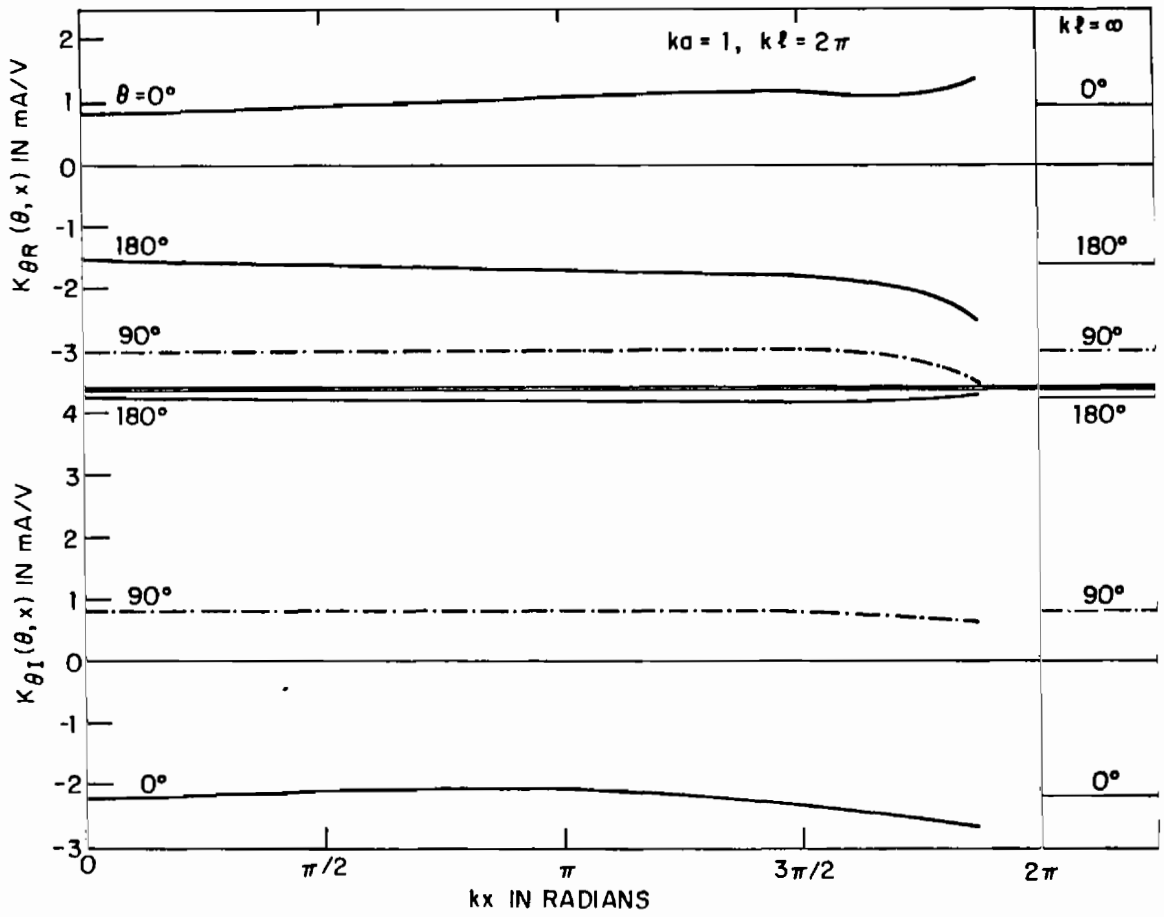

Fig. 76. Theoretical surface density of total transverse current $K_\theta(\theta,x)$ on tubular cylinder; H-polarization.

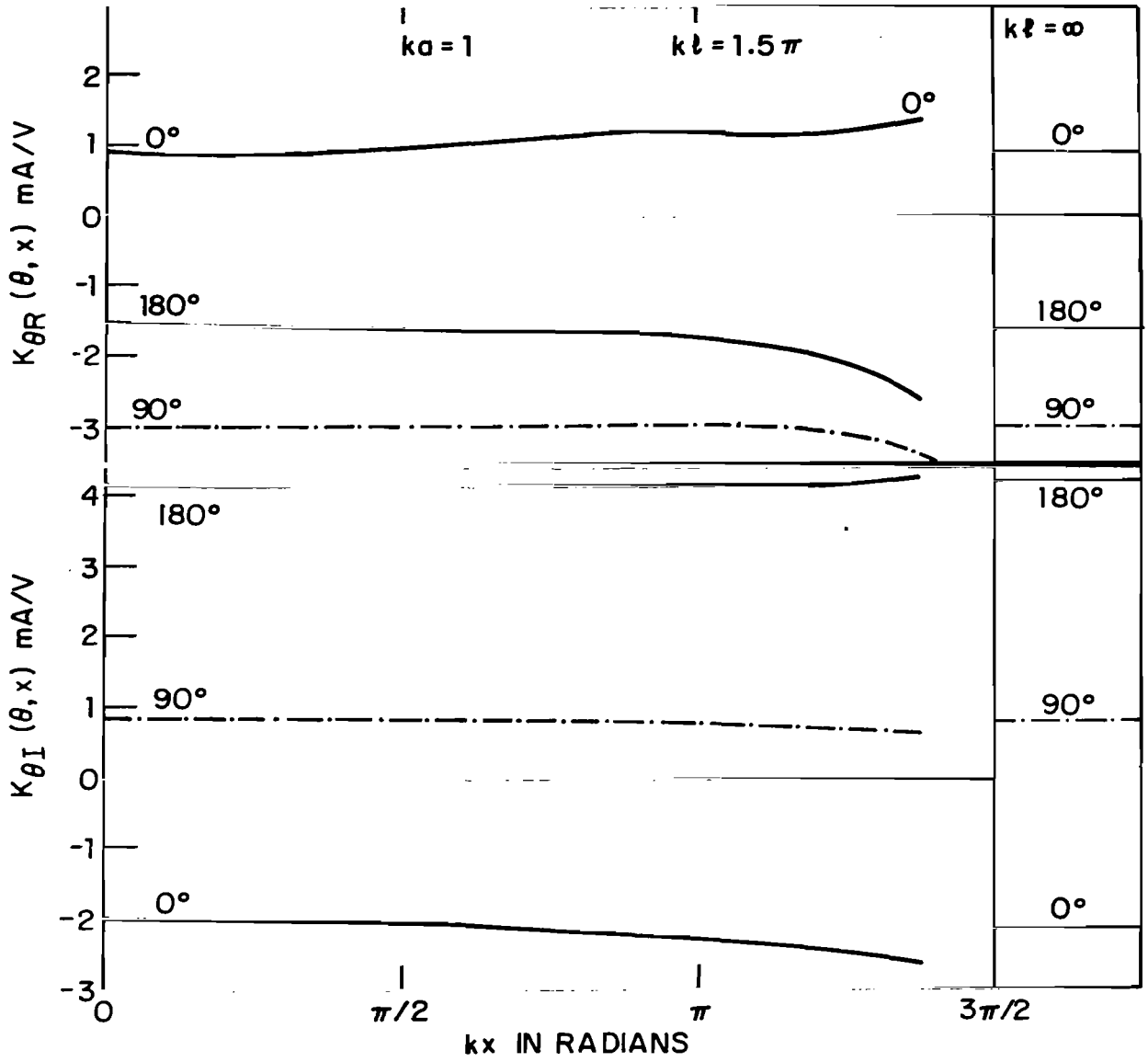

Fig. 77. Theoretical surface density of total transverse current $K_\theta(\theta,x)$ on tubular cylinder; H-polarization.

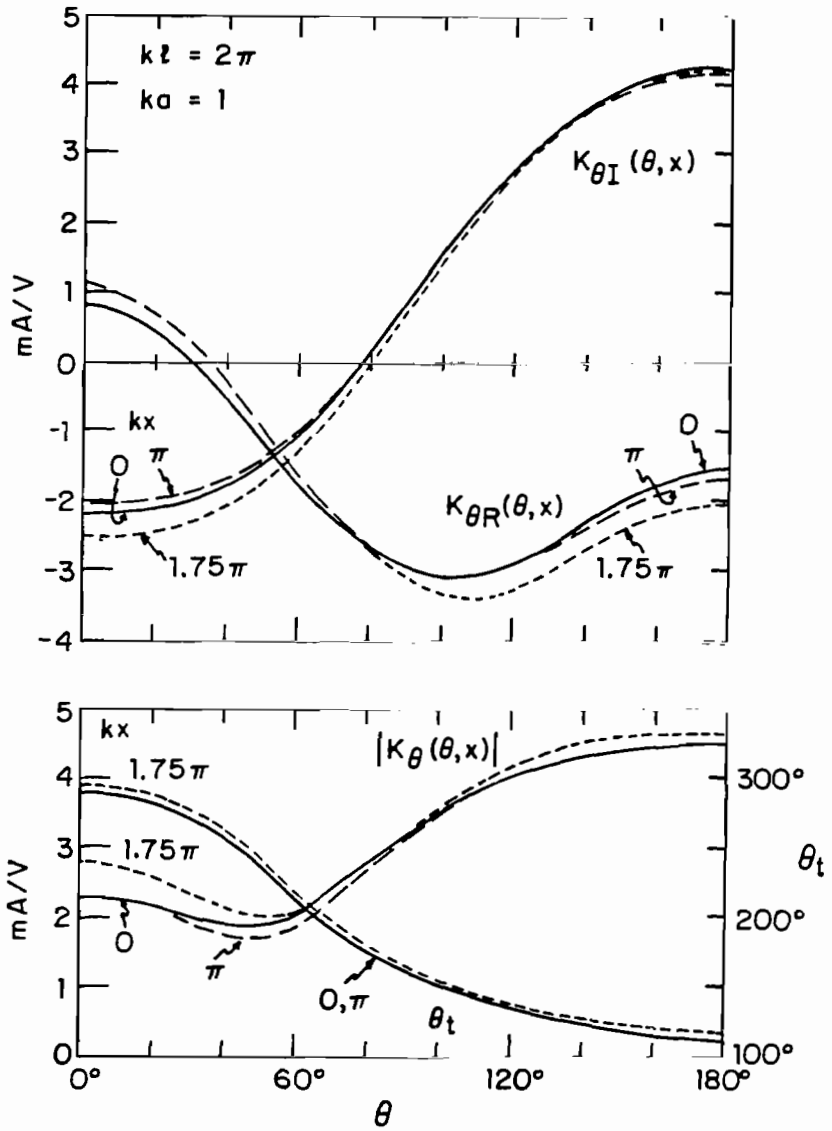

Fig. 78. Theoretical surface density of total transverse current $K_\theta(\theta,x)$ on tubular cylinder; H-polarization.

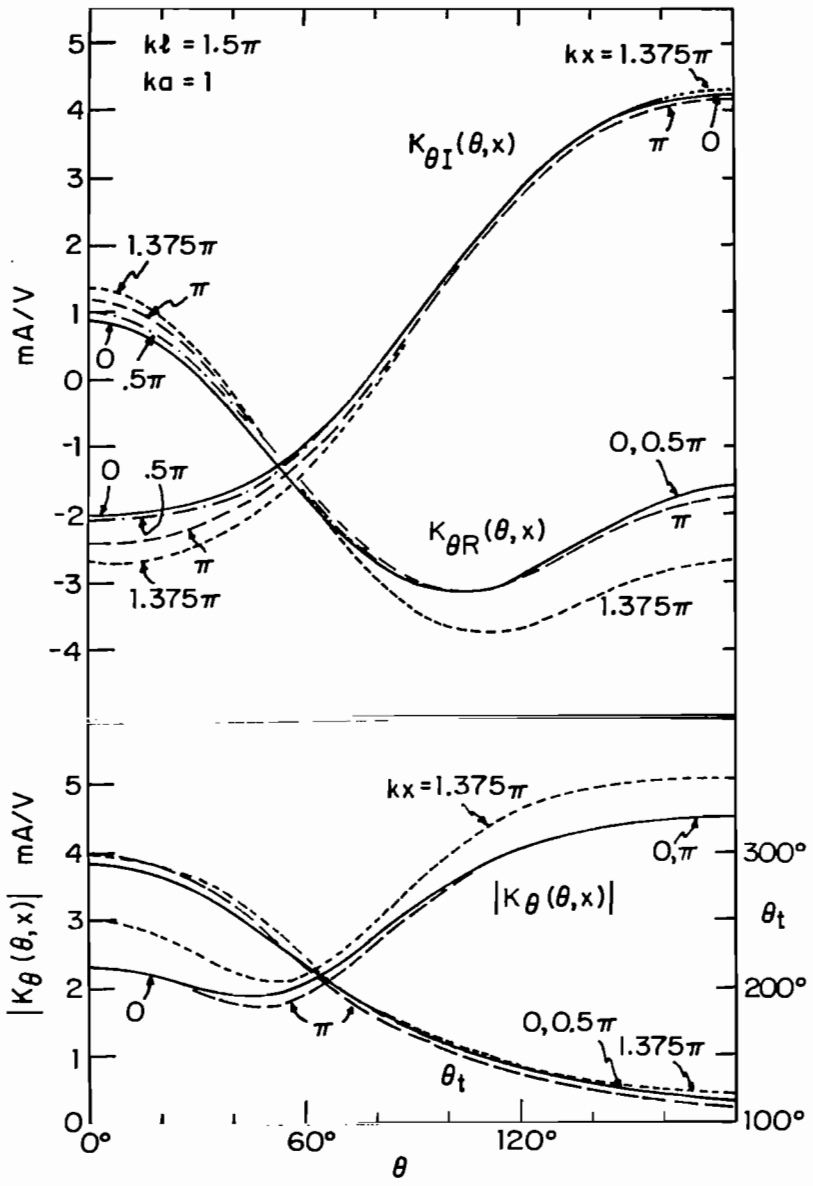

Fig. 79. Theoretical surface density of total transverse current $K_\theta(\theta,x)$ on tubular cylinder; H-polarization.

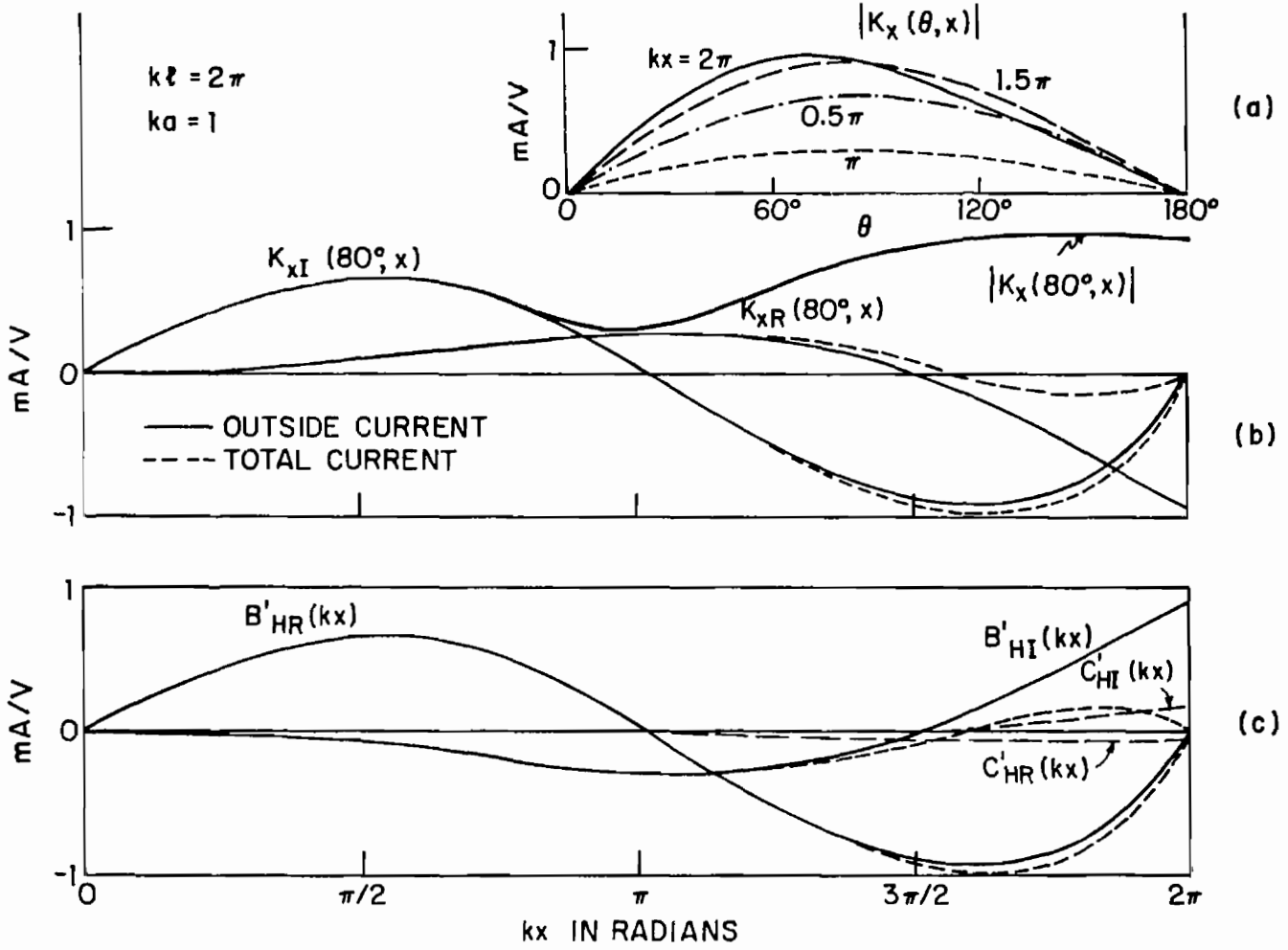

Fig. 80. Theoretical surface density of axial current on tubular cylinder; H-polarization. (a) $|K_x(\theta,x)|$ vs. θ. (b) Real and imaginary parts vs. kx. (c) Fourier components: $K_x(\theta,x) \doteq i[B'_H(kx)\sin\theta + C'_H(kx)\sin 2\theta]$.

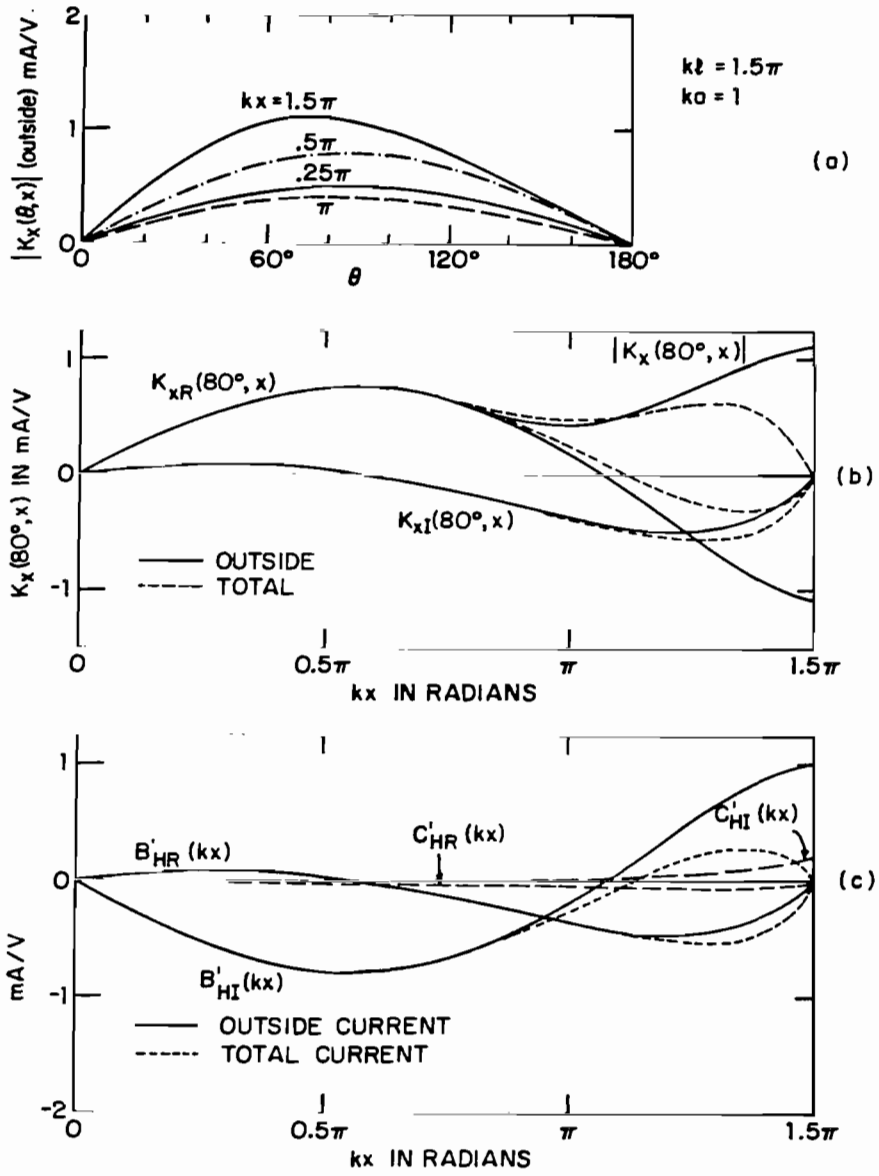

Fig. 81. Theoretical surface density of axial current on tubular cylinder; H-polarization. (a) $|K_x(\theta,x)|$ vs. θ. (b) Real and imaginary parts vs. kx. (c) Fourier components: $K_x(\theta,x) \triangleq i[B'_H(kx)\sin\theta + C'_H(kx)\sin 2\theta]$.

Table 7

FOURIER COEFFICIENTS IN mA/V FOR $K_x(\theta,x)$ AND $K_\theta(\theta,x)$ ON TUBULAR CYLINDER;

H-POLARIZATION, $k\ell = 2\pi$, $ka = 1$

kx	$B'_H(kx)$	$C'_H(kx)$	$A_H(kx)$	$B_H(kx)$	$C_H(kx)$	$D_H(kx)$
0	0	0	-1.67 + i0.91	1.18 - i3.44	1.33 + i0.11	0.00 + i0.21
0.25π	0.45 - i0.03	0.01 - i0.01	-1.66 + i0.92	1.19 - i3.42	1.33 + i0.11	0.00 + i0.21
0.50π	0.67 - i0.09	0.01 - i0.01	-1.65 + i0.94	1.25 - i3.39	1.33 + i0.11	0.00 + i0.21
0.75π	0.52 - i0.20	0.01 - i0.02	-1.63 + i0.95	1.32 - i3.35	1.34 + i0.11	0.00 + i0.21
π	0.06 - i0.29	-0.01 - i0.02	-1.60 + i0.94	1.38 - i3.34	1.34 + i0.11	0.00 + i0.21
1.25π	-0.50 - i0.25	-0.04 - i0.01	-1.59 + i0.91	1.43 - i3.37	1.34 + i0.10	0.00 + i0.21
1.5π	-0.89 - i0.02	-0.06 - i0.02	-1.62 + i0.83	1.46 - i3.45	1.33 + i0.09	0.00 + i0.21
1.75π	-0.84 + i0.41	-0.08 + i0.07	-1.77 + i0.74	1.57 - i3.58	1.33 + i0.09	0.00 + i0.21
2π	-0.01 + i0.90	-0.06 + i0.16	∞	∞	∞	∞

Table 8

FOURIER COEFFICIENTS IN mA/V FOR $K_x(\theta,x)$ AND $K_\theta(\theta,x)$ ON TUBULAR CYLINDER;

H-POLARIZATION, $k\ell = 1.5\pi$, $ka = 1$

kx	$B'_H(kx)$	$C'_H(kx)$	$A_H(kx)$	$B_H(kx)$	$C_H(kx)$	$D_H(kx)$
0	0	0	-1.66 + i0.96	1.20 - i3.31	1.34 + i0.11	0.00 + i0.21
0.125π	0.04 - i0.27	0.00 - i0.01	-1.66 + i0.96	1.21 - i3.31	1.34 + i0.11	0.00 + i0.21
0.25π	0.07 - i0.50	-0.01 - i0.02	-1.65 + i0.96	1.23 - i3.32	1.34 + i0.11	0.00 + i0.21
0.375π	0.08 - i0.68	-0.01 - i0.02	-1.63 + i0.95	1.26 - i3.33	1.34 + i0.11	0.00 + i0.21
0.5π	0.04 - i0.77	-0.02 - i0.03	-1.62 + i0.93	1.29 - i3.35	1.34 + i0.11	0.00 + i0.21
0.625π	-0.03 - i0.76	-0.03 - i0.03	-1.60 + i0.92	1.33 - i3.38	1.34 + i0.11	0.00 + i0.21
0.75π	-0.13 - i0.65	-0.04 - i0.02	-1.59 + i0.89	1.38 - i3.40	1.33 + i0.10	0.00 + i0.21
0.875π	-0.25 - i0.44	-0.05 - i0.01	-1.59 + i0.86	1.42 - i3.43	1.33 + i0.10	0.00 + i0.21
π	-0.36 - i0.16	-0.06 + i0.01	-1.61 + i0.82	1.46 - i3.46	1.33 + i0.09	0.00 + i0.21
1.125π	-0.44 + i0.17	-0.07 + i0.03	-1.66 + i0.78	1.52 - i3.49	1.33 + i0.09	0.00 + i0.21
1.25π	-0.47 + i0.52	-0.07 + i0.07	-1.76 + i0.74	1.64 - i3.54	1.33 + i0.08	0.00 + i0.21
1.375π	-0.38 + i0.85	-0.08 + i0.11	-2.01 + i0.72	2.01 - i3.70	1.37 + i0.09	0.00 + i0.21
1.5π	-0.20 + i1.06	-0.05 + i0.17	∞	∞	∞	∞

distributions of the Fourier components $B'_H(kx)$ and $C'_H(kx)$. The curves in solid lines are for the current density associated with the outside magnetic field; the broken lines are for the total current. It is seen in Fig. 80 with $k\ell = 2\pi$ that $K_x(80°,x) \doteq iK_{xI}(80°,x) = iB'_{HR}(kx)\sin 80° \doteq iB'_{HR}(\pi/2) \times \sin 80°$ sin kx for both the outside and total currents. The component $K_{xR}(80°,x)$ of the outside current is relatively small everywhere except in the range $(k\ell - 0.5\pi) \leq kx \leq k\ell$ where it rises to its largest value at $kx = k\ell$. (On a metal tube with walls that are thick compared to the skin depth, the outside current becomes the oppositely directed inside current at $x = \ell$.) With $k\ell = 1.5\pi$, Fig. 81 shows that for the outside current $K_x(80°,x) \doteq K_{xR}(80°,x) = -B'_{HI}(kx)\sin 80° \doteq -B'_{HI}(\pi/2)\sin 80°$ sin kx. The total current has the same form except in the range $\pi \leq kx \leq 1.5\pi$ where it becomes zero at $kx = k\ell = 1.5\pi$. $K_{xI}(80°,x)$ and $B'_{HR}(kx)$ are small outside this range. It is seen from Tables 7 and 8 that the maximum value of $|K_x(\theta,x)|$ is approximately 20% of the maximum value of $|K_\theta(\theta,x)|$.

The surface density of charge $\eta(\theta,x)$ on a cylinder of finite length in a normally incident, H-polarized field is given by

$$\eta(\theta,x) = -\frac{i}{c}\left[\frac{\partial K_x(\theta,x)}{k\,\partial x} + \frac{1}{ka}\frac{\partial K_\theta(\theta,x)}{\partial\theta}\right] \tag{65}$$

With (63) and (64),

$$c\eta(\theta,x) = \left[\frac{\partial B'_H(kx)}{\partial(kx)} + \frac{iB_H(kx)}{ka}\right]\sin\theta + \left[\frac{\partial C'_H(kx)}{\partial(kx)} + \frac{i2C_H(kx)}{ka}\right]\sin 2\theta + \ldots \tag{66}$$

Thus, the leading term in the distribution of $\eta(\theta,x)$ has the θ dependence given by sin θ. This has a positive maximum at $\theta = 90°$, a negative extreme at $\theta = 270°$. The theoretical surface densities of charge on cylinders with $k\ell = 2\pi$ and 1.5π are in Figs. 82 and 83, respectively. The θ dependences for both lengths are very much alike and also similar to that for the infinitely long cylinder shown in Fig. 73. All of the curves have an only slightly distorted form proportional to sin θ independent of both x and ℓ.

The axial variation of $\eta(\theta,x)$, shown in Figs. 84 and 85 for $k\ell = 2\pi$ and 1.5π, is approximately like cos kx outside the range $(k\ell - 0.5\pi) \leq kx \leq k\ell$.

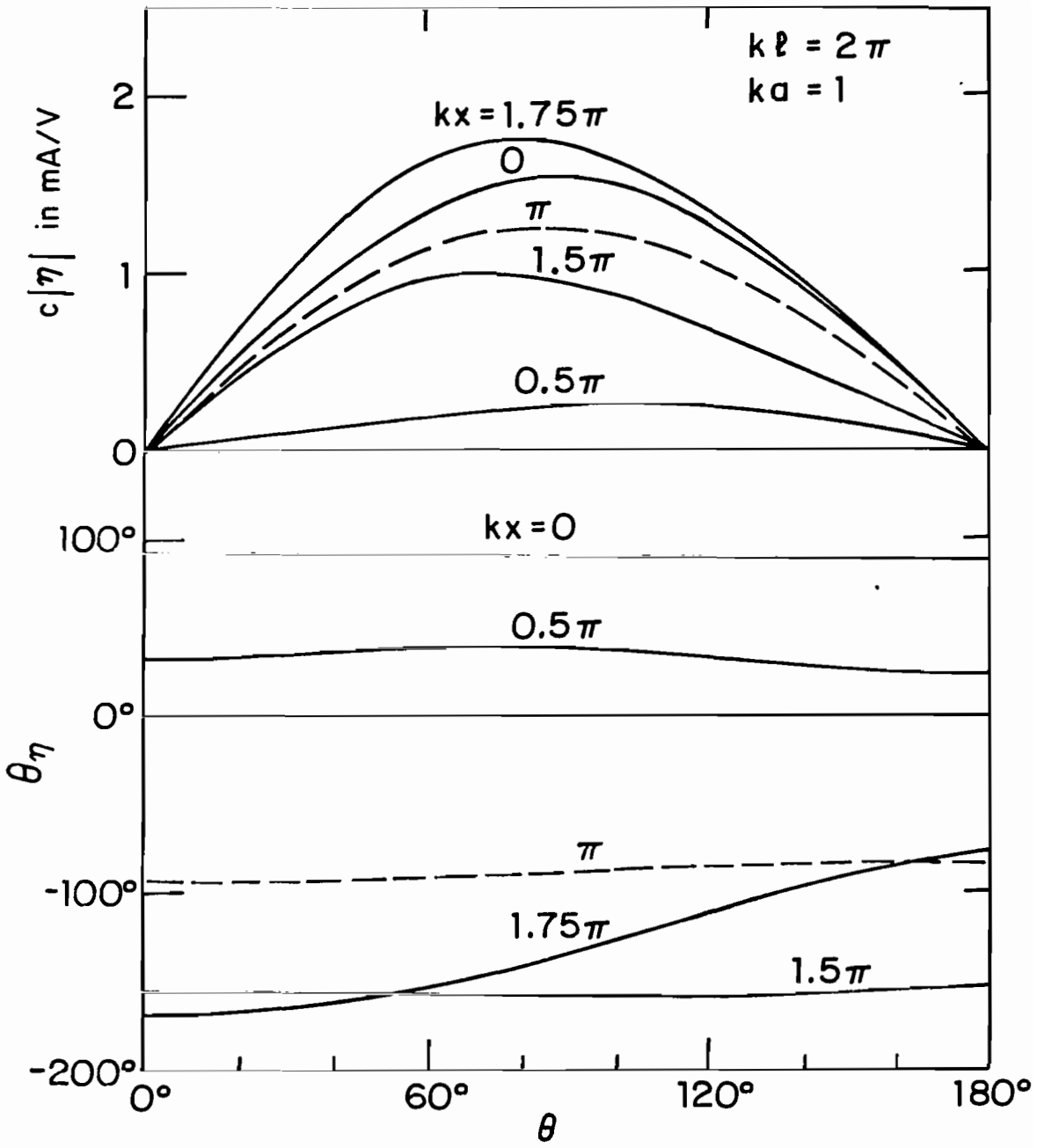

Fig. 82. Theoretical surface density of charge on tubular cylinder; H-polarization. ($c = 3 \times 10^8$ m/sec.)

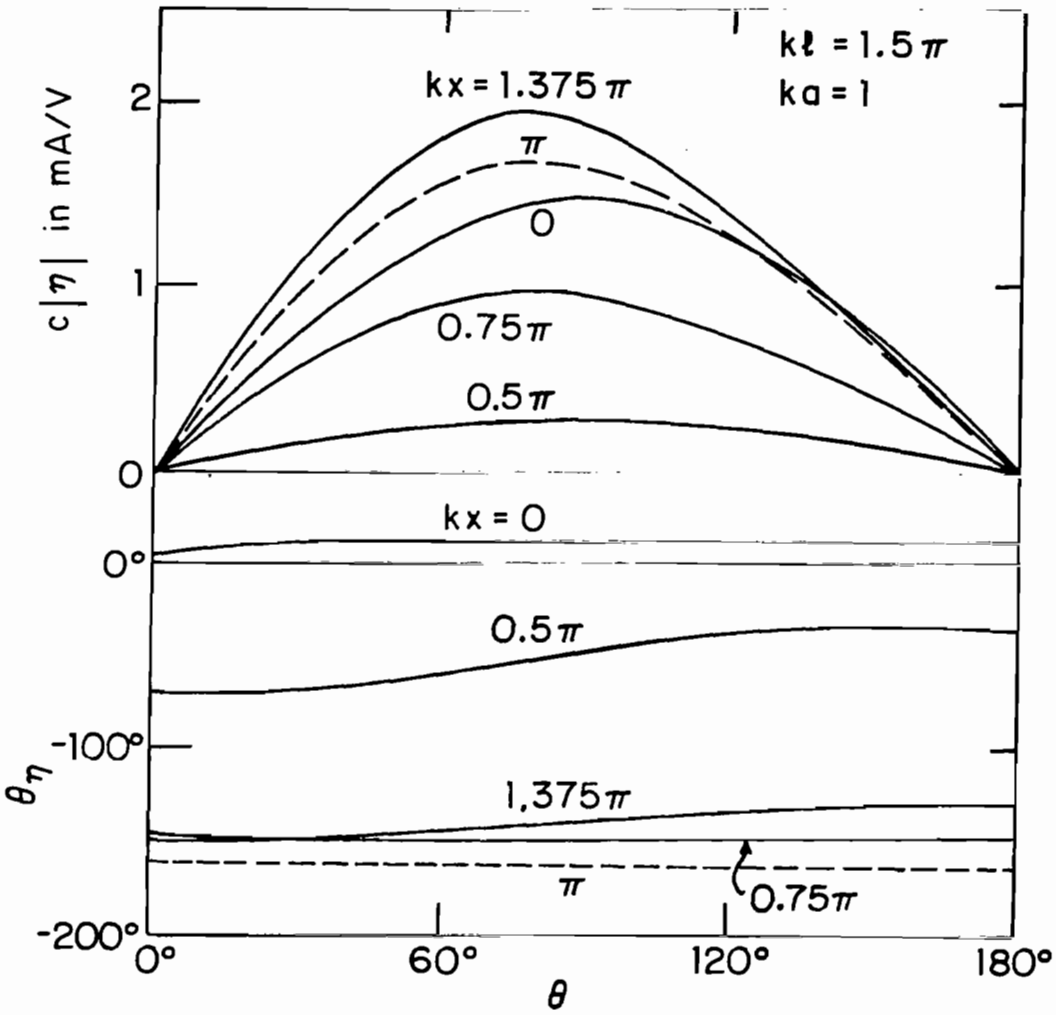

Fig. 83. Theoretical surface density of charge on tubular cylinder; H-polarization. ($c = 3 \times 10^8$ m/sec.)

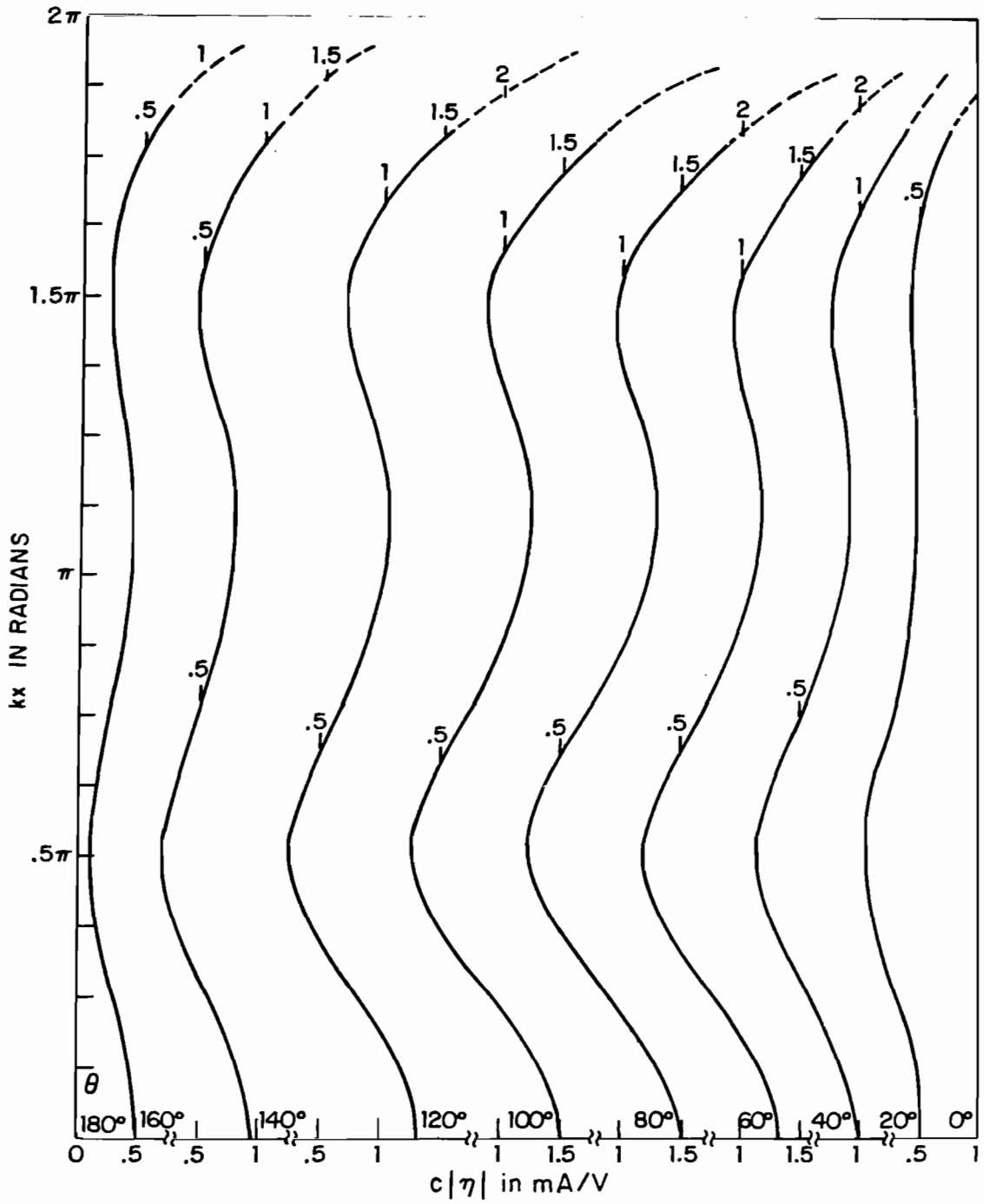

Fig. 84. Theoretical magnitude of surface density of charge $c|\eta|$ on tubular cylinder; H-polarization, $k\ell = 2\pi$, $ka = 1$. ($c = 3 \times 10^8$ m/sec.)

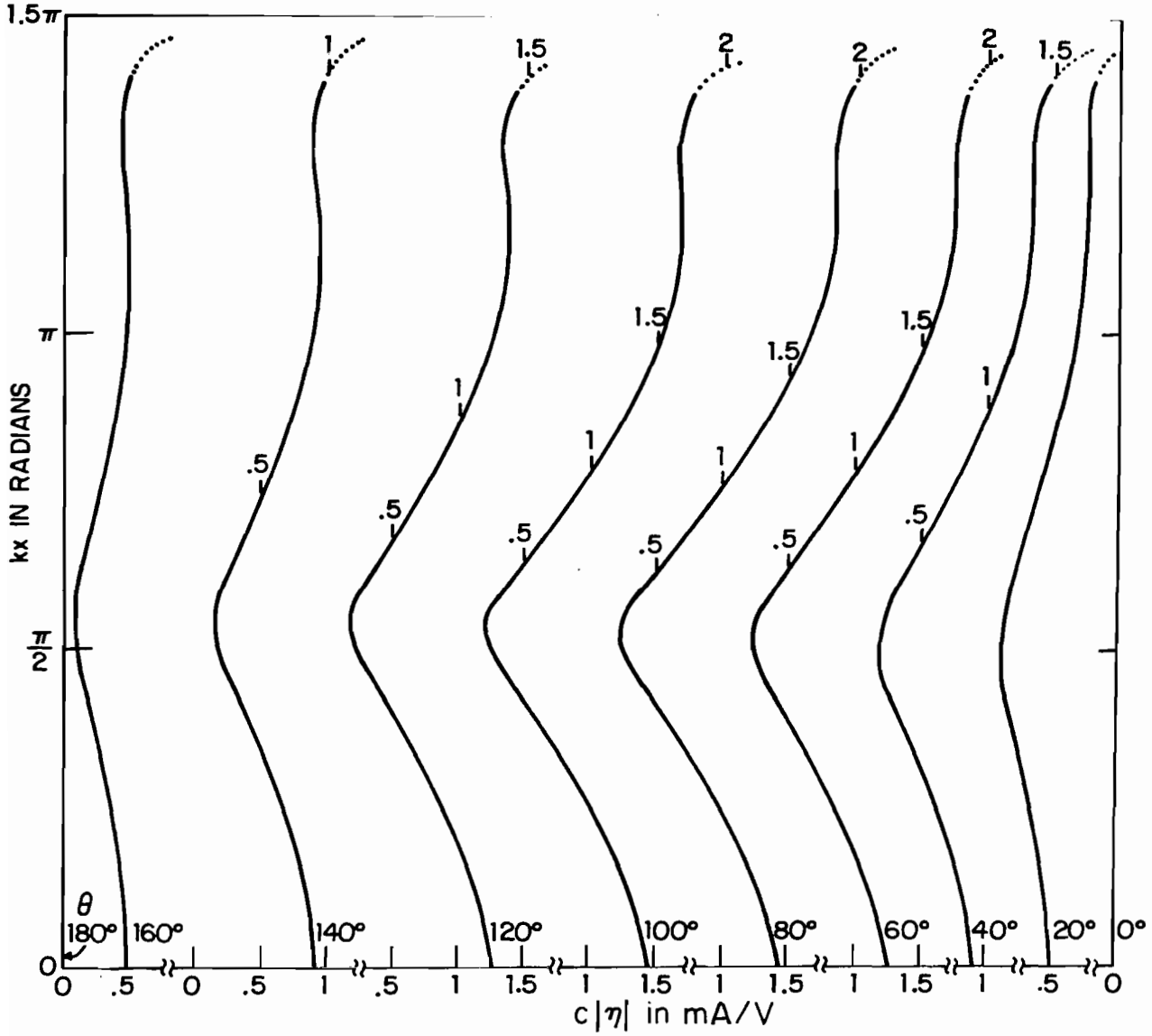

Fig. 85. Theoretical magnitude of surface density of charge $c|\eta|$ on tubular cylinder; H-polarization, $k\ell = 1.5\pi$, $ka = 1$. ($c = 3 \times 10^8$ m/sec.)

In this range the charge density increases rapidly as x approaches ℓ. The amplitude is zero at $\theta = 0°$ and 180° and greatest near $\theta = 80°$ and 280°. The contour diagrams of $|\eta(\theta,x)|$ corresponding to Figs. 84 and 85 are shown in Figs. 86 and 87. The two-dimensional standing-wave patterns along the entire surface are readily visualized. When $k\ell = 2\pi$, there are alternating positive and negative peaks of charge approximately at $\theta = 80°$ and 280° with $kx = 0, \pi, 2\pi$; there are saddle points at $kx = 0.5\pi$ and 1.5π, $\theta = 80°$ and 280°. Note that there is a rapid increase in amplitude as the open end is approached. When $k\ell = 1.5\pi$, there are positive and negative maxima at $kx = 0$, $\theta = 80°$ and 280°, and saddle points at $kx = 0.5\pi$, $\theta = 80°$ and 280°. The expected maxima at $kx = \pi$ are close enough to the open end to be engulfed in the rapid rise to infinity at $x = \ell$ so that they appear only as a flattening of the slope, as can be seen in Fig. 87. It is significant that except quite near the open end, the contour diagrams for $\eta(\theta,x)$ when $k\ell = 2\pi$ and 1.5π are very much alike.

6. CONCLUSION

The material presented in Sections III, IV and V provides a comprehensive theoretical and experimental picture of the surface densities of current and charge induced on an electrically thick tubular cylinder by an incident plane- and nearly plane-wave field with E- and H-polarizations. Simple analytical representations in terms of the forced and resonant parts of the transverse Fourier components have been provided for all sufficiently long cylinders. This information is directly applicable to isolated tubular or capped cylinders in the form, for example, of rockets on the launch pad. It also serves as the basis for understanding the currents and charges induced on crossed electrically thick cylinders when the vertical member with the length 2h is parallel to the incident electric field, the horizontal member with the length 2ℓ parallel to the incident magnetic field. This application is discussed in Section VI. An extension of the theoretical and measured results to even thicker cylinders, e.g., $ka = 2$, is contained in Section VII.

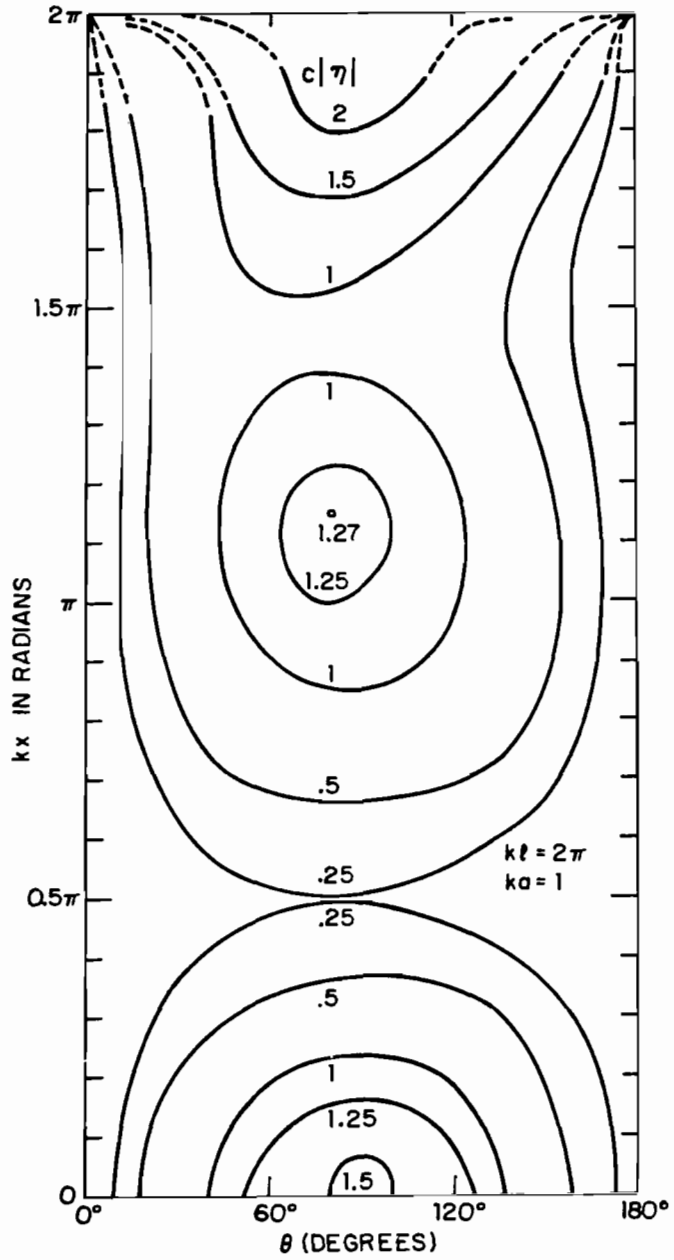

Fig. 86. Contour diagram of theoretical surface density of charge $c|\eta(\theta,x)|$ in mA/V on tubular cylinder; H-polarization. ($c = 3 \times 10^8$ m/sec.)

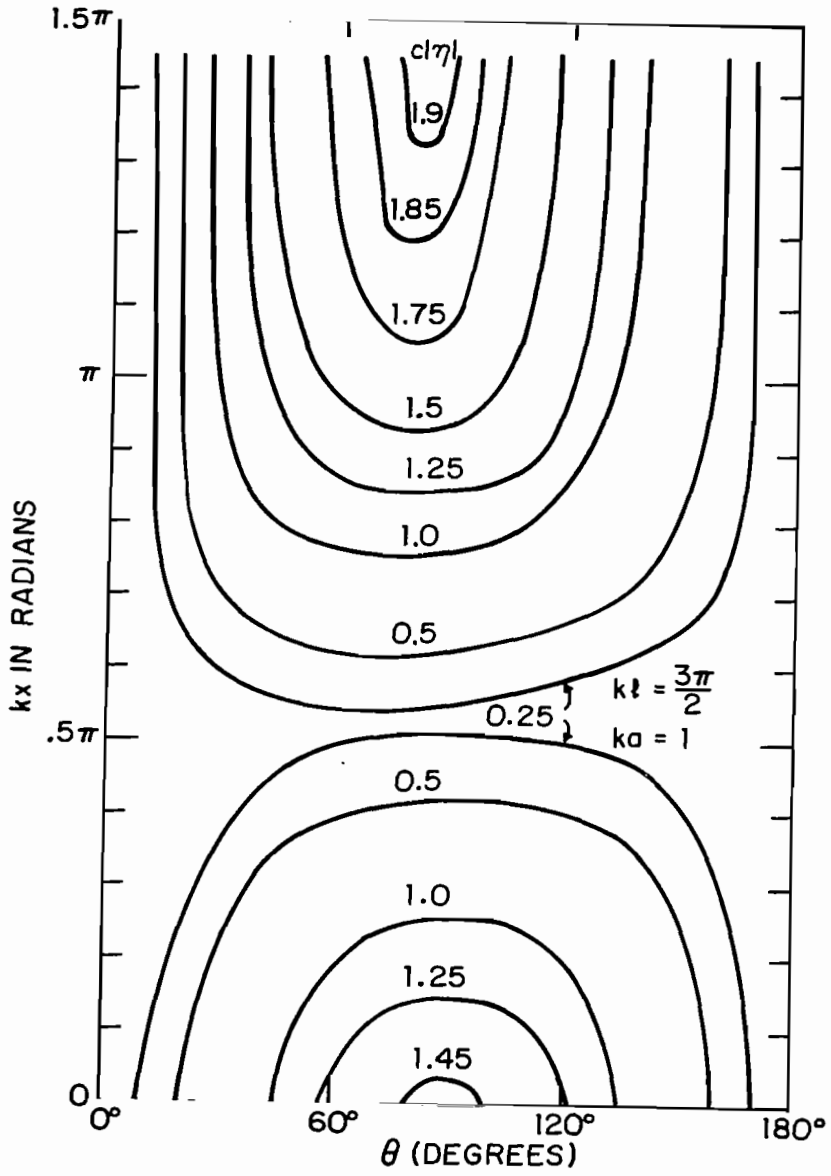

Fig. 87. Contour diagram of theoretical surface density of charge $c|\eta(\theta,x)|$ in mA/V on tubular cylinder; H-polarization. ($c = 3 \times 10^8$ m/sec.)

SECTION VI

CROSSED ELECTRICALLY THICK CYLINDERS IN A NORMALLY INCIDENT, PLANE-WAVE FIELD, MEASUREMENTS, $ka = 1$, $kh = 3.5\pi$; $kh_1 = 2.5\pi$, $kh_2 = \pi$, $k\ell_1 = k\ell_2 = \pi$, 1.5π and 2π; $kh_1 = 2\pi$, $kh_2 = 1.5\pi$, $k\ell_1 = k\ell_2 = 1.5\pi$ and 2π

1. INTRODUCTION

When an aircraft is illuminated by a plane electromagnetic wave or pulse of high intensity, the field penetrates into its interior through various small apertures and so presents a possible hazard to sensitive apparatus. Since the magnitude of the field inside a metal shell can be related to the currents and charges on its outside surface in the absence of the apertures, the determination of these is a first step in the evaluation of the internal fields. In general, this is a very difficult problem and has been accomplished analytically only when the frequency or frequencies involved are sufficiently low that the transverse dimensions of the wings and fuselage are all electrically small. In this case, all transverse currents are negligible and total axial currents and charges per unit length can be defined. Furthermore, junction regions are electrically so small that the charges on their surfaces can be ignored and their geometry treated as irrelevant. Under these conditions, thin-wire theory can be applied and a complete analytical solution obtained both when the exciting field is normally incident (ref. 3) and when it arrives at an angle (ref. 5). Unfortunately, the range of frequencies in possible incident fields generated, for example, by an electromagnetic pulse from a nuclear explosion can extend up to values for which the cross-sectional dimensions of wings and fuselage can reach several wavelengths. Under these conditions, all of the simplifying assumptions of thin-wire theory are invalid. In order to gain insight into the complicated three-dimensional distributions of surface currents and charges that can be excited at these higher frequencies, the aircraft has been modeled by crossed, electrically thick, tubular cylinders erected on a large ground plane at $z = 0$, as shown in Fig. 88. A systematic experimental study was carried out specifically with a normally incident, approximately plane, electromagnetic wave. This study also serves to provide data to verify the validity and accuracy of analytical or numerical methods that may be devised in the future. In the first

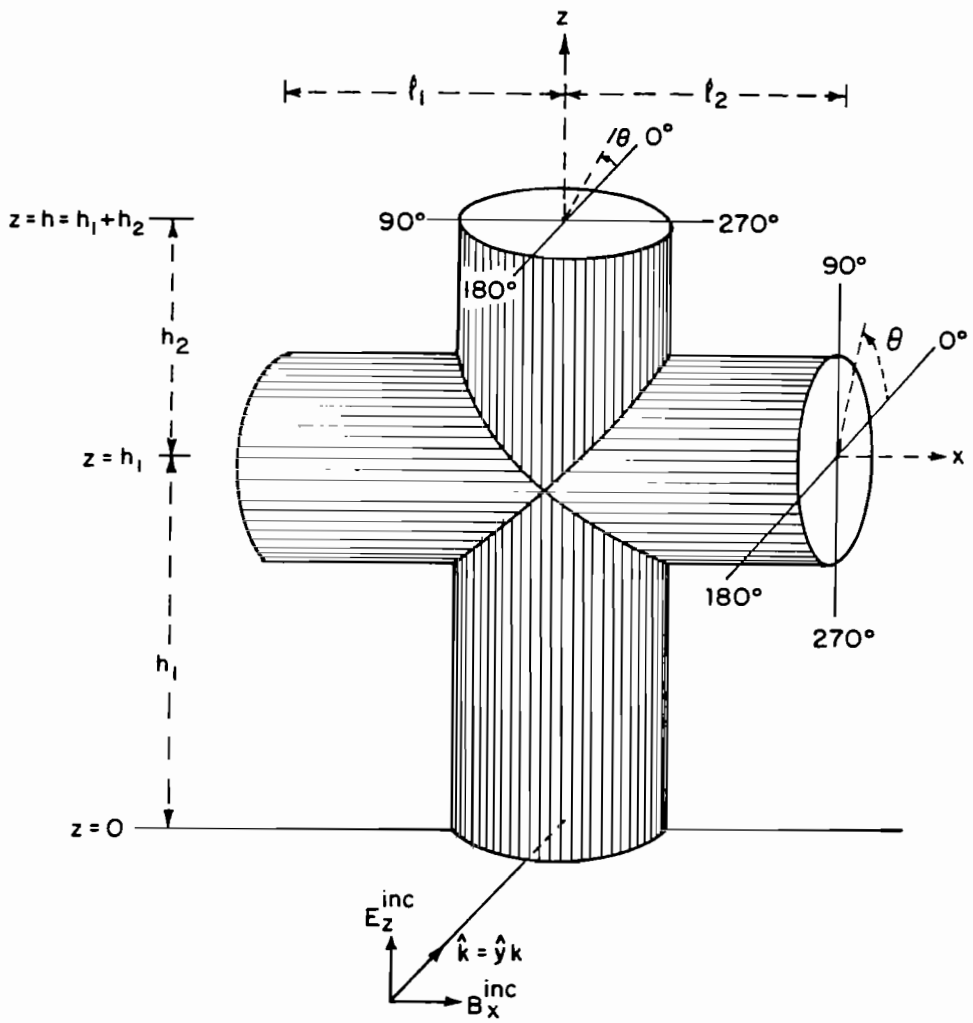

Fig. 88. Diagram of crossed electrically thick cylinders illuminated by a normally incident, plane-wave field. (The origin of the x-axis is at the z-axis.)

series of measurements, the electrical radius of the cylinders was chosen to be ka = 1; subsequent measurements were also made with ka = 2 (see Section VII).

The accuracy and the interpretation of the measurements made to determine the current and charge densities induced on the vertical and horizontal surfaces of the crossed cylinders depend on the comprehensive theoretical and experimental investigations of these quantities on single cylinders when excited by E- and H-polarized fields as described in Sections III - V.

As seen in Fig. 88, the incident field is E-polarized for the vertical cylinder, H-polarized for the horizontal one. The total surface currents on the vertical cylinder when alone in an E-polarized field are given in reference 8 in the form

$$K_z(\theta,z) = \sum_{n=0}^{\infty} C_z(n) K_z(z|n) \cos n\theta \tag{67}$$

$$K_\theta(\theta,z) = i \sum_{n=1}^{\infty} C_z(n) K_\theta(z|n) \sin n\theta \tag{68}$$

The currents on the horizontal cylinder when alone in an H-polarized field are

$$K_x(\theta,x) = i \sum_{n=1}^{\infty} C_\theta(n) K_x(x|n) \sin n\theta \tag{69}$$

$$K_\theta(\theta,x) = \sum_{n=0}^{\infty} C_\theta(n) K_\theta(x|n) \cos n\theta \tag{70}$$

where $K_u(u|n)$ and $K_\theta(u|n)$ are the Fourier coefficients of order n, and $C_z(n)$ and $C_\theta(n)$ are amplitude factors. The associated surface density of charge is

$$\eta(\theta,u) = -\frac{i}{c}\left[\frac{\partial K_u(\theta,u)}{k\ \partial u} + \frac{1}{ka}\frac{\partial K_\theta(\theta,u)}{\partial\theta}\right] \tag{71}$$

where u stands for z or x and $c = 3 \times 10^8$ m/sec. In terms of local cylindrical coordinates for each tube (i.e., ρ,θ,z for the vertical one; ρ,θ,x for the horizontal one, with $\theta = 0°$ the shadow center, $\theta = 180°$ the illuminated center for each tube), the primary induced current densities are $K_z(\theta,z)$ of the even-in-θ type defined in (67) on the vertical tube, $K_\theta(\theta,x)$

of the even-in-θ type in (70) on the horizontal tube. Due to reflections at the ends, transverse currents with the density $K_\theta(\theta,z)$ of the odd-in-θ type in (68) are generated on the vertical tube, and axial currents with the density $K_x(\theta,x)$ of the odd-in-θ type in (69) on the horizontal tube. These last excite additional transverse currents of the odd-in-θ type in (68) [with x written for z] that combine with the primary currents of the even-in-θ type in (70). These distributions generated on each cylinder when isolated are further complicated when the cylinders intersect as shown in Fig. 88 since additional reflections now occur at the junction.

The boundary conditions which determine the distributions of current and charge on the crossed tubular cylinders are: $\vec{E}_{tang} = 0$ at all points on the outside and inside surfaces of the crossed tubes and their images; $K_z(\theta,z) = 0$ at the open ends at $|z| = h_1 + h_2$ and $K_x(\theta,x) = 0$ at the open ends at $x = -\ell_1$ and $x = \ell_2$. Note that $K_z(\theta,z)$ and $K_x(\theta,x)$ are total densities, i.e., the sum of the currents on the outside and inside surfaces.

The complicated geometry of the crossed tubes makes the formulation and solution of coupled integral equations to determine $\vec{K}(\theta,z)$ and $\vec{K}(\theta,x)$ excessively difficult. However, it can be anticipated that at points not too close to the junction section the surface currents are distributed in a manner that can be approximated by a superposition of the leading components in (67) - (70). This requires experimental verification with the probes and techniques tested on the uncrossed cylinders and described in Sections IV and V. The distributions of current and charge density on the surfaces of the cylinders near and at the junction region are difficult to measure since probes cannot be moved over them conveniently. The junction region itself consists of sections of cylinders that meet in junction lines at angles that range from 90° at the top and bottom ($\theta = 90°$ and 270°) to 180° on the back and front ($\theta = 0°$ and 180°). These lines are effectively the bottoms of grooves that wind diagonally around the junction. Although the metal surface is continuous across each junction line, its slope is not except when the angle of intersection is 180° on the front and back. As a consequence, the component of the electric field normal to the surface has different directions as the junction line is approached from each side. It must, therefore, reduce to zero in magnitude if it is to be continuous across the line. This means that the surface density of charge — which is proportional to the normal component of the electric field on a metal

surface — must be zero along the entire junction line. (If the bottom of the groove is rounded instead of sharp, the zero becomes a minimum.) Thus, ideally, in a contour diagram of the charge density the junction line is a zero line. Since the current along the groove must vanish, the vector surface density of current crosses each groove at right angles and has a maximum or minimum there.

The fact that the charge density must be zero along each junction line does not mean that the sign of the charge is opposite on opposite sides or that the overall distribution in a standing-wave pattern determined by the boundaries of the structure as a whole is greatly modified. The charge density has substantially the same magnitude and sign at short distances on each side of a junction line and may rise quite rapidly from zero in directions along the surfaces perpendicular to it. A standing-wave pattern of the charge density (determined by the overall lengths and circumferences of the crossed tubes) can be expected to experience a locally sharp dip across a junction line and a spreading out of the pattern in both directions from it due to the local repulsion of charges with the same sign brought closer together on the sides of the groove than on a plane. But there should be no major change in the general shape of the pattern at a distance from the junction line. The zero occurs along the entire junction line except in small areas at the front and back where two junction lines cross and the angle of intersection of the surfaces of the horizontal and vertical cylinders is 180°. Monopole probes to measure the charge density can be moved axially along the entire lengths of both the horizontal and the vertical cylinders on the back and the front ($\theta = 0°, 180°$). However, since such a probe has a small but finite length, it measures the average charge density over a small area around its base. It is insensitive to sharp dips and nulls in the charge density that occur over distances comparable with its own length (unless the sign of the charge reverses).

In the study of measured current and charge distributions on crossed cylinders with $ka = 1$, the electrical length of the vertical member above the ground plane is kept at $kh = 3.5\pi$. The lengths of the horizontal arms are the same and three different values are used, viz., $k\ell_1 = k\ell_2 = k\ell = \pi$, 1.5π, and 2π. Two locations of the cross arm are investigated. These are $kh_1 = 2.5\pi$ and 2π. With $kh_1 = 2.5\pi$ (2π) the axis of the horizontal member

crosses the vertical cylinder at a maximum (minimum) of charge in the isolated condition.

2. DISTRIBUTIONS OF CHARGE DENSITY

It is advantageous to begin the investigation with the charge densities $\eta(\theta,z)$ and $\eta(\theta,x)$ respectively on the vertical and horizontal members because they are scalars with simple boundary conditions, viz., zero at the ground plane and in the grooves of the junction region.

a. Charges on the Vertical Cylinder When the Center of the Cross is at a Charge Maximum.

In Fig. 89 is shown the axial distribution of $|\eta(\theta,z)|$ in the range $0° \leq \theta \leq 180°$ when $kh_1 = 2.5\pi$, $kh_2 = \pi$ and $k\ell = \pi$, 1.5π and 2π. Note that $\eta(-\theta,z) = \eta(\theta,z)$; the angle θ is measured from the shadow center as shown in Fig. 88. The graphs of $|\eta(\theta,z)|$ for $\theta = 0°$ and $180°$ with $k\ell = \pi$ in Fig. 89 are repeated in Fig. 90 which also shows the phase. In the ranges that exclude the vicinity of the junction, viz., $0 \leq kz \leq 2\pi$, $3\pi \leq kz \leq 3.5\pi$, all three sets of curves for $k\ell = \pi$, 1.5π and 2π are substantially alike in the entire shadow region, $-90° < \theta < 90°$. They are also similar to the theoretical and measured curves for the vertical cylinder without the cross as shown in Section V in Figs. 56 and 65. In the range $0 \leq kz \leq 2\pi$ the charge density varies roughly like $|\sin kz|$ with some differences in amplitude and small shifts in the locations of the minima. With $-80° \leq \theta \leq 80°$, $|\eta(\theta,z)|$ is generally greatest for $k\ell = 1.5\pi$, with amplitudes somewhat smaller and roughly comparable in distribution for $k\ell = \pi$ and 2π. The differences are not large, and sharply resonant and antiresonant conditions like those on thin wires do not obtain. In the range $3\pi \leq kz \leq 3.5\pi$ for all θ's except $\theta = 0°$, $|\eta(\theta,z)|$ is generally substantially smaller when $k\ell = \pi$ than when $k\ell = 1.5\pi$ or 2π. It is shown later that $|\eta(\theta,x)|$ is greatest on the horizontal arms when $k\ell = \pi$. In summary, on the shadow side of the vertical cylinder the measured charge-density distributions with all three arm lengths are very much alike and also like both the measured and theoretical distributions in the absence of the horizontal member.

On the illuminated side ($100° \leq \theta \leq 260°$), the corresponding five distributions are dramatically different. Consider specifically the three graphs on the extreme right in Fig. 89 for the cross with $k\ell = \pi$, 1.5π and

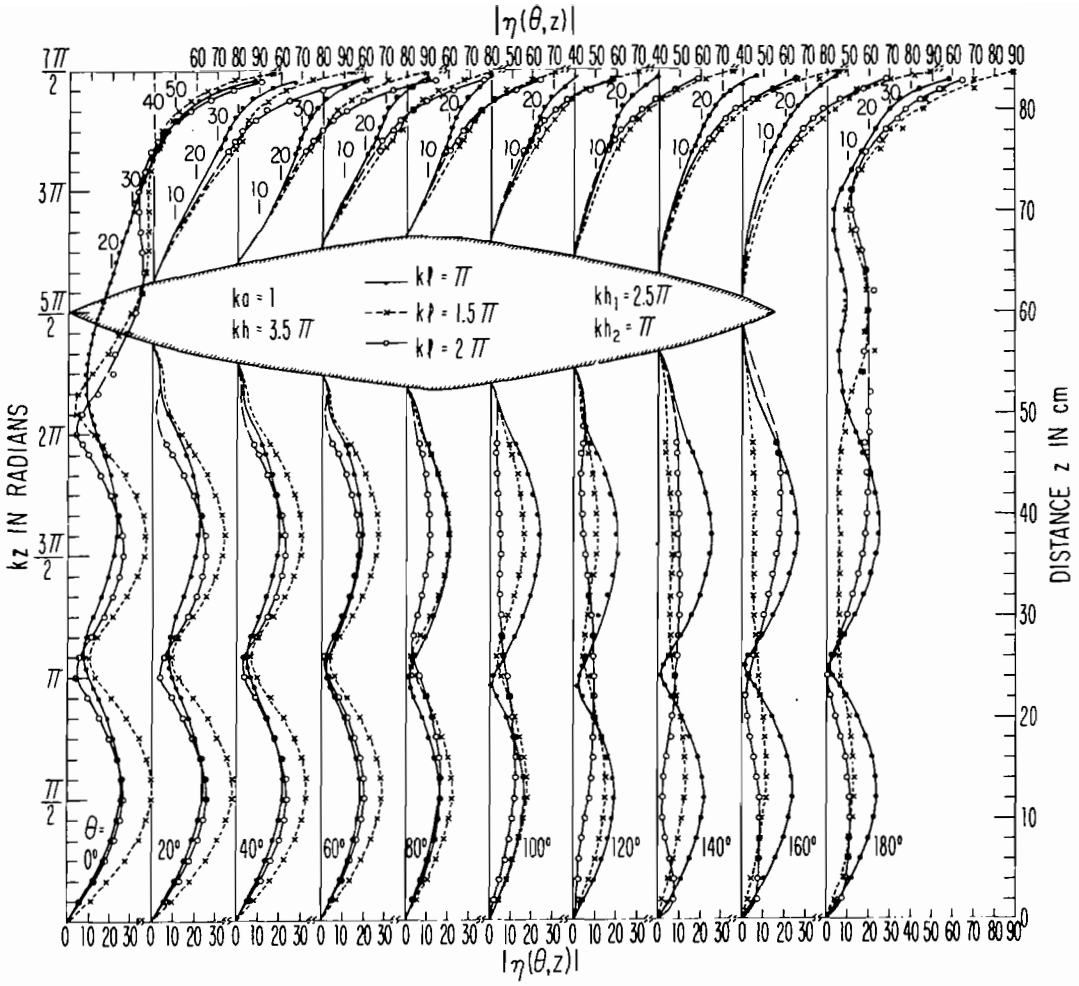

Fig. 89. Measured magnitude of surface density of charge on vertical member of crossed cylinders; E-polarization. ($|\eta|$ in arbitrary units.)

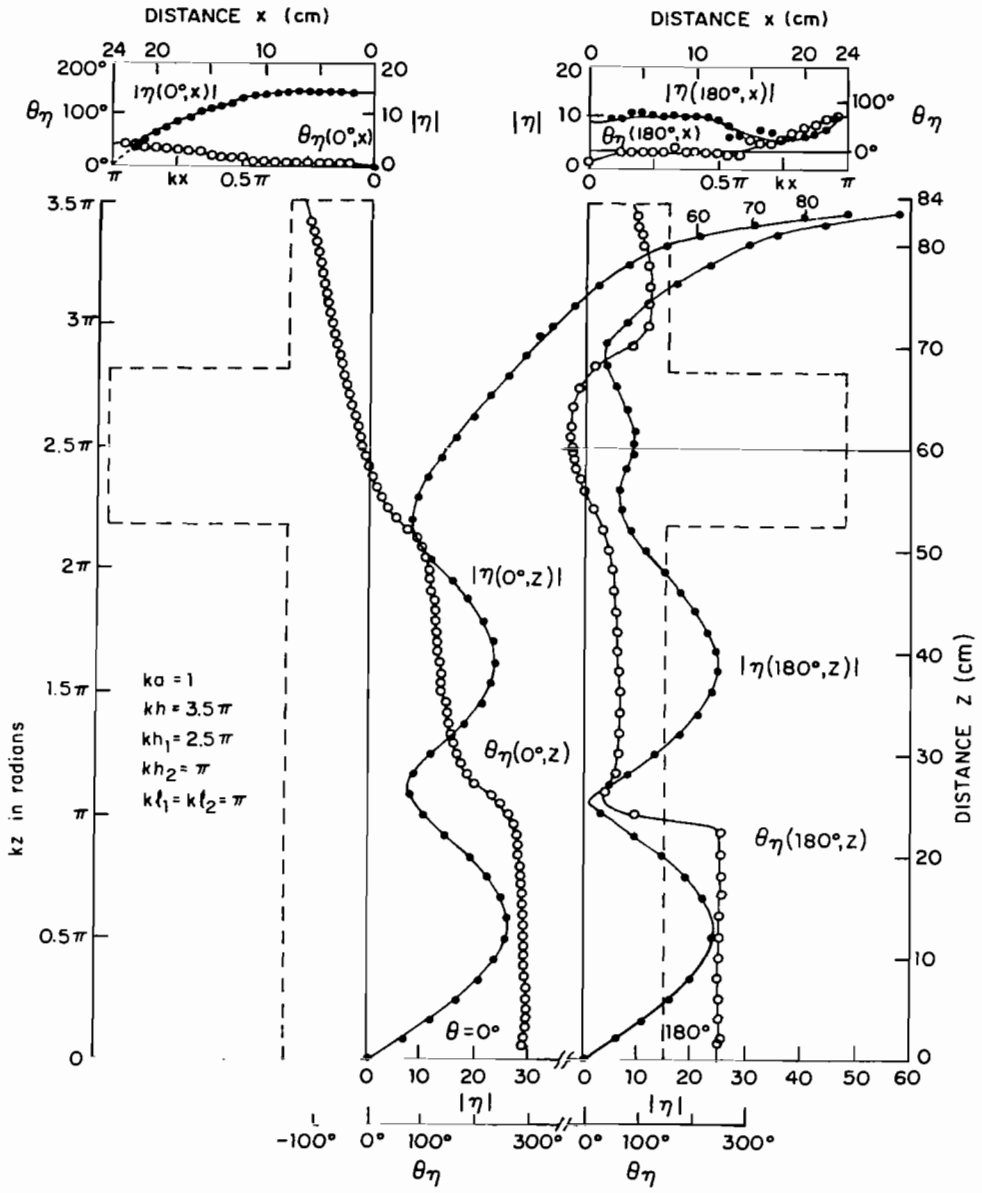

Fig. 90. Measured magnitude and phase of surface densities of charge on crossed cylinders; E-polarization for vertical cylinder; H-polarization for horizontal one. ($|\eta|$ in arbitrary units.)

2π, and the graphs on the left in Figs. 56 and 65 — all for $\theta = 180°$. A comparison shows the following: The curve for the measured charge density for the cross with $k\ell = \pi$ (shown in solid line in Fig. 89) resembles the corresponding theoretical curve for the isolated cylinder (on the left in Fig. 56) quite closely. The maxima at $kz = 0.5\pi$ and 1.5π and the minimum between them are well defined; even the maximum at $kz = 2.5\pi$ at the center of the cross appears but with greatly reduced amplitude. Note, however, that in Fig. 89 the amplitude of $|\eta(180°,z)|$ is almost equal to that of $|\eta(0°,z)|$ when the horizontal member is present and $k\ell = \pi$; when the horizontal member is absent, the theoretical amplitude of $|\eta(180°,z)|$ in Fig. 56 is only about one-third that of $|\eta(0°,z)|$. Thus, with $k\ell = \pi$ the charge-density distribution on the vertical member resembles the theoretical distribution for the isolated cylinder but with a three-fold increase in the relative amplitude on the illuminated side. Significantly, the sharp decrease in the relative amplitude of the maximum at $kz = 1.5\pi$ observed in the measured curve in Fig. 65 does not occur when the horizontal member is present and $k\ell = \pi$.

When $k\ell = 2\pi$, the distribution of charge density at $\theta = 180°$ is significantly different from that with $k\ell = \pi$ in that the two normal maxima at $kz = 1.5\pi$ and 2.5π appear as a single broad maximum with no minimum between them. When $k\ell = 1.5\pi$, the distribution at $\theta = 180°$ has yet another form. It now resembles the measured distribution shown in Fig. 65 for the cylinder without cross rather than the theoretical one in Fig. 56. The maxima at $kz = 0.5\pi$ and 2.5π are quite normal, but the expected maximum at $kz = 1.5\pi$ does not appear — presumably owing to the spherical instead of planar wave front of the incident field. The amplitude of $|\eta(180°,z)|$ is substantially smaller than that of $|\eta(0°,z)|$, which is also in agreement with the corresponding graph in Fig. 65.

The significant differences in the charge-density distributions on the illuminated side of the vertical member of the cross with $kh_1 = 2.5\pi$ as a consequence of changes only in the length of the horizontal member must be explained in terms of modifications in the field acting along its surface. Instead of only the incident field, there is now also the field generated on it by the charges on the adjacent horizontal member. These are determined by the H-polarized field acting uniformly along the entire length 2ℓ and by the mutual interaction with charges on the vertical member, especially

near the junction; they are also governed by transverse and axial resonances in the horizontal cylinder and by combined resonances with the vertical member. Note, however, that resonances on electrically thick structures are not as sharply defined as those on electrically thin crossed wires (refs. 2 and 3).

The comparison of the three sets of graphs for $k\ell = \pi$, 1.5π and 2π in Fig. 89 for $100° \leq \theta \leq 180°$ with the theoretical graphs for ideal plane-wave incidence in Fig. 56 and with the measured graphs for spherical-wave incidence in Fig. 65 — both for $k\ell = 0$ — leads to the following conclusions:

(1) The electrical half-length $k\ell = \pi$ for the horizontal member provides conditions that greatly augment the axially resonant part of the charge density so that this has the normal standing-wave distribution with greatly increased relative magnitude.

(2) The electrical half-length $k\ell = 1.5\pi$ for the horizontal cylinder provides conditions that have only a very small effect on the charges on the vertical member so that they are distributed substantially as when excited only by the incident spherical wave.

(3) When $k\ell = 2\pi$, conditions exist along the vertical cylinder that differ from both a dominant resonant distribution of charge density and from the largely unperturbed distribution generated by the incident field alone.

b. Charges on the Horizontal Cylinder When Centered at a Charge Maximum Along the Vertical Member of the Cross.

The reasons for the quite different effects on the charge-density distributions on the vertical member when the length of the horizontal cylinder is changed can be found in major part in the magnitudes and distributions of charge on the surfaces of the horizontal arms. Measured distributions of $|n(\theta,x)|$ on these when their axis intersects the axis of the vertical cylinder at $kh_1 = 2.5\pi$ are shown in Fig. 91 for the three electrical half-lengths $k\ell = \pi$, 1.5π and 2π. As illustrated in Fig. 88, the center of the shadow of the horizontal cylinder is at $\theta = 0°$, the center of the illuminated front at $\theta = 180°$ and the top and bottom shadow boundaries respectively at $\theta = 90°$ and $\theta = 270°$. Graphs are shown at intervals in θ of 20° for $k\ell = 1.5\pi$ and 2π, at intervals of 60° for $k\ell = \pi$. All of the measured

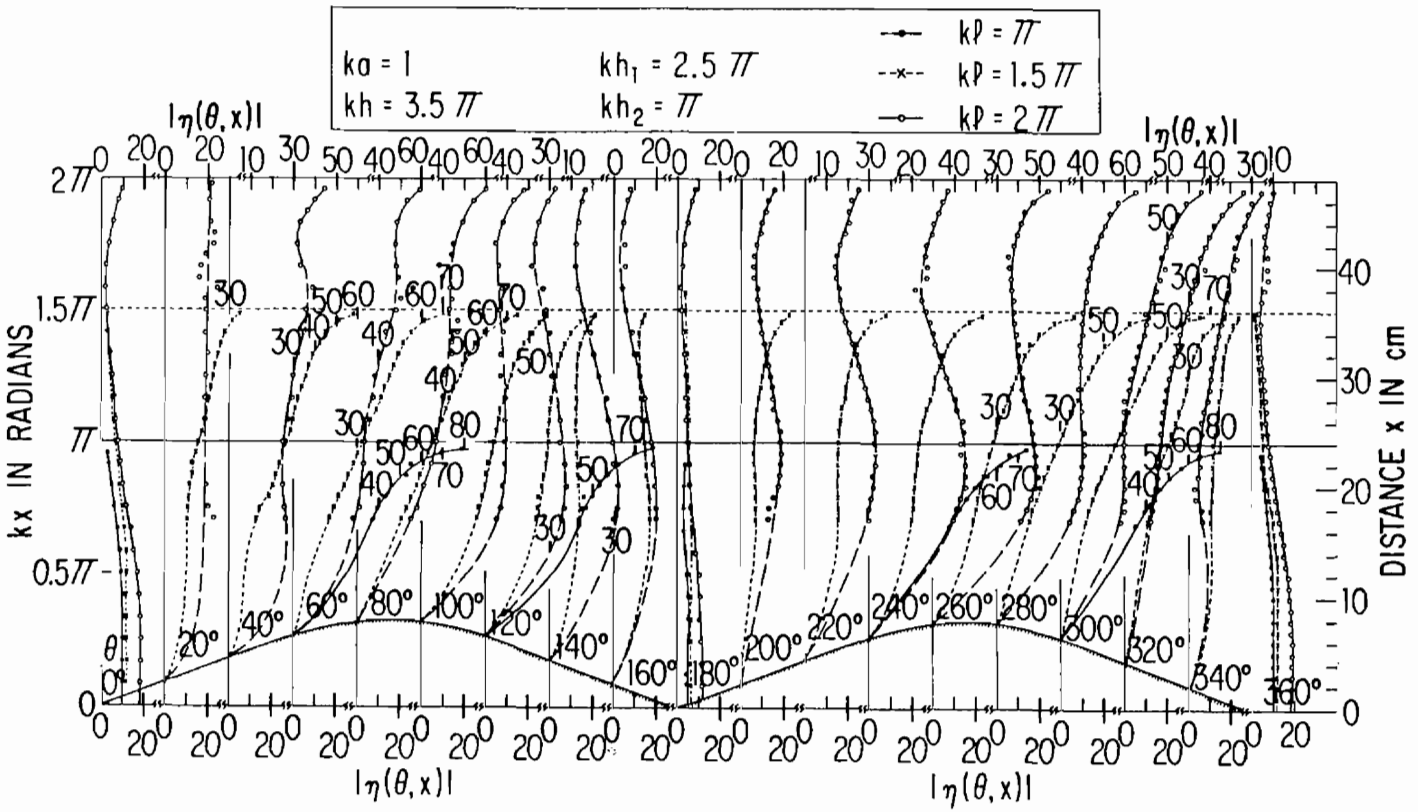

Fig. 91. Measured magnitude of surface density of charge on horizontal member of crossed cylinders for three different lengths, $k\ell = \pi$, 1.5π and 2π; H-polarization. ($|\eta|$ in arbitrary units.)

curves are shown extrapolated smoothly to zero at the junction lines of the horizontal and vertical cylinders. Not too close to the junction they resemble the corresponding theoretical graphs in Figs. 84 and 85 for the horizontal cylinder when isolated in an incident, H-polarized field. Figures 84 and 85 show axial and transverse standing-wave distributions with maxima near $kx = 0, \pi$; $\theta = 90°, 270°$; and minima near $kx = 0.5\pi, 1.5\pi$ when this is not at an open end. As the open end is approached, the charge density rises steeply to large values; but here, as at all other values of kx, the transverse distribution is preserved, with maximum magnitudes along the top and bottom ($\theta = 90°, 270°$) of the cylinder and deep minima on the shadowed back ($\theta = 0°$) and illuminated front ($\theta = 180°$). Relief maps of the charge density on horizontal and vertical half-cylinders, when isolated and when joined to form a cross, are shown in Fig. 92 as viewed from the illuminated side and in Fig. 93 as seen from the shadowed side with $k\ell = 2\pi$.

Of particular interest is an explanation of the differences in the charge distributions along the vertical member in their dependence on the length ℓ of the horizontal arms:

(1) It is seen in Fig. 91 that when $k\ell = \pi$, the magnitude of the charge density near the two open ends $x = \pm\ell$ is very large. The charge on the top is positive when that on the bottom is negative. The average difference between their respective distances to a point on the illuminated side of the vertical cylinder is only slightly less than a half wavelength so that their effects arrive practically in phase. This means that especially strong electric fields are maintained along the front ($\theta = 180°$) and back ($\theta = 0°$) of the vertical cylinder, and these fields evidently excite the large resonant distributions of charge actually observed. Since the fields are substantially greater nearer the cross, it is reasonable that the maximum near $kz = 1.5\pi$, $\theta = 180°$ should be slightly larger than the maximum at $kz = 0.5\pi$, $\theta = 180°$, instead of much smaller as in Fig. 65 for the vertical cylinder without the cross.

(2) When $k\ell = 1.5\pi$, the charge density on the horizontal member is seen from Fig. 91 to be substantially smaller in the entire region from the junction with the vertical cylinder to the open end at $kx = 1.5\pi$ than when $k\ell = \pi$. The largest charge density near $kx = 1.5\pi$ is also much further from points on the vertical cylinder so that a substantial cancellation of

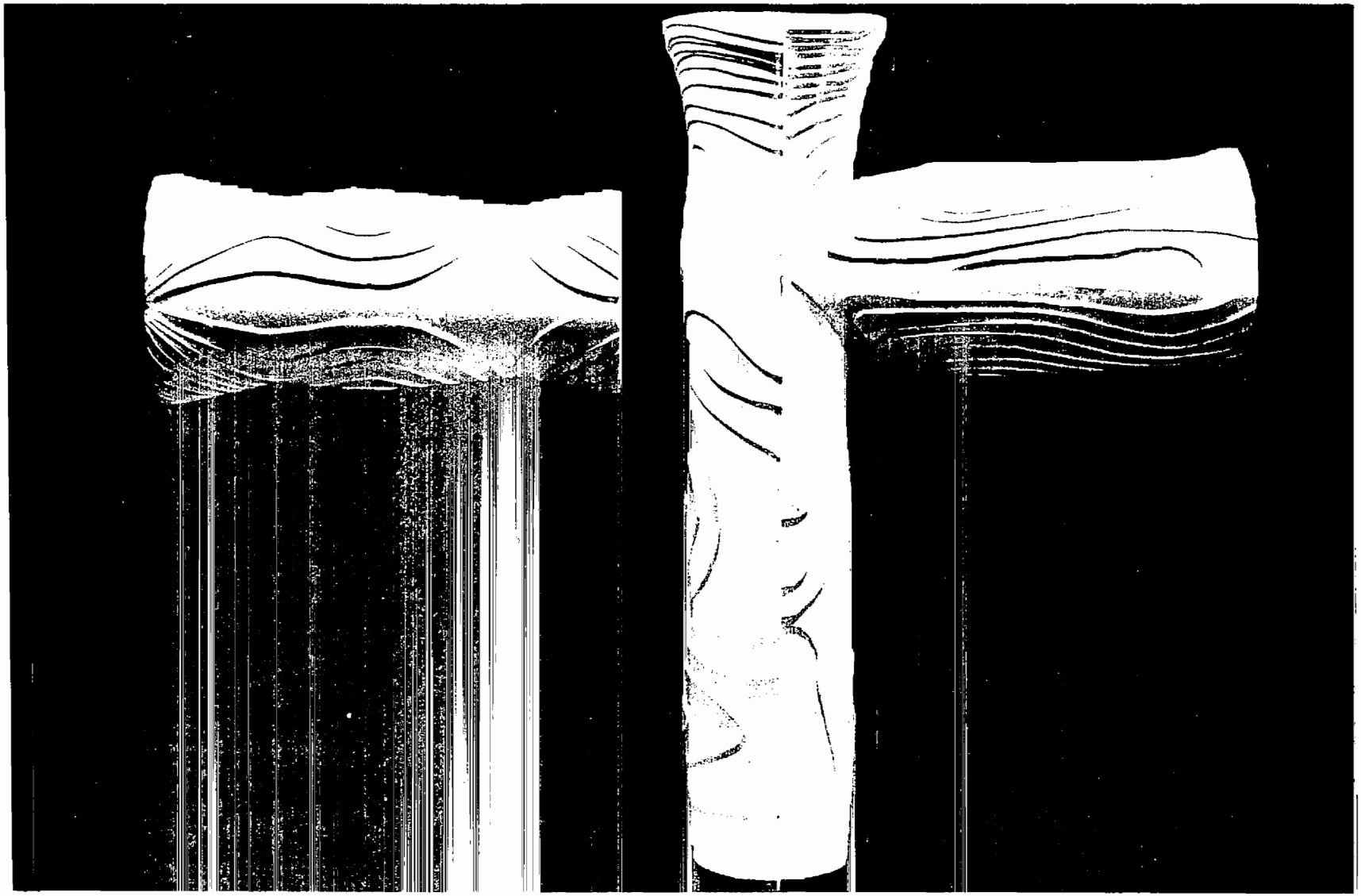

Fig. 92. Relief map of the magnitude of the charge densities $\eta(\theta,z)$ and $\eta(\theta,x)$ on isolated and crossed cylinders with $kh = 3.5\pi$, $kh_1 = 2.5\pi$, $k\ell = 2\pi$, $ka = 1$. View of illuminated side.

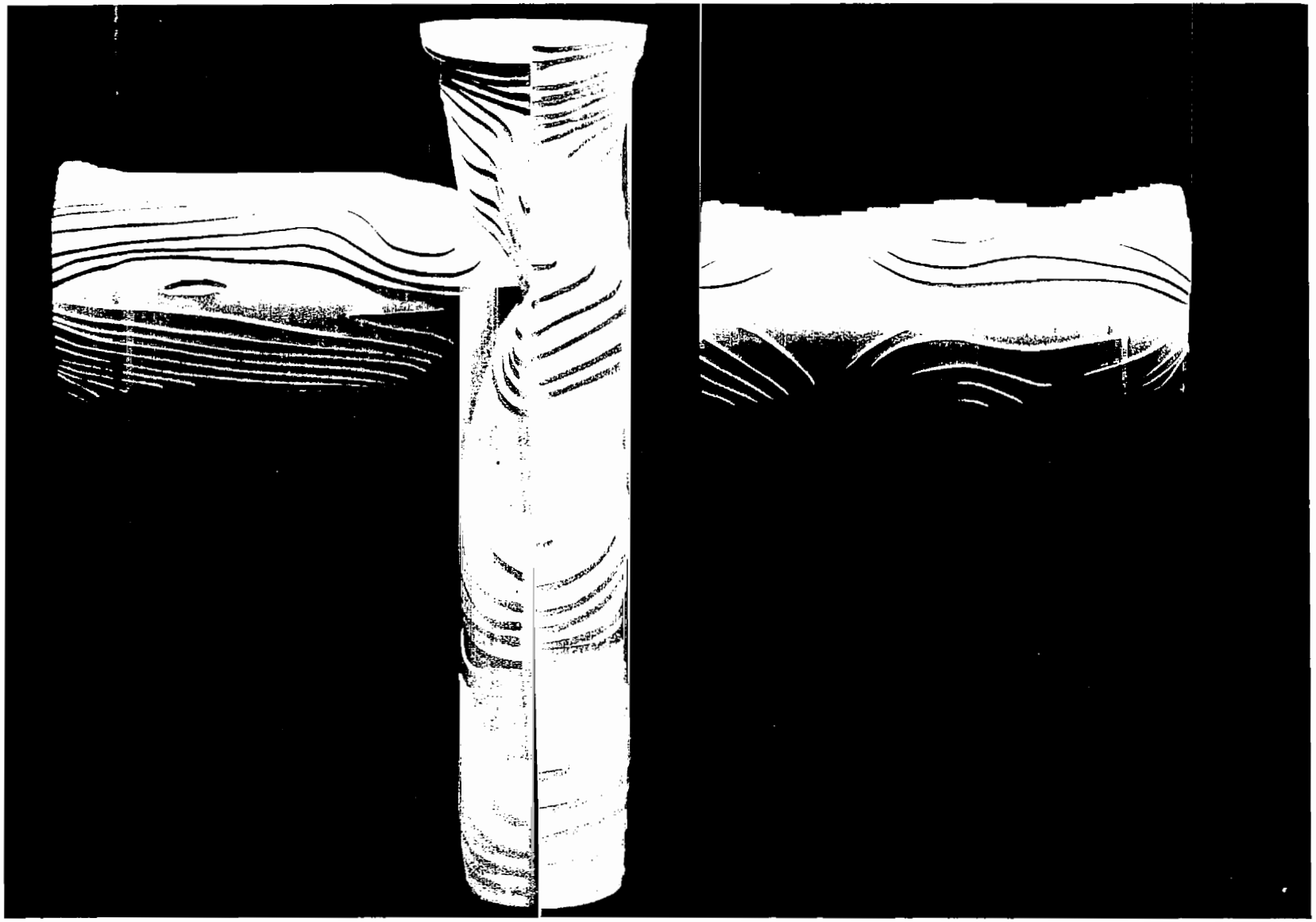

Fig. 93. Like Fig. 92 but viewed from shadowed side.

the fields, due to the maximum charges of opposite sign on the top and bottom of the horizontal cylinder, occurs with a further reduction in the field as compared with that when $k\ell = \pi$. The relatively weak field along the vertical cylinder due to the charges on the horizontal member evidently leaves the incident field with its spherical wave front the dominant force and this serves to explain the similarity between the charge density in the illuminated region of the vertical member and the corresponding charge density on the vertical cylinder when alone as shown in Fig. 65.

(3) Figures 91 - 93 show that, when $k\ell = 2\pi$, there are regions with large charge density on the horizontal member near $kx = \pi$, $\theta = 90°$ and 270° and also, but with instantaneously opposite sign, near $kx = 2\pi$, $\theta = 90°$ and 270°. Their different distances to points on the vertical cylinder, and the consequent differences in the amplitudes and especially the phases of the field generated by them and the incident field, produce the complicated distributions of the charge density on the illuminated side as shown in Fig. 89.

c. Charges on the Vertical and Horizontal Members When the Cross is Centered at a Minimum of Charge on the Vertical Cylinder.

The descriptions of the charge-density distributions on the crossed electrically thick cylinders given so far apply specifically to one location of the cross, viz., $kh_1 = 2.5\pi$ along a vertical member with $kh = k(h_1 + h_2) = 3.5\pi$. It is now of interest to lower the horizontal member a quarter wavelength so that $kh_1 = 2\pi$. The measured distributions of $|\eta(\theta,z)|$ on the vertical cylinder are shown in Fig. 94 with $k\ell = 1.5\pi$. The graphs for $\theta = 0°$ and 180° are also plotted in Fig. 95 which shows the phase. The charge density is seen to have a fairly normal distribution with typical maxima near $kz = 0.5\pi$ and 2.5π and minima near $kz = \pi$ and 3π. Actually, these are somewhat displaced toward longer lengths; and in the shadow region, $-80° \leq \theta \leq 80°$, the minimum near $kz = \pi$ is almost completely flattened out, presumably due to the fields generated by the charges on the horizontal member. This does not occur in the illuminated region. A comparison of the measured distributions of $|\eta(0°,z)|$ and $|\eta(180°,z)|$ for $kh_1 = 2\pi$, $kh_2 = k\ell = 1.5\pi$ with those for $kh_1 = 2.5\pi$, $kh_2 = k\ell = \pi$ is shown in Fig. 96, together with the corresponding measured distributions for the vertical cylinder alone. Although the general sinusoidal nature of the amplitude is

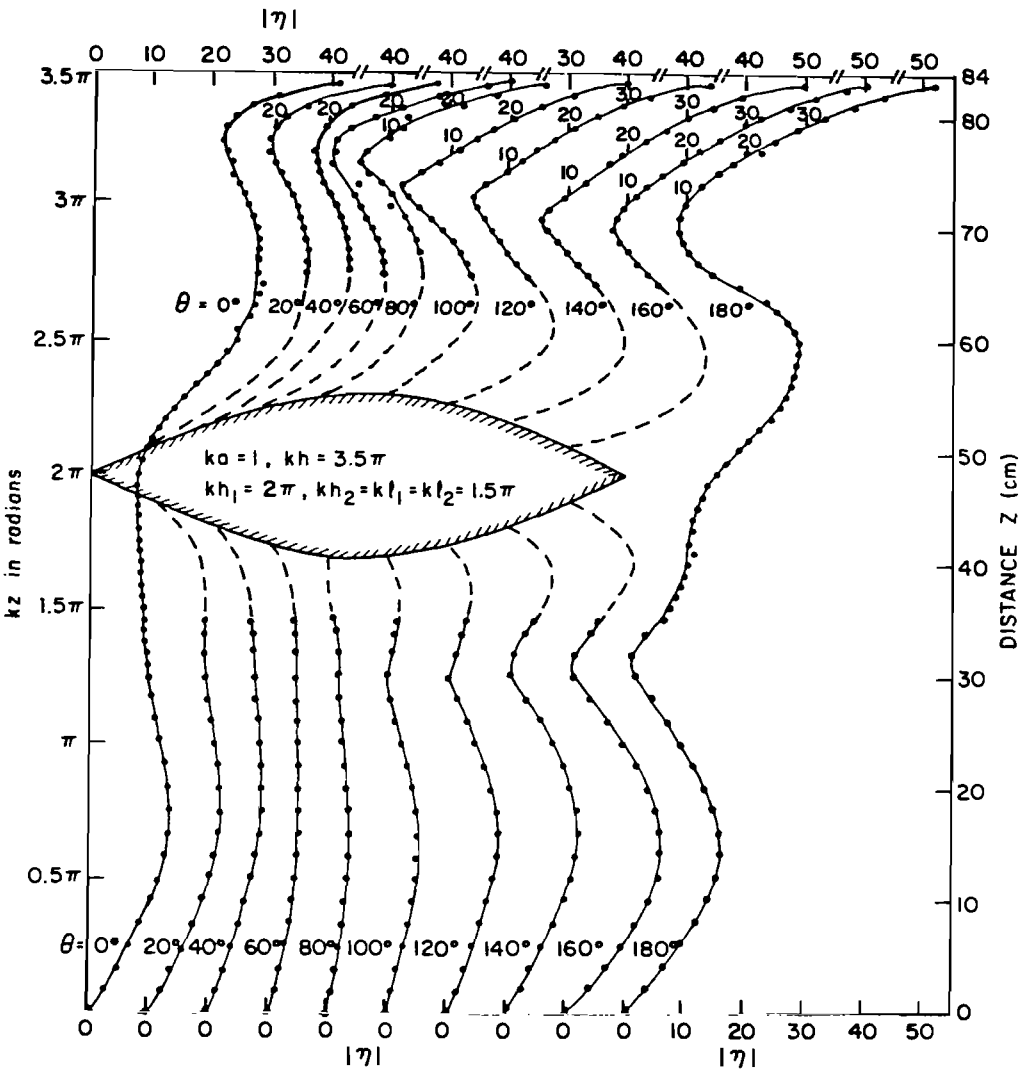

Fig. 94. Measured magnitude of surface density of charge on vertical member of crossed cylinders; E-polarization. ($|\eta|$ in arbitrary units.)

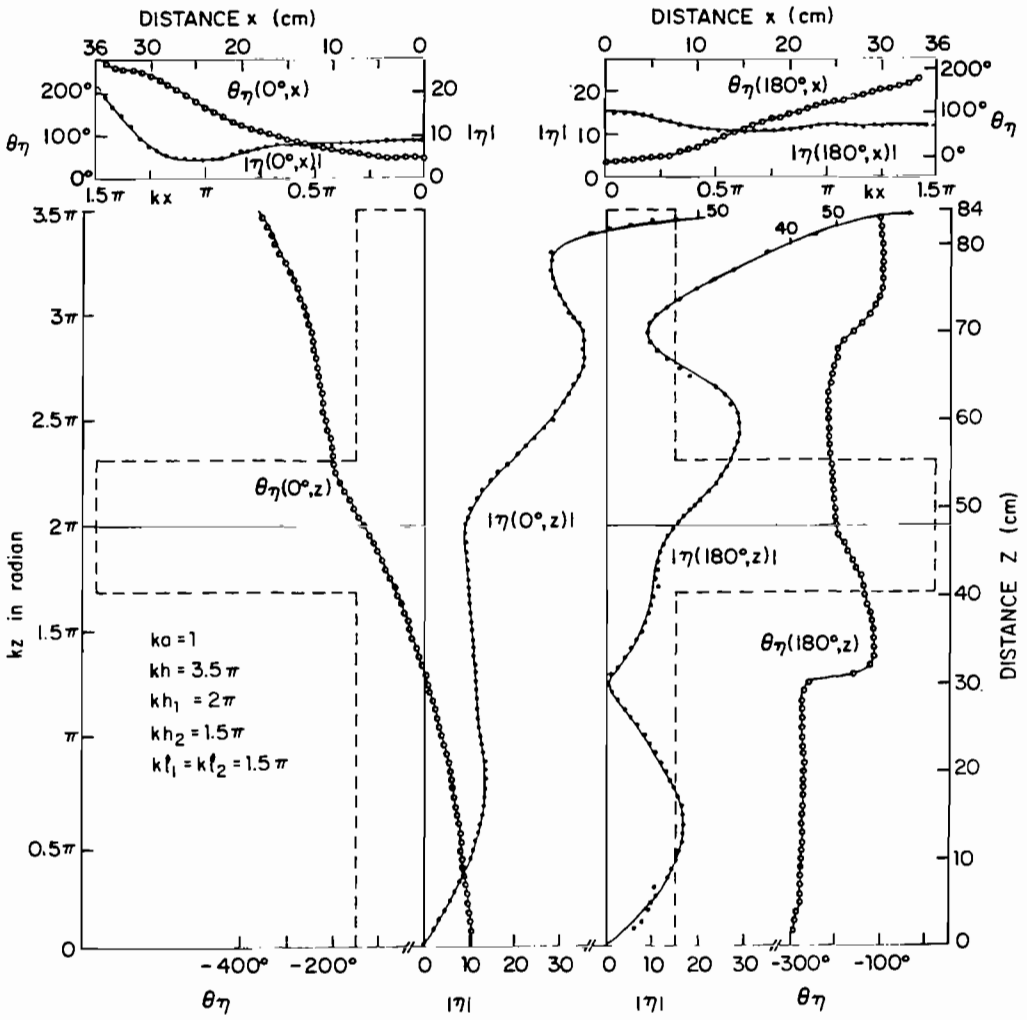

Fig. 95. Measured magnitude and phase of surface densities of charge on crossed cylinders; E-polarization for vertical cylinder, H-polarization for horizontal one. ($|\eta|$ in arbitrary units.)

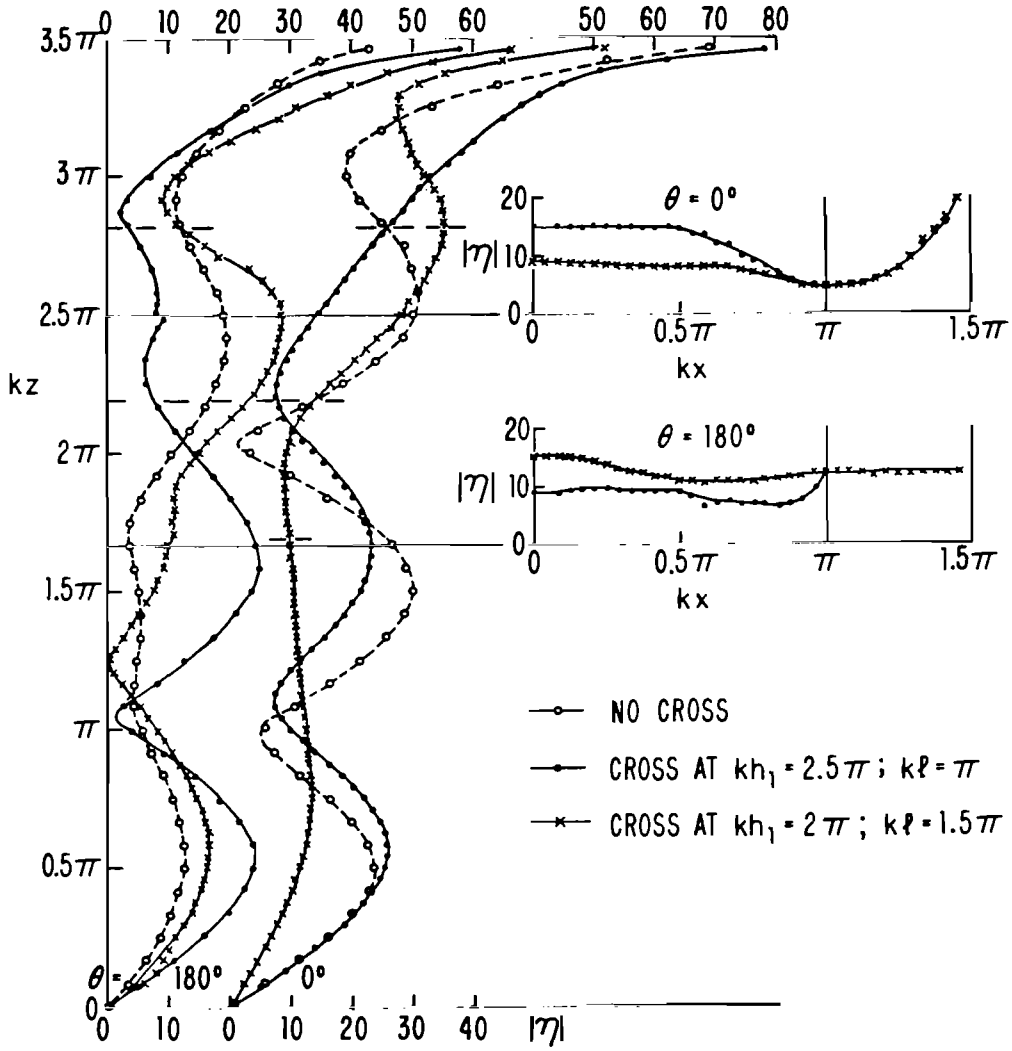

Fig. 96. Measured surface densities of charge on crossed cylinders with kh = 3.5π, ka = 1, for two locations of the junction and with no cross; E-polarization for vertical cylinder, H-polarization for horizontal one. ($|\eta|$ in arbitrary units.)

evident in all graphs, they differ substantially in detail. Since all are exposed to the same spherical approximation of an incident plane wave, these differences must be ascribed to the absence or presence with different relative locations, magnitudes, and phases of the charges on the horizontal arms. Note, however, that the distributions of charge density on the horizontal member are not greatly affected by the location of the junction. This can be seen in Fig. 97 which shows the measured axial distributions of $|\eta(\theta,x)|$ on the horizontal member with $k\ell = 2\pi$ and with the junction located at $kh_1 = 2\pi$ and 2.5π. The distributions are remarkably similar, presumably because they are determined primarily by the incident H-polarized field.

3. DISTRIBUTIONS OF THE SURFACE DENSITY OF CURRENT

The distributions of the axial surface density of current $K_z(\theta,z)$ associated with the charge distributions in Fig. 89 are shown in Fig. 98. Like the charge densities, the axial current densities in the extreme shadow, $-40° \leq \theta \leq 40°$, have distributions that are generally similar to one another and to those for isolated cylinders; they have large resonant components. In the central part of the illuminated region, $140° \leq \theta \leq 220°$, the graphs with $k\ell = \pi$ correspond closely to the ideal theoretical distributions on the cylinder without cross, which are superpositions of simple forced and resonant components. This is in agreement with the related charge-density distribution in Fig. 89, which similarly resembles the theoretical form for the isolated cylinder. The distributions with $k\ell = 1.5\pi$ and 2π, although superficially different, also have this general form. The interchange of maxima and minima in the graph for $k\ell = 2\pi$ as compared with those for $k\ell = \pi$ and 1.5π is only a matter of relative phase in the superposition of resonant and forced components. The behavior of the axial current density $K_z(\theta,z)$ when the horizontal cylinder is lowered to $kh_1 = 2\pi$ is quite similar as shown in Fig. 99. The transverse currents $K_\theta(\theta,z)$ on the vertical cylinder are generally small except within about a quarter wavelength of the open end where they are large and similar to those on the isolated cylinder.

The surface densities of current on the horizontal arms are very similar in both axial and transverse components to those on the same cylinder

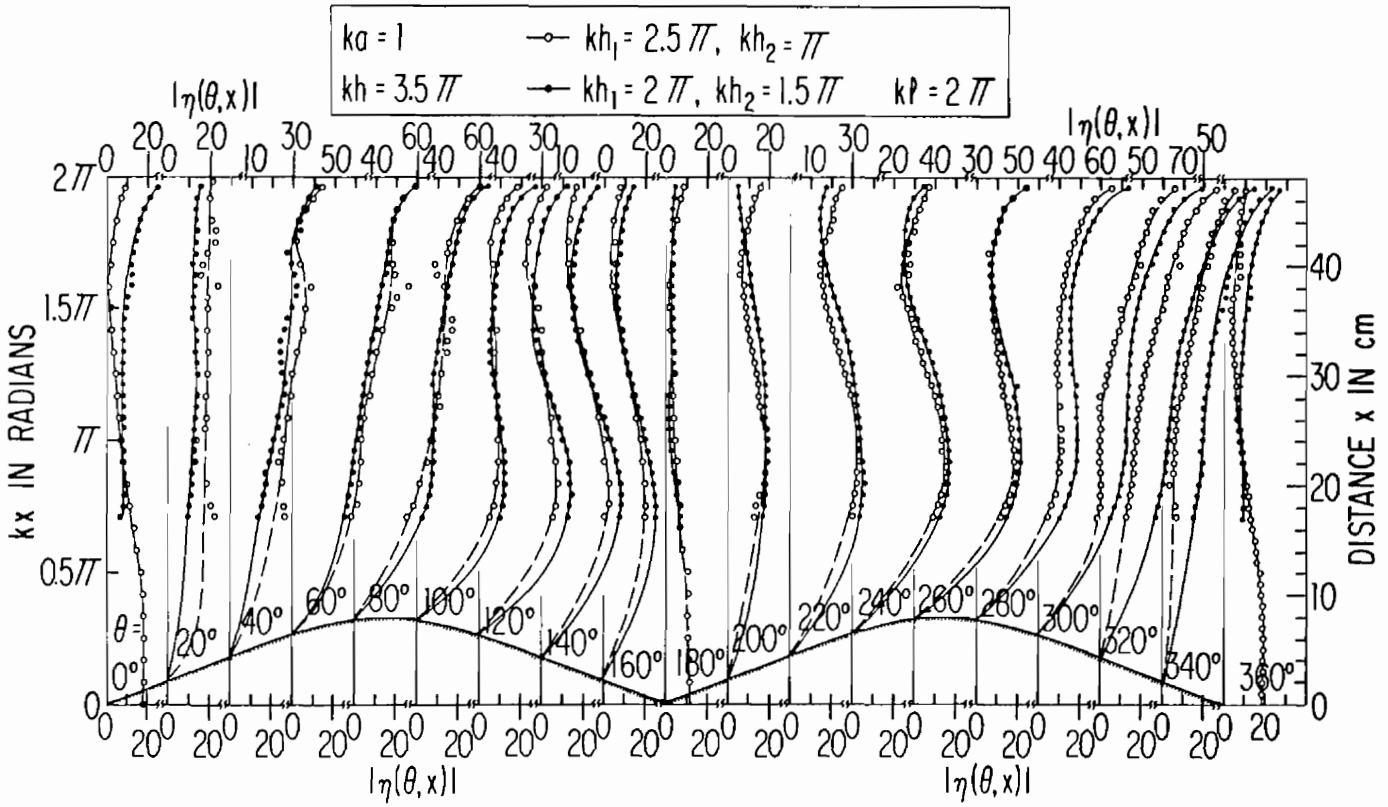

Fig. 97. Measured magnitude of surface density of charge on horizontal member of crossed cylinders for two locations of the junction; H-polarization. ($|\eta|$ in arbitrary units.)

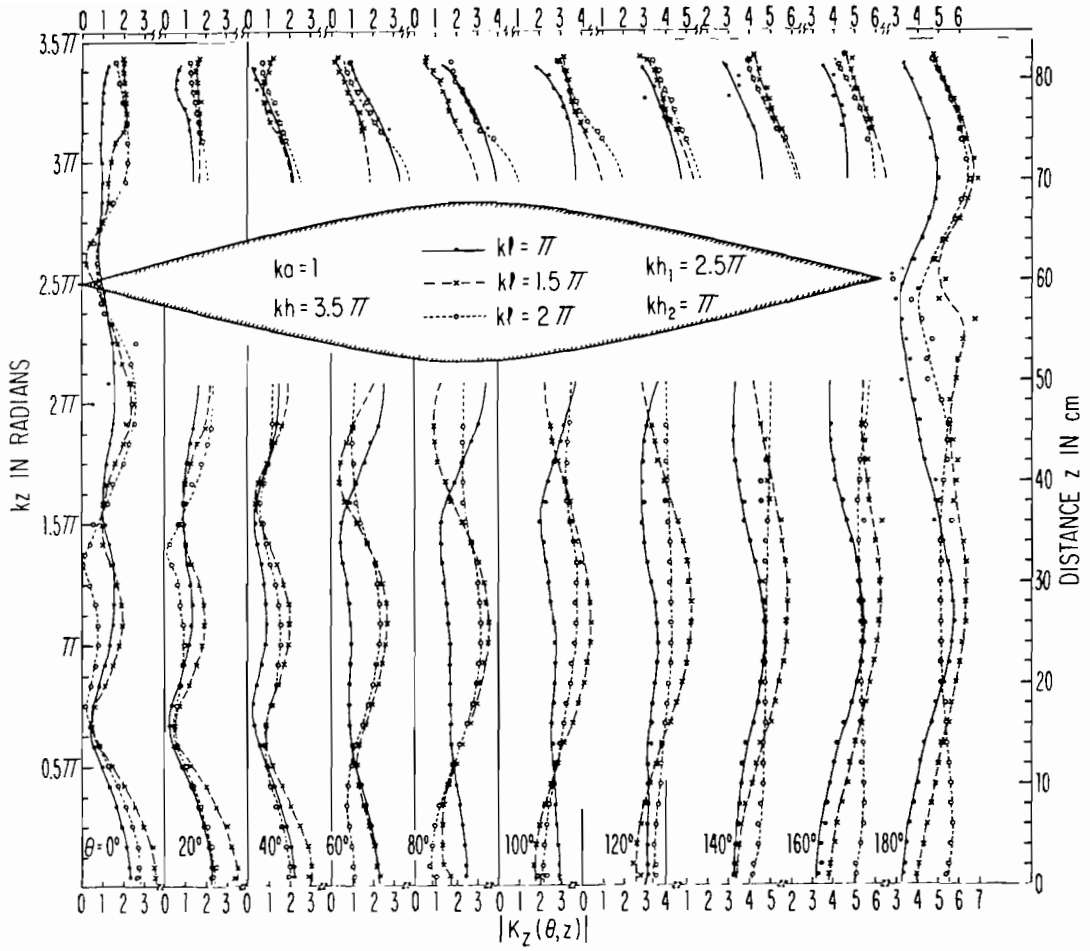

Fig. 98. Measured magnitude of surface density of axial current on vertical member of crossed cylinders; E-polarization. ($|K|$ in arbitrary units.)

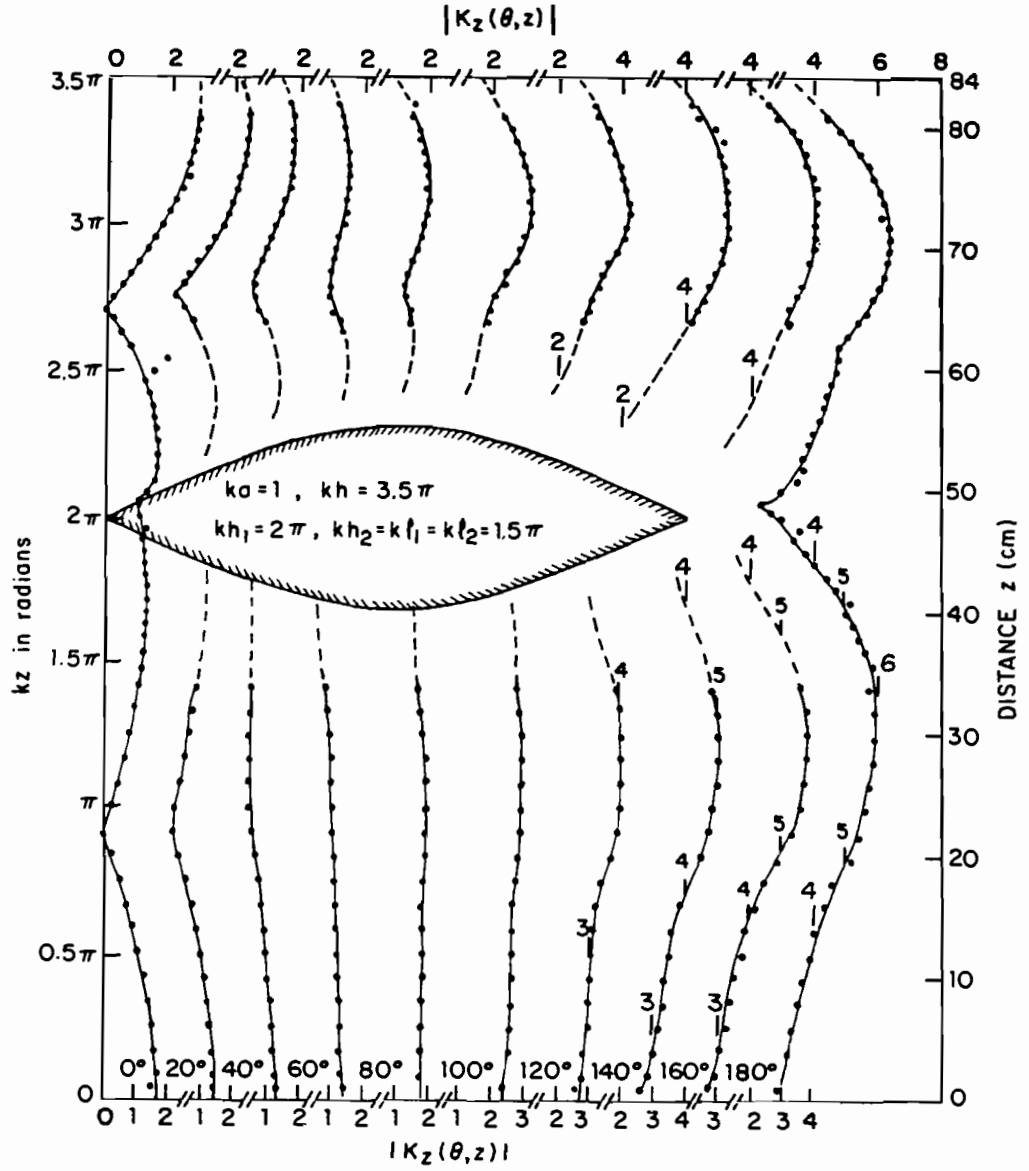

Fig. 99. Measured magnitude of surface density of axial current on vertical member of crossed cylinders; E-polarization. (|K| in arbitrary units.)

in the absence of the vertical member. The theoretical currents on the isolated horizontal cylinder in an H-polarized field are shown in Figs. 100 and 101, respectively, for $k\ell = 2\pi$ and 1.5π. Measured distributions of the surface currents on the horizontal member of a cross with $kh_1 = 2.5\pi$ and $k\ell = \pi$, 1.5π and 2π are shown in Fig. 102 for the axial currents, $K_x(\theta,x)$, and in Fig. 103 for the transverse currents, $K_\theta(\theta,x)$. Similar measured currents with $kh_1 = 2\pi$ and $k\ell = 1.5\pi$ are shown in Fig. 104.

4. CONCLUSION

An experimental study has been made of the distributions of the surface densities of current and charge induced on crossed, electrically thick, tubular cylinders on a large metal ground plane by a normally incident, approximately plane, electromagnetic wave. With $ka = 1$, $kh = 3.5\pi$, measurements have been made for two locations of the cross, viz., $kh_1 = 2.5\pi$ and 2π, with three lengths of the horizontal arms, viz., $k\ell = \pi$, 1.5π and 2π. Comparisons of the measured current and charge densities of the crossed cylinders with both measured and theoretical distributions on single vertical and single horizontal cylinders lead to the following conclusions:

a. The distribution of the charge density on an electrically thick tubular cylinder is much more sensitive to the nature of the incident field and the presence, dimensions and relative location of an intersecting cylinder than is the distribution of current density.

b. The charge density on the vertical member of the cross, which is directly excited by an E-polarized field, has significantly different distributions when the incident field is not plane, when the horizontal member is absent, its location is changed, or when the arm lengths are varied.

c. The distribution of the charge density on the horizontal cylinder is insensitive to the location of its intersection with the vertical member of the cross so long as the arms are equal in length. Its amplitude is sensitive to the length of the arms.

d. The axial current density on the vertical cylinder is substantially a superposition of forced and resonant components. The changes from the distribution along the single cylinder when a cross is present in different locations and with different arm lengths are primarily due to shifts in the relative phases of these components.

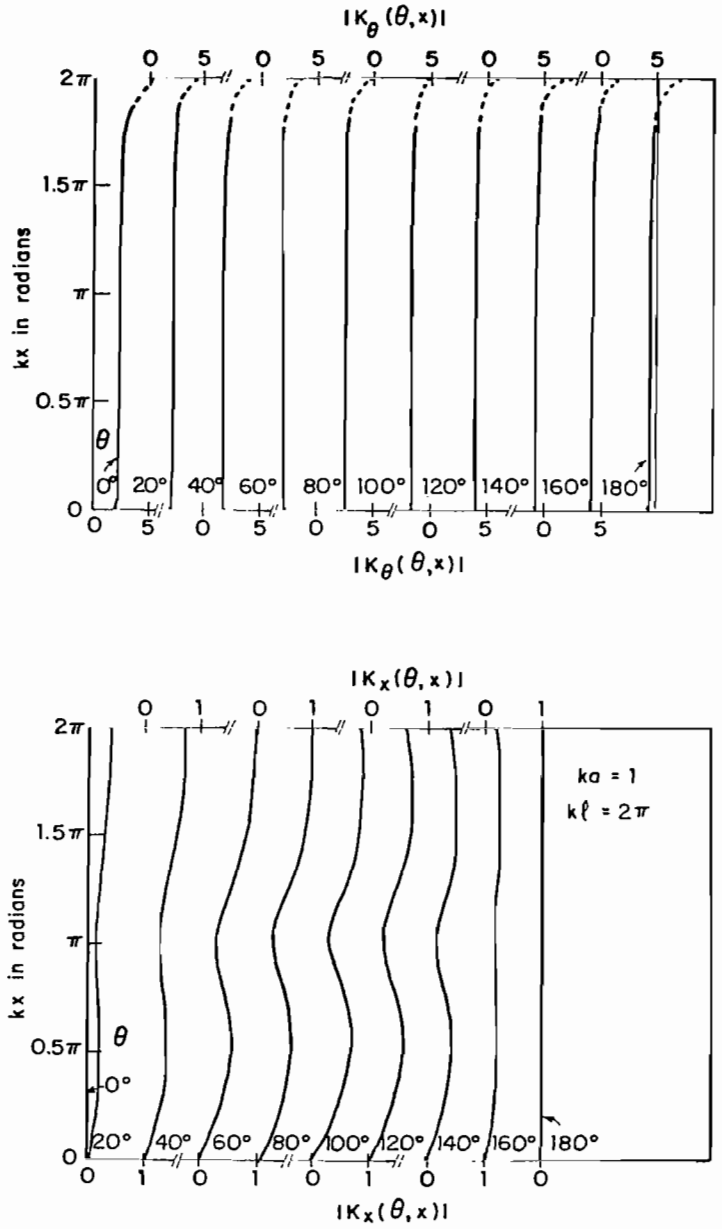

Fig. 100. Theoretical magnitude of surface densities of transverse and longitudinal current on isolated tubular cylinder; H-polarization. ($|K|$ in mA/V.)

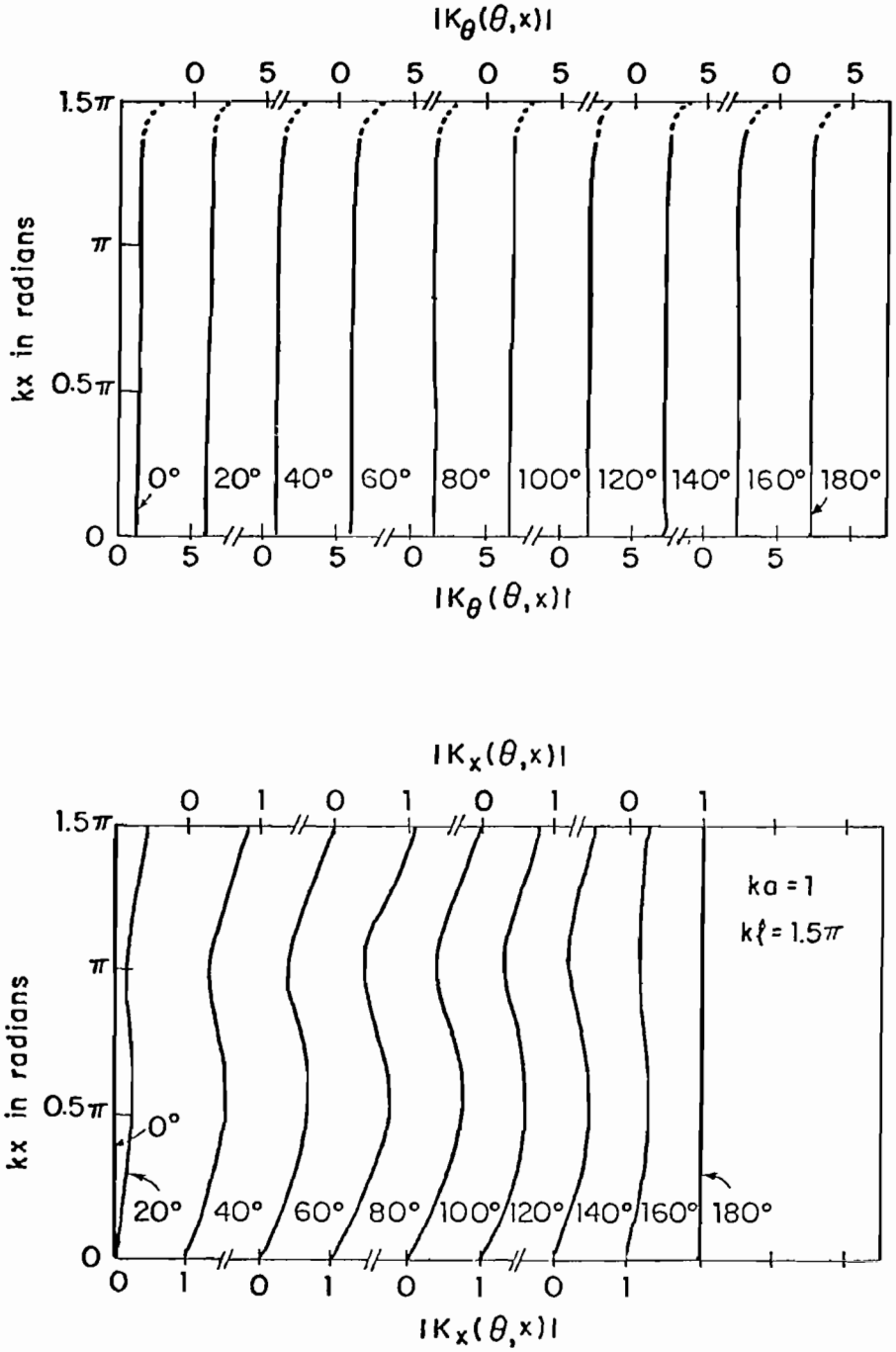

Fig. 101. Theoretical magnitude of surface densities of transverse and longitudinal current on isolated tubular cylinder; H-polarization. ($|K|$ in mA/V.)

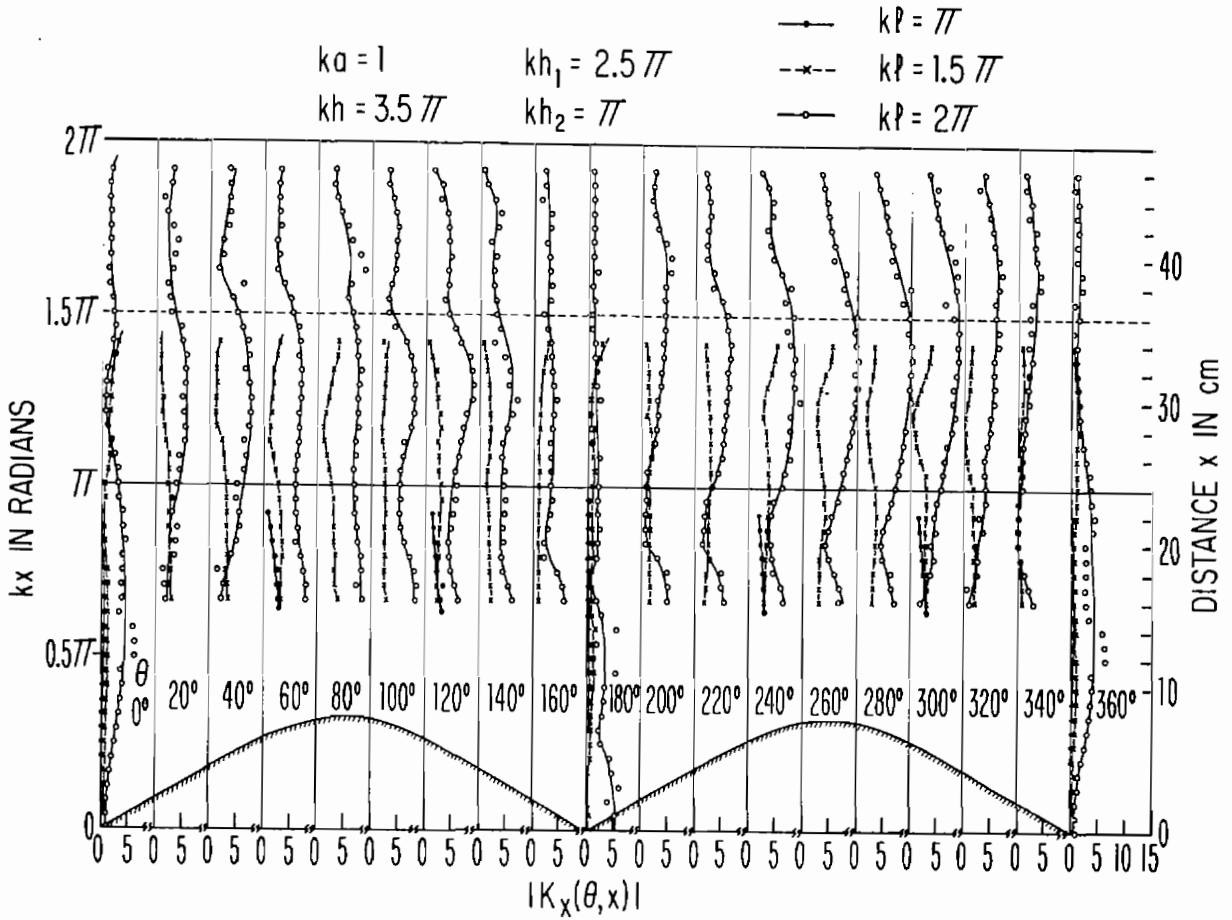

Fig. 102. Measured magnitude of surface density of axial current on horizontal member of crossed cylinders; H-polarization. ($|K|$ in arbitrary units.)

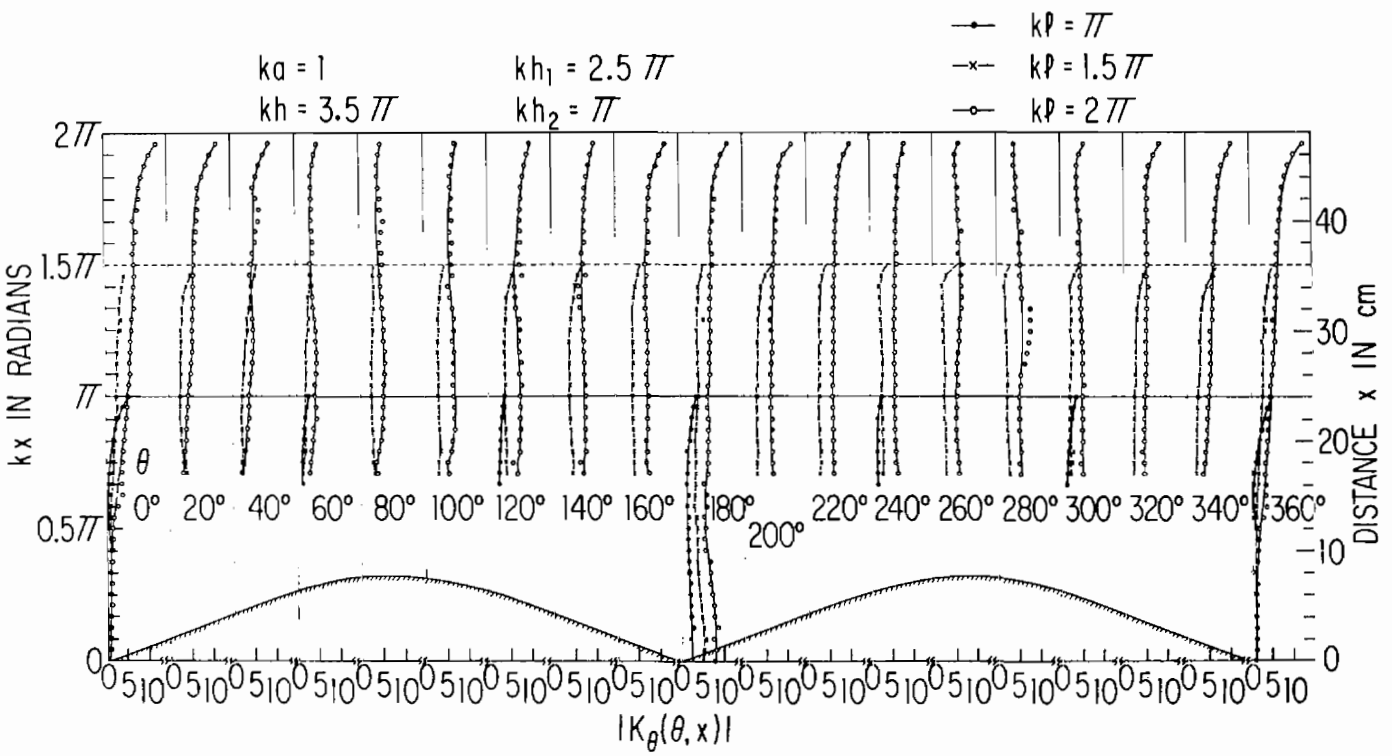

Fig. 103. Measured magnitude of surface density of transverse current on horizontal member of crossed cylinders; H-polarization. ($|K|$ in arbitrary units.)

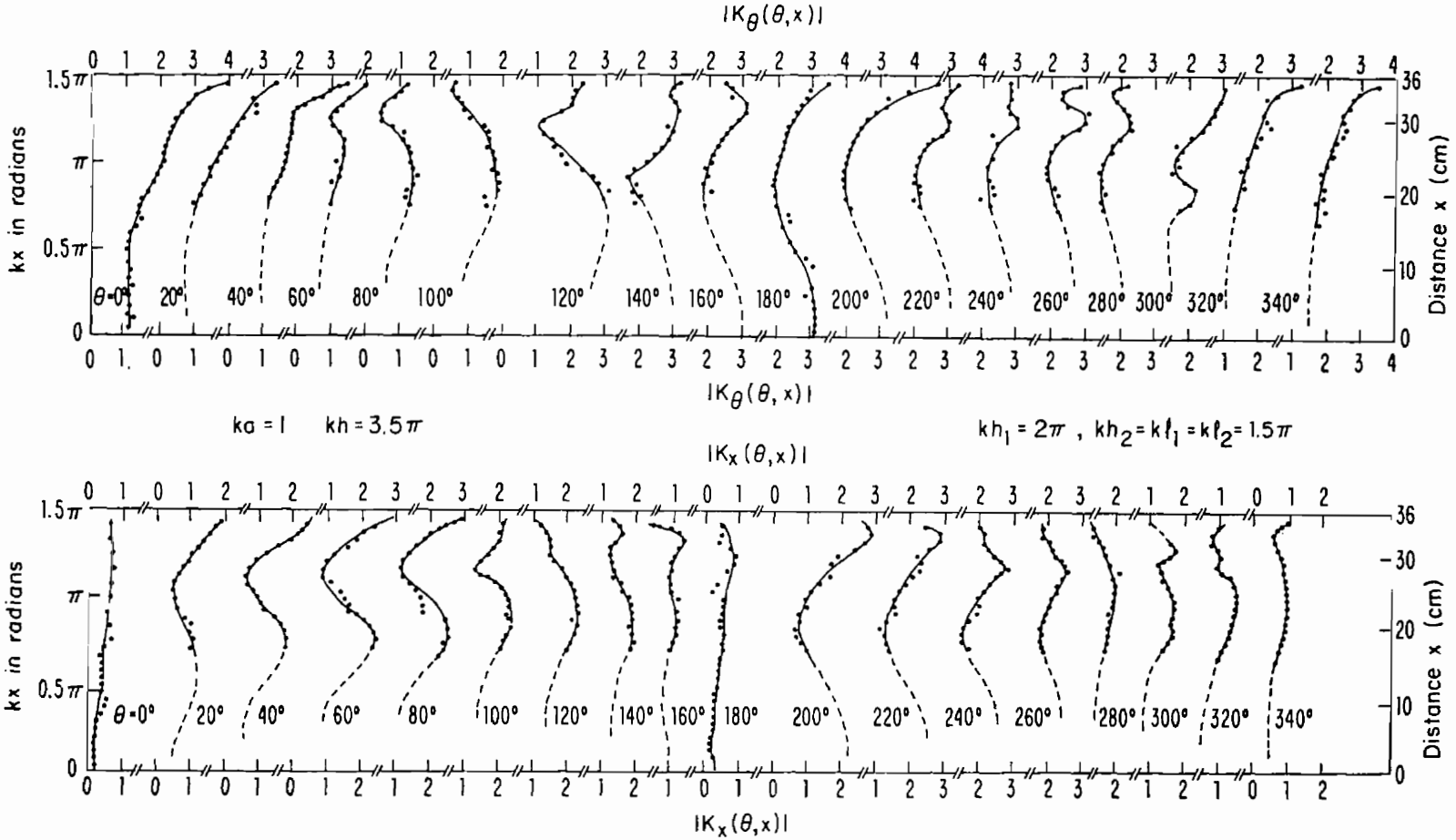

Fig. 104. Measured magnitude of surface densities of transverse and longitudinal current on horizontal member of crossed cylinders; H-polarization. ($|K|$ in arbitrary units.)

SECTION VII

ELECTRICALLY THICK CYLINDERS AND CROSSED CYLINDERS IN A NORMALLY INCIDENT, PLANE-WAVE FIELD, THEORY AND MEASUREMENTS, ka = 2;

Single Cylinder: kh = 3.5π, 5π and ∞ (Theory); kh = 3.5π (Measured)

Crossed Cylinders: kh = 3.5π, $kh_1 = 2.5\pi$, $kh_2 = k\ell_1 = k\ell_2 = 2\pi$ (Measured)

1. INTRODUCTION

The study of surface currents and charges induced on aircraft by possible electromagnetic pulses generated by nuclear explosions involves a frequency range for which the cross-sectional dimensions of the wings and fuselage may be several wavelengths. Quantitative insight into the distributions of current and charge possible on structures of this size is sought from an investigation of currents and charges induced on electrically very thick cylinders and crossed cylinders.

The theoretical determination of the currents and charges induced by an incident plane wave on the surface of a highly conducting tubular cylinder when its circumference is two wavelengths (ka = 2) is formally the same as when the circumference is one wavelength (ka = 1). Extensive theoretical studies for the latter for electrical half-lengths ranging from kh = 1.5π to 3.5π have been shown to be in good agreement with measured values (Sections III, IV and V) except for certain differences in the charge density on the illuminated side. These were ascribed to the spherical instead of planar wave front available in the experiment. This general agreement was obtained for the currents and charges on the outside surface of the cylinder. However, since with ka = 1 all interior waveguide modes are far below the cut-off radius, the inside currents and charges decay rapidly to negligible values within the tube. It follows that with ka = 1 the total currents and charges differ insignificantly from the outside ones except close to the open end.

The situation with ka = 2 is different because the radius is now greater than the cut-off value for propagating waveguide modes in the interior. Specifically, the cut-off radius a_c for the TE_{11} mode is

$$a_c = \lambda/3.41 \quad \text{or} \quad ka_c = 1.84 \tag{72}$$

Since a propagating TE_{11} mode can be maintained for radii $a > a_c$, $ka = 2$ is well above cut-off. On the other hand, the TM_{01} mode is below the cut-off given by $a_c = \lambda/2.61$ or $ka_c = 2.4$. This means that substantial inside currents and charges in the TE_{11} mode can be generated at the open end and propagated into the interior when $ka = 2$. These have an axial wave number $k_g = k[1 - (\lambda/\lambda_c)^2]^{1/2}$ where λ is the free-space wavelength and $\lambda_c = 3.41a$. With $ka = 2$, $\lambda_c = 3.41 \times 2/k = 1.085\lambda$ and $k_g = 0.39k$. Thus, while the wave number for the outside current and charge is k, that for the current and charge inside the waveguide is $k_g = 0.39k$ — a much smaller value.

Theoretical distributions of the magnitude of the surface density of charge $|\eta(\theta,z)|$ on the outside surface of a perfectly conducting tubular cylinder with $ka = 2$ and $kh = 5\pi$ are shown in Fig. 105 for E-polarization. The associated distributions on the inside surface are shown in Fig. 106. These latter are excited by coupling to the outside charges at the open end. Since the surface density of charge of the TE_{11} waveguide mode is similar in its transverse distributions to the charge on the outside of the tube in that both have significant values near $\theta = 90°$ and $270°$, the coupling between the two modes is quite strong. Accordingly, the standing waves of the inside charges have amplitudes comparable to those of the outside charges.

In the study of currents and charges induced on the outside surface of a tubular cylinder, the simultaneous excitation of significant currents and charges on the inside surface is an undesired complication. Although the charge distributions on the outside surface appear to have axial distributions quite like the comparable ones on the thinner cylinder with $ka = 1$, the associated axial outside currents in Fig. 107 suggest significant differences. Note, in particular, the unexpectedly large amplitude in the shadow region, specifically where $\theta = 0°$. This current rises to an especially large value near the open end where its amplitude even exceeds that on the illuminated side at $\theta = 180°$. Presumably this is a consequence of the close coupling at the open end to the inside charges in the TE_{11} propagating waveguide mode.

2. THEORETICAL CHARGES AND CURRENTS WITH E-POLARIZATION

In order to provide a useful comparison among currents and charges induced on the extensively studied cylinder with $ka = 1$ and those of present interest with $ka = 2$, theoretical calculations have been made for a cylinder

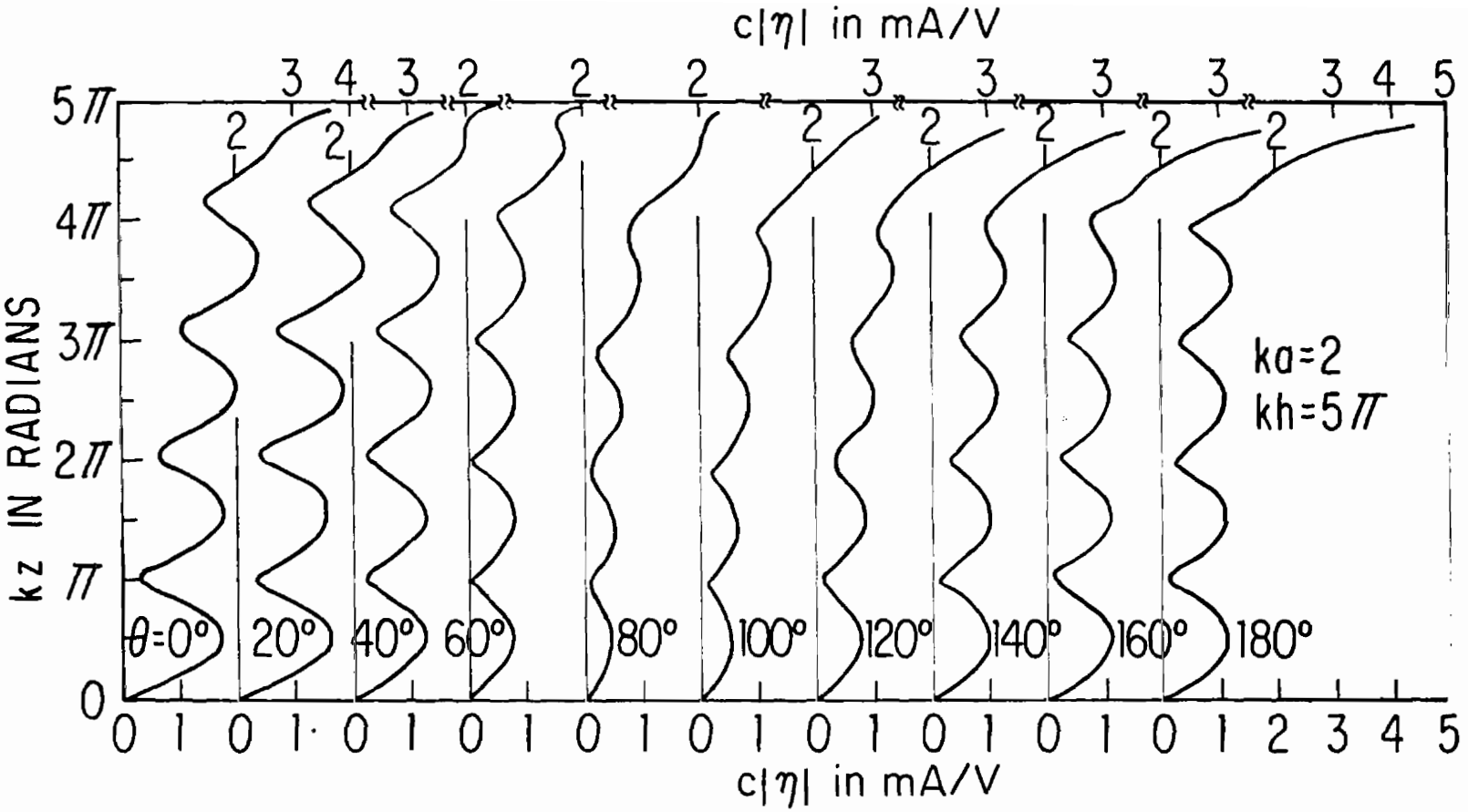

Fig. 105. Theoretical magnitude of surface density of outside charge on tubular cylinder; E-polarization. ($c = 3 \times 10^8$ m/sec.)

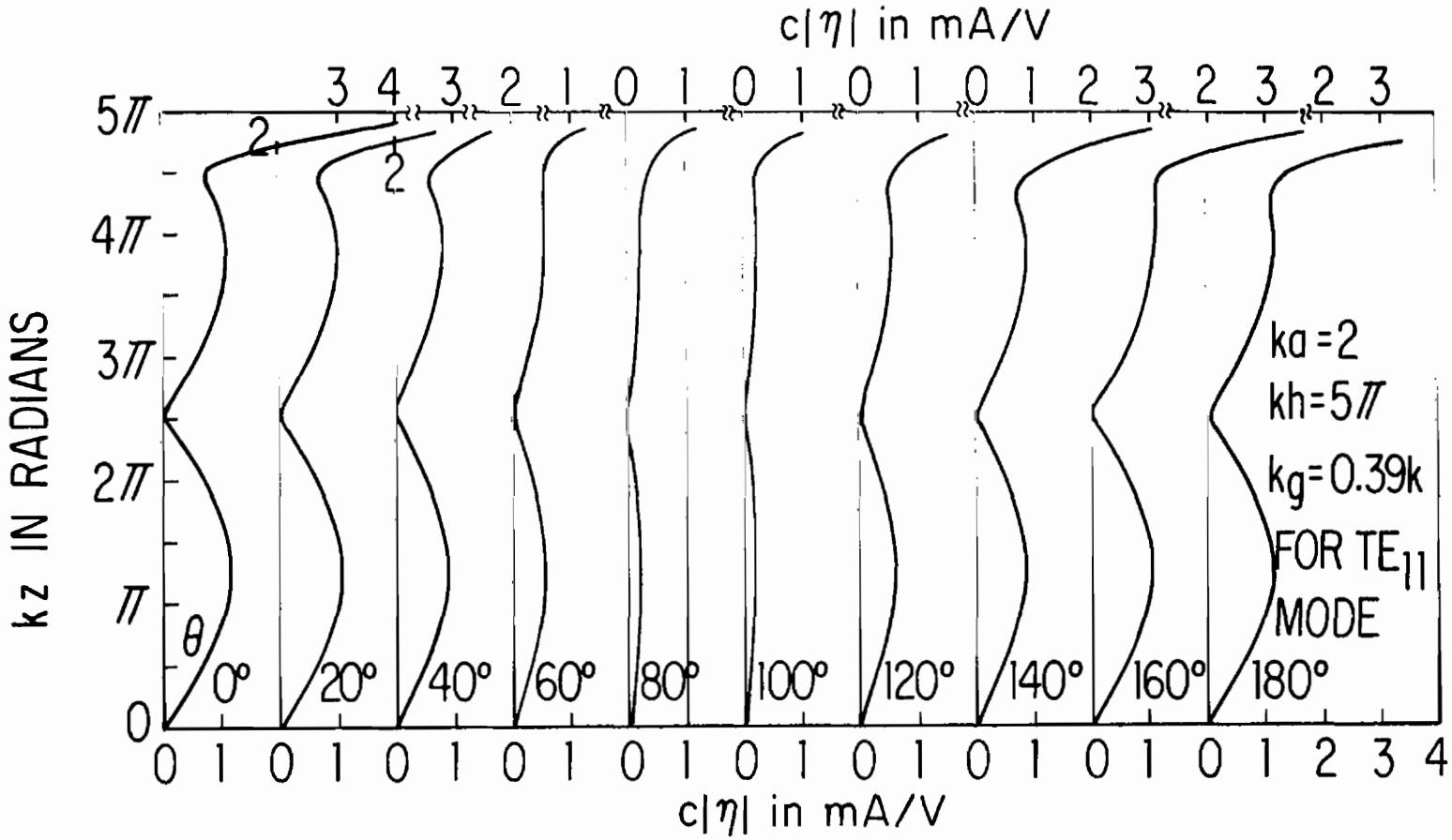

Fig. 106. Theoretical magnitude of surface density of inside charge in tubular cylinder; E-polarization. ($c = 3 \times 10^8$ m/sec.)

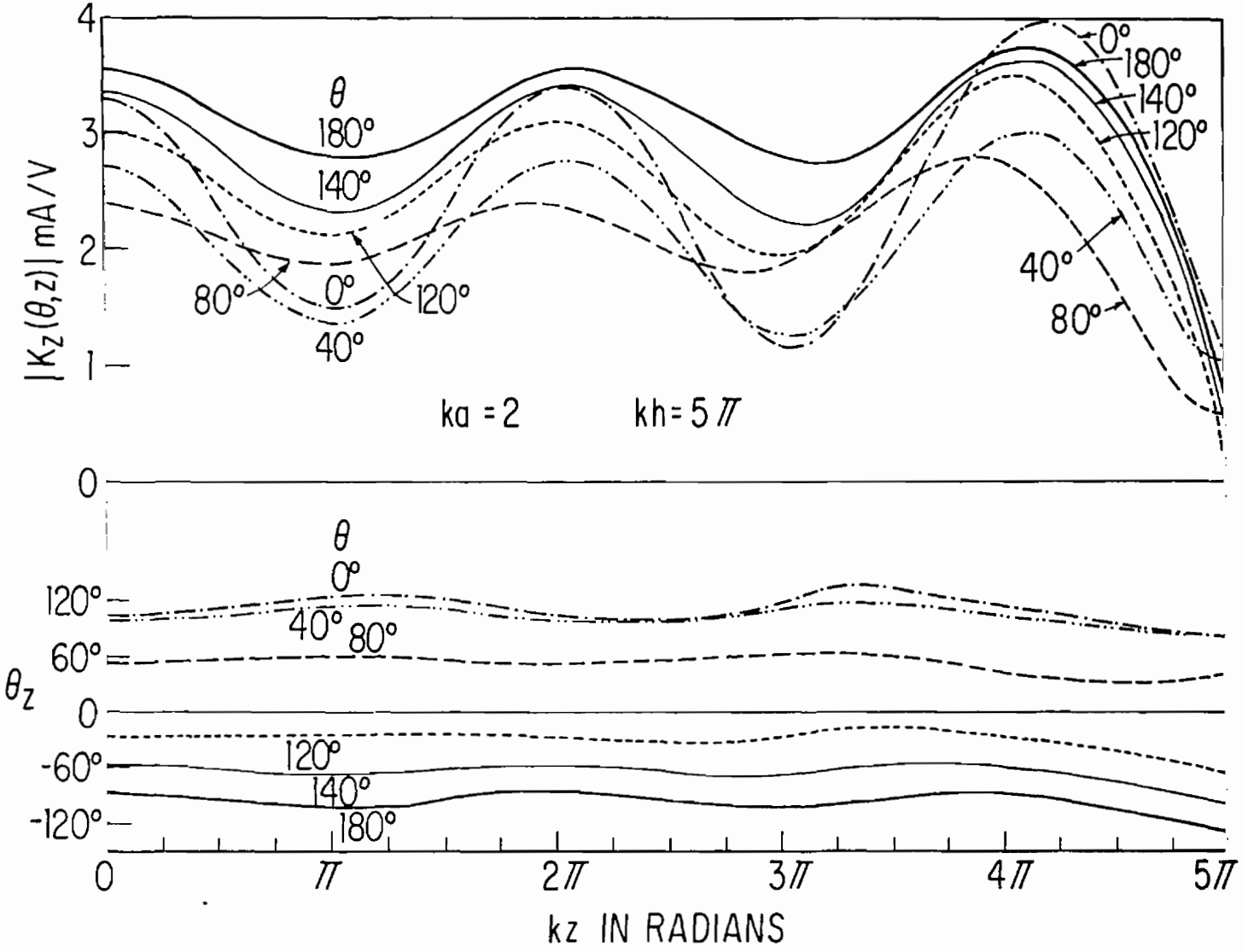

Fig. 107. Theoretical magnitude and phase of surface density of axial outside current $K_z(\theta,z)$ on tubular cylinder; E-polarization.

with the same electrical half-length, kh = 3.5π. The theoretical magnitude $|\eta(\theta,z)|$ of the surface density of outside charge on the cylinder is shown in Fig. 108, the associated phase θ_η (referred to the electric field along the axis) is in Fig. 109. The axial distributions of both are similar to the comparable distributions for ka = 1 given in Section V in Figs. 56 and 57. Note that the amplitude of the standing waves with ka = 2 is greater at θ = 0° in the shadow than at θ = 180° on the illuminated side just as with ka = 1. However, the change in amplitude from θ = 0° to θ = 180° along a ridge such as kz = 0.5π is not a uniform decrease as when ka = 1, but a decrease to a minimum near 80° and an increase (with a change in the sign of the charge) to another maximum at θ = 180°. This follows from Fig. 110 which shows for both ka = 1 and ka = 2 the phase angle θ_η as a function of θ from the center of the shadow on the left to the center of the illuminated side on the right at two values of kz corresponding to relative maxima, viz., kz = 0.5π and 1.5π. With ka = 1, the phase for each kz is virtually constant for all values of θ and the constant values at kz = 0.5π and 1.5π differ by about 180°. With ka = 2, the angle θ_η is constant from θ = 0° to θ = 60° where it decreases rapidly by about 180° to a new value which is maintained from θ = 90° to θ = 180°. The graphs for kz = 0.5π and 1.5π are parallel and displaced by about 180°. Thus, with ka = 1 the charge density has the same sign for all values of θ at kz = 0.5π, the opposite sign at kz = 1.5π for all θ. With ka = 2 the charge density, if essentially positive for kz = 0.5π when $0° \leq \theta < 80°$, is essentially negative when $80° < \theta \leq 180°$. For kz = 1.5π the charge density is distributed as for kz = 0.5π but with opposite sign.

The theoretical surface density of axial outside current on the cylinder with ka = 2 is shown in Fig. 111 in amplitude and phase. A direct comparison with the corresponding graphs for ka = 1 in Fig. 53 reveals that with ka = 2 the standing-wave ratio on the illuminated side is substantially greater. Also the relative magnitude of the current is larger in the shadow when ka = 2 than when ka = 1. This is especially true near the open end where the close coupling to the large inside currents has significant effects. Note that $ka > ka_c$.

The transverse distributions of the real and imaginary parts of the axial current $K_z(\theta,z) = K_{zR}(\theta,z) + iK_{zI}(\theta,z)$ are shown in Fig. 112 at

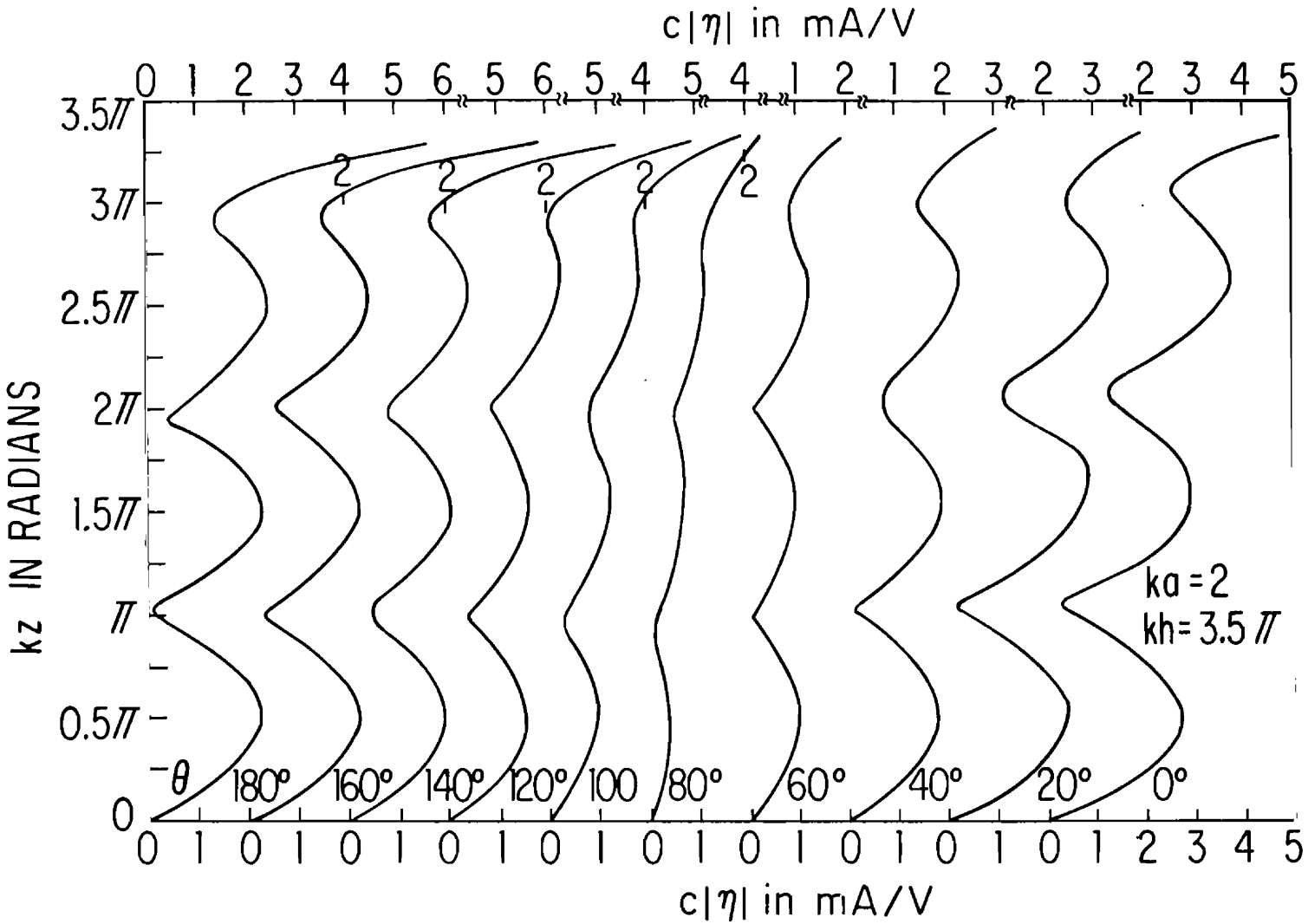

Fig. 108. Theoretical magnitude of surface density of outside charge on tubular cylinder; E-polarization. ($c = 3 \times 10^8$ m/sec.)

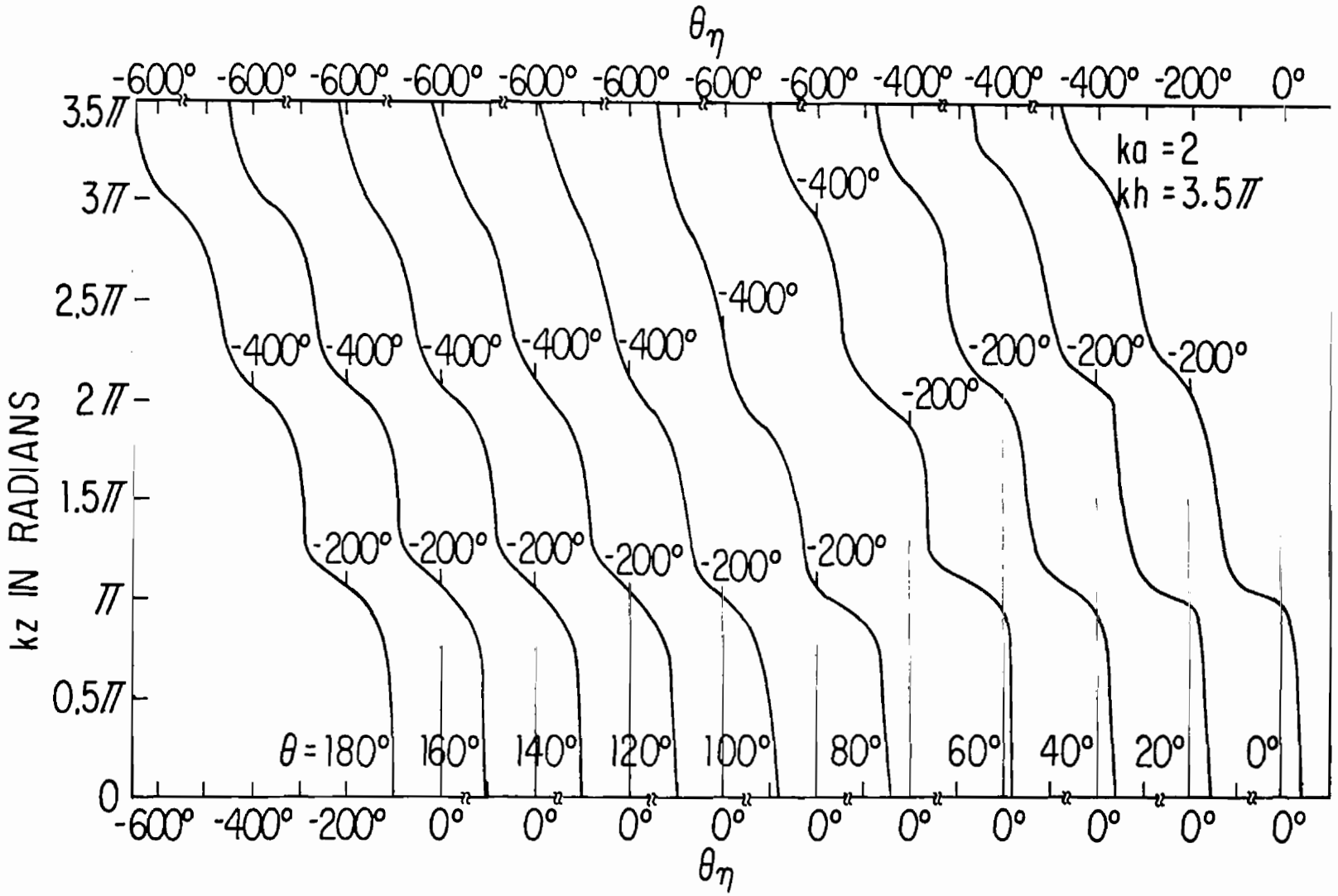

Fig. 109. Theoretical phase of surface density of outside charge on tubular cylinder; E-polarization.

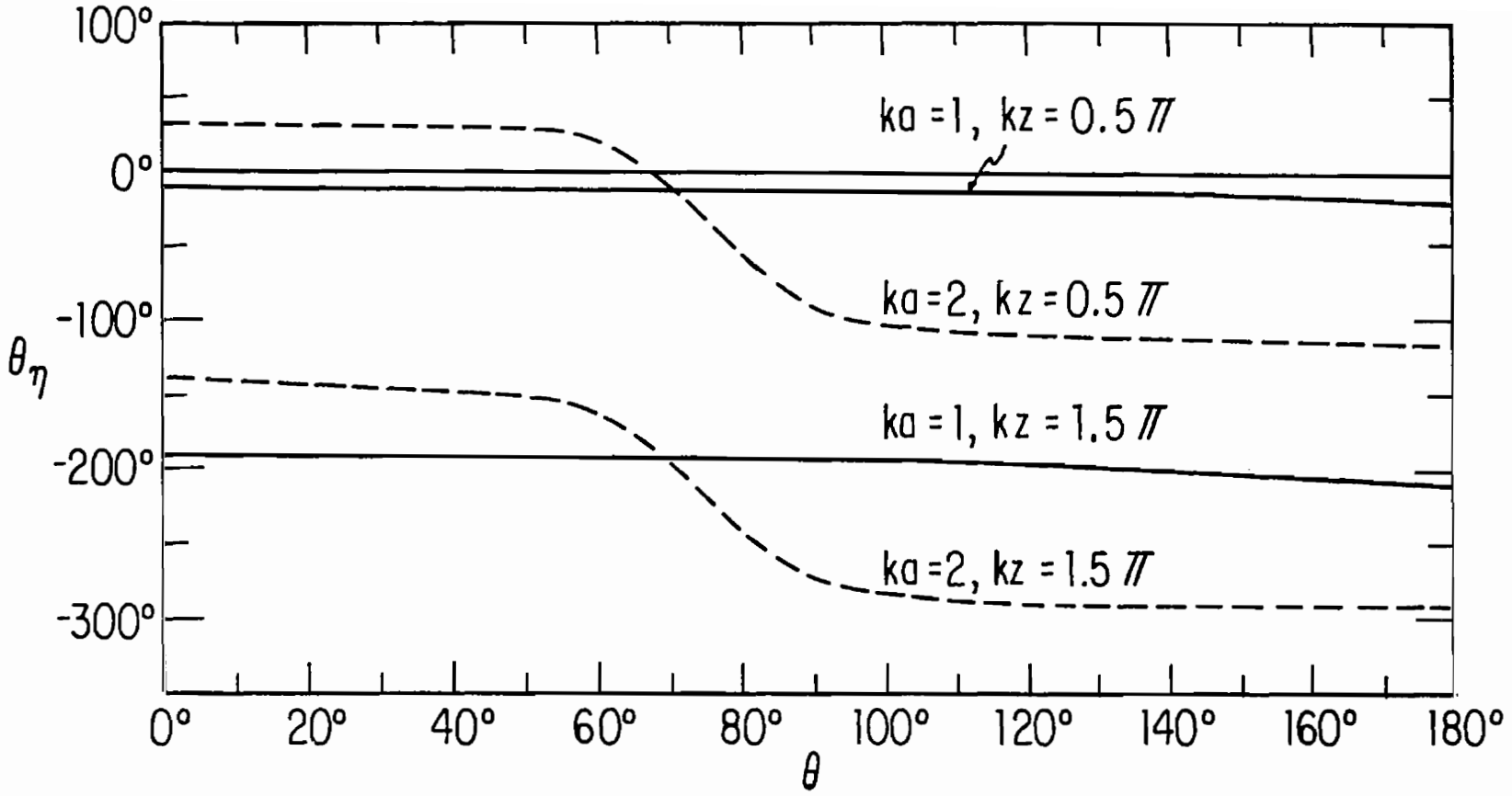

Fig. 110. Theoretical phase of surface density of outside charge on tubular cylinder; E-polarization, kh = 3.5π.

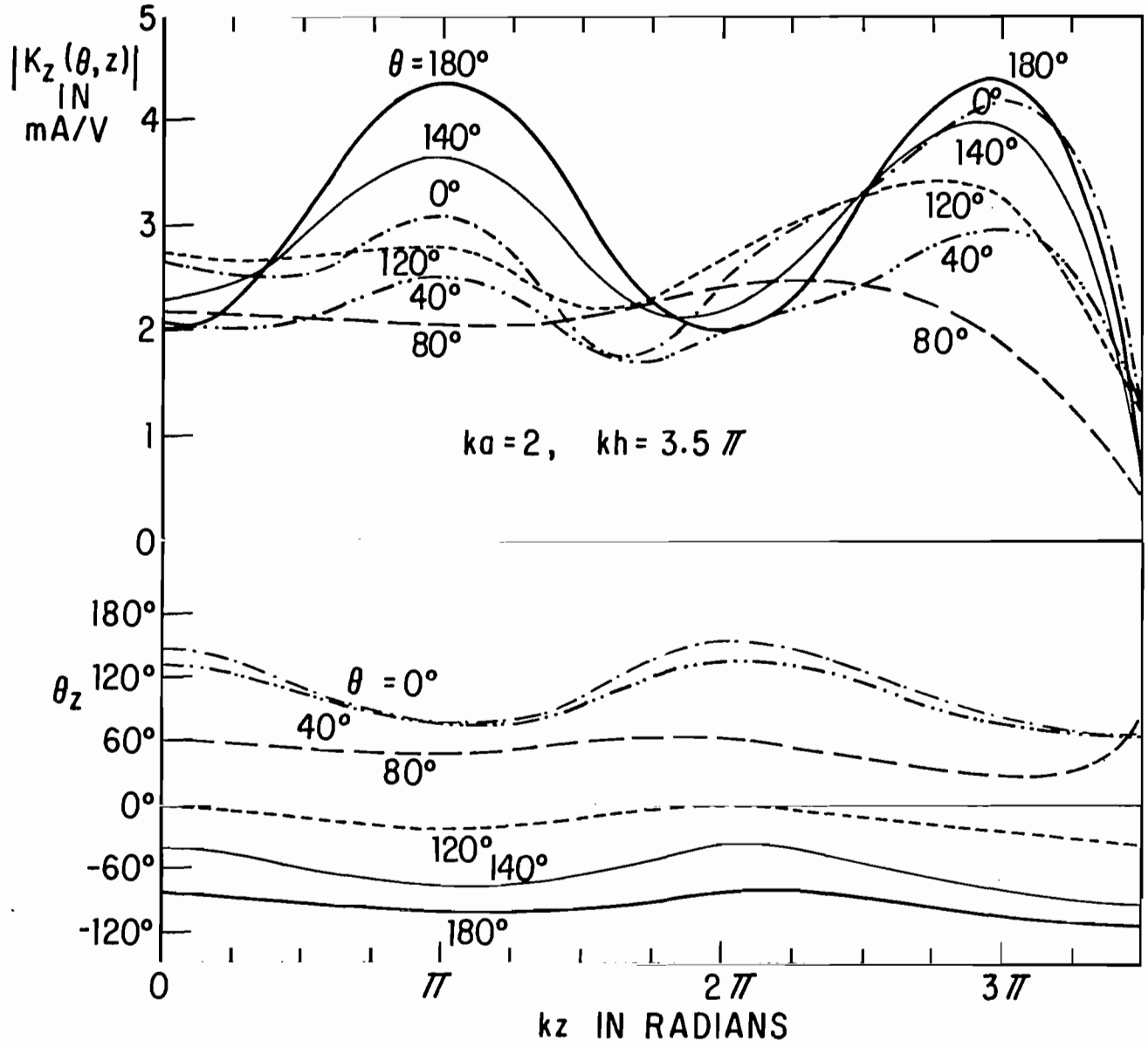

Fig. 111. Theoretical magnitude and phase of surface density of axial outside current $K_z(\theta,z)$ on tubular cylinder; E-polarization.

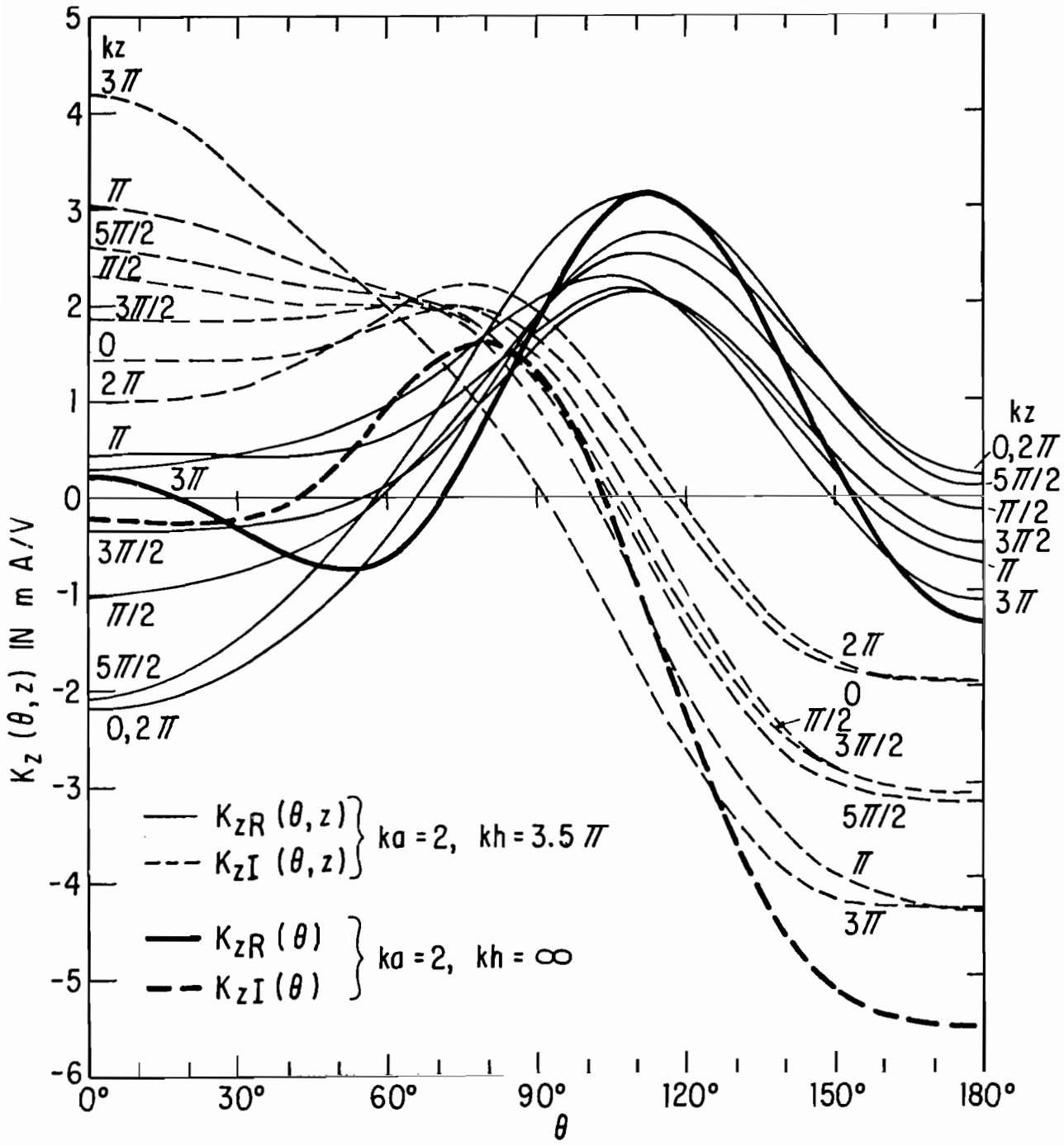

Fig. 112. Theoretical transverse distributions of real and imaginary parts of $K_z(\theta,z)$ on tubular cylinder; E-polarization.

values of kz of 0.5π, 1.5π and 2.5π, as well as 0, 2π and 3π. Also shown are the transverse distributions when $kh = \infty$. These resemble some of the distributions with a finite length in certain respects, but differ substantially in other respects.

The theoretical surface density of transverse outside current $K_\theta(\theta,z)$ is shown in Fig. 113. At the top are the transverse and axial distributions of the magnitude and phase of the transverse component of current; at the bottom are the real and imaginary parts referred to the field along the axis. The transverse distribution of $|K_\theta(\theta,z)|$ is seen to have two distinct maxima, the larger one near $\theta = 50°$, the smaller one near $\theta = 130°$ with a phase difference between them near 180°, i.e., the currents at these locations are instantaneously in opposite directions around the cylinder. The axial distribution of $|K_\theta(\theta,z)|$ shows the expected rapid decrease in amplitude at increasing distances from the open end, much as with thinner cylinders. With E-polarization this component of current is generated entirely by reflections at the open end.

The Fourier coefficients A(kz) through E(kz) of the axial outside current,

$$K_z(\theta,z) \doteq A(kz) + B(kz)\cos\theta + C(kz)\cos 2\theta + D(kz)\cos 3\theta + E(kz)\cos 4\theta \quad (73)$$

are shown in Fig. 114. As is to be expected with $ka = 2$, by far the largest component is $B(kz) = B_R(kz) + iB_I(kz)$ in both its real and imaginary parts. Next in size is C(kz) and then A(kz). With $ka = 1$ only A(kz) and B(kz) have significant resonant parts; C(kz) and D(kz) are entirely forced components with constant amplitude except near the open end. With $ka = 2$, A(kz), B(kz) and C(kz) have resonant parts superimposed on the constant forced components. Beginning with D(kz), the Fourier components are characteristic of purely forced currents. With $ka = 1$ the first four terms are sufficient; for comparable accuracy with $ka = 2$ the first five or six terms must be retained.

3. THEORETICAL CHARGES AND CURRENTS WITH H-POLARIZATION

In order to understand the induced currents and charges on the horizontal member of crossed cylinders, the theoretical distributions on an

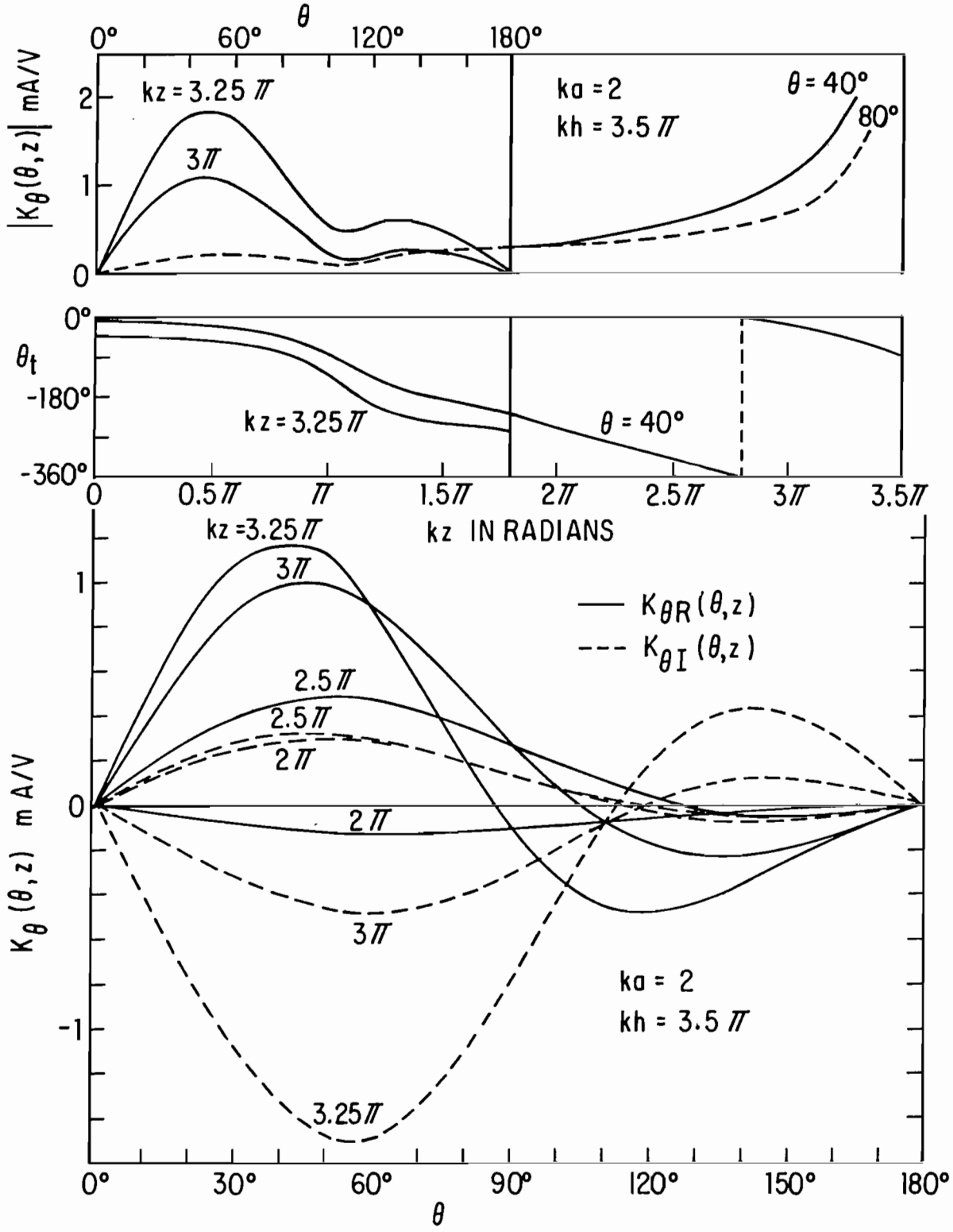

Fig. 113. Theoretical surface density of transverse outside current $K_\theta(\theta,z)$ on tubular cylinder; E-polarization.

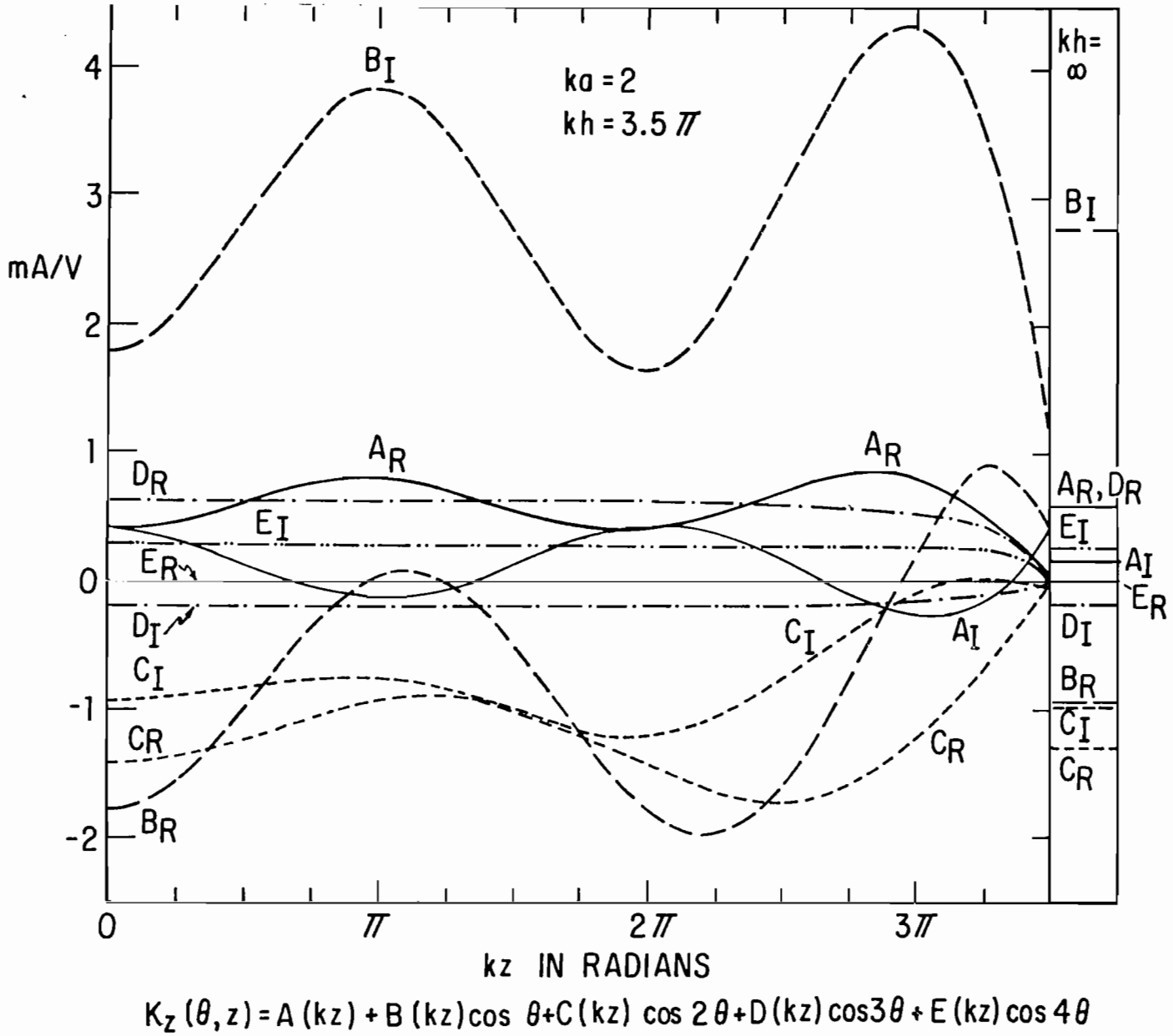

Fig. 114. Fourier coefficients of surface density of axial outside current on tubular cylinder; E-polarization.

isolated cylinder in an H-polarized field are useful. Since the general nature of the distributions with H-polarization is more clearly deduced from longer cylinders than the shorter ones ($k\ell \leq 2\pi$) actually used for the arms of the cross, it is convenient to study them with $k\ell = 3.5\pi$ and $ka = 2$. With the incident field characterized by E_z^{inc} and H_x^{inc}, the cylinder is now oriented parallel to the x-axis and extends from $x = -\ell$ to $x = \ell$. The magnitudes of the theoretical induced outside currents are shown in Fig. 115 with the axial component $|K_x(\theta,x)|$ at the top, the transverse component $|K_\theta(\theta,x)|$ at the bottom. It is seen from the scales that $|K_\theta(\theta,x)|$ at its greatest at $\theta = 0°$ is about 9 times as large as $|K_x(\theta,x)|$ at $\theta = 60°$, $kx = 0.5\pi$. $|K_\theta(\theta,x)|$ is almost constant for each value of θ from $kx = 0$ at the center to kx quite close to the open end. It is largest at $\theta = 0°$ in the shadow, decreases to virtually zero at $\theta = 60°$, and then rises again to a slightly smaller maximum at $\theta = 180°$ on the illuminated side. The phase angle θ_t of $K_\theta(\theta,x)$ is virtually the same for all values of kx from zero to near $k\ell = 3.5\pi$; it is shown in Fig. 116. Note that in its dependence on θ θ_t is fairly constant from $\theta = 0°$ to $\theta = 60°$ where it drops abruptly by about 180° as is typical of standing-wave distributions. However, from $\theta = 60°$ to $\theta = 120°$ the phase changes almost linearly as for a traveling wave (in this case a creeping wave around the shadow boundary at $\theta = 90°$). It then changes relatively little from $\theta = 120°$ to $\theta = 180°$. Evidently the transverse current oscillates predominantly as a standing wave in the sectors $-60° \leq \theta \leq 60°$ in the deep shadow and $120° \leq \theta \leq 240°$ on the illuminated side; it behaves like a traveling wave in the sectors $60° \leq \theta \leq 120°$ and $240° \leq \theta \leq 300°$ which include the shadow boundaries at $\theta = 90°$ and 270°.

The much smaller axial component of current $K_x(\theta,x)$ has a typical axial standing-wave pattern that is independent of θ in its shape but has a maximum amplitude near $\theta = 60°$ [where $K_\theta(\theta,x) \doteq 0$] and zeros at $\theta = 0°$ and 180° [where $K_\theta(\theta,x)$ has maxima]. The phase angle θ_x of $K_x(\theta,x)$ is also shown in Fig. 116 as a function of θ near the maxima at $kx = 0.5\pi$ and 1.5π in the axial standing-wave pattern. θ_x is seen to vary with θ in substantially the same manner at the two values of kx and to differ by about 180° from $kx = 0.5\pi$ to $kx = 1.5\pi$. This indicates that the axial current is instantaneously oppositely directed at the two standing-wave maxima as would be expected. The change in θ_x from the center of the shadow to the center of the illuminated region is only about 90°.

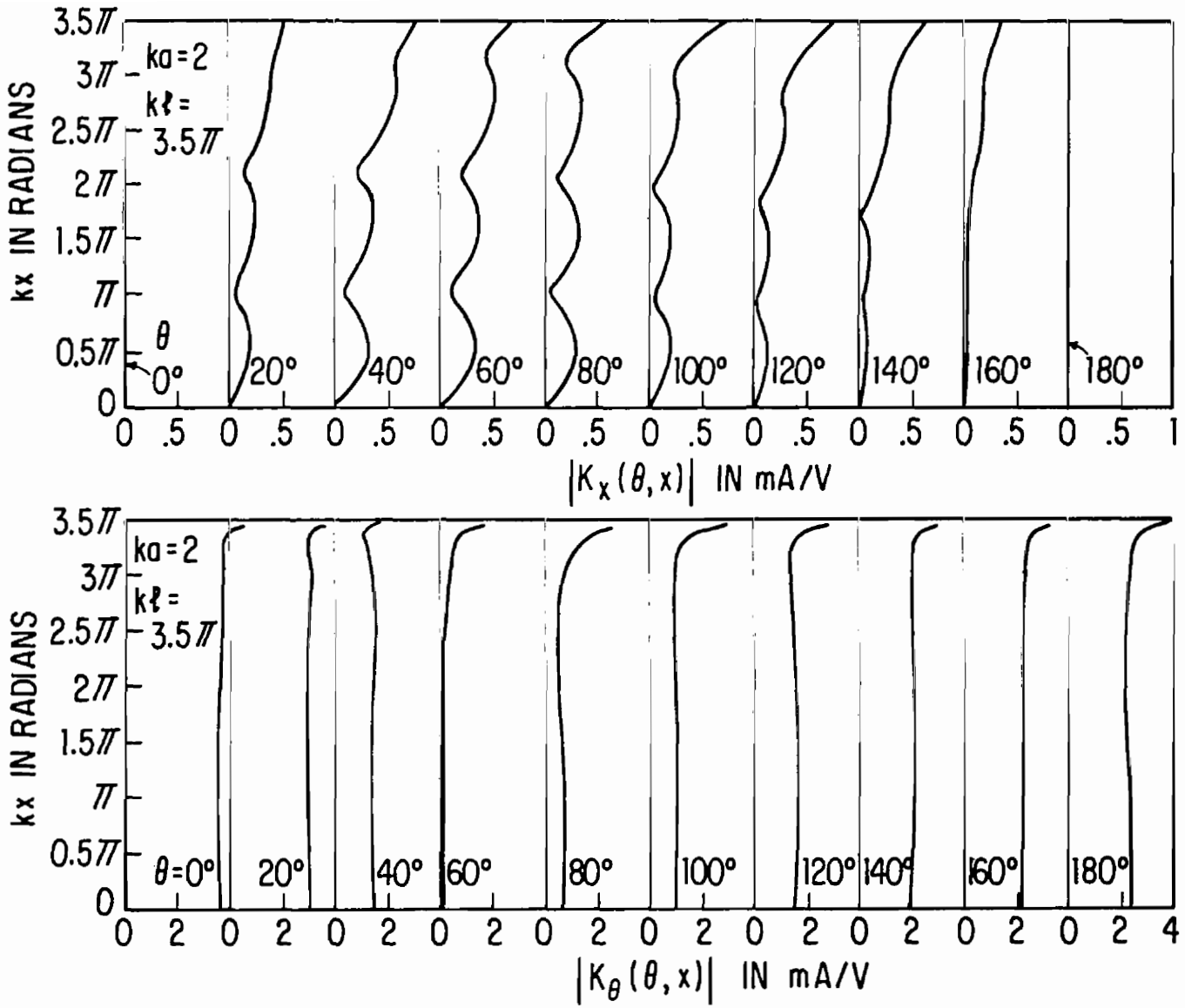

Fig. 115. Theoretical magnitude of surface densities of axial and transverse outside current on tubular cylinder; H-polarization.

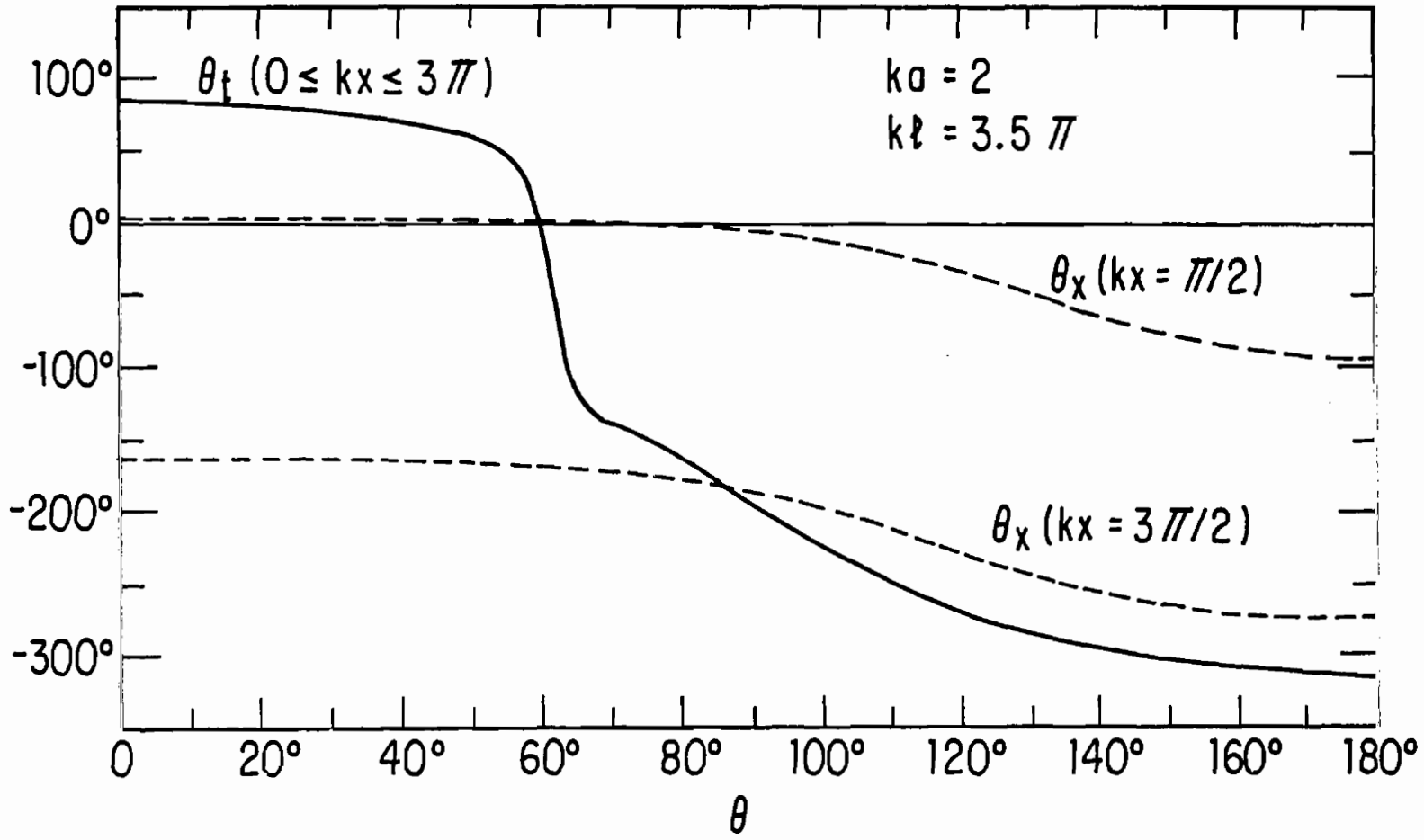

Fig. 116. Theoretical phase of surface densities of axial and transverse outside current on tubular cylinder; H-polarization.

The theoretical magnitude of the surface density of outside charge associated with these currents is shown in Fig. 117 as a function of kx with θ as the parameter, in Fig. 118 in a contour diagram. The axial standing-wave pattern in Fig. 117 is determined almost entirely by $\partial K_x(\theta,x)/\partial x$ [since $K_\theta(\theta,x)$ is almost constant in x], the transverse distribution by $\partial K_\theta(\theta,x)/\partial\theta$. Note that its amplitude is largest at $\theta = 60°$ where $K_\theta(\theta,x)$ is zero. Thus, the transverse currents oscillate as sheets over the entire length to locate ridges of charge along the axial lines $\theta = \pm 60°$, and nulls along the lines $\theta = 0°$ and 180°. Simultaneously, the axial currents have a superimposed axial standing-wave pattern with relative minima near $kx = 0.5\pi$, 1.5π and 2.5π, maxima near $kx = 0$, π and 2π. With $ka = 1$, the ridges of charge are along $\theta = \pm 90°$, and the transverse currents have codirectional maxima (oppositely directed with respect to θ) across the lines $\theta = 0°$ and 180°. With $ka = 2$, the ridges of charge are at $\theta = \pm 60°$, and the transverse currents have almost oppositely directed maxima (same direction around the cylinder with respect to θ) across the lines $\theta = 0°$ and 180°. The phase reversal with $ka = 2$ is a consequence of the traveling-wave sectors between about $\theta = \pm 65°$ and $\theta = \pm 125°$ — these are absent when $ka = 1$.

The axial and transverse components of current can be expressed as sums of Fourier components as follows:

$$K_x(\theta,x) = i[B'_H(kx)\sin\theta + C'_H(kx)\sin 2\theta + \ldots] \tag{74}$$

$$K_\theta(\theta,x) = B_H(kx)\cos\theta + C_H(kx)\cos 2\theta + D_H(kx)\cos 3\theta + E_H(kx)\cos 4\theta + F_H(kx)\cos 5\theta + \ldots \tag{75}$$

The Fourier coefficients $B'_H(kx)$ and $C'_H(kx)$ for $K_x(\theta,x)$ with H-polarization are shown at the top in Fig. 119; higher-order coefficients are negligible. The corresponding coefficients $B_H(kx)$, $C_H(kx)$, ..., $F_H(kx)$ for $K_\theta(\theta,x)$ with H-polarization are shown at the bottom in Fig. 119; higher-order coefficients are negligible. The coefficients $E_H(kx)$ and $F_H(kx)$ are largely independent of x except in the quarter wavelength near the open end where they reduce to zero. The representation of the current on a cylinder with $ka = 2$ in an H-polarized field is significantly more complicated than when $ka = 1$.

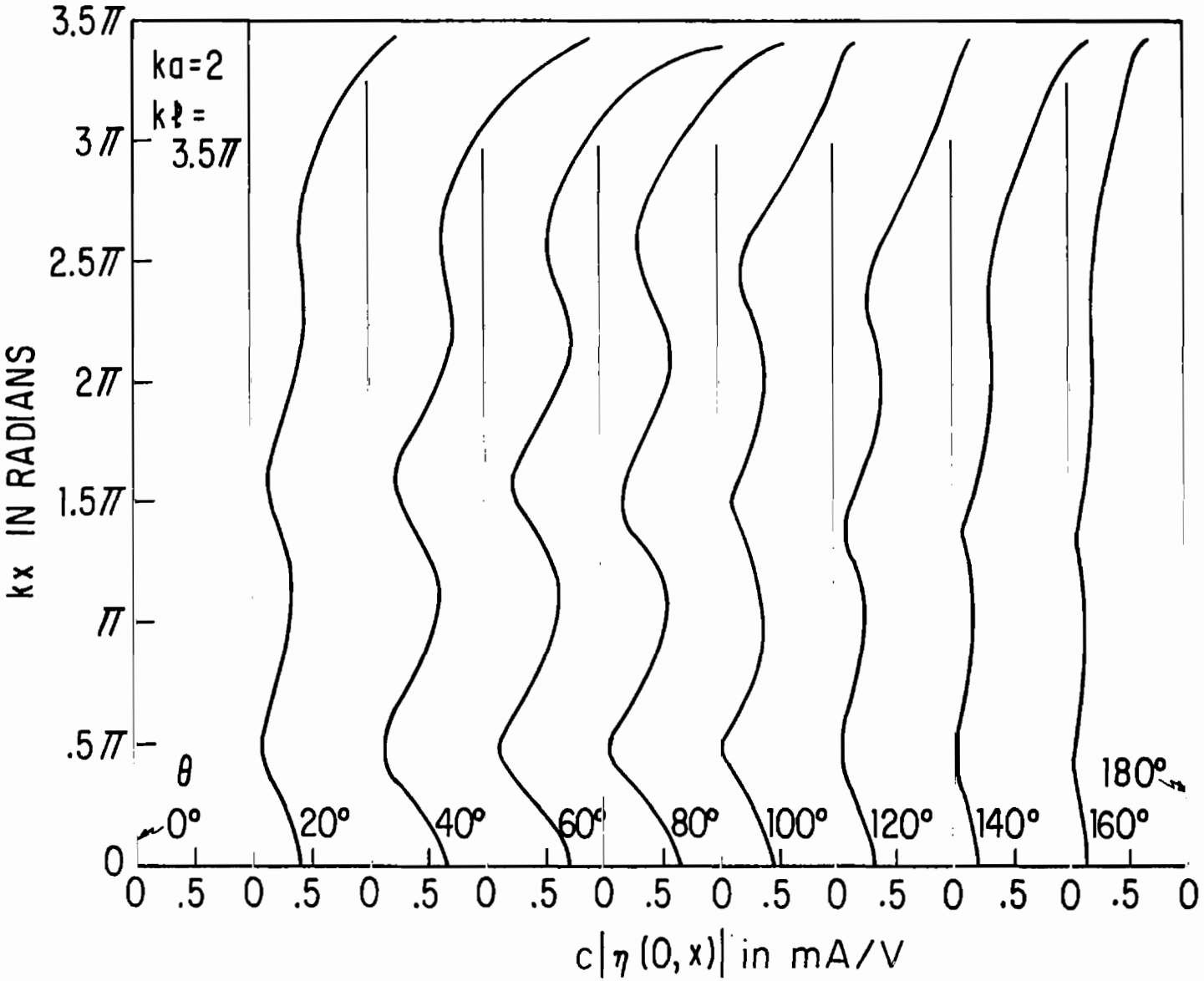

Fig. 117. Theoretical magnitude of surface density of outside charge on tubular cylinder; H-polarization. ($c = 3 \times 10^8$ m/sec.)

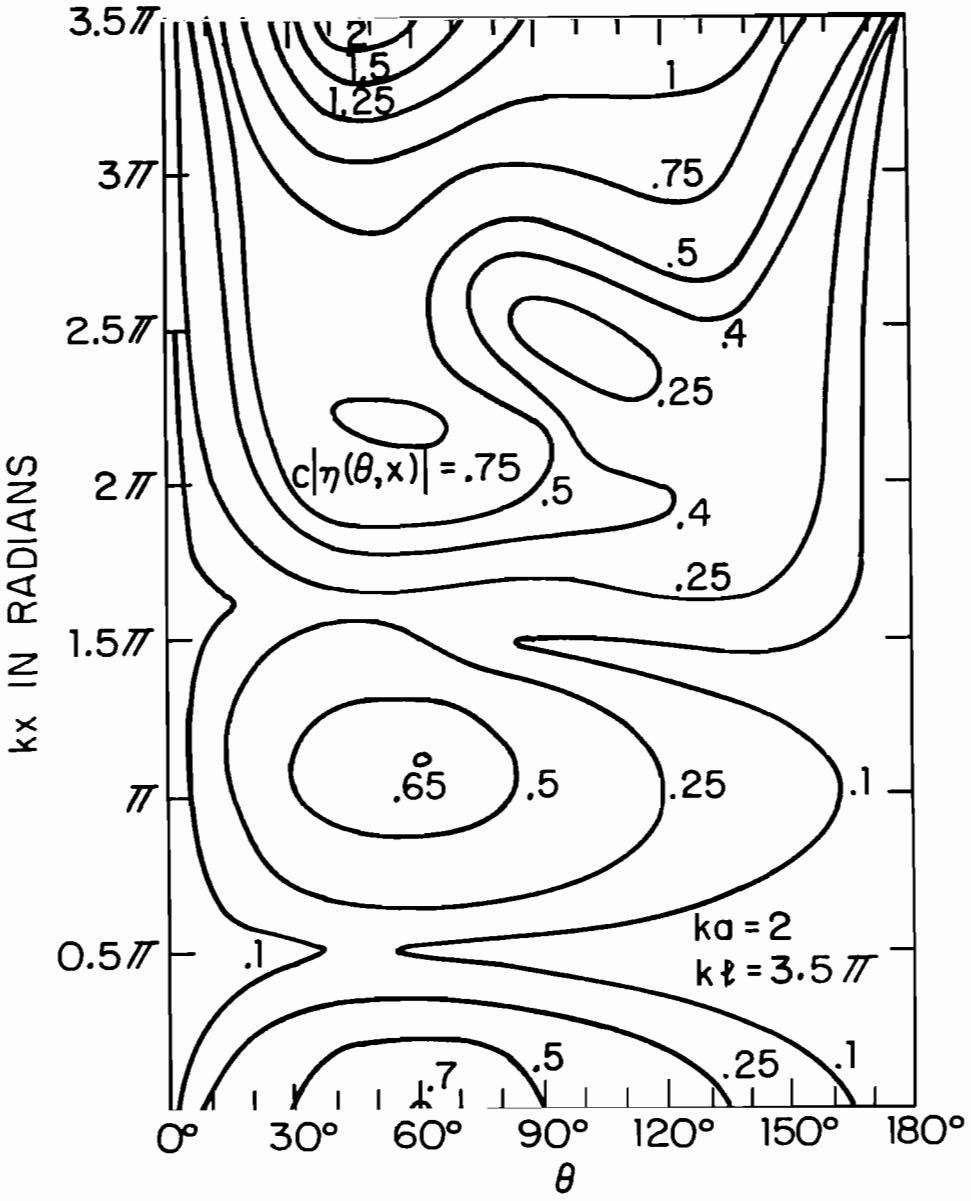

Fig. 118. Theoretical contours of constant magnitude of surface density of outside charge on tubular cylinder; H-polarization. ($c|\eta|$ in mA/V; $c = 3 \times 10^8$ m/sec.)

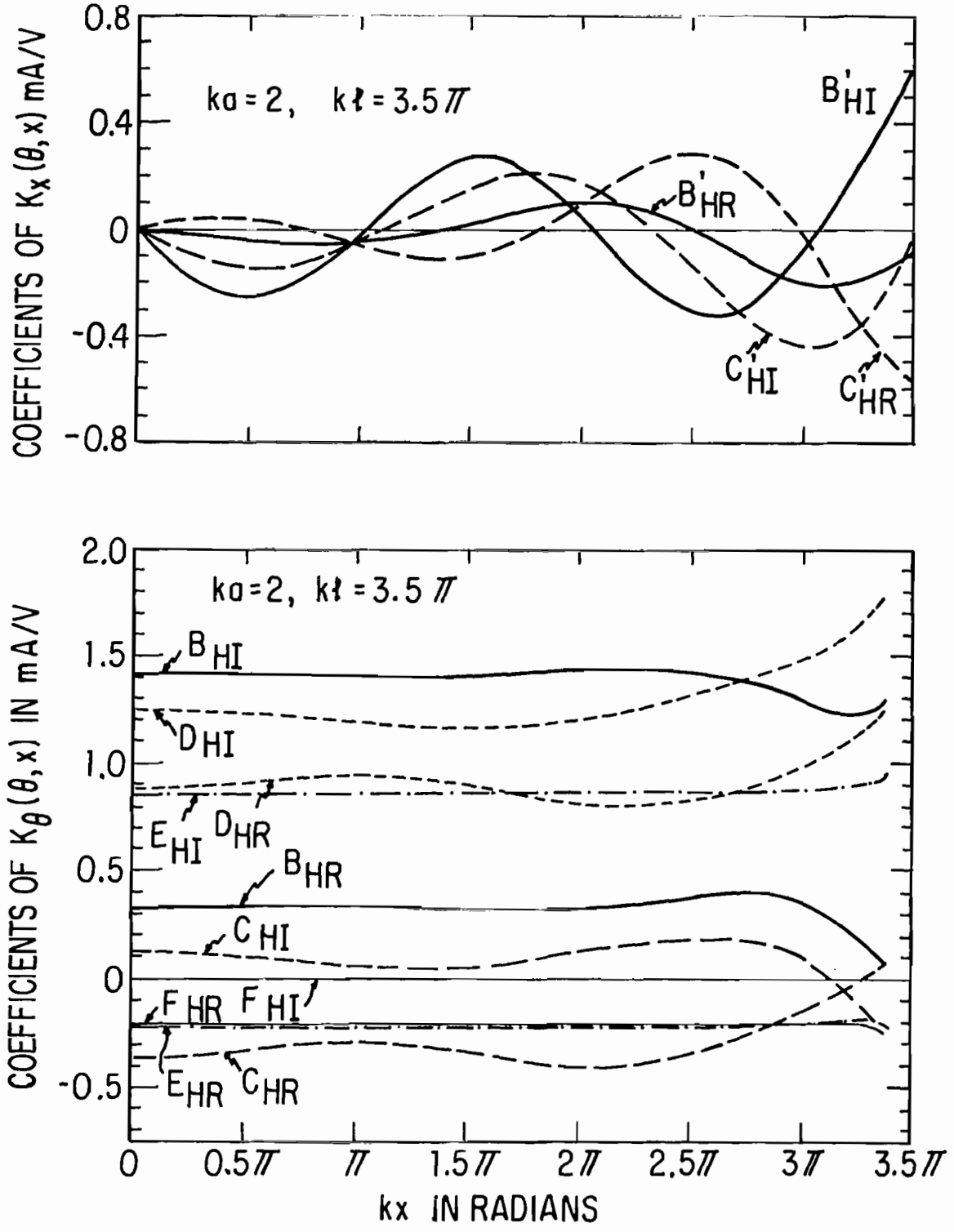

Fig. 119. Fourier coefficients of surface densities of axial and transverse current on tubular cylinder; H-polarization.

4. MEASUREMENTS ON SINGLE CYLINDER; E-POLARIZATION

In order to avoid the excitation of possible internal waveguide resonances in crossed cylinders with ka = 2, it was deemed advisable to cap all of the open ends. Actually, owing to the relatively thick walls (1/4 in.) of the tubes, the inside electrical radius is $ka_i = 1.83$ when the outside is ka = 2. Since the cut-off radius for the TE_{11} mode is $ka_c = 1.84$, the inside radius ka_i of the cylinders used in the measurements is slightly below cut-off, while that in the theory (with its infinitely thin, perfectly conducting tube) is well above cut-off. As a consequence, the inside waveguide currents and charges actually excited in the experiments with $ka_i = 1.83$ are quite small compared with those calculated theoretically with $ka_i = 2$. In fact, just as in Section V for ka = 1, the effect of an end cap on the measured current and charge densities is quite small. This is shown in Fig. 120. At the top are the measured magnitudes of the current density $K_z(\theta,z)$ at $\theta = 0°$, 120° and 180° with open and capped ends; at the bottom is the charge density $|\eta(\theta,z)|$ at $\theta = 0°$ and 180°. The differences between the graphs for capped and open ends are minor. Note that the amplitude of the current in the shadow ($\theta = 0°$) is only about one quarter of that on the illuminated side ($\theta = 180°$) — a condition quite different from the corresponding theoretical curves in Fig. 111. Note also that the outside currents at the end z = h are not zero. When the end is open, the outside axially directed current continues over the edge to become an equal and opposite inside current. This is rapidly attenuated when the radius ka_i is below cut-off. When the end is capped, the outside axial current becomes a radial current on the flat end cap. With the end open the inside currents would be quite different if the TE_{11} mode could propagate in the tube with $ka_i > ka_c$ as in the theoretical curves with ka = 2 shown in Fig. 111. The close coupling between inside and outside charges at and near the open end would lead to modified outside current and charge distributions. These do not occur in the measurements because $ka_i < ka_c$.

Figure 121 shows the measured axial distributions of the magnitude of the outside charge density $\eta(\theta,z)$ on a monopole cylinder with ka = 2, kh = 3.5π, and a capped end for values of θ from $\theta = 0°$ in the center of the shadow to $\theta = 180°$ in the center of the illuminated region. The associated phase distributions are in Fig. 122. A comparison with the corresponding theoretical distributions in Figs. 108 and 109 shows complete agreement in

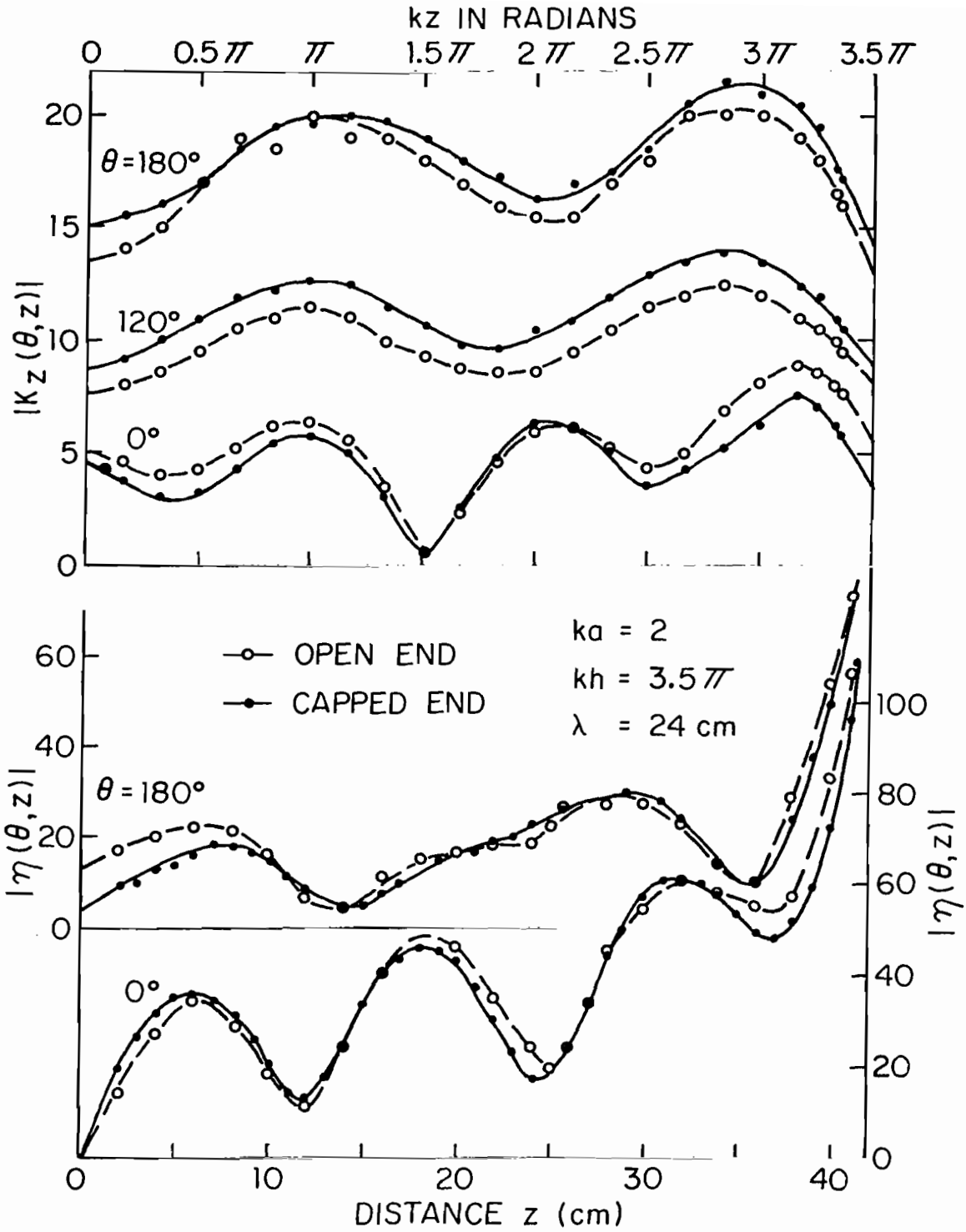

Fig. 120. Measured magnitude of surface densities of outside current and charge on tubular cylinder with open and capped ends; E-polarization. ($|K|$ and $|\eta|$ in arbitrary units.)

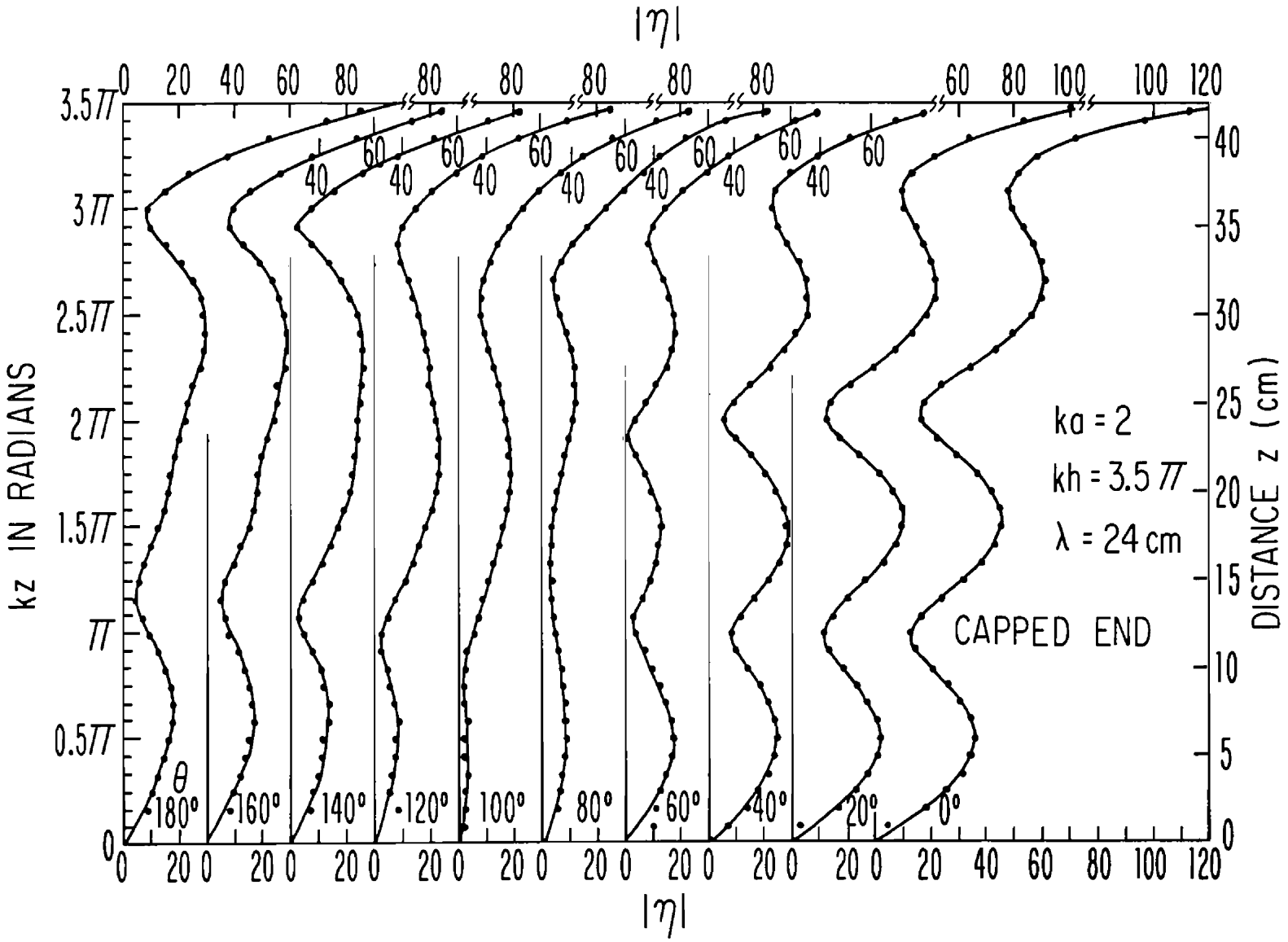

Fig. 121. Measured magnitude of surface density of outside charge on tubular cylinder with capped end; E-polarization. ($|\eta|$ in arbitrary units.)

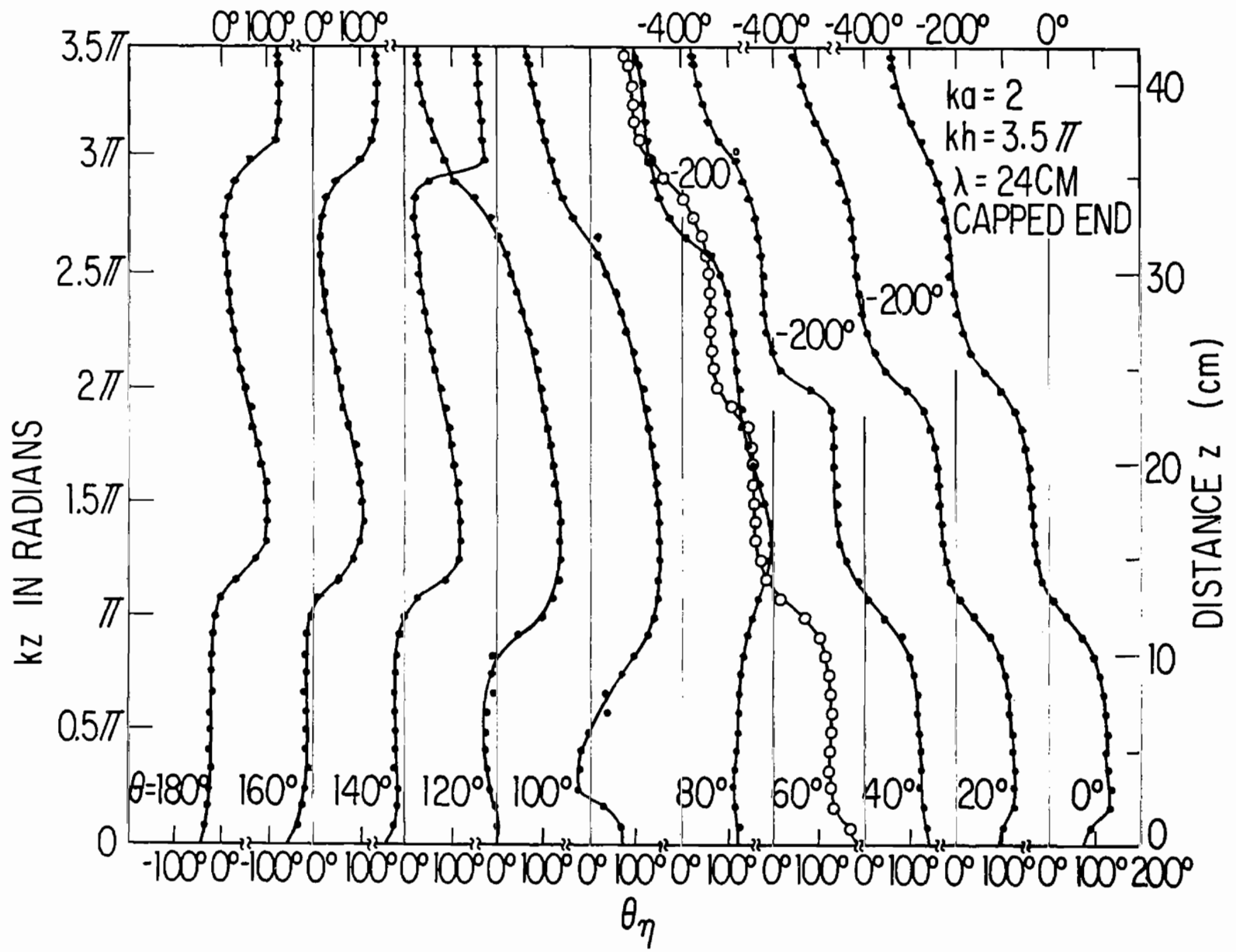

Fig. 122. Measured phase of surface density of outside charge on tubular cylinder with capped end; E-polarization.

the shadow region, $0° \leq \theta \leq 80°$. The axial distributions are also very much like those with ka = 1 and kh = 3.5π given in Figs. 65 and 66, but the amplitude of the standing-wave pattern when ka = 2 decreases to a minimum near θ = 90° which does not exist when ka = 1. In the illuminated region, $100° \leq \theta \leq 180°$, the measured axial distributions in Figs. 121 and 122 differ substantially from the corresponding theoretical ones in Figs. 108 and 109. The three ideally almost uniformly spaced theoretical maxima and minima are greatly distorted in the measured graphs with corresponding differences in the phases. Although the distortions from the ideal differ significantly in shape from those for ka = 1 in Figs. 65 and 66, they are no doubt also due to the spherical instead of planar wave front of the incident field. The incident electric field tangent to a spherical wave front has a component perpendicular to the surface of the cylinder — which is absent with a normally incident plane wave — that distorts the normal standing-wave pattern.

The measured distributions of the axial component of current on the cylinder with ka = 2, kh = 3.5π are shown in Fig. 123. As expected, they differ appreciably from the theoretical values shown in Fig. 111 since they are not coupled to a large inside current in the TE_{11} waveguide mode as are the theoretically calculated currents.

The theoretical and measured graphs of the surface densities of charge and current on a tubular cylinder with ka = 2 are not in as good agreement as the corresponding graphs with ka = 1 because they are not strictly comparable. The fact that a large propagating inside current in the TE_{11} mode is excited in the infinitely thin-walled tubular cylinder to which the theory applies, but is not excited in the cylinder used in the measurements, necessarily involves major differences. In comparing currents and charges on single cylinders with those on the vertical member of crossed cylinders, reliance will have to be placed primarily on the measured values rather than the theoretical ones, although the latter are useful in providing a general overview.

5. MEASUREMENTS ON CROSSED CYLINDERS; THE VERTICAL MEMBER

The studies of crossed cylinders with ka = 1 were carried out on a vertical cylinder with kh = 3.5π mounted on a ground plane. The horizontal

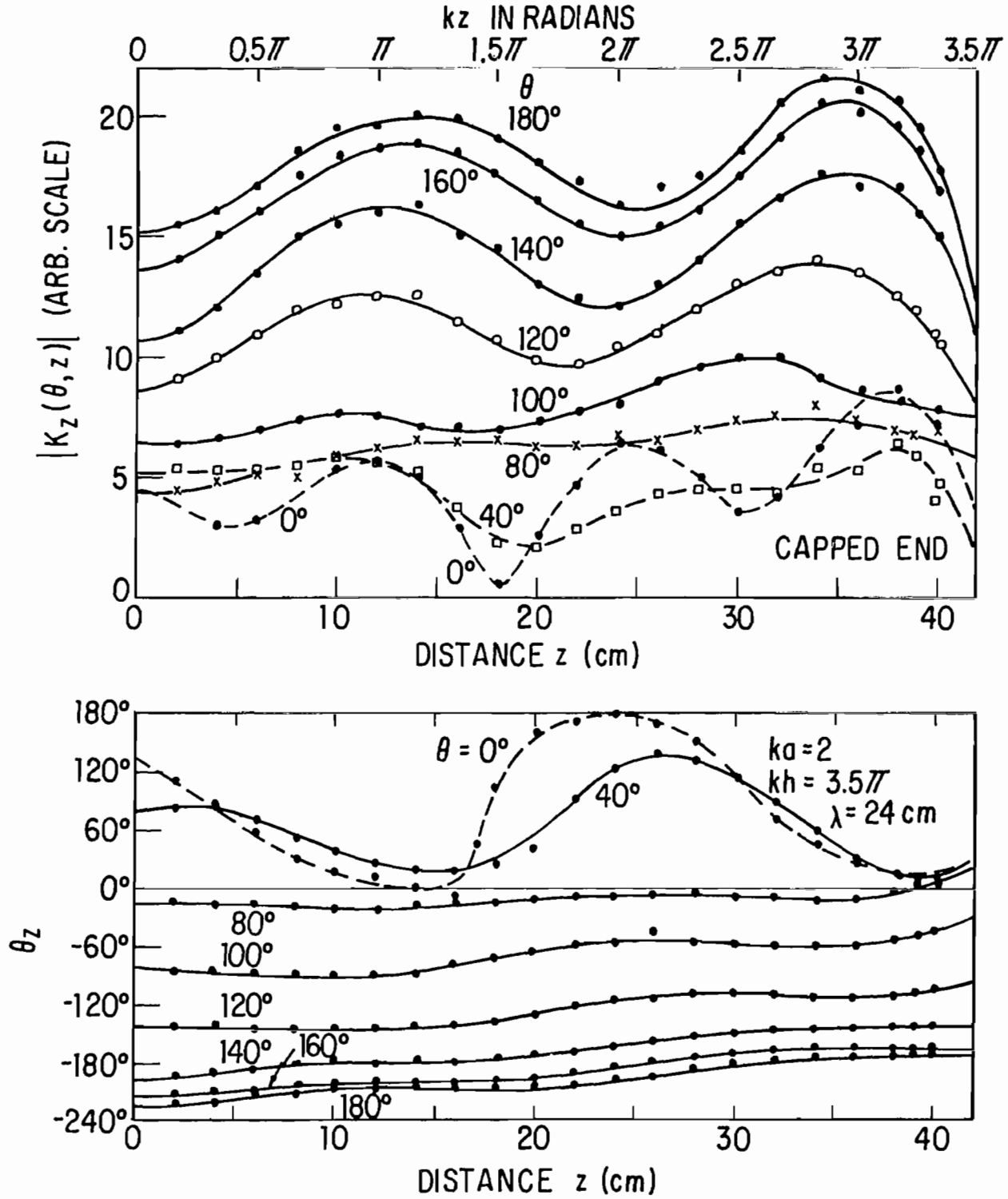

Fig. 123. Measured magnitude and phase of surface density of axial outside current on tubular cylinder with capped end; E-polarization.

member had equal arms with successive axial lengths of $k\ell = \pi$, 1.5π and 2π and was located successively at $kh_1 = 2\pi$ and 2.5π (Section VI). The corresponding measurements on crossed cylinders with ka = 2 and $kh = 3.5\pi$ are more limited owing to the larger electrical diameters of the tubes for which the electrical diameter 2ka is 4 instead of 2. When the horizontal arms are centered at $kh_1 = 2\pi$, their bottom is only at the electrical distance $(2\pi - 2) = 4.28$ radians or at an actual distance of 0.68λ from the ground plane. This is rather close, and coupling to the image at 1.36λ may have significant effects. On the other hand, with $kh_1 = 2.5\pi$ the section of the vertical cylinder above the cross is too short to permit meaningful measurements on its surface except on the central illuminated and shadow lines, respectively, at $\theta = 180°$ and $\theta = 0°$. Since the behavior of the charge density and current density near the open end is quite well understood, this is not a serious difficulty. Accordingly, the measurements on crossed cylinders with ka = 2 have been made with $kh_1 = 2.5\pi$. The arms were chosen to have the longest length used with ka = 1, viz., $k\ell = 2\pi$.

The measured distributions of the magnitude of the axial component of the current density $K_z(\theta,z)$ on the lower part of the vertical cylinder are shown in Fig. 124. They resemble the corresponding currents on the isolated cylinder in Fig. 123 in general shape and magnitude. Note that both with and without the horizontal arms, the magnitude is about three times as large on the illuminated side ($\theta = 180°$) as in the shadow ($\theta = 0°$); the standing-wave ratio is much greater in the shadow. An interesting difference is the appearance in Fig. 124 of current maxima instead of minima for most values of θ at kz = 0. This is a consequence of the presence of the horizontal arms which effectively change the conditions of axial resonance by providing large reflecting surfaces. In Fig. 124 the measured graphs have been extrapolated to the junction with the horizontal member. The parts of the graphs in broken lines are, therefore, estimates only.

The distribution of charge density on the vertical cylinder is shown in Fig. 125. Below the horizontal arms it is remarkably like the ideal theoretical distribution shown in Fig. 108 in both shadowed and illuminated regions. The distortion of the curves in the illuminated region — which is observed in the measured curves in Fig. 121 for the cylinder without the cross — is completely absent. A similar effect was noted for the crossed

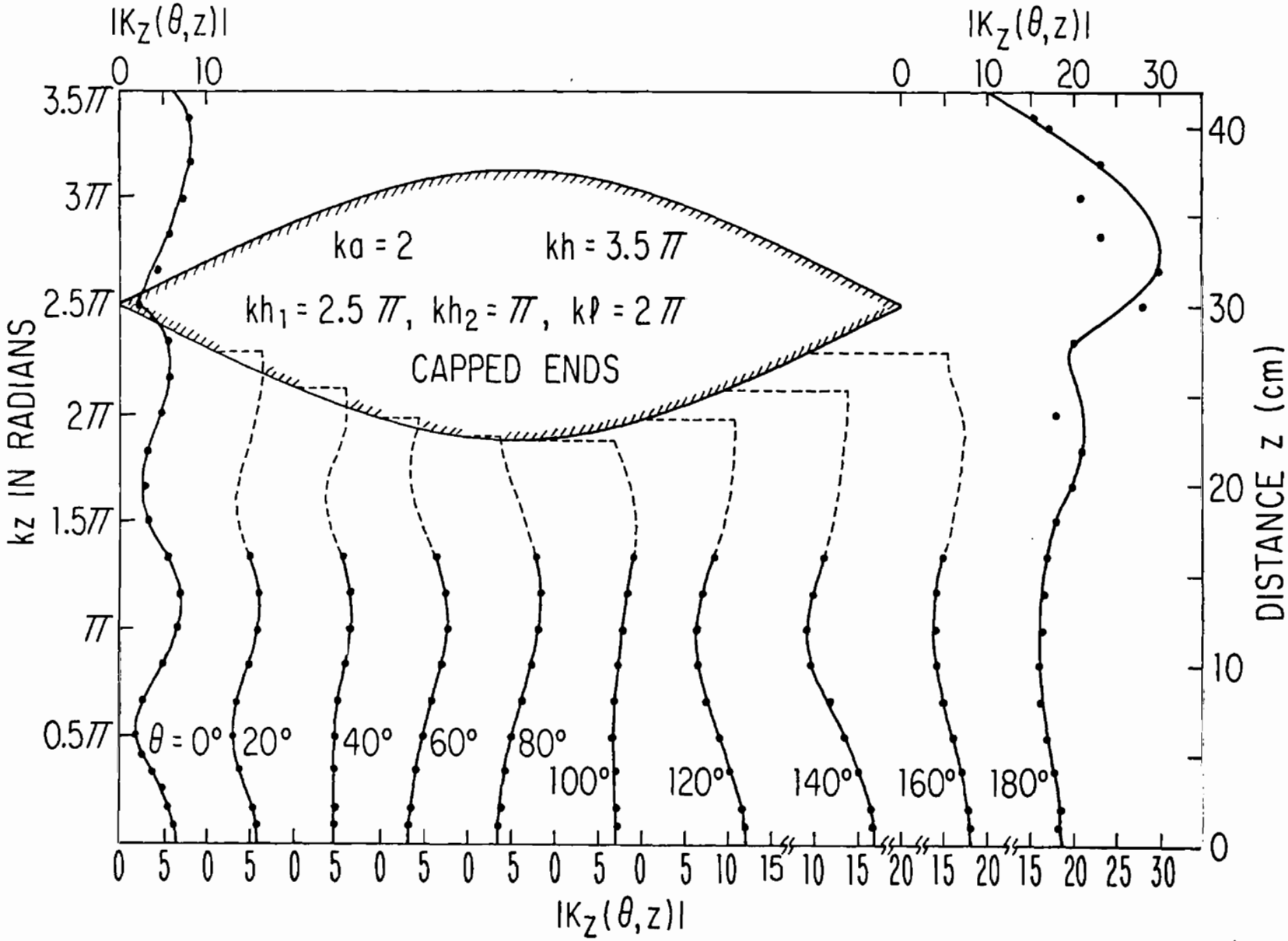

Fig. 124. Measured magnitude of surface density of axial outside current on vertical member of crossed cylinders with capped ends; E-polarization, λ = 24 cm. ($|K|$ in arbitrary units.)

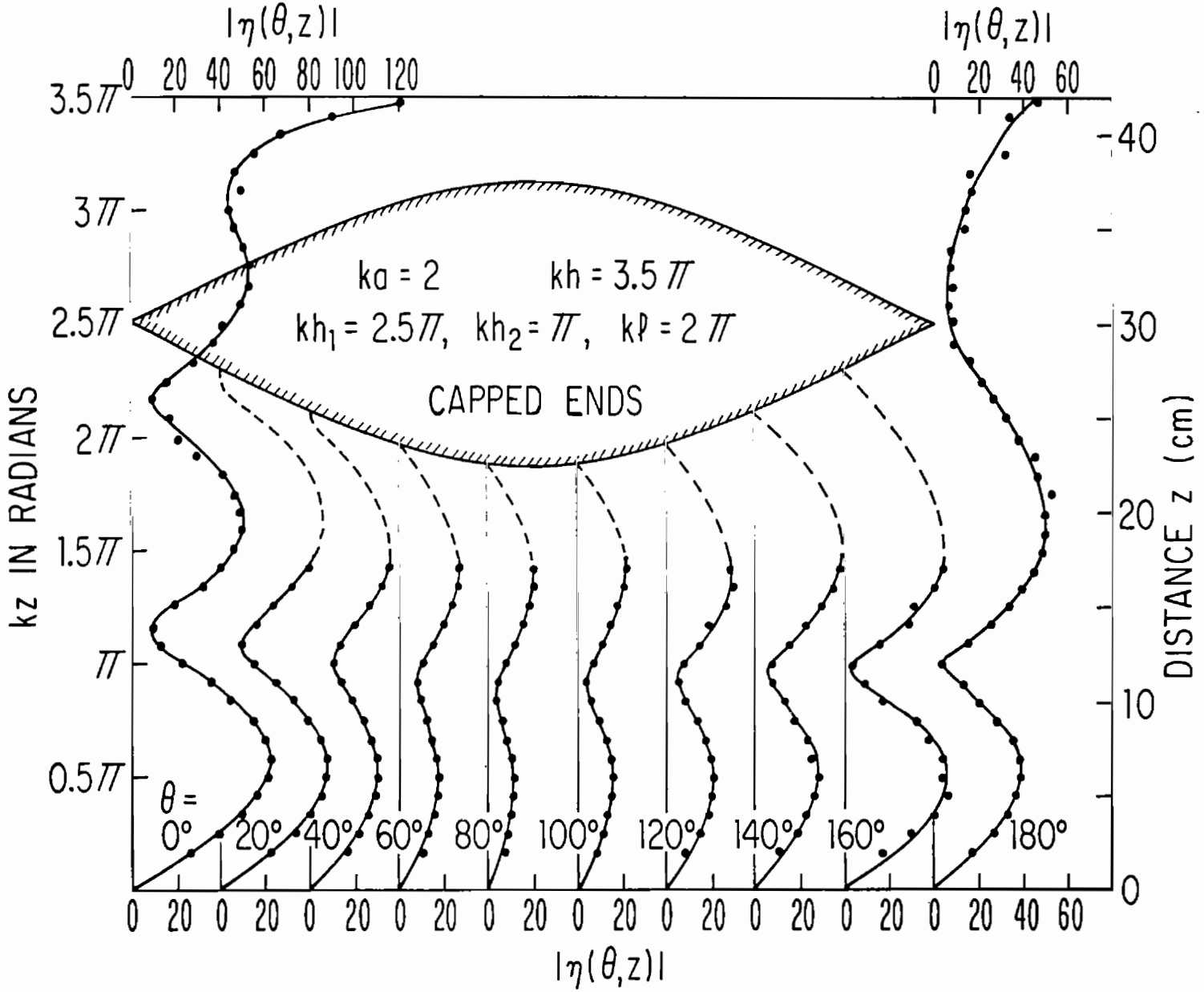

Fig. 125. Measured magnitude of surface density of outside charge on vertical member of crossed cylinders with capped ends; E-polarization, λ = 24 cm. ($|\eta|$ in arbitrary units.)

cylinders with ka = 1. Evidently, the contribution to the electric field near the vertical cylinder by the adjacent currents and charges on the horizontal arms cancels the effects of the spherical wave front and provides distributions substantially like those expected with an incident plane wave (Fig. 108). The graphs in Fig. 125 have been extrapolated to the junction lines between the horizontal and vertical cylinders, where the charge density must vanish at the sharp inside corners. These exist all along the junction lines except near $\theta = 0°$ and $\theta = 180°$. A contour diagram showing surfaces of constant charge density, constructed from Fig. 125, is shown in Fig. 126. Clearly visible are the ridges of the charge density around the cylinder at $kz \doteq 0.5\pi$ and 1.5π with maxima in both the shadow ($\theta = 0°$) and the illuminated region ($\theta = 180°$). The charges at $\theta = 0°$ and $\theta = 180°$ have opposite signs and there is a deep minimum (null) between them at $\theta = 90°$.

6. MEASUREMENTS ON CROSSED CYLINDERS; THE HORIZONTAL ARMS

The measured surface density of charge on one of the symmetrical horizontal arms is shown in Fig. 127; the associated contour diagram is in Fig. 128. Although the actual distance from the junction lines of the cross to the nearest approach of the movable probes is the same as for ka = 1, the electrical distance with ka = 2 is twice as great. The range over which estimated curves are needed is, therefore, relatively much larger. It extends from the nearest measurements (at x = 17 cm) to the junction lines (where the charge density vanishes) which are located between x = 0 and about x = 8 cm. The broken-line parts of the graphs in Fig. 127 represent the estimated locations which provide the consistent and smoothly varying contours of constant charge shown in Fig. 128.

As in the theoretical graphs in Figs. 117 and 118 for an isolated cylinder with ka = 2 in an H-polarized field, the measured charge density on the horizontal member of the cross increases to maxima at the points $\theta = 60°$ and $300°$, $x = \ell$. Along the line $\theta = 60°$ in Fig. 117 (and $\theta = 300°$) it increases with a superimposed axial standing wave from $kx = 0$ to $kx = k\ell = 3.5\pi$. If the measured charge distributions in the electrical distance within 1.5π of the open end in Fig. 127 are compared with the corresponding theoretical distributions on the isolated cylinder in Fig. 117, they are

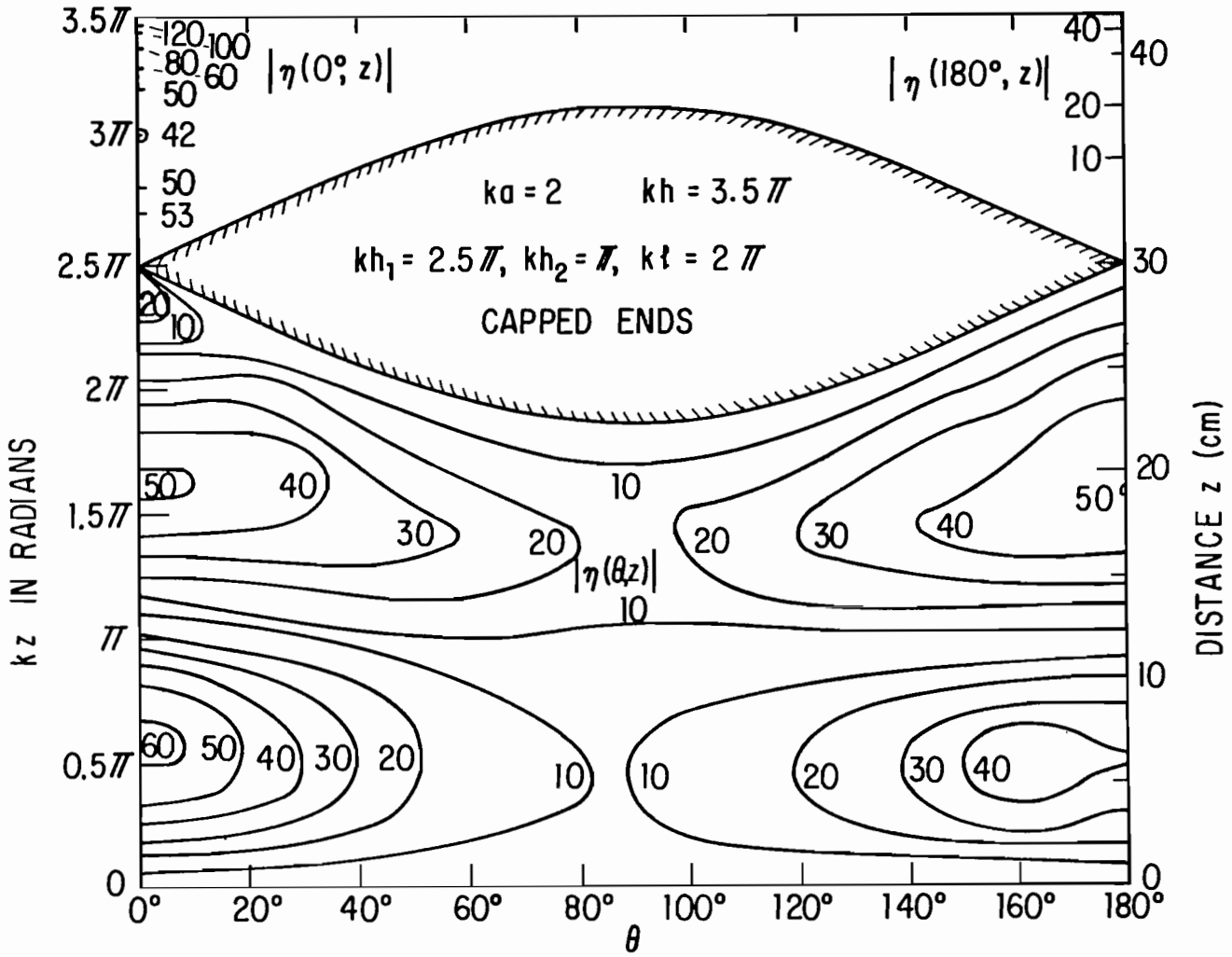

Fig. 126. Measured contours of constant magnitude of surface density of outside charge on vertical member of crossed cylinders with capped ends; E-polarization, λ = 24 cm. ($|\eta|$ in arbitrary units.)

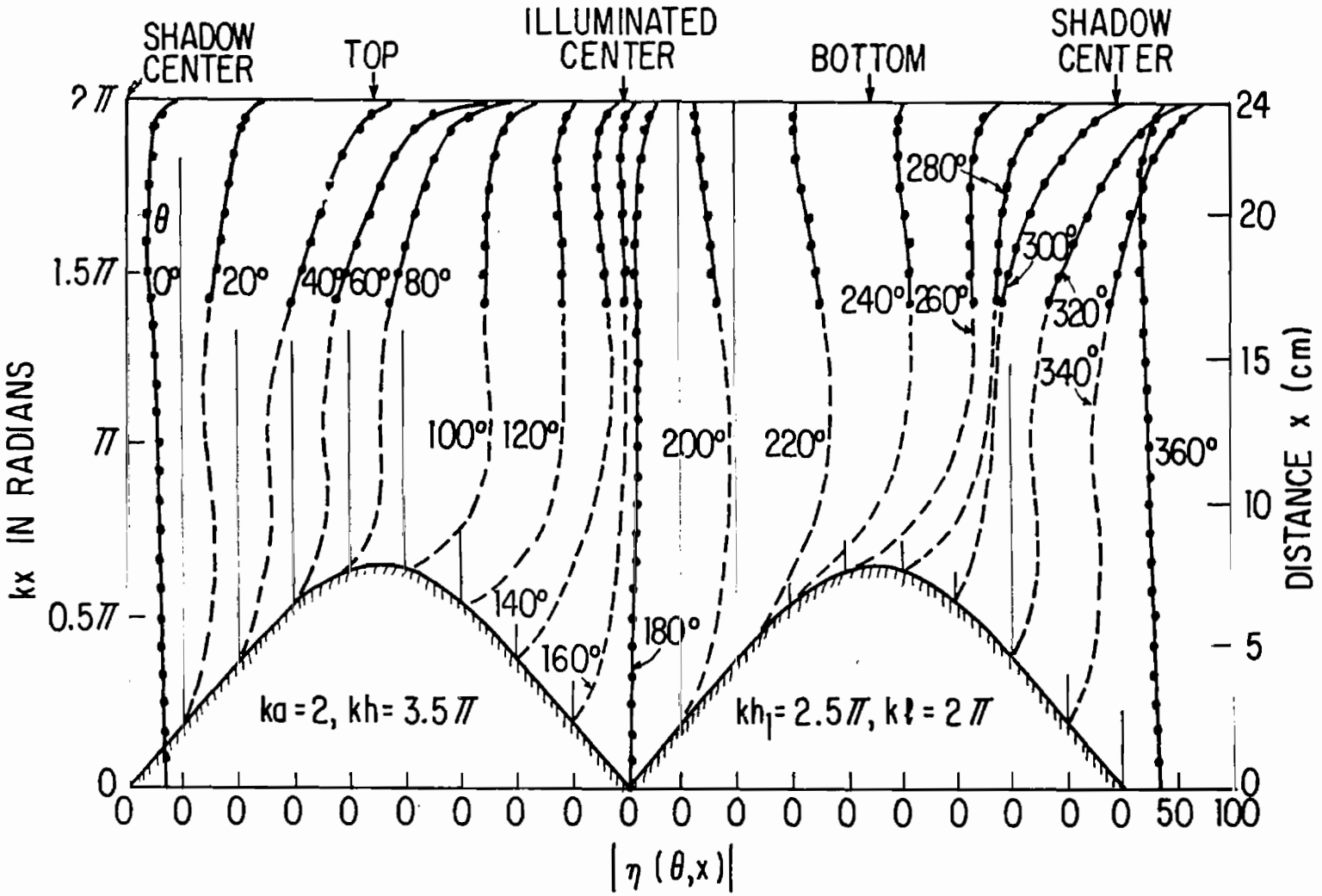

Fig. 127. Measured magnitude of surface density of outside charge on horizontal member of crossed cylinders with capped ends; H-polarization, λ = 24 cm. ($|\eta|$ in arbitrary units.)

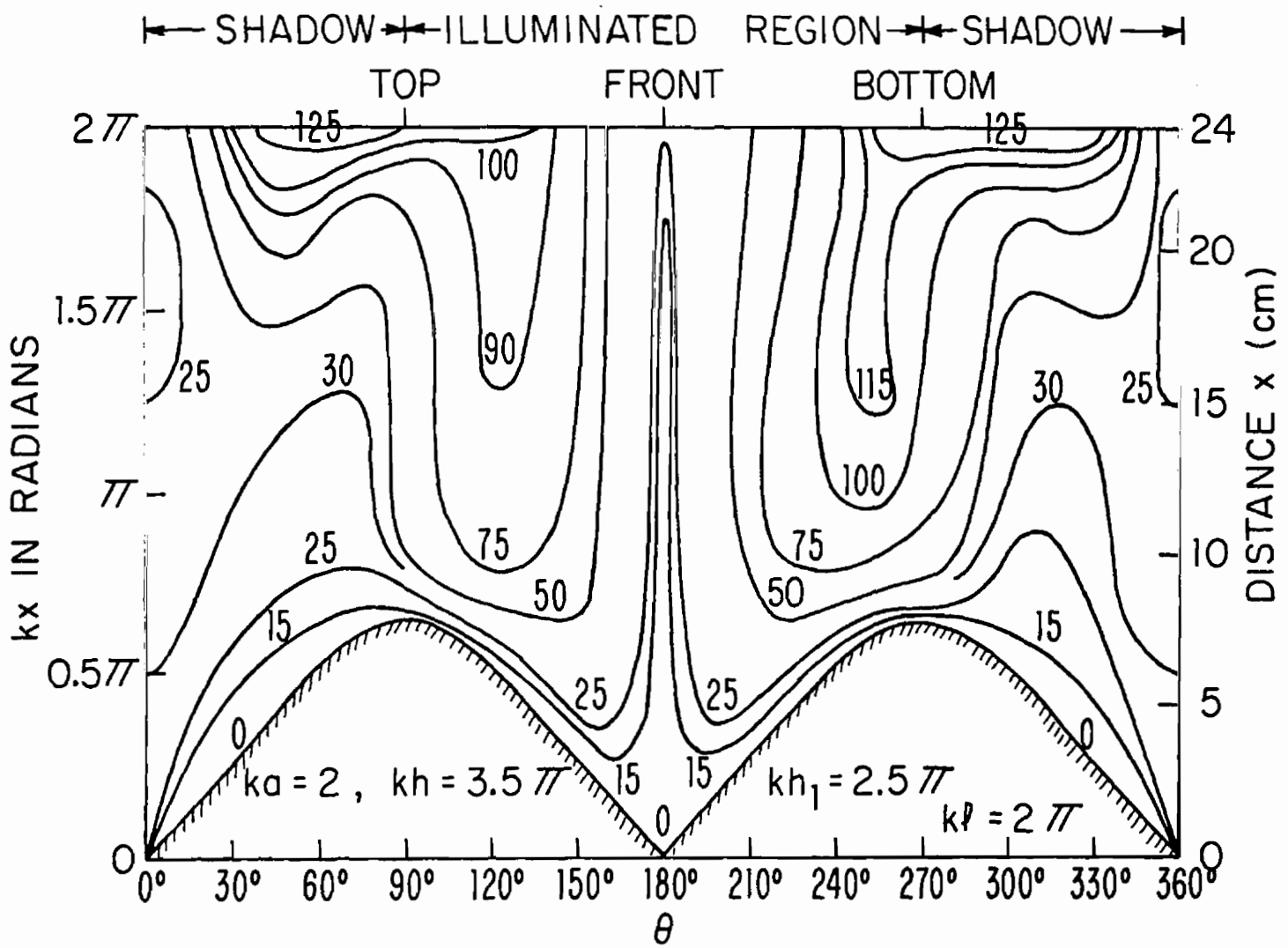

Fig. 128. Measured contours of constant magnitude of surface density of outside charge on horizontal member of crossed cylinders with capped ends; H-polarization, $\lambda = 24$ cm. ($|\eta|$ in arbitrary units.)

seen to be in general agreement in the shadow region within the requirement that the charge vanish at the junction line. However, in the illuminated region there is a very significant difference in that in the measured data for the cross the maxima of charge move from the lines $\theta = 60°$ and $300°$ near and at the open end toward the illuminated side as the cross is approached. Thus, as seen from Fig. 128, the maxima of the charge density occur near $\theta = 120°$ and $240°$ in the range $0.5\pi \leq kx \leq 1.5\pi$ and approach to within $20°$ of $\theta = 180°$ near $kx \doteq 0$. The effect of the presence of the vertical cylinder in moving the charge maxima from their normal positions with $ka = 2$ near $\theta = 60°$ and $300°$ toward the illuminated side is consistent with the very similar effect for crosses with $ka = 1$. In this case the maxima of the charge density are moved from their normal positions at $\theta = 90°$ and $270°$ toward the illuminated side.

The measured current density on the horizontal arms of the cross is shown in Figs. 129 and 130 for the two components, $K_\theta(\theta,x)$ and $K_x(\theta,x)$. The magnitude of the larger, transverse component $K_\theta(\theta,x)$ is shown in Fig. 129. As on the isolated cylinder (Fig. 115, bottom), this component of current is quite constant in amplitude with respect to kx with only a small oscillation until quite close to the open end where it rises somewhat. The measured component $|K_x(\theta,x)|$ on the horizontal member of the cross is shown in Fig. 130; it has an axial standing-wave pattern much like that on the isolated cylinder (Fig. 115, top). This is associated with the related axial standing wave of the surface density of charge shown in Figs. 127 and 128.

7. CONCLUSION

The study of crossed cylinders with $ka = 2$ is complicated by the existence of a propagating TE_{11} waveguide mode in the interior of the theoretically assumed infinitely thin-walled model and its absence in the actual cylinders with an inside radius slightly below cut-off. However, the theoretically determined outside currents and charges have distributions sufficiently like those that would obtain if there were no coupling to a propagating interior mode to be useful in the interpretation of measured distributions on single cylinders in both E- and H-polarized plane-wave fields and on crossed cylinders with the vertical member in an E-polarized

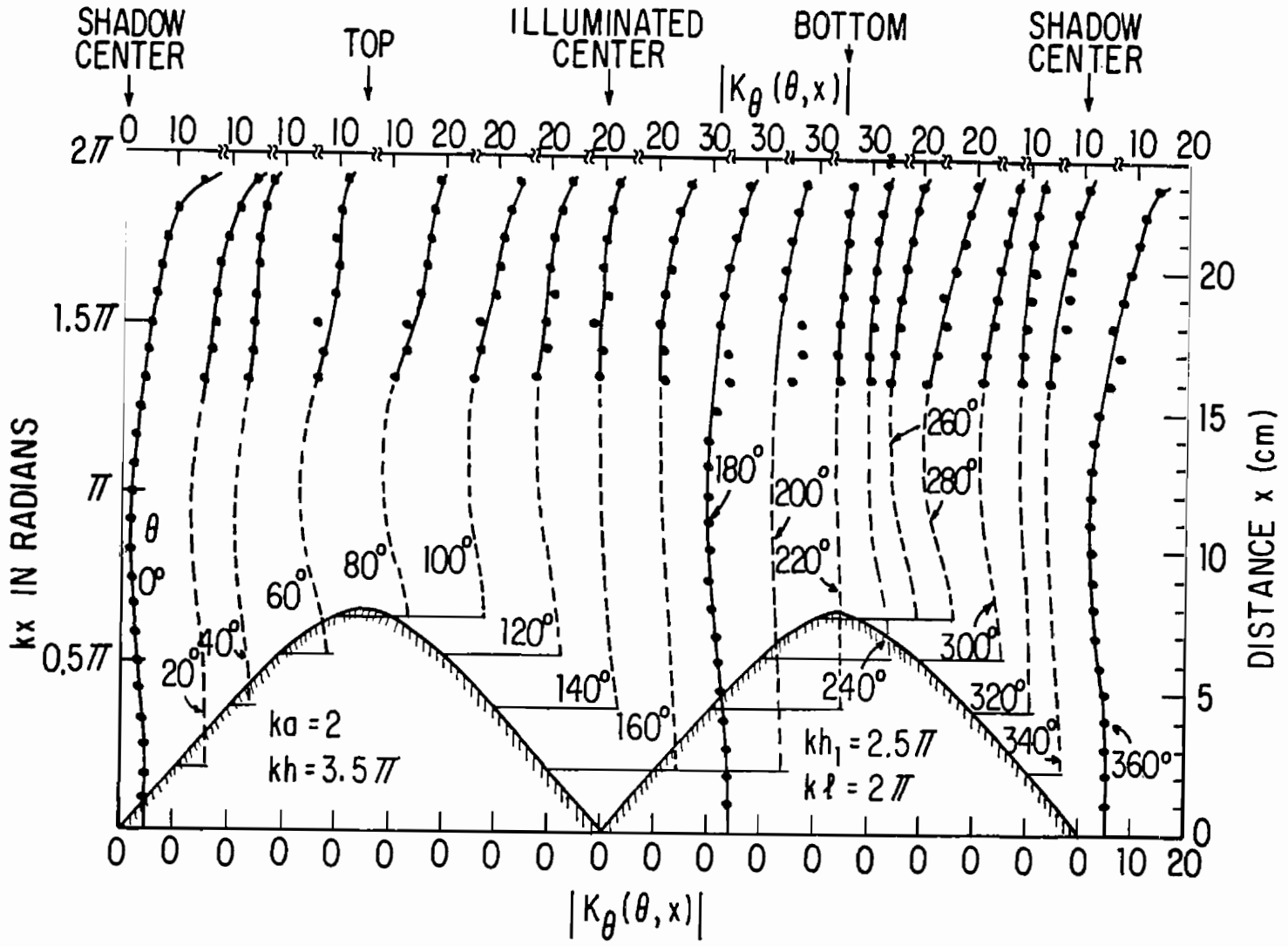

Fig. 129. Measured magnitude of surface density of transverse outside current on horizontal member of crossed cylinders with capped ends; H-polarization, λ = 24 cm. (|K| in arbitrary units.)

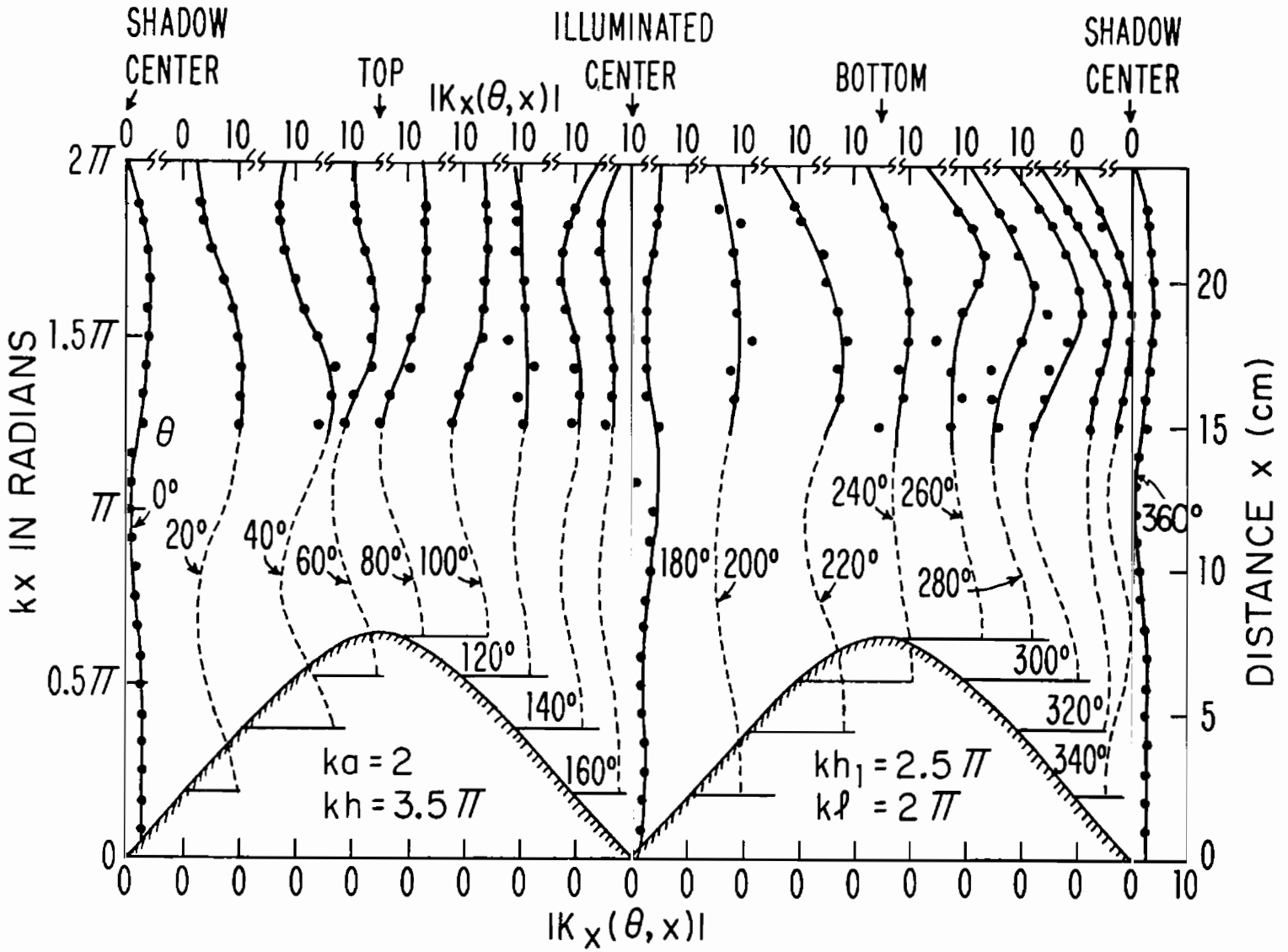

Fig. 130. Measured magnitude of surface density of axial outside current on horizontal member of crossed cylinders with capped ends; H-polarization, λ = 24 cm. (|K| in arbitrary units.)

field, the horizontal arms in an H-polarized field. Except for changes in the transverse distributions resulting from the larger circumference, the current and charge densities on single cylinders and crosses with ka = 2 resemble those on the corresponding elements with ka = 1. The analytical representation for single cylinders in terms of a sum of transverse Fourier components is complicated by the requirement of several more terms in order to achieve sufficient accuracy. The use in the measurements of an incident field with a spherical instead of a planar wave front leads to differences entirely comparable to those encountered with thinner cylinders. They are limited essentially to the charge-density distribution on the illuminated side of the cylinder where the ideal axial standing-wave pattern is distorted significantly when monopole cylinders with electrical length of kh = 3.5π are used in a field originating 7.5 wavelengths away. This sensitivity of the charge density on the illuminated side to the nature of the incident wave front provides a useful tool for determining the degree to which a given field approximates a plane-wave front.

Theoretical and measured currents and charges on cylinders and crosses with ka = 1 and ka = 2 suggest that it should be possible to obtain a rough general picture of the distributions of currents and charges on cylinders with ka greater than 2, e.g., ka = 3 or ka = 4, from a study of the theoretical outside currents and charges on single cylinders with these values of ka. However, a set of measurements on single cylinders with the same ka and with capped ends should be made in order to determine the relative significance of the coupling to inside propagating modes in the theory and of the radial currents and associated charges on the experimentally used end caps.

SECTION VIII

ELECTRICALLY THICK CYLINDER CROSSED WITH A FLAT PLATE IN A NORMALLY INCIDENT, PLANE-WAVE FIELD, MEASUREMENTS;

Cylinder Dimensions: $ka = 1$, $kh = 3.5\pi$, $kh_1 = 2.5\pi$

Plate Dimensions: $k\ell = 1.5\pi$, $kL = 0.5\pi$, $kT = 0.054\pi$

1. INTRODUCTION

A systematic study of the distributions of current and charge induced on crossed metal structures was begun with electrically thin wires for which complete analytical (refs. 3 and 5) and experimental (refs. 1 and 2) solutions were obtained. The study was continued with crossed electrically thick tubular cylinders for which no theoretical analysis is available so that a primarily experimental investigation was carried out (Section VI). However, theoretical distributions of the currents and charges on isolated tubular cylinders with arbitrary lengths and radii were evaluated (Sections III and V) with E- and H-polarized illuminations both for standardizing the techniques of measurement (Section IV) and for interpreting the experimental observations on crossed cylinders. The initial measurements were carried out using cylinders and crossed cylinders with $ka = 1$. These were extended to cylinders and crossed cylinders with $ka = 2$ (Section VII) so that a fairly complete description of the distributions of current and charge on electrically thick crossed cylinders has been completed.

The next major step in an approach to a model of an aircraft is a study of the currents and charges on the surfaces of an electrically thick circular cylinder with a transverse member consisting of a flat plate as shown in Fig. 131. The vertical cylinder has a radius a and a length h above a large ground screen. The horizontal plate extends out equal distances ℓ from the surface of the cylinder. Its width is $2L$ and its thickness T. The plate is centered at the height h_1 above the ground plane. In carrying out the measurements, dimensions corresponding to those used with crossed cylinders were selected. Specifically, for the cylinder: $ka = 1$, $kh = 3.5\pi$ and $kh_1 = 2.5\pi$; for the plate: $k\ell = 1.5\pi$ so that $k(\ell + a) = 1.82\pi$, $kL = 0.5\pi$ and $kT = 0.054\pi$. With the origin of coordinates on the ground plane at the center of the cylinder, the cylinder extends from $z = 0$ to $z = h$ and the center line of the horizontal plate crosses the axis at $z = h_1$. The flat plate extends in the horizontal x-direction from $x = -(\ell + a)$ to

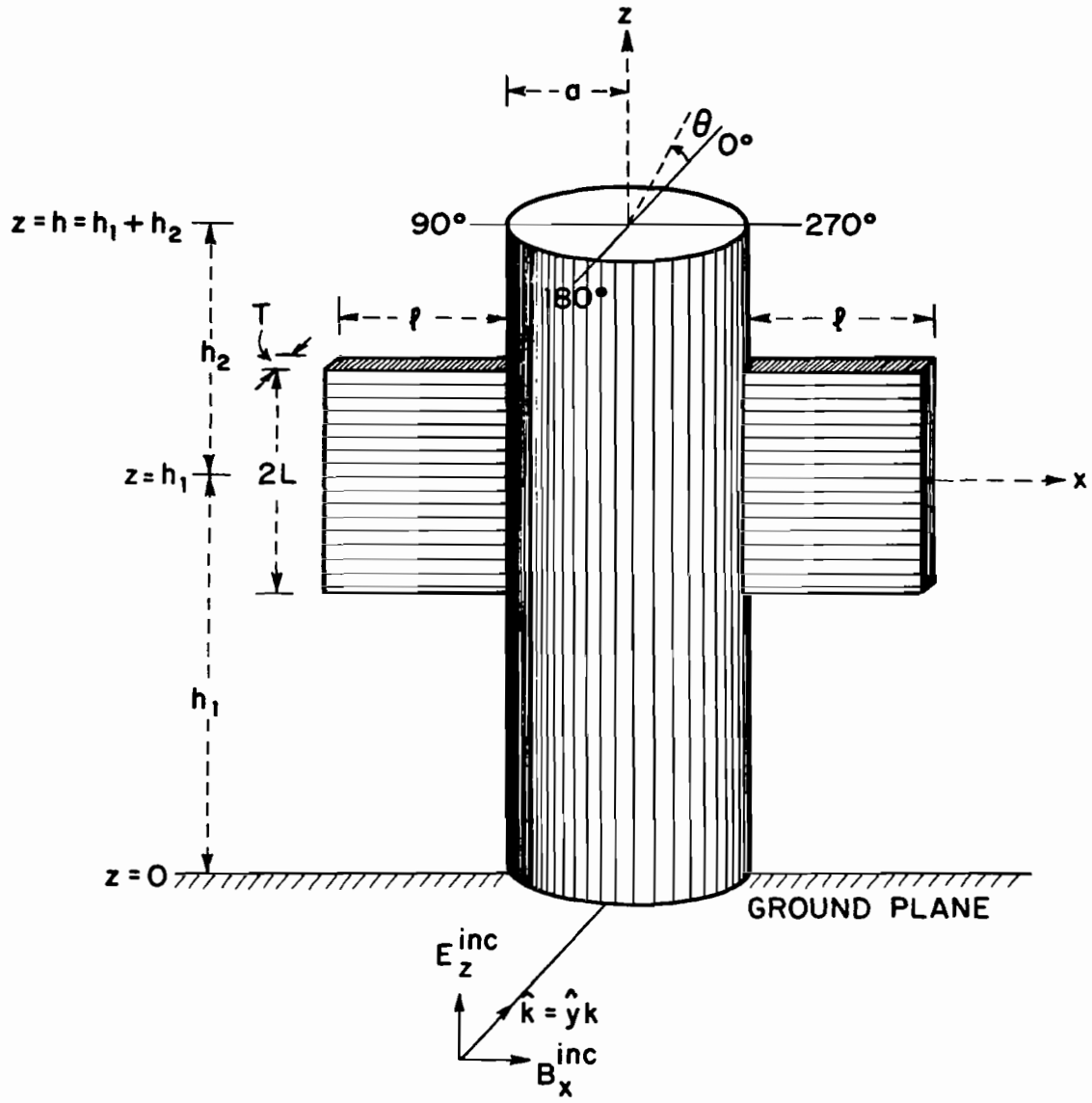

Fig. 131. Diagram of flat plate crossed with an electrically thick cylinder illuminated by a normally incident, plane-wave field. (The origin of the x axis is at the z axis.)

$x = -a$ and from $x = a$ to $x = \ell + a$; in the vertical direction it is bounded by $z = h_1 - L$ and $z = h_1 + L$. The incident plane electromagnetic wave travels in the direction of the positive y-axis with the electric field $\vec{E}^{inc} = \hat{z}E_z^{inc}$ and the magnetic vector $\vec{B}^{inc} = \hat{x}B_x^{inc}$. The propagation vector $\vec{k} = \hat{y}k$. The angle θ is measured around the z-axis from the positive y-axis so that the line $\theta = 0°$, $\rho = a$, is at the center of the shadow; the line $\theta = 180°$, $\rho = a$, is at the center of the illuminated region.

2. MEASUREMENTS

The measurement of the two components of the current density and the charge density on the crossed cylinder and plate were carried out in the same general manner as with crossed cylinders and with the same apparatus (Section VI). Slots with closed backs for the traveling current and charge probes were cut at the angles $\theta = 0°$, 20°, 40°, 60°, 75°, 105°, 120°, 140°, 160° and 180° along the entire length of the vertical cylinder. Similar slots in the horizontal element extended from $kx = ka = 1$ to $kx = k(a + \ell) = 1 + 1.5\pi$ at $kz - 2.5\pi = -1.44$, -1.22, -0.65, 0, 0.65, 1.22 and 1.44. All slots were kept covered. Measurements were made on the illuminated side of the horizontal plate when the slotted section pointed in the direction of $\theta = 270°$, on the shadow side when the slotted section pointed in the direction $\theta = 90°$.

3. MEASURED DISTRIBUTIONS OF THE CHARGE DENSITY ON THE VERTICAL CYLINDER

The charge-density distribution measured along the vertical cylinder is shown in its magnitude $|\eta(\theta,z)|$ in Fig. 132, in its relative phase angle θ_η in Fig. 133, both as a function of the distance z from the ground plane. A contour diagram of the magnitude of half of the cylinder is shown in Fig. 134. In each figure the location of the horizontal plate is indicated schematically. When compared with the corresponding distribution for the isolated cylinder in Fig. 65 (Section V), it is seen that the presence of the horizontal plate has a relatively very small effect in modifying the amplitude $|\eta(\theta,z)|$ except very close to the junction lines where the charge density drops to zero. In particular, and as compared with the theory for the isolated cylinder, the normal second maximum near $kz = 1.5\pi$ on the illuminated side ($\theta = 180°$) is virtually absent with and without the horizontal

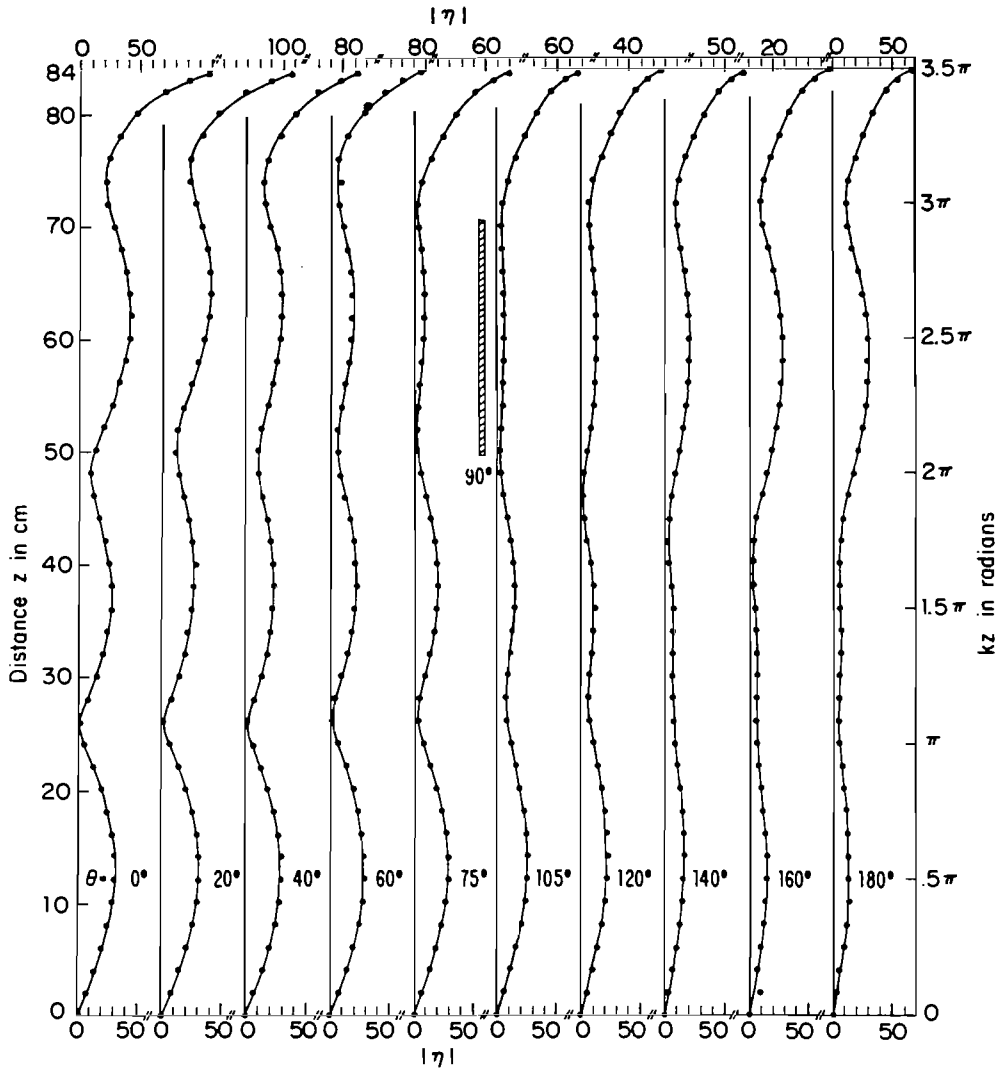

Fig. 132. Measured magnitude of surface density of charge on vertical cylinder with crossed flat plate; ka = 1, kh = 3.5π, kh_1 = 2.5π; kℓ = 1.5π, kL = 0.5π, kT = 0.054π. ($|\eta|$ in arbitrary units.)

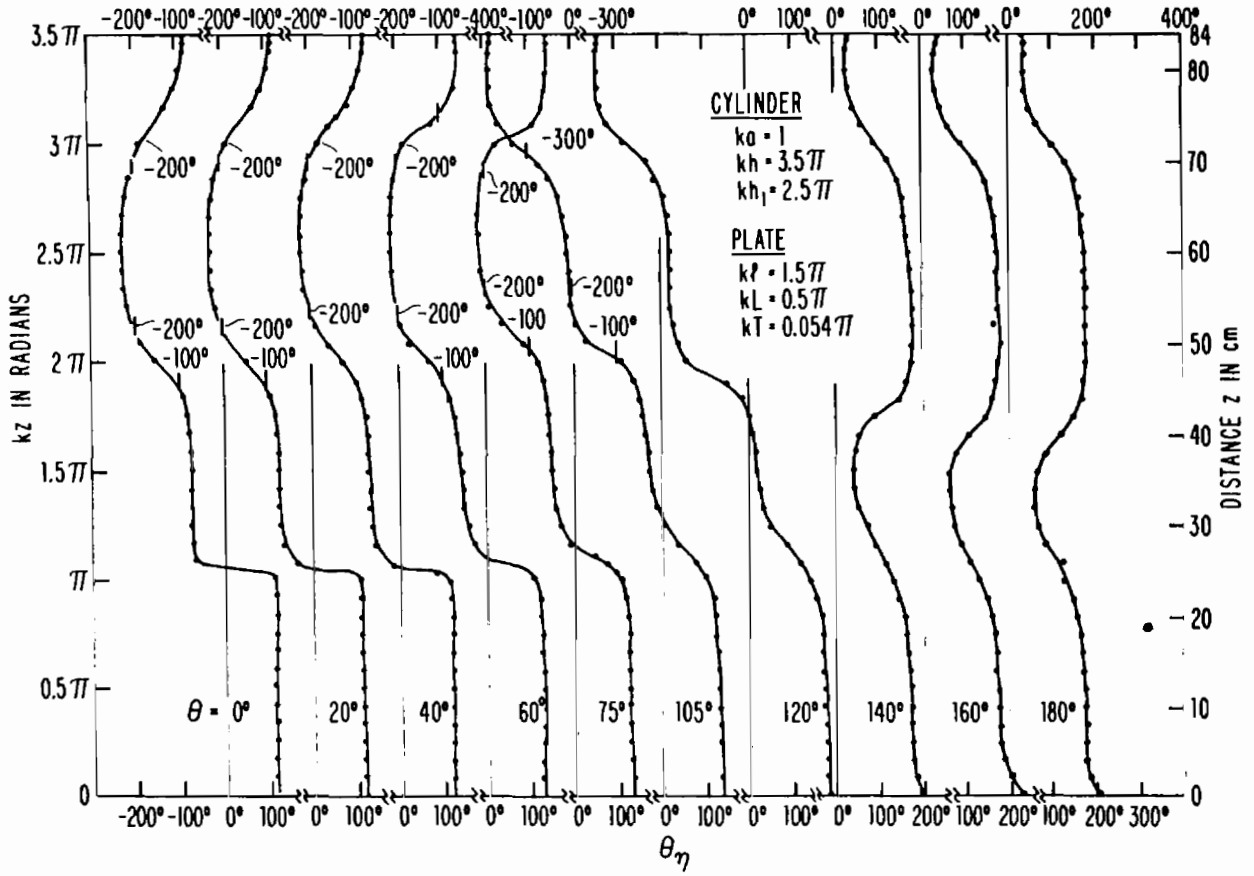

Fig. 133. Measured phase angle of the surface density of charge on vertical cylinder with crossed flat plate.

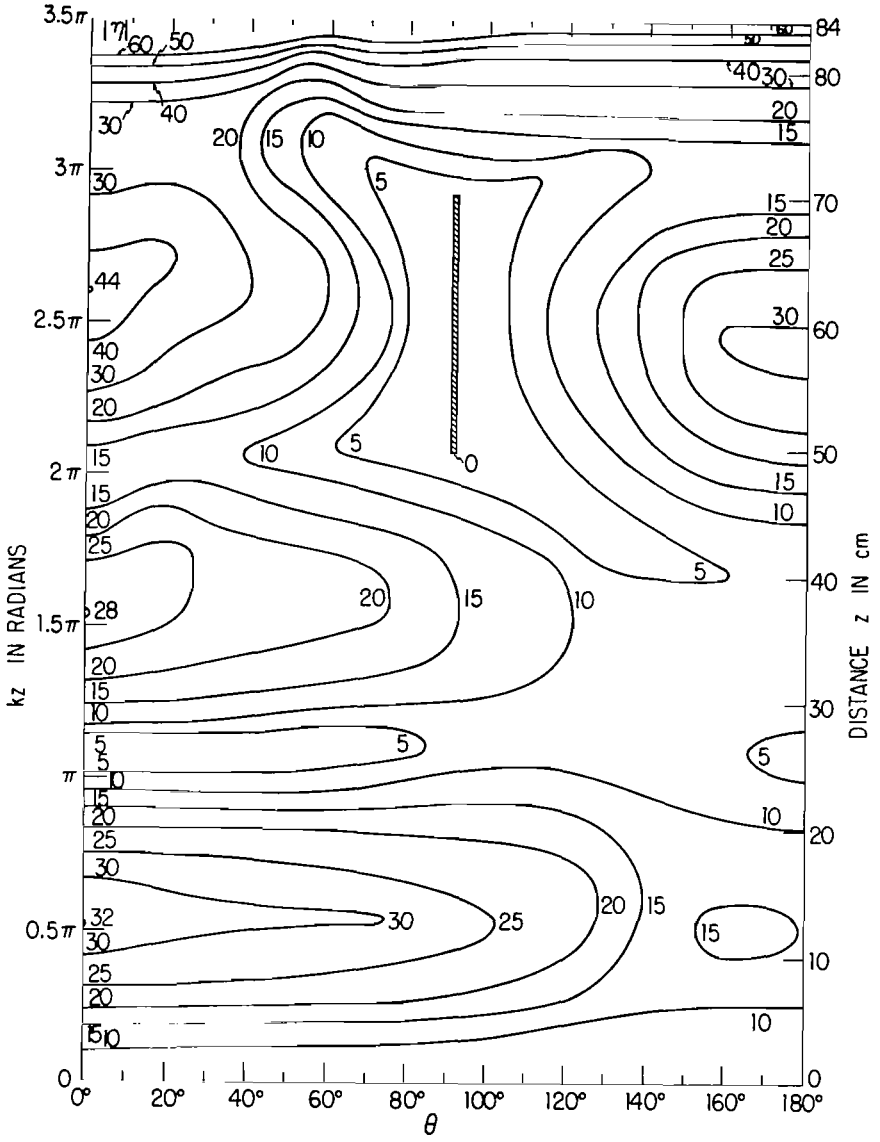

Fig. 134. Contour diagram of measured magnitude of surface density of charge on tubular cylinder with crossed flat plate; ka = 1, kh = 3.5π, kh_1 = 2.5π; kℓ = 1.5π, kL = 0.5π, kT = 0.054π. ($|\eta|$ in arbitrary units.)

plate. As shown in Section V in conjunction with Fig. 70, this is due to the use of an incident spherical wave in the measurements instead of the plane wave assumed in the theory. At moderate distances from the junction the distribution of $|\eta(\theta,z)|$ with a horizontal cylinder in place of the flat plate, shown in Fig. 89 in Section VI, is also quite similar when $k\ell = 1.5\pi$. For this length of the arms, the coupling between the charges on the horizontal member and those on the vertical cylinder is quite small, so that the dominant electric field acting along the illuminated side of the vertical cylinder is simply the incident field.

The relative phase angle θ_η of $\eta(\theta,z)$ shown in Fig. 133 differs from that shown in Fig. 90 for the same cylinder with a horizontal tube instead of a plate both on the illuminated side and on the shadow side especially in the range $1.5\pi \leq kz \leq 3\pi$. Much of this part of the vertical cylinder is behind or in front of the horizontal member where the shielding and reflecting effects of the tube with $ka = 1$ are understandably different from those of the plate with $kL = 0.5\pi$. However, this difference is sufficient only to modify the relative phase without much effect on the distribution curves of the relative amplitudes.

The features of the distribution of charge on the vertical cylinder are particularly evident in the contour diagram in Fig. 134. This shows the typical ridges of maximum charge at $kz = 0.5\pi$, 1.5π and 2.5π with minima between them near $kz = \pi$, 2π and 3π. The main evidence of the presence of the flat plate is the deep minimum all around the plate. The junction line is, of course, a line of zero charge density.

4. DISTRIBUTION OF CHARGE ON THE HORIZONTAL FLAT PLATE

The measured distributions of the magnitude of the charge density $|\eta(x,z)|$ on the illuminated and shadow sides of the horizontal flat plate are shown in Fig. 135 as functions of the electrical distance $k(x - a)$ from the surface of the vertical cylinder; the corresponding phase angles θ_η are in Fig. 136. The phase angles as a function of the electrical distance $kz - 2.5\pi$ from the horizontal center line are in Fig. 137. They show that in both amplitude and phase the standing-wave patterns on the illuminated and shadow sides are almost identical. Horizontally along the plate the magnitude of the charge density begins with zero along the junction line at

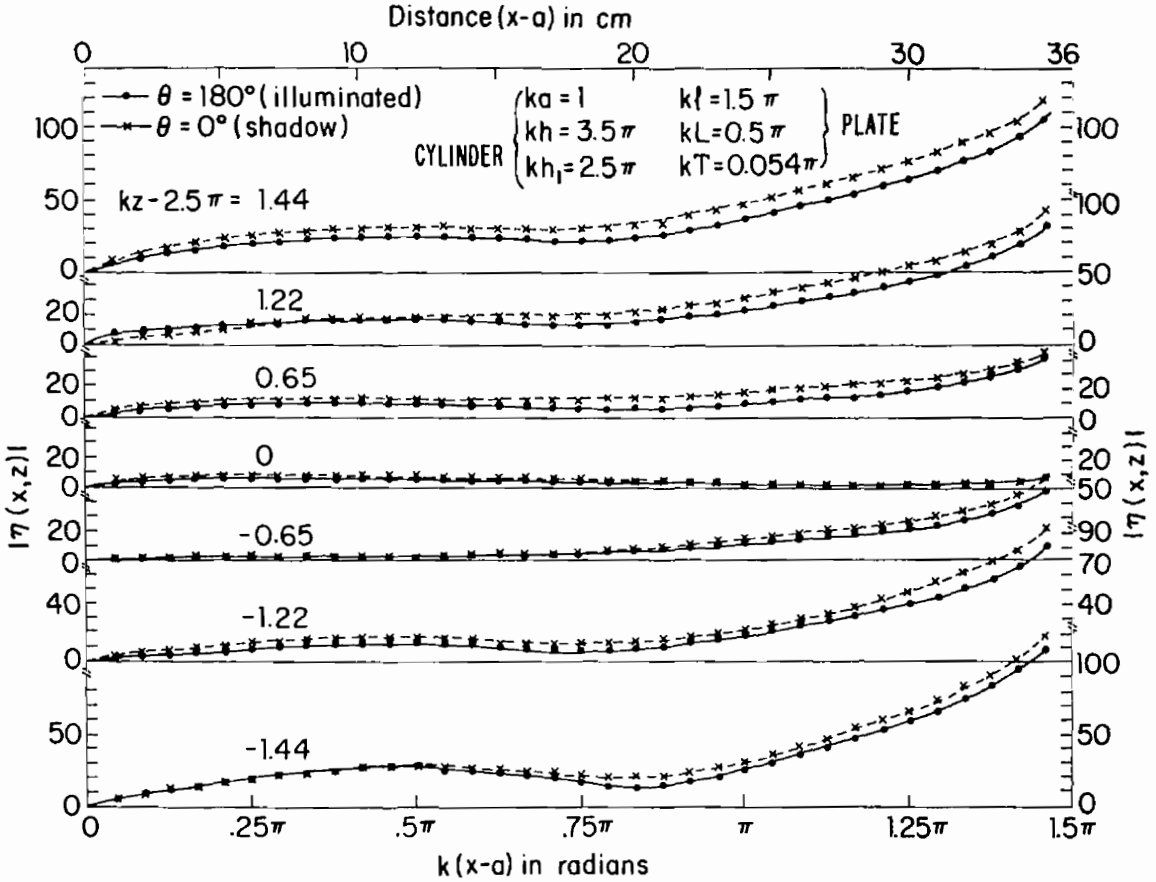

Fig. 135. Measured magnitude of surface density of charge on horizontal flat plate. ($|\eta|$ in arbitrary units.)

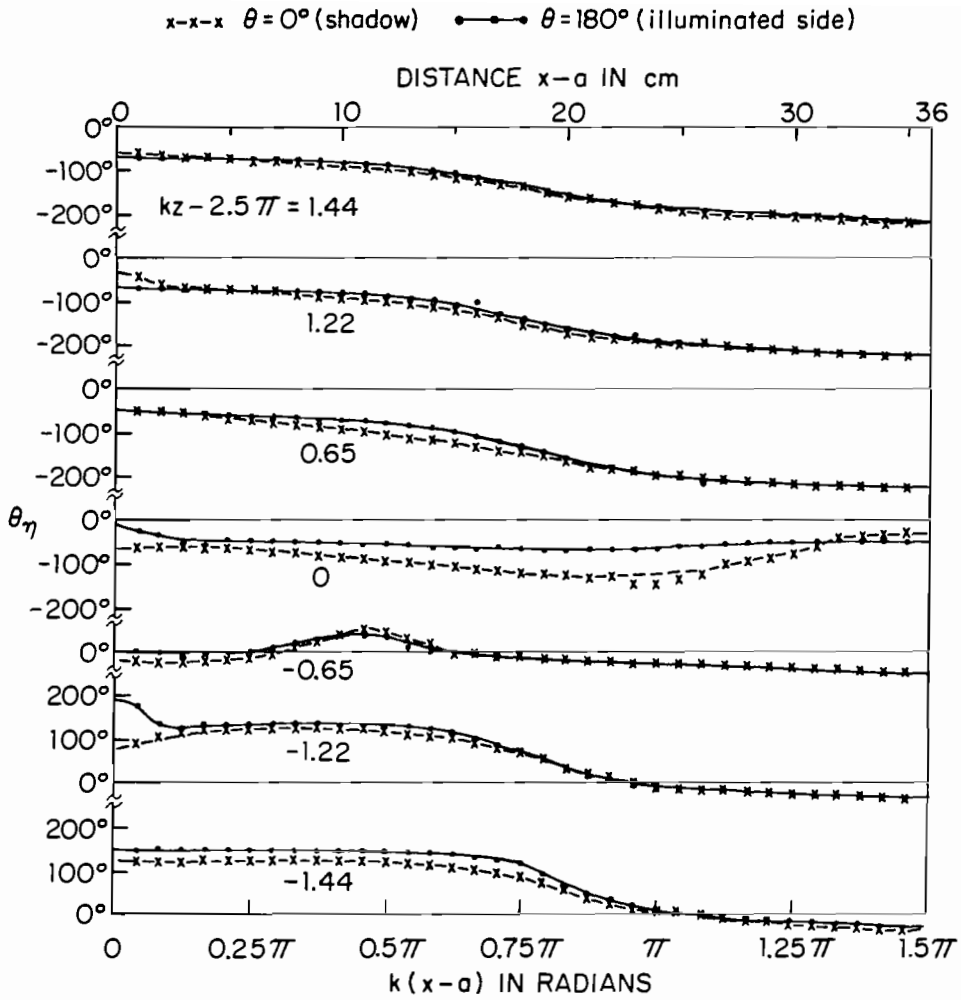

Fig. 136. Measured phase angle of the surface density of charge on horizontal flat plate; ka = 1, kh = 3.5π, kh_1 = 2.5π; kℓ = 1.5π, kL = 0.5π, kT = 0.054π.

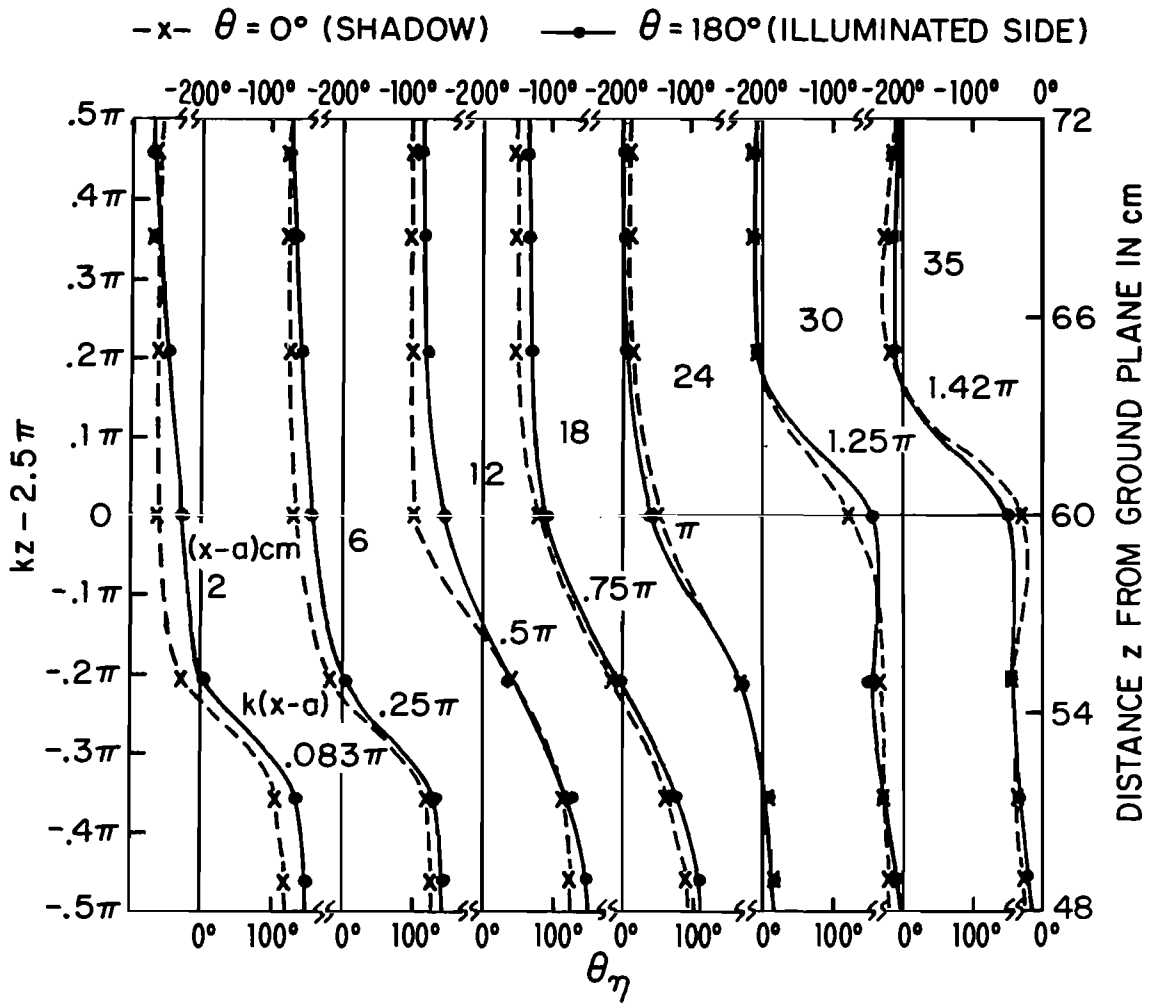

Fig. 137. Measured phase angle of the surface density of charge on horizontal flat plate; ka = 1, kh = 3.5π, kh_1 = 2.5π; kℓ = 1.5π, kL = 0.5π, kT = 0.054π.

$x = a$, rises to a maximum at $k(x - a) = 0.5\pi$, decreases to a minimum near $k(x - a) = 0.75\pi$, and rises to a much higher maximum at the free end, $k(x - a) = k\ell = 1.5\pi$. In the vertical direction $|\eta(x,z)|$ has a relative maximum along the bottom edge at $kz - 2.5\pi = -0.5\pi$. It decreases to a minimum near the center at $kz - 2.5\pi = 0$ and increases to another maximum along the top edge at $kz - 2.5\pi = 0.5\pi$. These distributions resemble those in Fig. 97 for the crossed cylinders. The phase curves show that when the two-dimensional standing-wave pattern has a positive maximum along the bottom edge at $kz - 2.5\pi = -0.5\pi$, $k(x - a) = 0.5\pi$, it has a negative maximum along the top edge at $kz - 2.5\pi = 0.5\pi$, $k(x - a) = 0.5\pi$. Similarly, the maximum at the bottom corner $kz - 2.5\pi = -0.5\pi$, $k(x - a) = 1.5\pi$ is positive, that at the top corner $kz - 2.5\pi = 0.5\pi$, $k(x - a) = 1.5\pi$ is negative. These standing-wave distributions are especially clear on the contour diagrams in Figs. 138 and 139. Note the large maxima at the corners on the right and the much smaller ones at $k(x - a) = 0.5\pi$ along the upper and lower edges. Note also the large areas with very little charge that extend from the entire left side — the junction line with the vertical cylinder — outward toward the free end. The actual minimum — shown in dashed lines — is displaced downward from the horizontal center line. This is a consequence of the asymmetry induced by the presence of the charges on the vertical cylinder. These are, of course, not symmetric with respect to the horizontal center line of the flat plate.

A complete picture of the distributions of charge magnitude on both the vertical cylinder and the horizontal flat plate is provided by the full scale contour diagrams of the illuminated and shadow sides in Figs. 140 and 141.

5. DISTRIBUTIONS OF CURRENT

As for both the isolated cylinder and the crossed cylinders, the current density on the vertical member of the cylinder with crossed plate consists essentially only of the axial component $K_z(\theta,z)$ except near the open end. The transverse component $K_\theta(\theta,z)$ is negligibly small everywhere except within a quarter wavelength of the open end where it rises steeply to large values. The measured magnitude of the axial current on the cylinder with the crossed flat plate is shown in Fig. 142 as a function of kz with θ as the parameter. The distributions resemble those for the isolated cylinder

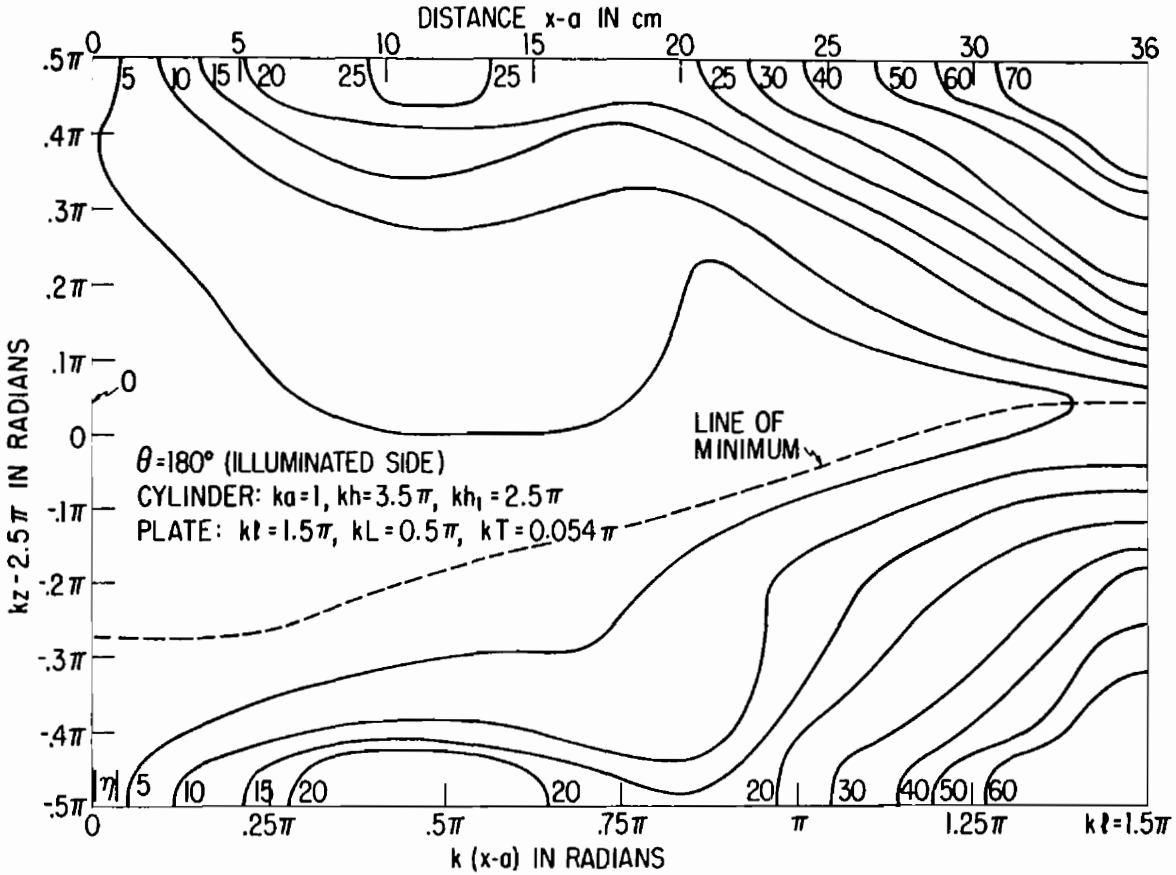

Fig. 138. Contour diagram of measured magnitude of surface density of charge on horizontal flat plate. ($|\eta|$ in arbitrary units.)

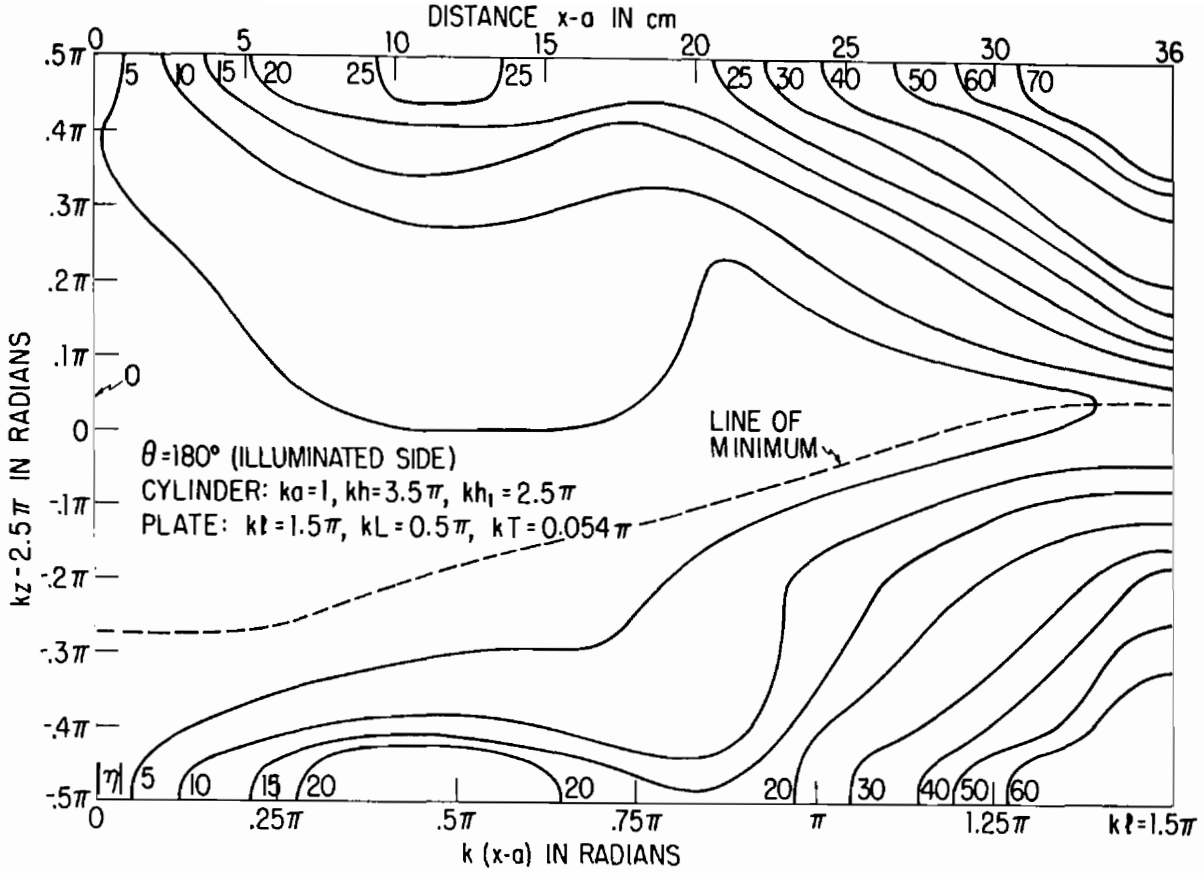

Fig. 139. Contour diagram of measured magnitude of surface density of charge on horizontal flat plate. ($|\eta|$ in arbitrary units.)

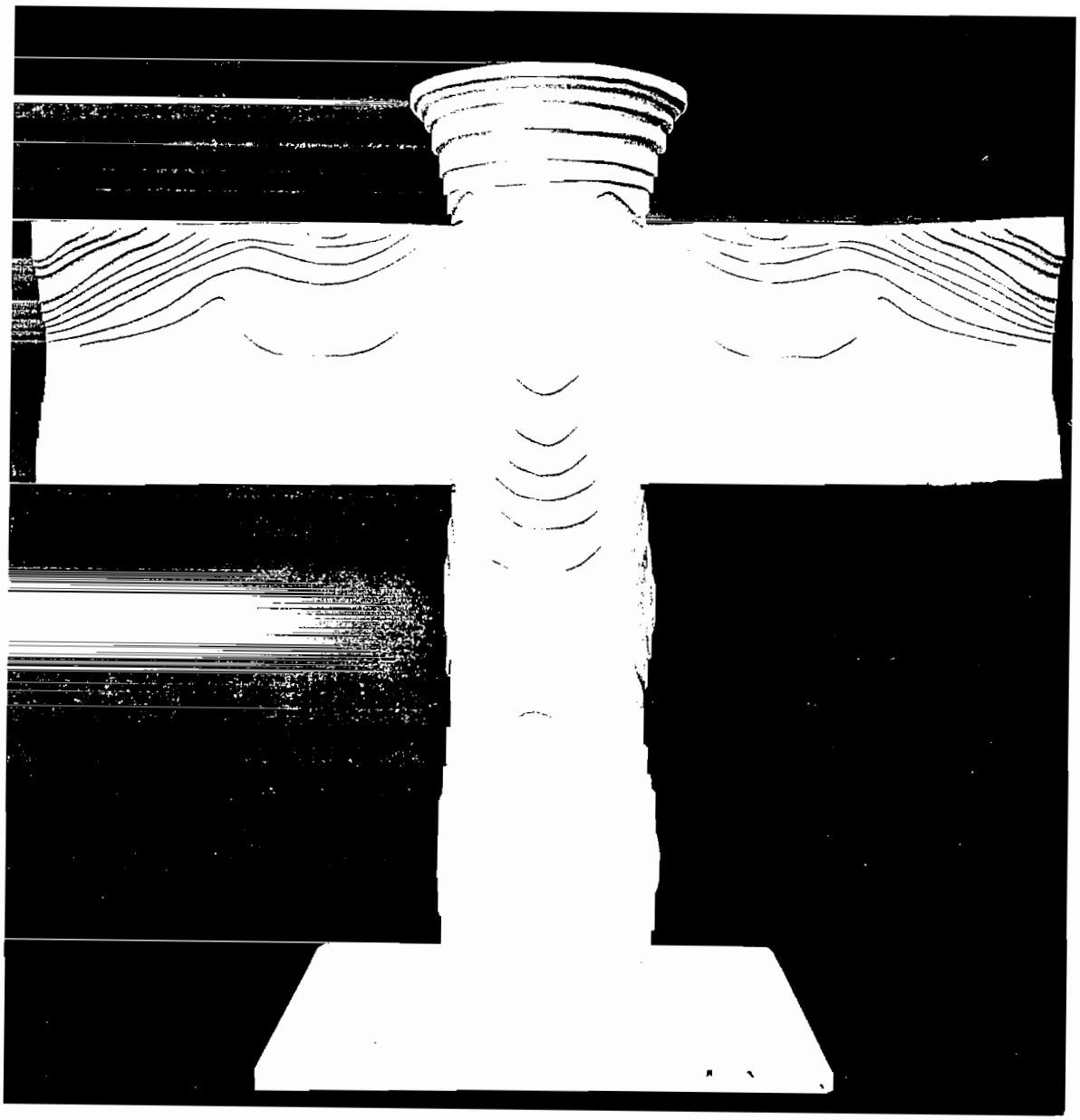

Fig. 140. Relief map of the magnitude of the charge densities $\eta(\theta,z)$ and $\eta(x,z)$ on a vertical tubular cylinder ($ka = 1$, $kh = 3.5\pi$, $kh_1 = 2.5\pi$) crossed with a horizontal flat plate ($k\ell = 1.5\pi$, $kL = 0.5\pi$, $kT = 0.054\pi$). View of illuminated side. ($|\eta|$ in arbitrary units.)

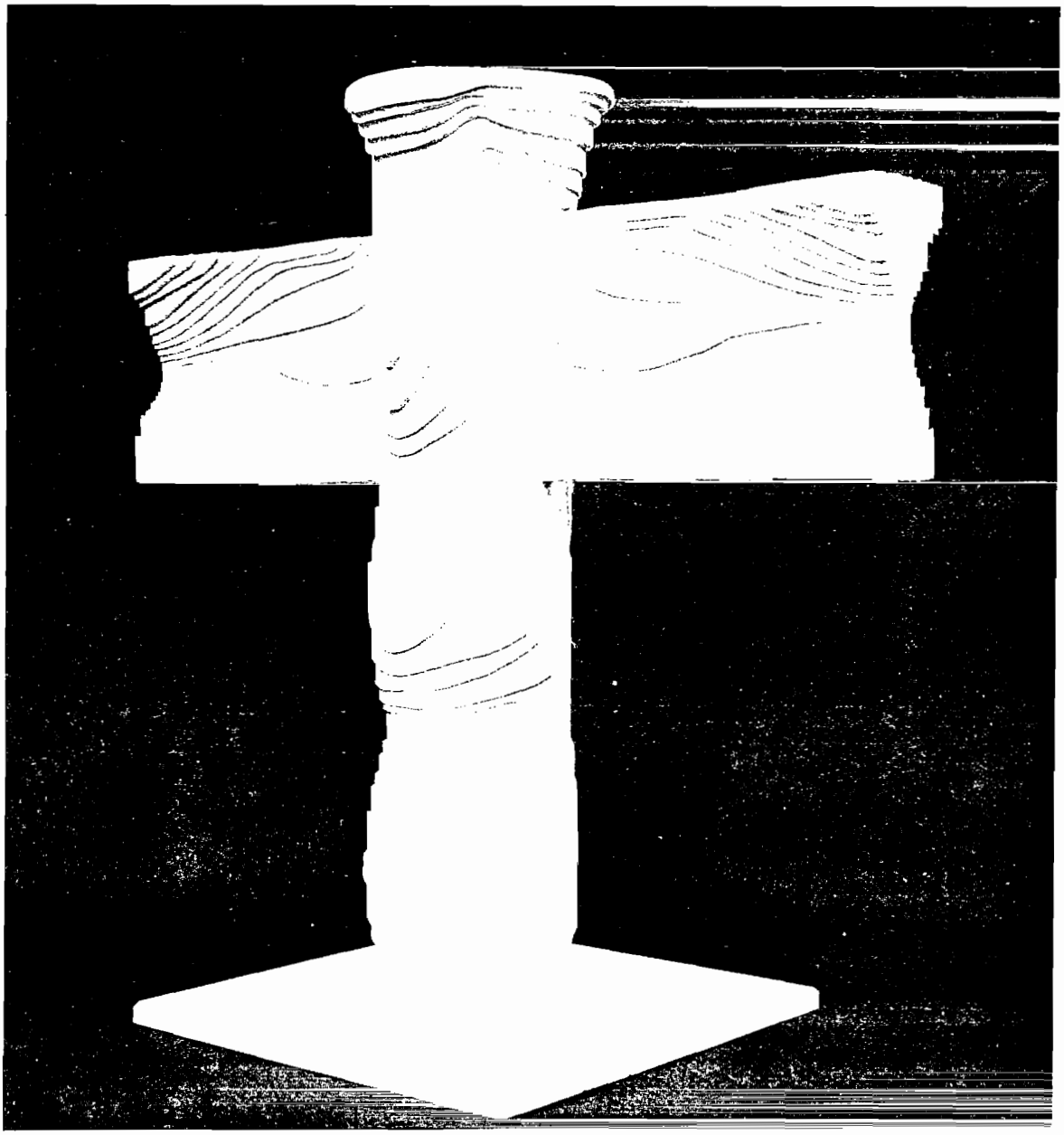

Fig. 141. Like Fig. 140 but viewed from shadowed side.

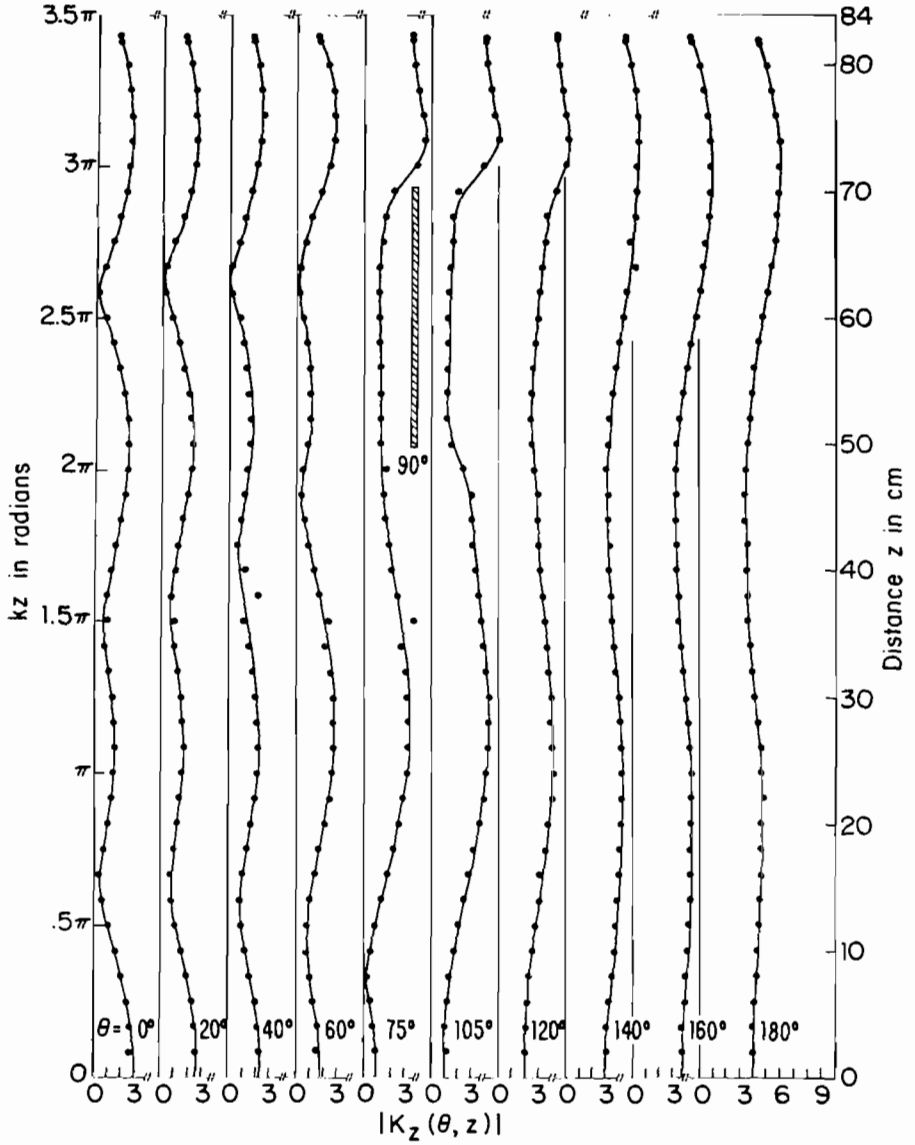

Fig. 142. Measured magnitude of surface density of axial current on vertical cylinder with crossed flat plate; ka = 1, kh = 3.5π, kh_1 = 2.5π; kℓ = 1.5π, kL = 0.5π, kT = 0.054π. (|K| in arbitrary units.)

in Fig. 64 in Section V and for the crossed cylinders in Fig. 98 in Section VI. The range near the junction where this has a significant effect is, of course, much smaller with the thin horizontal plate than with the horizontal cylinder.

The current density $\vec{K}(x,z)$ on the horizontal plate consists of two components, the transverse part $K_z(x,z)$ and the longitudinal part $K_x(x,z)$. The former is excited directly by the incident field $\vec{E}^{inc} = \hat{z}E_z^{inc}$, the latter exists only because the horizontal member is finite in length with charge concentrations at the open ends that excite longitudinal currents. (On an infinitely long strip, $K_x(x,z) = 0$ when $\vec{E}^{inc} = \hat{z}E_z^{inc}$.) The magnitude of $K_z(x,z)$ depends on the magnitude of the incident field and on the electrical width 2kL of the plate. In the measurements this was selected to be $2kL = \pi$ since the theory of the infinitely long strip (ref. 15) shows that this width yields a transverse current with a maximum amplitude. This is to be expected since in any resonant standing-wave pattern the distance between maxima of positive and negative charges is near a half wavelength.

The longitudinal distributions of the magnitude $|K_z(x,z)|$ of the transverse currents on both the illuminated ($\theta = 180°$) and shadowed ($\theta = 0°$) sides of the plate are shown in Fig. 143 with $k(x - a)$ as the variable and $kz - 2.5\pi$ as the parameter. Along the junction line on the left where the charge density $\eta(a,z) = 0$, the current density $K_z(a,z) = 0$. With only a very small superimposed oscillation, $K_z(x,z)$ for each value of $kz - 2.5\pi$ rises steadily with increasing x to a maximum near the open end. The distributions on both sides of the plate are similar, but the amplitude is substantially larger on the illuminated side. The associated phase angle θ_z is shown in Fig. 144. The transverse currents on the two sides differ in phase by an angle that decreases from the junction line at $x = a$ to the open end at $x = a + \ell$ where it approaches zero. The transverse distribution of $K_z(x,z)$ at selected values of x is shown in Fig. 145 in both amplitude and phase. It differs substantially from the ideal distribution on an infinitely long strip with the same width (ref. 15) as a consequence of the presence of longitudinal currents $K_x(x,z)$, the amplitudes and phases of which are shown, respectively, in Figs. 146 and 147. Although $K_x(x,z)$ has a generally much smaller amplitude than $K_z(x,z)$, it is very significant near the edges at $kz = 2\pi$ and 3π where it is comparable in magnitude to

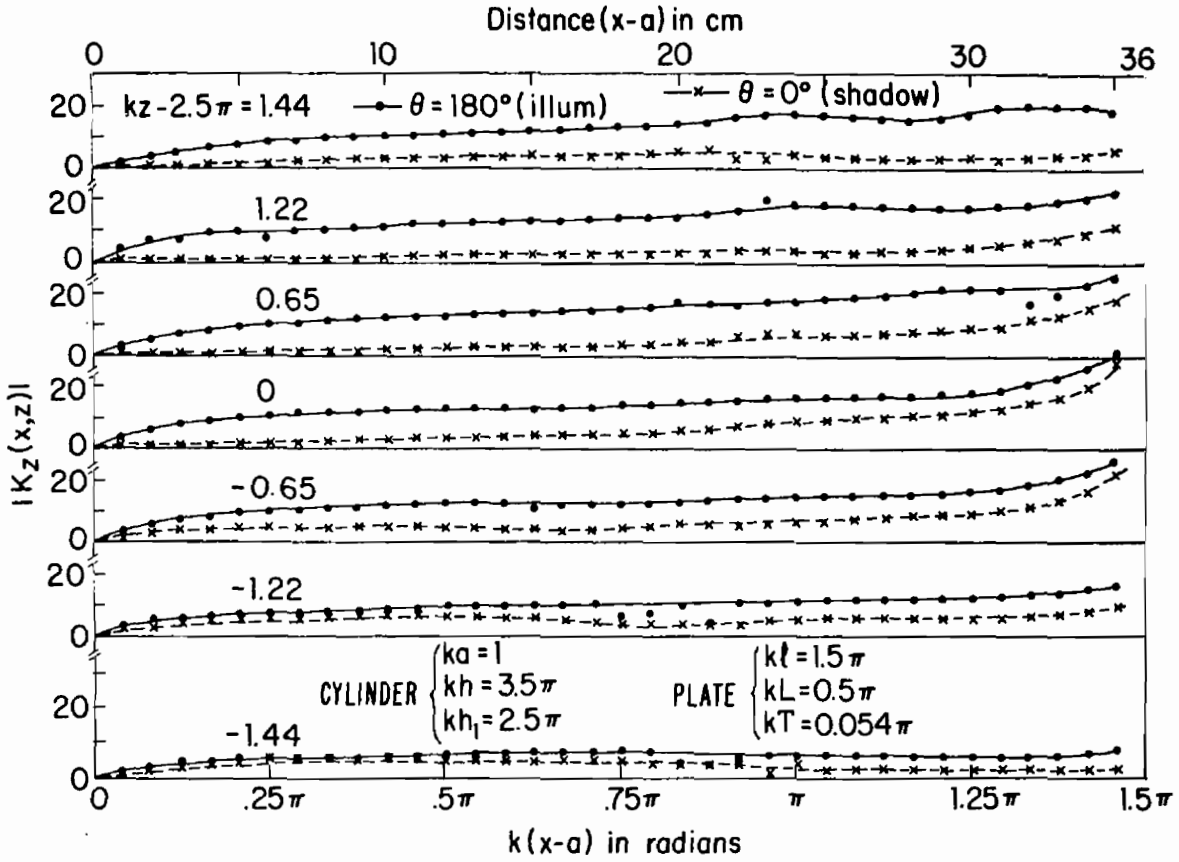

Fig. 143. Measured magnitude of surface density of current $K_z(x,z)$ on horizontal plate. ($|K|$ in arbitrary units.)

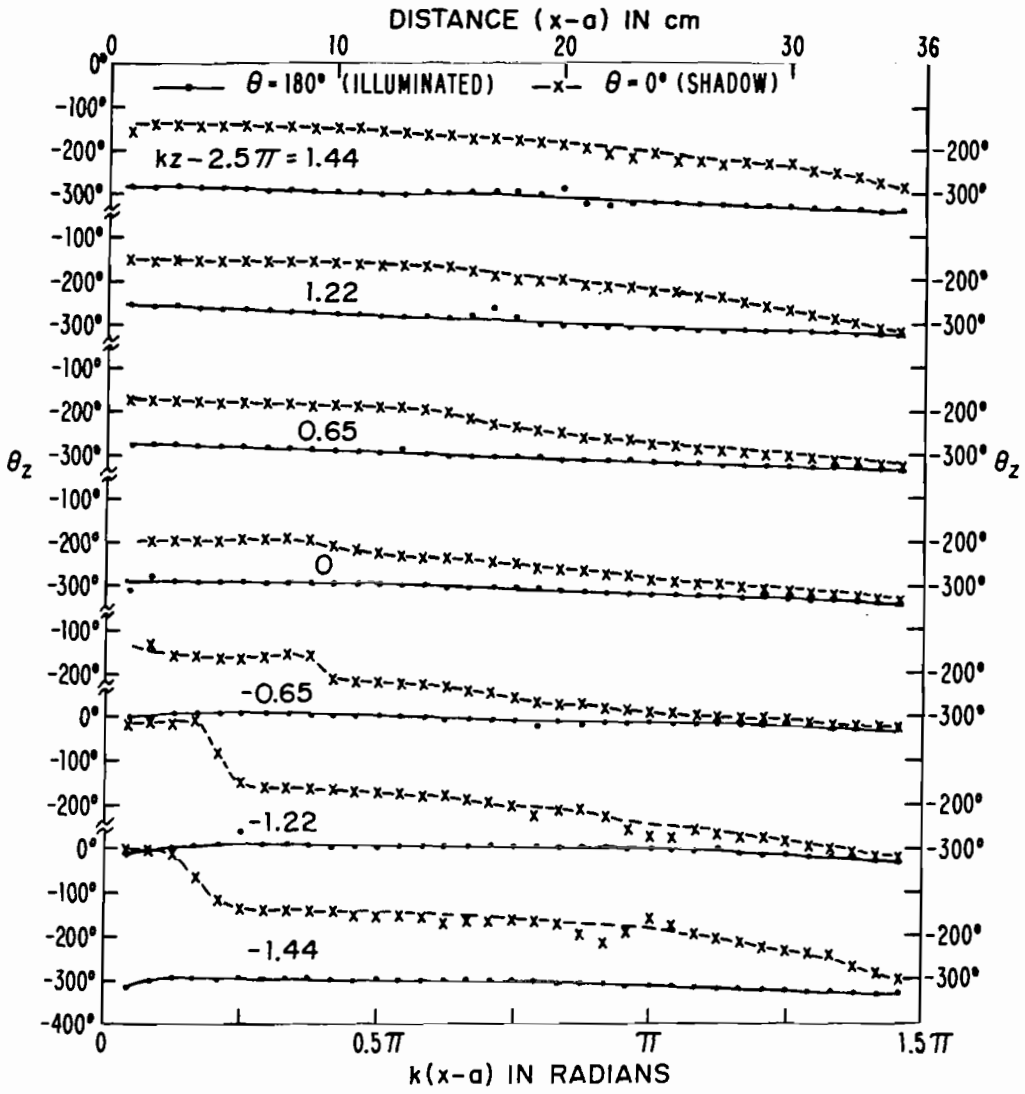

Fig. 144. Measured phase angle of surface density of current $K_z(x,z)$ on horizontal flat plate; ka = 1, kh = 3.5π, kh_1 = 2.5π; kℓ = 1.5π, kL = 0.5π, kT = 0.054π.

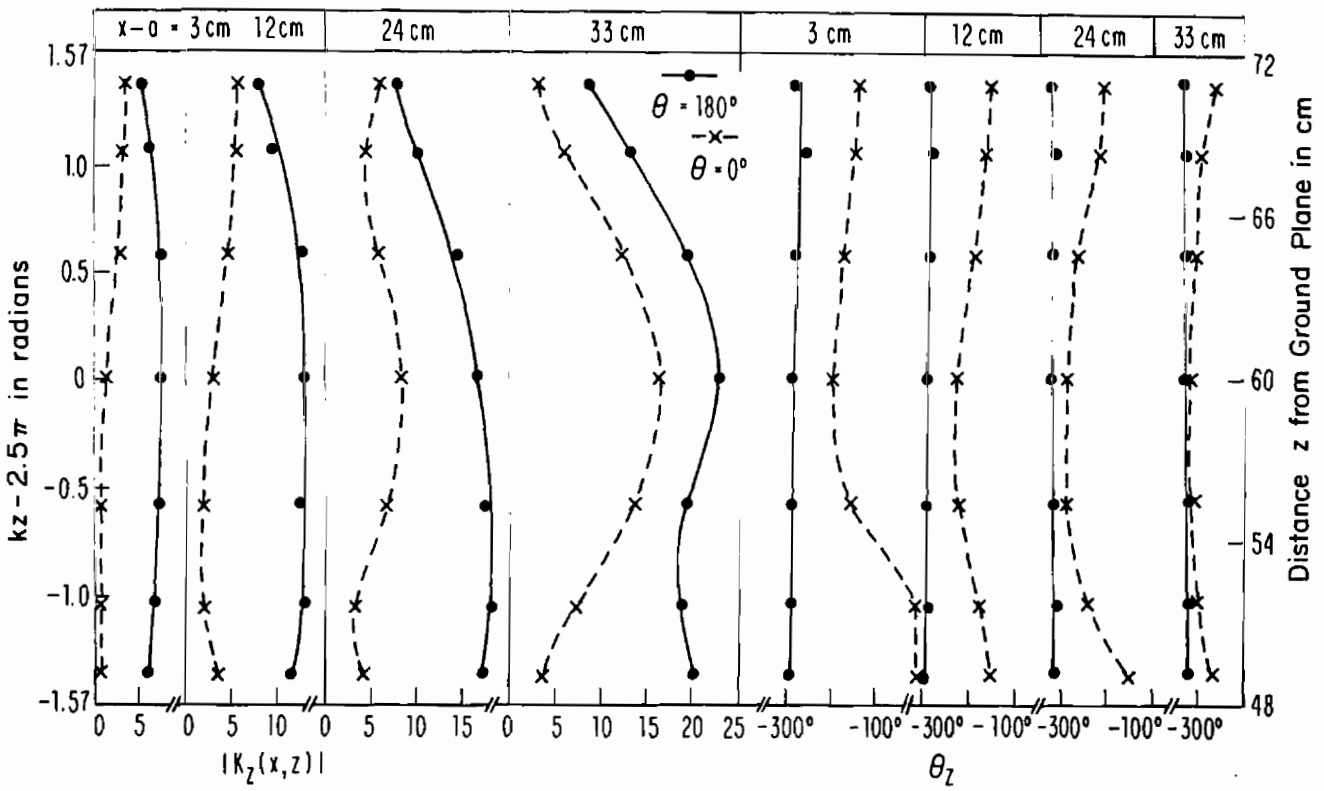

Fig. 145. Measured magnitude and phase angle of surface density of current $K_z(x,z)$ on horizontal flat plate; ka = 1, kh = 3.5π, kh_1 = 2.5π; kℓ = 1.5π, kL = 0.5π, kT = 0.054π. ($|K|$ in arbitrary units.)

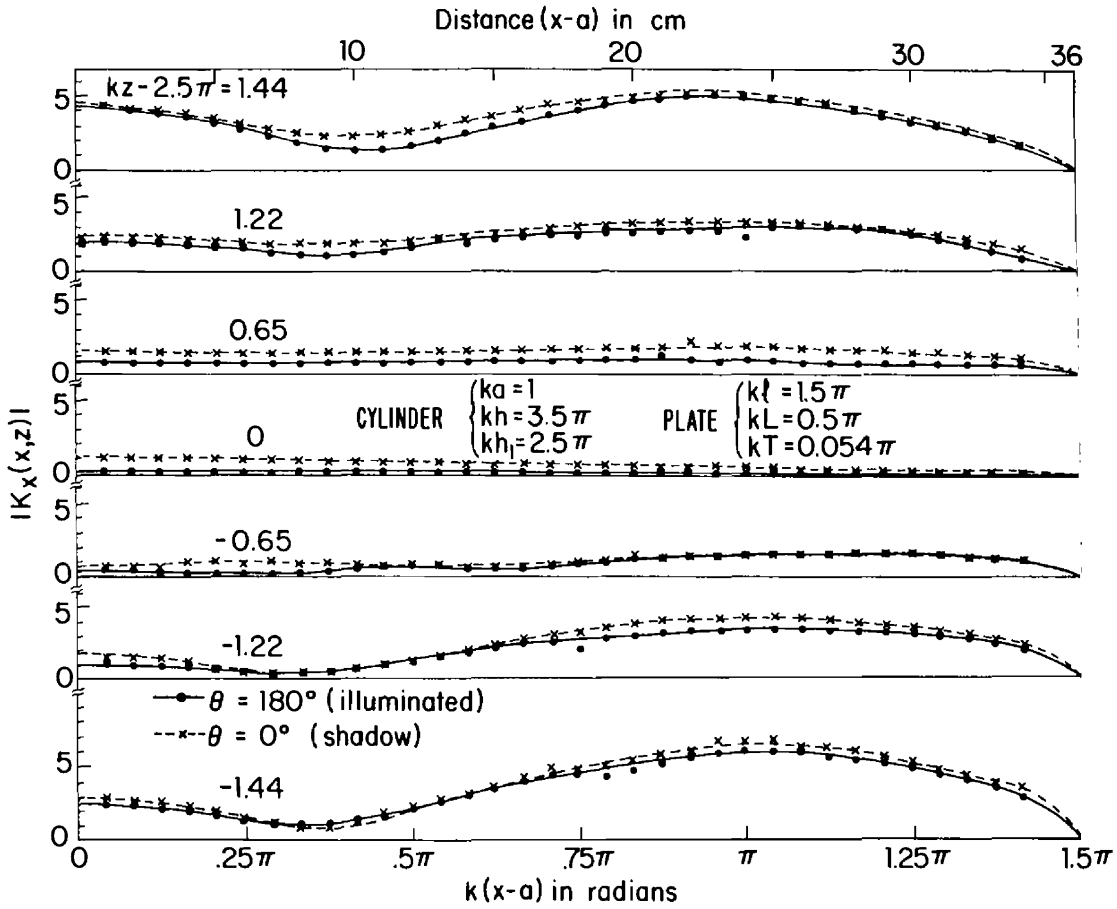

Fig. 146. Measured magnitude of surface density of current $K_x(x,z)$ on horizontal flat plate. ($|K|$ in arbitrary units.)

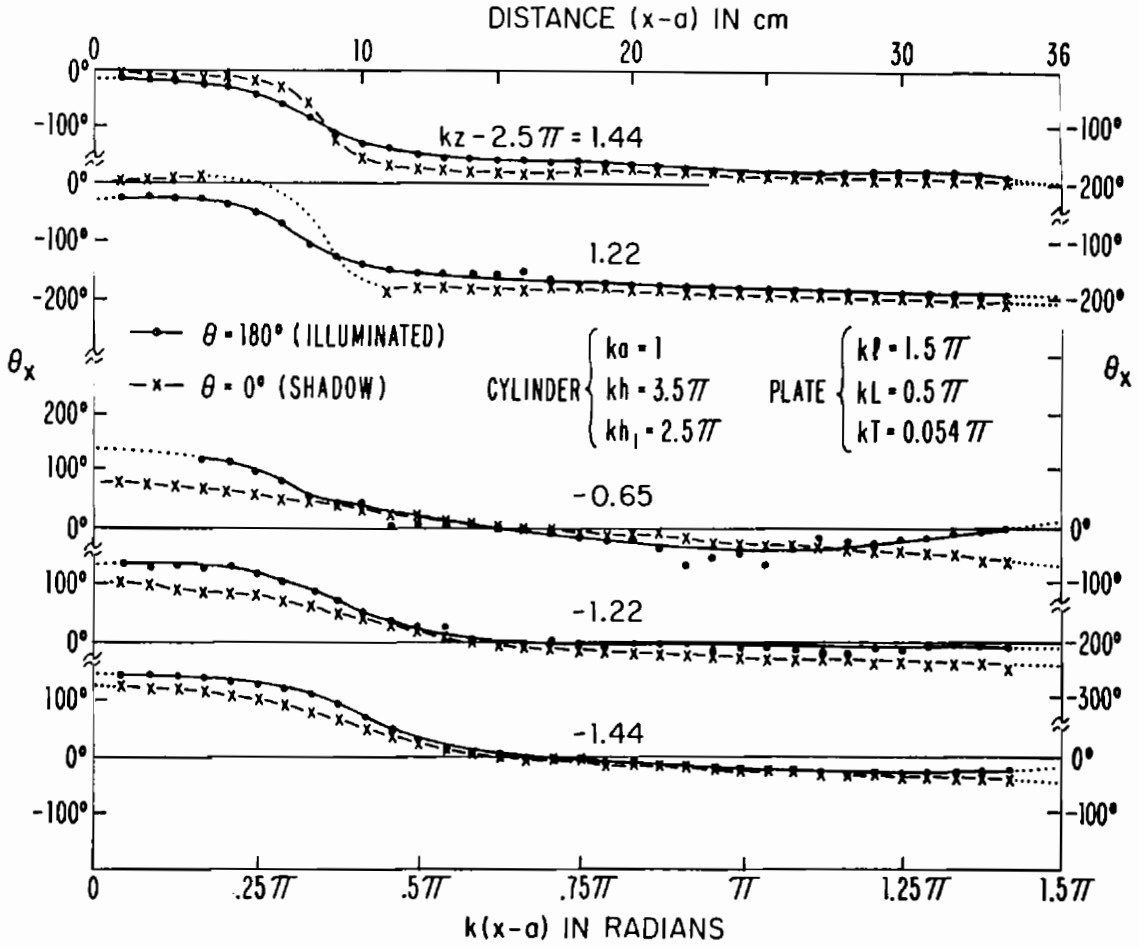

Fig. 147. Measured phase angle of surface density of current $K_x(x,z)$ on horizontal flat plate.

$K_z(x,z)$. This is seen in Fig. 148 which shows the transverse distribution of the longitudinal component $K_x(x,z)$ in both amplitude and phase. The former rises to quite large values at the edges. On the other hand, near the horizontal center line $K_x(x,z)$ is very small — so small that accurate measurements of the phase were not possible. It is for this reason that the curves for $kz - 2.5\pi = 0$ and 0.65 have been omitted in Fig. 147. Unlike $K_z(x,z)$, the currents $K_x(x,z)$ on the two sides of the plate are almost equal in magnitude and nearly in phase so that they individually go to zero at the open end, i.e., $K_x(\ell + a,z) \doteq 0$. Thus, there is a longitudinal standing wave of the component $K_x(x,z)$ primarily along and near the upper and lower edges. In effect, these currents oscillate between the positive and negative charge maxima at $k(x - a) = 0.5\pi$ and 1.5π. Simultaneously and partially superimposed on these maxima, there is a transverse standing wave of $K_z(x,z)$ across the width 2L of the plate. This is associated with the same maxima of the charge density. The two overlapping distributions of the two mutually perpendicular components of surface current combine to form a two-dimensional standing-wave pattern in which the current density vector $\vec{K}(x,z)$ changes in magnitude and direction. In general, it is elliptically polarized.

6. CONCLUSION

The distributions of current and charge density on all of the surfaces of a cross consisting of an electrically large tubular cylinder with a transverse plate have been determined experimentally when the cross is erected on a ground plane and illuminated by a normally incident, approximately plane wave. The observed distributions have been compared with those on crossed electrically thick cylinders and isolated cylinders. In general, the currents and charges on a horizontal plate are less closely coupled to the currents and charges on the vertical cylinder than are those on a horizontal cylinder. The distributions are relatively simple and provide an interesting set of data for the development and testing of numerical methods. They are a useful approximation of the surface currents and charges induced on an aircraft.

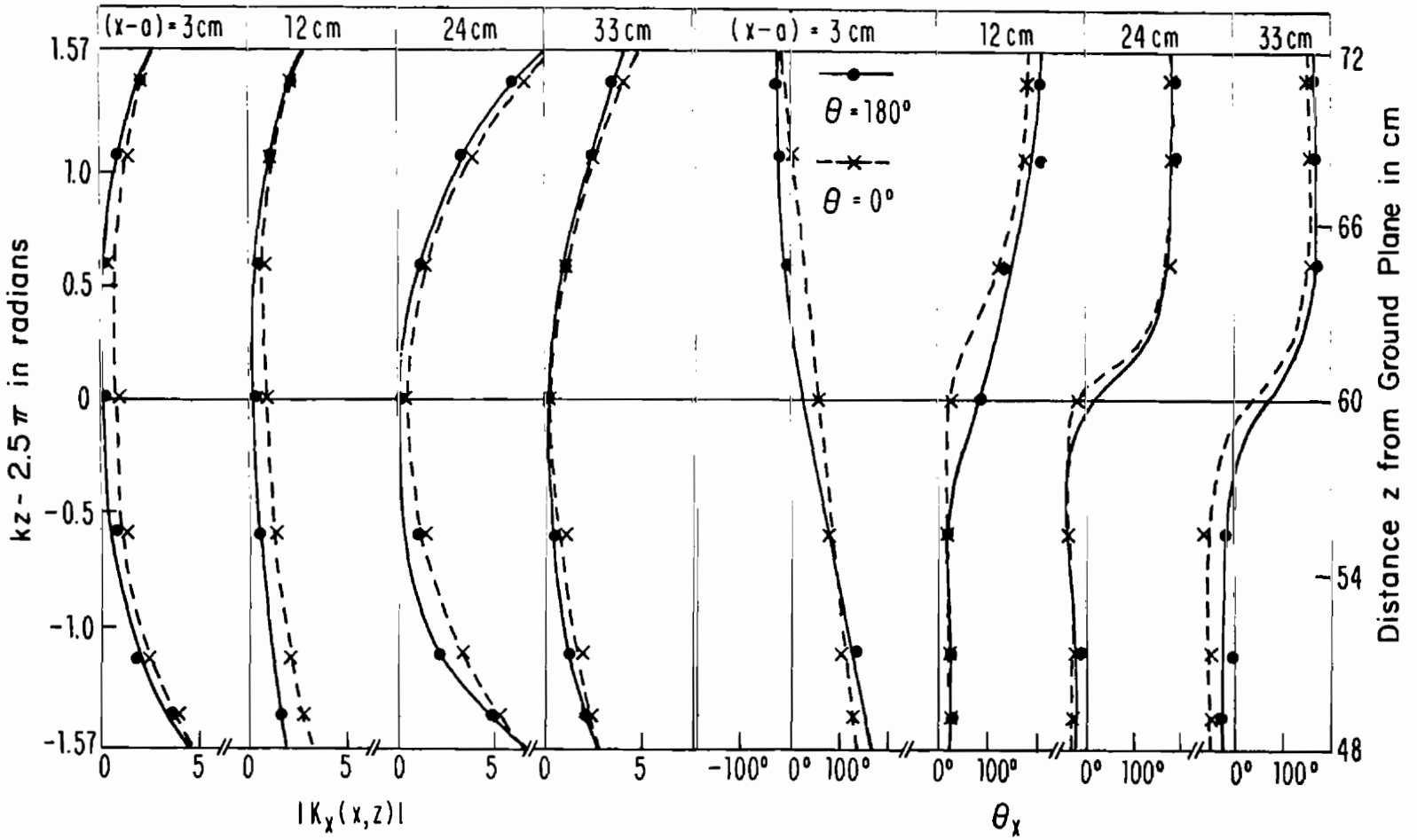

Fig. 148. Measured magnitude and phase angle of surface density of current $K_x(x,z)$ on horizontal flat plate; ka = 1, kh = 3.5π, kh_1 = 2.5π; kℓ = 1.5π, kL = 0.5π, kT = 0.054π. (|K| in arbitrary units.)

REFERENCES

1. Burton, R. W., and King, R. W. P., "Induced Currents and Charges on Thin Cylinders in a Time-Varying Electromagnetic Field," IEEE Trans. Electromagn. Compatib., EMC-17, pp. 140-155, August 1975, and also Interaction Note 257, August 1975.

2. Burton, R. W., and King, R. W. P., "Measured Currents and Charges on Thin Crossed Antennas in a Plane-Wave Field," IEEE Trans. Antennas Propagat., AP-23, pp. 657-664, September 1975, and also Interaction Note 258, September 1975.

3. King, R. W. P., and Wu, T. T., "Analysis of Crossed Wires in a Plane-Wave Field," IEEE Trans. Electromagn. Compatib., EMC-17, pp. 255-265, November 1975, and also Interaction Note 268, November 1975.

4. King, R. W. P., Burton, R. W., and Shen, L. C., "Induced Currents and Charges on Cylinders and Crossed Cylinders by an Electromagnetic Field," Interaction Note 335, December 1976.

5. King, R. W. P., "Currents Induced in a Wire Cross by a Plane Wave Incident at an Angle," IEEE Trans. Antennas Propagat., AP-25, pp. 775-781, November 1977.

6. Wu, T. T., and King, R. W. P., "The Tapered Antenna and Its Application to the Junction Problem for Thin Wires," IEEE Trans. Antennas Propagat., AP-24, pp. 42-45, January 1976, and also Interaction Note 269, January 1976.

7. Harrison, C. W., Jr., and King, R. W. P., "Excitation of a Coaxial Line Through a Transverse Slot," IEEE Trans. Electromagn. Compatib., EMC-14, pp. 107-112, November 1972, and also "Excitation of a Coaxial Line by the Propagation of an Electromagnetic Field Through a Transverse Slot in the Sheath", Interaction Note 87, October 1971.

8. Kao, C. C., "Electromagnetic Scattering from a Finite Tubular Cylinder: Numerical Solutions and Data. I. Development of Theory. II. Tables," Scientific Report No. 6 on A.F. Contract F19628-68-C-0030 (AFCRL-69-0535 (I,II)), Div. of Engrg. & Appl. Phys., Harvard University, December 1969.

9. Kao, C. C., "Three-Dimensional Electromagnetic Scattering from a Circular Tube of Finite Length," J. Appl. Phys., 40, pp. 4732-4740, November 1969.

10. Kao, C. C., "Electromagnetic Scattering from a Finite Tubular Cylinder: Numerical Solutions," Radio Science, 5, pp. 617-624, March 1970.

11. Kao, C. C., "Currents on Semi-Infinite Tube Illuminated by Electromagnetic Waves," Radio Science, 5, pp. 853-359, May 1970.

12. Bowman, J. J., Senior, T. B. A., and Uslenghi, P. L., Eds., Electromagnetic and Acoustic Scattering by Simple Shapes, North-Holland Publishing Co., Amsterdam, 1969.

13. King, R. W. P., and Wu, T. T., Scattering and Diffraction of Waves, Harvard University Press, Cambridge, MA, 1959.

14. Kao, C. C., "Measurements of Surface Currents on Finite Circular Tube Illuminated by an Electromagnetic Wave", IEEE Trans. Antennas Propagat., AP-18, pp. 569-573, July 1970.

15. Myers, J. M., "Symmetry in Scattering by a Strip," Ph.D. Thesis, Harvard University, Cambridge, MA, 1962.